https://doi.org/10.35662/unine-thesis-3052

University of Neuchâtel, Switzerland

Faculty of Sciences

Centre for Hydrogeology and Geothermics (CHYN)

Hydro-geological modeling of the Roussillon aquifer: Integrating geological knowledge uncertainties and geostatistical methods in groundwater modeling

Thesis presented for the degree of

Docteur ès sciences

by

Dall'Alba Valentin

Thesis advisor:	Prof. Philippe Renard, University of Neuchâtel (CH)
	Dr. Yvan Caballero, BRGM (FR)
Examiners:	Prof. Alain Dassargues, University of Liège (BE)
	Prof. Erwan Gloaguen, INRS (CA)
	Dr. Julien Straubhaar, University of Neuchâtel (CH)

Defended on the 12th of June 2023

unine
Université de Neuchâtel
Faculté des sciences

Rue Emile-Argand 11
CH-2000 Neuchâtel
doctorat.sciences@unine.ch

IMPRIMATUR POUR THESE DE DOCTORAT

La Faculté des sciences de l'Université de Neuchâtel autorise l'impression de la présente thèse soutenue par

Monsieur Valentin DALL'ALBA

Titre :

"Hydro-Geological modeling of the Roussillon aquifer: integrating geological knowledge, uncertainties and geostatistical methods in groundwater modeling"

sur le rapport des membres du jury composé comme suit:

- Prof. Philippe Renard, directeur de thèse, Université de Neuchâtel, Suisse
- Dr Julien Straubhaar, Université de Neuchâtel, Suisse
- Dr Yvan Caballero, BRGM, Montpellier, France
- Prof. Erwan Gloaguen, INRS, Québec, Canada
- Prof. Alain Dassargues, Université de Liège, Belgique

Neuchâtel, le 14 juillet 2023

Le Doyen, Prof. R. Bshary

Vous savez ce qui me fait bizarre?
Vous avez réussi à aligner cinq phrases de suite
sans faire la moindre citation...

Enki Bilal, Animal'z 2009

Remerciements

Je tiens tout d'abord à remercier mon directeur de thèse, le Professeur Philippe Renard, qui m'a orienté vers mon choix de master, m'a proposé une thèse au sein de son équipe et m'a accompagné et motivé tout au long de ces quatre années.

Je me souviens que lors de notre dernière année de Master au CHYN, alors que nous devions choisir un sujet de mémoire, Philippe nous a demandé, à mon ami François et à moi, lors d'une de nos discussions de fin de cours, si nous voulions vraiment consacrer six mois de notre temps à réaliser une étude hydrogéologique "classique", sous-entendu peu stimulante, un travail que nous risquions de reproduire tout au long de notre carrière. Il nous a alors proposé de consacrer ces six mois à apprendre de nouvelles choses, à coder et à développer nos compétences. Ce raisonnement infaillible nous a convaincus, et quelques semaines plus tard, François et moi nous sommes retrouvés en réunion avec Philippe pour décider de notre sujet de mémoire.

Deux options se présentaient à nous : reprendre un algorithme de modélisation de système karstique ou appliquer des méthodes géostatistiques pour modéliser un aquifère côtier en France. François a choisi la modélisation karstique, et quant à moi, j'ai opté pour l'aquifère côtier. Si ce choix peut sembler anodin, il a en réalité été très important puisque, six ans plus tard, François travaille toujours avec succès sur le développement de son algorithme PyKasso, que j'ai moi-même utilisé dans le cadre d'un travail de modélisation avec mon collègue Alexis. Quant à moi, je suis toujours engagé dans l'étude de mon aquifère côtier. Enfin, je termine.

Je ne pense pas avoir été particulièrement disposé à commencer une thèse, mais une fois de plus, la possibilité de travailler avec Philippe m'a convaincu. Je tiens donc à le remercier directement de m'avoir offert cette incroyable opportunité qu'est le travail de thèse. Pouvoir travailler de manière indépendante sur un projet personnel, apprendre, tester, me tromper, recommencer, enseigner, tout cela de manière continue pendant quatre ans. Merci à toi, Philippe, d'avoir toujours pris le temps de partager ta soif d'apprendre et de découvrir.

Je souhaite également remercier Yvan Caballero, mon co-encadrant de Master et de thèse au BRGM, qui a toujours été des plus amicaux envers moi lors de mes visites dans le sud et qui s'est battu avec nous pour la réalisation de ce projet. Merci pour ton soutien, ton expérience et ta sympathie contagieuse.

Je tiens également à remercier le BRGM pour le financement de cette thèse, ainsi que Sandra, Eric, Benoît et toutes les personnes du projet Dem'Eaux Roussillon et du BRGM de Montpellier pour leur temps et leur aide tout au long de ce projet.

Un grand merci également à mon jury de thèse, au Professeur Erwan Gloaguen, au Professeur Alain Dassargues et au Dr Julien Straubhaar pour leurs corrections de manuscrits et les discussions lors de la soutenance, qui m'ont permis de clôturer la dernière page mentale de ce parcours de thèse.

Un grand merci également à toi, Julien, membre du labo, collègue, membre de mon jury, soutien constant pour la modélisation et médecin de tous les petits bobos informatiques. Je ne retire que des super expériences d'avoir pu travailler avec toi.

Bien que nous commencions souvent une thèse un peu seuls, perdus dans cet objectif un peu abstrait, je pense qu'il nous est impossible de la continuer et de la terminer sans être aidés, entourés de collègues et d'amis qui nous permettent de rafraîchir notre esprit et de réorienter nos pensées. Je tiens donc à remercier ces personnes : François, Arnaud, Adeline, Léa, Thanushika, Morgan, Théo, Ludovic et Hugo. Un remerciement particulier à Réza, collègue et ami, qui m'a toujours permis de relativiser mes problèmes passagers. Un deuxième grand merci à Alexis, avec qui j'ai partagé des articles, des conférences, des aventures aux quatre coins du monde et sans qui je n'aurais pas pu surmonter la moitié des petits et grands obstacles jalonnant le parcours de la thèse.

Merci à mes amis du Master, de Genève, de Lausanne, à Aurélien, Médéric, Romain, Anaïs, Charlène, Olivier, Elsa, Martin, Victor, Margaux, Jean-David, Prisca, Agnese, Babak, Olivier, Charlotte, Marine et à tous ceux que je ne peux citer ici par peur d'en oublier. Vous êtes une super source d'inspiration et vous êtes formidables !

Un petit paragraphe pour un immense merci à Armelle, qui a toujours cru en moi, qui m'a permis de m'évader lors de nos nombreuses et magnifiques dates qui n'ont été que bouffées d'air frais et de plaisir lors de ces deux dernières années !

Enfin, je voudrais remercier ma famille, qui m'a toujours recadré, motivé, laissé libre de mes choix et m'a toujours soutenu. Merci Papa, Maman, Mamie, Josette, Elisa, mes tantes et oncles, cousins et cousines, et surtout merci à Tom et Léa d'être le plus bel exemple qu'il puisse exister pour un grand frère.

Je pense avoir été très chanceux d'avoir pu vivre pendant quatre ans une expérience académique que je considère comme complète, qui m'a permis de travailler librement sur mon projet de recherche, de participer à des projets académiques variés avec de nombreux instituts, de participer à des conférences internationales et de valoriser mon travail à travers la publication d'articles scientifiques. Je suis extrêmement reconnaissant envers l'Université de Neuchâtel, l'institut du CHYN, mon laboratoire de recherche et mes collègues de m'avoir offert cette opportunité. Je tiens à exprimer ma gratitude envers tous mes collègues et professeurs qui ont contribué de différentes manières à ce projet.

À vous tous et à ceux que j'ai oubliés, merci encore pour ces quatre années de vie qui m'ont enrichi d'une manière incommensurable.

Abstract

The presented study focuses on the geological and hydrodynamic modeling of the Roussillon aquifer. Located in southern France, near the Mediterranean Sea, the Roussillon plain covers an area of over 800 km^2 and serves as the most important source of fresh water for the local community, supporting various needs such as irrigation, drinking water, and industrial usage. This aquifer is situated in one of the driest regions of France. Additionally, the aquifer experiences heavy water abstraction, mainly for drinking and agricultural purposes, leading to a steady decline in its water level over the years. The region is also affected by climatic changes, including rising sea levels and potential disruptions in precipitation patterns, which further impact the aquifer's water availability. Balancing water management and conservation in the face of increasing population and climate change poses significant challenges for the Roussillon aquifer. The primary aim of the thesis is to enhance the geological understanding of the Roussillon aquifer and develop a hydrodynamic model to gain deeper insights into the functioning of the aquifer system. Additionally, the study aimed to create a solid foundation for investigating the potential consequences of climate change on this essential regional resource.

The geological model consists of three main units, starting with the deepest unit, the Marine Pliocene unit, followed by the Continental Pliocene unit, and finally at the top the Quaternary unit. The initial phase of this work involved compiling a comprehensive geological database using onshore and offshore data sets to develop a conceptual understanding of the aquifer's structures and to interpolate the main 2D surfaces that separate the 3D geological model. Within the Continental Pliocene layer, four sub-intervals were defined, and the elevation map of the three surfaces dividing these sub-intervals was mapped and interpolated using geophysical logs and offshore seismic data. The geological data set, although limited in resolution and coverage, served as conditioning data for the geostatistical simulation of the Continental Pliocene layer.

We then used the multiple-point simulation approach (MPS) to simulate realistic lithofacies patterns representative of the sediment spatial distribution in the Continental Pliocene layer. The 3D model of the Continental Pliocene layer was created by stacking 2D simulations controlled by vertical conditioning

sampling. The results demonstrated satisfactory reproduction of sedimentary structures at the regional scale.

In addition to the MPS simulation, two other approaches, a depth-related approach and a Sequential Indicator Simulation (SIS) set, were used to generate hydro-physical property fields for the aquifer. The depth-related approach is based on the interpretation of hydraulic pumping tests, to assign hydraulic conductivity values based on the cell's depth in the grid. The SIS employed a variogram-based algorithm to simulate simple lithofacies structures (more simple compared to the MPS models). These three sets of hydraulic conductivity and specific storage values are used to feed the hydrodynamic simulations and estimate the propagated uncertainty of the sedimentological models on the hydrodynamic simulations.

This work then focuses on defining the conceptual hydrodynamical model of the Roussillon aquifer. We present the main boundary conditions, their associated budgets, available piezometric observations, and the main modeling assumptions, linked to the different components of the MODFLOW 6 hydrodynamic model.

In the first modeling step, a steady-state calibration is performed to calibrate river parameters and mean hydraulic conductivity of simulated facies with the goal of preserving the simulated lithofacies patterns while matching the hydrodynamic observations. Once calibrated, we used these parameters for transient hydrodynamic models over a 20 years period. The three model approaches are used and compared in this study.

It appears that reproducing the piezometric transient observation series presented some difficulties, with the models failing to capture the main trend of the piezometric levels on some locations. The reproduction of these piezometric series suffered from limited data availability, simplified river systems, and uncertainties regarding the local hydraulic conductivity and specific storage parameters. To better reproduce the piezometric series, this work ends with a short study on the use of the ES-MDA approach to attempt local corrections of the hydraulic conductivity and specific storage parameters. These initial tests faced limitations, as many forward models failed to converge during the process, limiting the applicability of the calibration process.

Overall, this work proposes a unique regional comparison of sedimentological modeling approaches and their influence on hydrodynamic simulations. It also identifies directions for improving the aquifer model's performance. Obtaining more reliable observation data series, as well as more onshore sedimentological information, especially in areas with significant deviations from simulated water levels, is highly recommended for improving the Roussillon hydrogeological model. This would aid in better understanding the system's behavior and facilitate localized modifications of the sedimentological model and the hy-

drodynamic conditions. Despite the challenges faced, the study contributes to understanding the aquifer's transient state, emphasizing the importance of sedimentological models in hydrodynamic studies, and identifying major sources of uncertainty in the current model of the Roussillon aquifer.

Keywords

Hydro-Geological modeling, Geostatistic, Multiple-point Statistics (MPS), Hydrodynamical modeling, MODFLOW6, Roussillon aquifer.

Résumé

Ce travail de thèse porte sur la modélisation géologique et hydrodynamique de l'aquifère du Roussillon, en mettant l'accent sur la transition d'un modèle géologique détaillé, utilisant la méthode géostatistique de simulation multi-point (MPS), vers des modèles hydrodynamiques.

La première étape de ce travail de thèse a consisté à créer les enveloppes du modèle géologique 3D du Roussillon. Les principales unités géologiques de l'aquifère du Roussillon comprennent le Pliocène marin, le Pliocène continental et le Quaternaire. La compilation d'une base de données géologiques, composés de logs géophysiques et de ligne sismiques, a permis de comprendre les structures de l'aquifère et d'interpoler les surfaces 2D qui délimitent le modèle géologique 3D.

Une fois les enveloppes interpolées, la seconde étape de modélisation de ce travail s'est concentrée sur la simulation des faciès sédimentaire composant l'aquifère du Pliocène Continental. L'utilisation de l'approche de simulation multi-point (MPS) a permis de créer des modèles réalistes de faciès sédimentaire dans l'unité du Pliocène continental, en reproduisant des structures alluviales à l'échelle régionale.

En complément de la simulation MPS, deux autres modèles sédimentaires ont été créés. Le premier est déterministe et se base sur l'interprétation d'essais de pompage pour caractériser les propriétés physiques du Pliocène Continental. Le second utilise une approche géostatistique appelée simulations séquentielles d'indicateurs (SIS) pour générer les propriétés hydrodynamiques de l'aquifère. Cette seconde approche géostatistique est plus couramment utilisée que le MPS et est plus simple à mettre en œuvre.

La troisième étape de ce travail consiste en la définition du modèle hydrodynamique de l'aquifère du Roussillon. Le modèle hydrodynamique a été réalisé en considérant les conditions aux limites, les budgets de prélèvement associés, les observations piézométriques disponibles, et a été pré-calibrer en régime d'écoulement permanent dans une première phase de modélisation. Les modèle d'écoulement ont été réalisés avec le logiciel MODFLOW 6.

La dernière étape de modélisation consiste en la création de modèle d'écoulement en régime transitoire ainsi que dans la création d'une approche de calibration des paramètres physique du modèle MPS du Pliocène Continental. Un défi important de ce travail réside dans la conciliation des modèles géologiques avec les données hydrodynamiques, ce qui nécessite une approche spécifique pour garantir de préserver les structures sédimentaires simulées, lors du processus de calibration. Il convient de noter que peu d'études existent sur la calibration des modèles MPS régionaux, et que souvent, les processus de calibration ne prennent pas en compte les éléments structuraux géologiques.

La comparaison des approches de modélisation sédimentologique, effectuée en régime d'écoulement permanent et transitoire, met en avant une homogénéité des résultats entre les différentes approches. Les résultats en régime permanent sont satisfaisants pour les trois approches, mais peine à reproduire certains signaux en régime transitoire. Les problèmes des modèles en régime transitoire sont probablement dus à un problème d'initialisation du système hydrodynamique et de calibration des conditions limites.

Ce travail propose donc une comparaison d'approches de modélisation sédimentologique et de leur impact sur les simulations hydrodynamiques. Il met en évidence des améliorations potentielles pour le modèle hydrogéologique de l'aquifère du Roussillon. Des données d'observation plus fiables et des informations sédimentologiques supplémentaires sont fortement recommandées, en particulier dans les zones présentant des différences significatives par rapport aux niveaux d'eau simulés, afin d'améliorer le modèle hydrogéologique. Cela permettrait de mieux comprendre le fonctionnement du système et de faciliter les ajustements locaux du modèle sédimentologique et des conditions hydrodynamiques. Malgré les difficultés rencontrées, notamment concernant la reproduction de certain signal piézométrique lors des simulations en régime transitoire, cette étude contribue à la compréhension de l'état de l'aquifère en identifiant les principales sources d'incertitude dans le modèle actuel de l'aquifère du Roussillon.

Mots-clés

Modélisation hydro-géologique, Géostatistique, Statistiques multipoint (MPS), Modélisation hydrodynamique, MODFLOW6, Aquifère du Roussillon.

Contents

Chapter 1

Introduction

Water is an essential resource for the life and development of our societies. Additionally, of being use as drinking water, it is used for agriculture, industry, or tourism activities. This resource is precious and is likely to undergo at least a mid-stress in the near future due to the global climatic changes that face our society. More than 30% of the freshwater used worldwide by our society came from groundwater extraction [Famiglietti, 2014]. This percentage is likely to rise in the next decade following the global increase of temperatures, of surface water scarcity, of the global world population, and the disturbance of the global water temporal and local distribution [IPCC, 2022]. Groundwater is stored in aquifers, which can display very different characteristics around the world, depending on their bearing materials (sandy, carbonate, or granitic fractured reservoirs), the climatic context in which they are located, and the intensity of pumping to which they are subjected.

Coastal aquifers harbor a fragile groundwater resource, and represent one of the main water resource for a large part of the world population. Martínez et al. [2007] show that 41% of the world population, representing more than 2.5 billion of people, lives within 100 km, inland, from the coastline. Coastal reservoirs can represent large fresh water resources since they can extend over the coastal area into the sea domain [Post et al., 2013]. However, this resource is often considered endangered due to intensive exploitation and contact with seawater, which can contaminate fresh coastal groundwater resources. Seawater intrusion can happen in two main ways: when the piezometric level drops below sea level, or due to the density effect. The density effect occurs because saltwater has a higher density than freshwater, making it easier for seawater to intrude into aquifers. This process is facilitated by the changing hydraulic gradient where the seawater and freshwater fronts meet, leading to accelerated circulation. In addition to natural processes, intense storms or flooding events in low coastal areas can also contribute to seawater intrusion and contamination of wells. These events can be linked to a decrease in recharge or excessive extraction of groundwater from aquifers. Wells that are located in vulnerable areas and are

not adequately protected or have been damaged are particularly susceptible to seawater intrusion [Calvache and Pulido-Bosch, 1997; Guo and Jiao, 2007; Shi and Jiao, 2014]. Finally, climatic changes involving global sea level rise can also have a large impact on the quality and the amount of resource available in these areas [Masterson and Garabedian, 2007; McGranahan et al., 2007; Werner and Simmons, 2009; Caballero and Ladouche, 2015].

This thesis project focuses on the characterization and modeling of the Roussillon coastal aquifer, located in the southern part of France (Fig. 1.1). This aquifer is of a regional importance as it is the main freshwater resource of the area. This resource is under an increasing stress since a few decades due to the touristic activities of the region, the increase in population, the agriculture use and the present and future climatic conditions. The main objective of the thesis is to improve the geological knowledge on this aquifer and build a hydrodynamical model to better understand the system, as well as establishing a suitable ground to study the climatic change that will likely affect this regional resource.

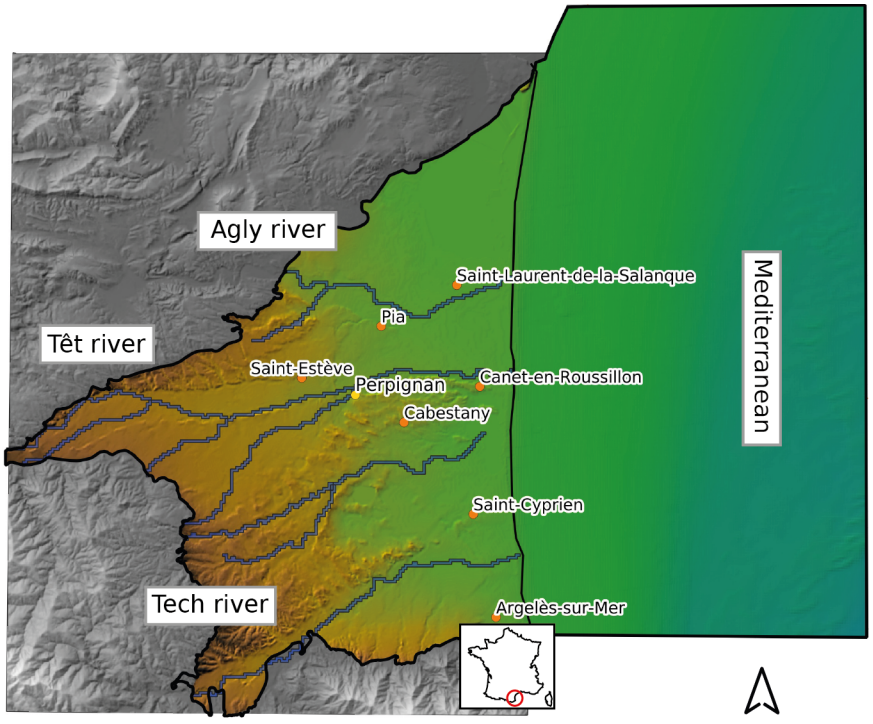

Figure 1.1: Roussillon region. The colored region corresponds to the extent of the study site.

1.1 Regional context

The Roussillon aquifer is an underground reservoir of water-bearing sediments that is located near Perpignan, in the Roussillon region, south of France. It is an important source of fresh water for the local community and is used for a variety of purposes, including irrigation, drinking water and industrial uses. This alluvial plain and its aquifer cover an area of more than 800 km^2 inland, and is located in one of the driest regions of France, with an average annual rainfall of 600 mm (2000-2020 average from SAFRAN[1] data). This aquifer is considered a coastal aquifer as it extends both inland and offshore and is subject to interaction with the saline waters of the Mediterranean Sea [Aunay, 2007]. Coastal aquifers are usually subject to many stresses and are considered most likely to undergo degradation with the current and potential future climate changes [Werner and Simmons, 2009]. In addition, coastal aquifers can be vulnerable to contamination from seawater intrusion, pollutants and other sources, and it is important to carefully manage and protect these valuable resources.

The Roussillon aquifer is the region's main freshwater source, accounting for 90% of the drinking water supply. It is also used for agricultural activities, which have historically been widespread in the area, putting a second stress on the resource. Touristic activities are also important in the plain, especially during the summer, as the population in the seashore region can almost double, which causes a large stress on the water resource during its driest period. In total, water abstraction from the Roussillon aquifer reaches around 80 Mm^3 per year, which has led to a steady decline in the level of the aquifer throughout the plain in recent decades [Caballero et al., 2022b].

In addition, this region is affected by climatic changes [Caballero and Ladouche, 2015; IPCC, 2022]. The sea level is likely to rise, while the precipitation that recharges the aquifer is projected to either decrease annually or be spatially and temporally disturbed, with more intense rain events occurring, leading to more probable flooding events [IPCC, 2022]. With the temporal distribution of rainfall events being disturbed, the aquifer may likely suffer from less water available to recharge its reservoirs, leading to an annual decrease in the amount of water available. Other climatic factors will have a direct or indirect impact on water resources through changes in water use, local vegetation or even local and global economic factors.

All these elements are putting the Roussillon aquifer under stress. The past, present, and future decisions on how to manage this resource were, are and will be challenging to take, especially in the global context of growing population increase and climate changes.

[1] Système d'Analyse Fournissant des Renseignements Atmosphériques à la Neige - Météo-France

1.2 Origin of the aquifer

In order to describe the Roussillon aquifer, we briefly present the main geological events that led to the creation of this aquifer.

The Roussillon aquifer is considered to be a multi-layered aquifer, and is one of the sedimentary systems of the passive margin of the Gulf du Lion [Duvail, 2008]. This aquifer founds its origin with the closing of the Mediterranean Sea during the Messinian salinity crisis, that almost dried out the Mediterranean Sea. The large sea level drop creates a large eroding surface in the Miocene sediment near the ancient coastline location. This eroded surface created an empty space that was then filled by Pliocene sediments at the end of the Messinian salinity crisis [Clauzon et al., 2015].

If we look at the different geological water bearing bodies, we can divide the Roussillon aquifer into three sub-aquifers, going from top to bottom:

- Quaternary aquifer (abbreviated as QT): mainly composed of Quaternary alluvial deposits.
- Continental Pliocene aquifer (abbreviated as PC): a complex system of ancient alluvial channel deposits.
- Marine Pliocene aquifer (abbreviated as PMS): sitting on top of the Miocene eroding surface, this aquifer is mainly composed of a mix of sand and clay deposits originating from large prograding Gilbert delta structures.

This Roussillon aquifer is complex in its internal composition with high heterogeneity and thus requires specific approaches in order to be modeled correctly. A good geological modeling framework is an essential part of the modeling process when carrying out a regional hydrodynamical study [Naranjo-Fernández et al., 2018].

1.3 The project

In 2018, the Dem'Eaux Roussillon project was launched by the French Geological Survey (BRGM), in partnership with various local and regional partners from industry, water management agencies and decision makers [Caballero et al., 2022a]. This 5 years project aimed to improve the general understanding of the behavior of the Roussillon aquifer. More specifically, the project aimed to create a regional geological and hydrogeological model, to assess the regional economic and sociological use of the water resource, and to study some specific local water uses and their interaction with the surrounding environment.

The water resource in this region is scarce and needs to be protected. A good understanding of its seasonal distribution and dynamics, the available amount that can be withdrawn from it, or the future uses and needs of this resource are key information for decision-makers in order to create appropriate action plans for sustainable water use and to protect tourism activities, agriculture and, most importantly, the regional groundwater resource in the context of a growing population, climate changes and complex economical decisions in the present and near future.

It is not frequent that a project of this magnitude is launched, bringing together so many specialists from so many different fields. Geologists, hydrogeologists, geochemists and economists have all worked on this project during 5 years to collect data and gain valuable insights by integrating all natural and anthropological issues. The Roussillon project finished in early 2023, and has led to the production of numerous reports and numerous high-quality data sets[2]. Bachelor's and Master's theses have been supervised jointly between the BRGM and universities, and scientific articles have been published in various scientific reviews [Caballero et al., 2022b; Lanini et al., 2022; Fioravanti et al., 2022; Duvail et al., 2022, 2021; Dall'Alba et al., 2020].

1.4 Scope of the research

This PhD project had the unique opportunity to be associated with, and cofunded, by the Dem'Eaux Roussillon project. The proposal was to interact on some of the leading research topics such as the geological modeling of the aquifer envelopes, the modeling of the internal structures of the main aquifer, the Continental Pliocene, and the hydrogeological modeling in steady-state and in a transient regime of the Roussillon plain.

Benefiting from the support of the specialists working within the project, this thesis aimed to test new approaches and algorithms on a regional study and to provide new insights into the problem at hand, the characterization of the

[2] https://www.brgm.fr/fr/reference-projet-acheve/dem-eaux-roussillon-mieux-connaitre-volumes-eau-pouvant-etre-preleves

water resource of the Roussillon aquifer. Taking advantage of the work and data produced by the main team of the project, this research focused on two main parts:

- Modeling the spatial distribution of the sediments that make up the Continental Pliocene layer of the aquifer using an advanced Multi-Point Statistical algorithm, and generating an ensemble of geostatistical models.
- Set up a steady-state and a transient model for hydrodynamical simulations using open source code and the MODFLOW 6 software [Langevin et al., 2017], and estimate the uncertainty associated with the different physical parameters on the model output and resource characterization.

Relevance of the stochastic approach

Two different paradigms coexist in hydrogeological and geological simulations; the deterministic approach and the stochastic approach. Deterministic and stochastic approaches are two methods for modeling data and making predictions. The main difference between them is in the way they deal with uncertainty. On one hand, deterministic models are based on the idea of creating a unique representation of the reality, using mathematical equations to describe the behavior of a system and making predictions based on them. These models do not take into account uncertainty or variability in data sets, and assume that the data can be described by a single set of calibrated parameters. On the other hand, the stochastic approaches are based on probabilistic assumptions, which aims to estimate the uncertainty on the answer of a problem, by simulating several equiprobable realities, by taking into account the uncertainty of the input data or parameters, and then calculating the propagated uncertainty.

In geology and hydrogeology, data sets are often scarce compared to the simulation domain. Moreover, even when data are available, it is difficult to determine how representative and unbiased is a data set [McMillan et al., 2018]. Non-representative data sets can result from sampling bias, measurement error or miscalculation in the processing of raw data and can lead to misleading conceptual descriptions of the study area and, later, to the creation of non-realistic models. The use of a stochastic approach, as opposed to a deterministic one, can overcome some of these limitations [Hu and Chugunova, 2008; Renard et al., 2013]. The stochastic approach works with a set of equiprobable simulations, from which it is possible to study the ensemble variability of a system and the effect of the associated parameter's uncertainties on the model's outcomes.

A simple stochastic approach is the Monte Carlo method, where random samples are taken from a prior distribution of parameters to estimate the expected value of a function or parameter [Metropolis and Ulam, 1949]. Each of the models can then be used, creating multiple realizations and multiple outputs from which descriptive statistics can be calculated. This approach of using

multiple models to estimate the final uncertainty of a system is essential for non-linear processes, where the uncertainty of an input data set cannot be easily propagated to the desired final results. The stochastic approach is also able to estimate the sensitivity of the model to its parameters, which can be really useful when developing a conceptual model. A correct estimation of the uncertainty of the model outputs is essential when using these models for decision-making, as understanding the performance of a model and its limitations is as important as the final outputs of the model [Freeze et al., 1990]. As uncertainty is present in all the different steps of a project, it is important, if not essential, to consider the stochastic approach in this type of large regional complex geological project.

The creation of geological and sedimentological models is a non-unique process due to the many choices that must be made during their conception. The choice of geological and sedimentological depositional concepts, the choice of modeling strategy (stochastic or deterministic), and the type of algorithm used for simulations (Multiple-point Statistic or MPS, Sequential Gaussian Simulation or SGS, Kriging, Truncated Gaussian Simulation or TGS, ...) are all factors that influence the final models. One set of data processed with two different modeling approaches can produce two really different results and lead to two different final conclusions about the system under study.

The relevance of the stochastic approach does not end with the geological models that feeds the hydrodynamical simulations. Other important hydrodynamical stress factors, such as the recharge values, the amount of water pumped out of the system for drinking or agricultural purposes, or the boundary conditions, also have a decisive influence on the model outputs. While some of these stress factors can be obtained from accurate sources and their associated uncertainties may be manageable for local case studies, the doubt on the data set and measurement error generally increases with the size of the study area. Wells may be omitted from the database, precipitation or, more specifically, the recharge estimation process may suffer from zonal approximation and uncalibrated transfer functions, or even defined fluxes imposed at the boundary may suffer from subjective assignment or approximation. For example, in the Roussillon plain, if we look at the available data, the total amount of water extracted for agricultural use has increased by a factor of ten between 2017 and 2018, which was surprising [Lanini et al., 2022]. It turns out that the legislation had changed between these two years, resulting in many old, undeclared wells finally being regularized to the authorities. This is a good example of how a data set should be treated with care and sometimes considered unreliable.

All of these parameters' inaccuracy can affect the output of the final models. By defining pre-calibrated distributions of these parameters and then sampling from them, the stochastic approach can be used as a powerful tool to estimate the uncertainty of a complex hydrodynamical system.

The Roussillon case study

As briefly introduced, the methodology followed in this thesis project focuses in modeling in a stochastic framework the internal sedimentological facies distribution of the Continental Pliocene layer of the aquifer, and then using the ensemble of created models as input for a stochastic uncertainty analysis regarding the hydrodynamical behavior of the aquifer system. We will explore different approaches, compare them, and understand the impact of each approach on the hydrodynamical model's outputs.

The first step therefore focused on the creation of the geological envelopes of the aquifers, the processing of the available data and the creation of a conceptual geological model describing the spatial distribution of the litho-facies present in the Continental Pliocene layer. This specific layer contains the most important water resource of the aquifer and is composed of a complex spatial arrangements of alluvial sediments. It has been shown that adding complexity during the spatial modeling of the internal structure of such systems helps to improve the final reproduction of the hydrodynamical signals [Hu and Chugunova, 2008]. In the case of the Continental Pliocene, the layer is described as an entanglement of alluvial channels that represent potential preferential water storage units.

We propose to use the advanced geostatistical Multiple-point Statistics algorithm (MPS) DeeSse [Straubhaar, 2019], to model the 3D facies spatial distribution of the litho-facies composing the Continental Pliocene aquifer. The use of MPS relies on the definition of a conceptual representation of the system, this conceptual representation is called a training data set (TDS) (also referred before as training image) [Strebelle et al., 2002]. A TDS represents the spatial distribution of the facies aimed to be modeled and incorporates expert knowledge. MPS is a stochastic approach designed to overcome the limitations of the two-point statistical approach, and is able to compensate for the potential lack of information of a small conditioning data set by using the additional conceptual description provided by the TDS. Moreover, compared to classical Gaussian or Multi-Gaussian approaches that are based on two-point statistics, the MPS one is able to simulate more complex realistic patterns such as river braided systems, and can handle a large or small number of conditioning data [Strebelle et al., 2002; Mariethoz et al., 2010; Straubhaar et al., 2020a,b; Straubhaar and Renard, 2021].

The DeeSse algorithm proposes a simulation approach that is able to work with multiple TDSs, auxiliary data maps (created by experts or derived from field data), and hard conditioning data. It is based on the direct sampling method proposed by Mariethoz et al. [2010] and the algorithm developed by Straubhaar et al. [2011]. In collaboration with the geologists and sedimentologists of the Dem'Eaux Roussillon project, we developed a conceptual representation of the Continental Pliocene stratigraphy and its internal spatial facies arrangement, and used the DeeSse algorithm to generate an ensemble of sedimentological

models [Dall'Alba et al., 2020]. One objective was to test the applicability and potential benefits of using advanced geostatistical models, such as MPS, to model the internal distribution of complex, large regional scale aquifers.

Another goal was to test different sedimentological settings and modeling approaches, of different complexities, to compare them with the MPS approach during the hydrodynamical simulations. Sequential Indicator Simulations (SIS) were carried out to be compared to the MPS approach. SIS is a simpler approach that cannot reproduce complex patterns, but it is often used in this type of project because it can accommodate auxiliary data and is easy to work with. A deterministic model, that described the permeability field only as a depth function, was also considered. All of these sedimentological approaches are used as physical inputs for the hydraulic conductivity and specific storage parameters during the hydrodynamical simulations.

In order to test these models, a steady-state and a transient model setup were created for the Roussillon aquifer. The aim was to test the different permeability fields in order to estimate the propagated geological uncertainty in the hydrodynamical simulations. An integrated process was developed using open source Python libraries and MODFLOW 6 through the FloPy Python library to convert the geological model into physical models and use them directly in hydrodynamical simulations. The main indicator for comparing the different models will be the reproduction of the piezometric head records. Moreover, the final ensemble of hydrogeological models and results will characterize the hydrogeological uncertainty and help to increase the robustness of the water resource characterization.

After analyzing some preliminary results of pre-calibrated transient models, we finally propose in this work to test a calibration process using the Ensemble Smoother with Multiple Data Assimilation method (ES-MDA). ES-MDA is a calibration approach that relies on the ensemble approach proposed by Emerick and Reynolds [2013]. This method calibrated automatically all the different model's parameters, returning an ensemble of calibrated models.

1.5 Thesis structure

Chapter 2 summarizes the geological setting of the Roussillon aquifer. The main structural envelopes are described, as well as the four geological sub-intervals composing the Roussillon aquifer. This chapter provides the conceptual geological knowledge and scenarios that have been established for the simulation of the Continental Roussillon aquifer. Finally, this chapter introduces the different geological data sets that are used for the stochastic geological litho-facies simulations.

Chapter 3 presents the details of the MPS approach that is implemented to model the geological heterogeneity within the Continental Pliocene. One particular aspect is the lack of a three-dimensional training data set that led us to build a 3D model based on a combination of 2D simulations.

Chapter 4 presents the other two sedimentological models created for this study, using SIS and deterministic approaches. It also details the hydraulic conductivity and specific storage assignation processes, as well as a description of the upscaling approach used to transfer the physical properties to the hydrodynamical simulation grid.

Chapter 5 describes the main hydrogeological settings of the plain, presents the regional conceptualized hydrodynamical model, as well as the data series used as boundary conditions to represent the different stress factors for the MODFLOW simulations.

Chapter 6 describes some initial calibration steps that have been carried out using steady-state MODFLOW simulations. This chapter focuses on pre-calibrating the hydraulic conductivity parameters of the simulated MPS and SIS facies, as well as the hydrodynamical parameters of the river systems.

Chapter 7 presents the ensemble of transient-state models, run over a 20 years period. It presents the simulated piezometric data series, some piezometric maps, as well as some zonal budget analysis. This chapter also presents the approach tested to calibrate the hydrodynamical fields of the transient simulations and the preliminary results associated.

Chapter 8 summarizes some general conclusions about the tested methodologies, and the applicability of the different approaches to such a large-scale regional model.

Chapter 2

Geological setting of the Roussillon plain

Abstract

Coastal aquifers in the Mediterranean basin are complex reservoirs whose geometries are generally poorly understood. Often located in multi-layered sedimentary formations, they are often backed by limestone (aquifers) or crystalline reliefs, from which they receive surface or underground flows. The Roussillon aquifer fits this description. Dating back to the Messinian salinity crisis, it is a multi-layered coastal aquifer located on the border of the Mediterranean Sea, on the French side of the Pyrenees. It is filled with Pliocene and Quaternary sediments. The history of the filling of the Roussillon plain is complex due to two main factors, the first one being the complex multi-source systems from which the sediments originate and the second being its wide extension both inland and offshore.

In this work, we are interested in the whole Roussillon aquifer, the main objective being to create a complete regional hydrogeological model of the system. We are also interested in simulating more local groundwater interactions and are therefore interested in putting some effort into the internal modeling of the Continental Pliocene layer, which is the main aquifer reservoir, and also the more complex. From field study, and sedimentological cross-sections analysis, it was decided to divide the Continental layer into four sub-reservoirs. These reservoirs are characterized by different sedimentological concepts and will be simulated accordingly. In order to describe this aquifer and to create a 3D geological model, existing data sets consisting of maps, seismic profiles, and borehole databases were studied in addition to newly acquired data sets (realization of two core drilling, field surveys, offshore seismic acquisition and geophysical logging). These data sets are essential to correctly model the different envelopes of the 3D model, and to understand the geometry of the main structures that make up the aquifer.

This chapter introduces the main geological information regarding the sedimentological history of the formation of the Roussillon aquifer, as well as the geological data sets used for the construction of the geological model, internal surfaces, and used for the geostatistical simulations.

2.1 Introduction

Located in southern France, this 800 km^2 onshore sedimentary basin is bounded by the foothills of the Pyrenees to the south and west, the Corbières massif to the north and the Mediterranean Sea to the east (Fig. 2.1). The basin is a complex, multi-layers system composed of sedimentary formations. The Roussillon aquifer is laying on top of Miocene sediments, which act as an impermeable hydrogeological limit, and is divided into two main hydrogeological units: the shallow Quaternary aquifer and the deep Pliocene aquifer. The shallow aquifer consists of a series of Quaternary alluvial formations, while the deep aquifer consists of a series of Pliocene formations, with sandy-clayey alluvial deposits in the upper part, and silty-clayey deposits in the lower part.

This basin originated from the opening of the Gulf of Lion (Oligocene to Miocene), before being largely eroded by the Messinian Salinity Crisis (MSC) [Clauzon et al., 2015]. The Messinian salinity crisis, also known as the

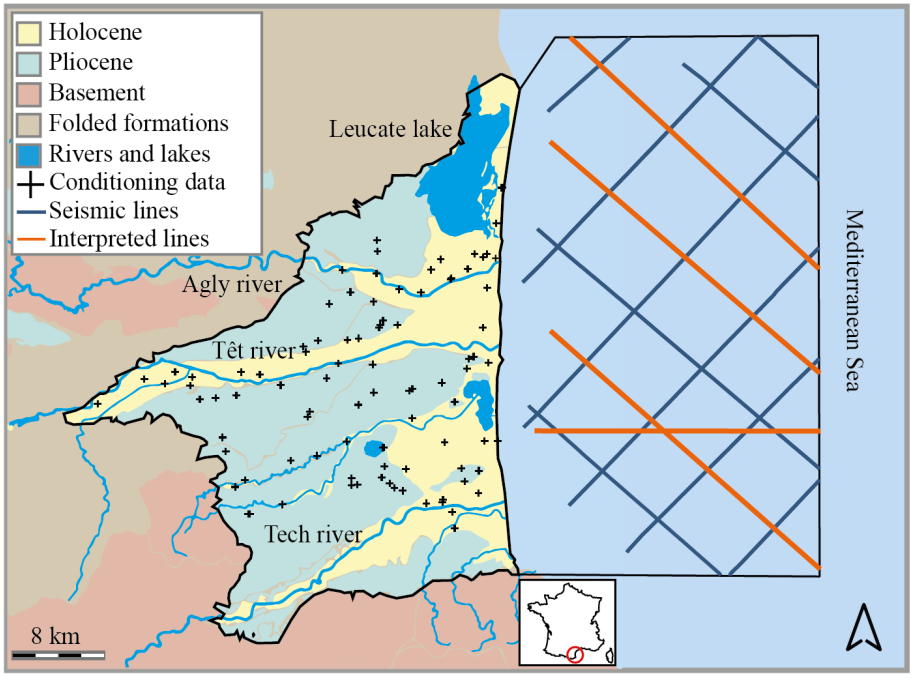

Figure 2.1: Hydrogeological model extension and conditioning data location.

Messinian event, is an episode of extreme aridity that affected the Mediterranean Sea during the Messinian period (7.2-5.3 million years ago). During this period, the Mediterranean Sea experienced a period of intense desiccation, leading to the complete disappearance of its waters. This event was caused by the closure of the Strait of Gibraltar, which prevented the influx of seawater from the Atlantic Ocean, leading to the rapid evaporation of the Mediterranean Sea. The Messinian salinity crisis had a major impact on the surrounding environment, as the extreme drought caused a change in the vegetation, fauna, and also in the climatic condition of the basins along the ancient Mediterranean coastline. From a geological point of view, this event created large erosion basins along the entire coastline as a result of the lowering of the Mediterranean Sea level. This is the case for the Roussillon basin, where the Miocene formation was exposed and eroded, about 6 My ago [Lofi et al., 2005]. This process led to the creation of a large available space for sedimentary deposition to take place once the Mediterranean Sea reconnected with the Atlantic Ocean.

During the Pliocene, when the Mediterranean Sea was reconnected to the Atlantic Ocean, the basin was filled up with Gilbert-type delta reworking the sediments generated by the subaerial Messinian unconformity. The sediments grade from wave-dominated deltas, corresponding to the Marine Pliocene layer, toward fluvial dominated delta with the continental part corresponding to the Continental Pliocene layer. Quaternary sediments associated with river and lagoon systems were deposited on top of the stratigraphic stack.

In order to characterize and model this aquifer, the first part of this thesis consisted in creating a 3D geological model of the Roussillon aquifer. A model is always a simplified representation of the reality that serves a defined purpose. The chosen domain extension, the type of grid (structured or unstructured), the discretization of the grid, and the degree of detail and realism introduced in the modeling process, are selected to answer a specific problem, which is in our case the hydrogeological modeling of the Roussillon aquifer.

The first task in the modeling workflow is to define the main surfaces separating the three aquifers. The geological model includes the onshore extension bounded by the main geological massifs (Fig. 2.1) and the offshore domain of the main aquifers, going from top to bottom, from the Quaternary aquifer, to the Continental Pliocene aquifer, and ending with the Marine Pliocene aquifer (Fig. 2.2). Inside the Continental Pliocene, three surfaces divided the Continental Pliocene layer (Fig. 2.2). The Miocene eroding surface defines the lower elevation of the model and represents a hydrogeological barrier.

The 3D model extends more than 30 km offshore. The transition between the onshore and offshore models is carefully managed, incorporating boreholes and offshore seismic lines, in order to create realistic aquifer envelopes. The offshore domain boundary is in this work fixed to include an offshore zone into the hydrogeological simulation and to limit boundary effects during the hydro-

dynamical simulations. However, it is important to clarify that the external limits of the offshore domain do not represent the true offshore domain boundary of the aquifer, which is located further from the coast in the Mediterranean Sea domain. This boundary is selected arbitrarily, sufficiently far to minimize artifacts during the groundwater flow simulations in the coastal region, without increasing too much the computational cost required for a larger simulation domain.

The second task of this work concerned the definition of the internal geological heterogeneity within the Continental Pliocene layer. This layer contains the main aquifer resource of the region and will be modeled using MPS stochastic

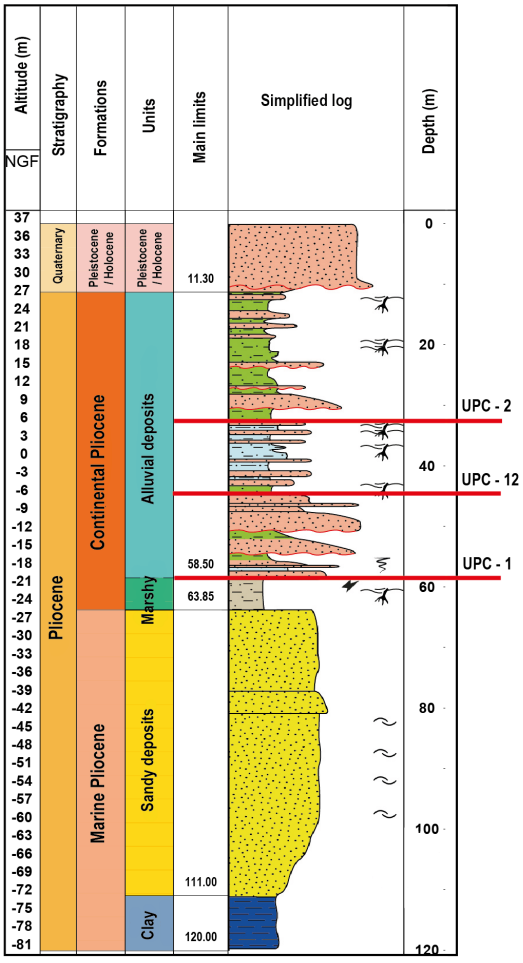

Figure 2.2: Simplified stratigraphic log of the Roussillon geology, modified from Duvail et al. [2021].

approach. In order to simulate its internal composition, the grid resolution of this layer must be sufficient in both horizontal and vertical directions. A high grid resolution allows representing complex structures and benefits for the maximum of the conditioning data set that are usable. The 3D geological model is therefore created using a rather fine x and y resolution of 50 m. In addition, three additional surfaces are interpolated within the Continental Pliocene layer, called the UPC surfaces (Upper-Pliocene Continental), in order to divide the Continental Pliocene aquifer into four sub-intervals to better represent the internal structure of the aquifer, and improve the realism of the MPS simulations along the z direction. These sub-intervals have different spatial distributions of their sediments' structures.

Once the objectives of the model have been clearly identified, the second step in the creation of a geological model consists in the historical study of the previous geological work carried out in the past [Duvail et al., 2001; Duvail, 2008; Clauzon et al., 2015], and the collection of the data sets already available [Issautier et al., 2021; Duvail et al., 2022]. Borehole data sets have been compiled into a large database defining the transition elevation between the main aquifers' surfaces. In the offshore domain, previous seismic data sets have also been compiled and used to interpolate the main stratigraphic envelopes delimiting the Quaternary, the Continental and the Marine Pliocene layers [Duvail et al., 2022; Fioravanti et al., 2022].

In order to complete the previous description of the formations that make up the Roussillon aquifer, new sedimentological field campaigns were carried out to map the outcrops and define the main sedimentological facies of the plain [Issautier et al., 2021]. To complete the borehole database, new data sets were acquired between 2019 and 2021 [Duvail et al., 2021; Fioravanti et al., 2022]. In the onshore domain, 101 geophysical logs have been acquired, providing resistivity and gamma-ray response curves for each one of the logged wells. In the offshore domain, new seismic reflection data lines have been acquired between 2017 and 2020. These new sets aim to better model the onshore/offshore continuum for the interpolation of the main surfaces of the model [Duvail et al., 2022].

The main surfaces, separating the Digital Terrain Model (DTM), Quaternary, Continental Pliocene and Marine Pliocene layers, were first interpolated by a partner of the Dem'Eaux Roussillon project, using the compiled borehole data set and automatic interpolation methods [Fioravanti et al., 2022]. The onshore/offshore interfaces were modeled by coupling onshore borehole geophysical logs, high resolution interpreted seismic lines and conceptual cross-sections of the system [Fioravanti et al., 2022].

The second set of surfaces, composed of UPC-1, UPC-12 and UPC-2, are dividing the Continental Pliocene into four sub-intervals (Fig. 2.2). These sub-intervals correspond to different dispositional concepts and formations within

the Continental Pliocene. The surfaces were interpolated from the geophysical logs and the interpreted high resolution seismic lines set, using the GOCAD software[3] and the Discrete Smooth Interpolation approach [Mallet, 1992]. These surfaces are then automatically corrected using python scripts in order to respect the stratigraphic stack of the layers, and to correct numerical artifacts resulting from the interpolation method.

As well as being used to interpolate the main surfaces and sub-interval horizons, the two new data sets are also used as conditioning data for the geostatistical simulation of the Continental Pliocene litho-facies. Hard conditioning data play a central role in MPS simulation and geostatistical methods, as they are used to constrain the simulation.

In this chapter, we first present the main structural surfaces that delimit the main units within the geological model. The next section introduces the borehole geophysical data set and the facies interpretation process. The seismic data set is then presented with a focus on the facies interpretation process. The next section presents the interpolated surfaces created to divide the Continental Pliocene. The final section introduces the main sedimentary concepts related to the four sub-layers of the Continental Pliocene. The newly interpolated surfaces and their sedimentological concepts are used to create the MPS modeling workflow (in chapter 3), while the borehole and seismic data sets are used in the conditioning data for the MPS and SIS simulations of the Continental Pliocene layer (presented in chapters 3 and 4).

2.2 Main geological surfaces

The Roussillon is composed of three aquifers, the Quaternary, the Continental Pliocene and the Marine Pliocene, with the Continental Pliocene being divided by three internal surfaces. The surfaces are 1404×1307 cells, with a 50×50 m resolution, composed the model. These surfaces are from top to bottom:

- Digital Terrain Model (DTM) layer
- Quaternary bottom layer
- UPC-2 layer (internal Continental Pliocene layer)
- UPC-12 layer (internal Continental Pliocene layer)
- UPC-1 layer (internal Continental Pliocene layer)
- Continental Pliocene bottom layer
- Marine Pliocene bottom layer

[3] https://www.aspentech.com/en/products/sse/aspen-skua

This section presents the main structural surfaces that delimit the three aquifer units within the 3D geological model of the Roussillon basin. These surfaces cover both the onshore and offshore domains and have been constructed using onshore cross-sections from Duvail [2008] re-interpreted with the new gravimetric and seismic data from the offshore domain. The analysis of the existing seismic profiles, complemented by the new profiles acquired during the three campaigns carried out by the CEFREM teams within the framework of the project, has then made it possible to propose a description of all the formations overlying the Messinian erosion surface [Duvail et al., 2022]. This work has also benefited from the compilation of a geological data set based on more than 500 boreholes' log located on the Roussillon plain.

The process of interpretation carried out by Duvail et al. [2022] had for objectives to extend the concept of the onshore vertical stratigraphic units to the marine domain, and to create a realistic onshore/offshore continuum. In his work, Duvail et al. [2022] has enabled the identification of the Messinian paleo erosion surface, caused by the sharp drop in sea level with the closure of the Strait of Gibraltar. This surface is considered as the bottom layer of the Roussillon aquifer system. The land-sea correlation of the main surfaces of the Quaternary and Pliocene formations, led to the creation of the paleogeographical maps of the Roussillon system [Duvail et al., 2022].

The four interpolated surfaces, presented in Fioravanti et al. [2022], are used in this work as the envelopes for the three main layers that make up the Roussillon aquifer. They have been locally corrected to remove some interpolation artifacts and to ensure that all the surfaces share the same extension (Fig. 2.3). The extension of the offshore domain has been fixed for the hydrogeological modeling of the aquifer and corresponds to the one presented in figure 2.1. This model extent is designed to include the offshore reservoir in the hydrodynamical simulations and also to avoid potential boundary effects during the simulation.

We can observe from thickness maps that the offshore extension of the model is the main potential reservoir of the different aquifers. The total aquifer thickness can be up to 300 m thick in the offshore domain of the Continental Pliocene layer, while the onshore part of the domain is generally around 50 to 100 m thick.

2.3 Onshore data sets

We now have a look at the borehole logs used to create the conditioning data for the Continental Pliocene sub-surfaces interpolation and for the facies geostatistical simulation. This section focuses on the onshore data set consisting of 101 geophysical logs (gamma-ray, spontaneous polarization, and resistivity data), and on the information extracted from the geological map of the region, which is also used as conditioning data in the geostatistical simulation.

Geophysical logging method

A geophysical campaign was carried out in 2020 to acquire geophysical logs on existing wells in the Roussillon plain. A total of 101 geophysical logs are available for the Roussillon plain. Geophysical logging techniques record the physical and chemical properties of the underground. Contrary to lithological logs, the geophysical logs offer quantitative measurements that can be interpreted as sedimentological facies and deposit sequences. The most frequent geophysical logging methods are gamma-ray (GR), spontaneous polarization (SP), and resistivity logs (Res).

The boreholes are homogeneously distributed across the plain, with some zones having a higher density of data, such as along the Têt river or in the coastal zone of the Roussillon plain (Fig. 2.1). Borehole depths range from 20 m to 150 m, with an average depth of 77 m.

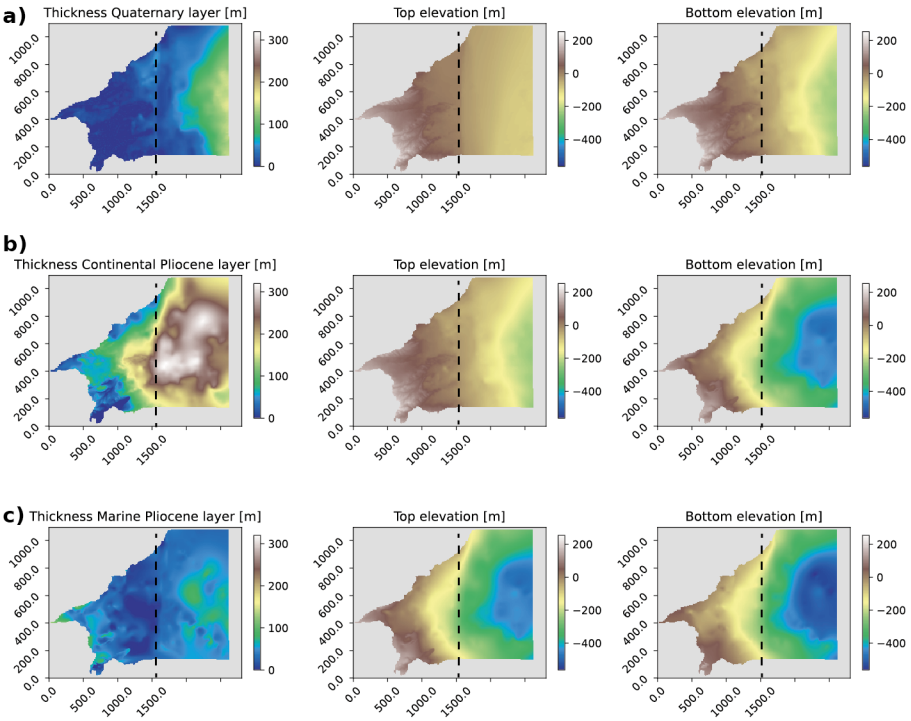

Figure 2.3: Thickness, top and bottom elevation maps of the a) Quaternary aquifer, b) Continental Pliocene aquifer and c) Marine Pliocene aquifer. The black dashed line represents the actual coastline.

The different types of log composing the onshore database are :

- Lithological logs. They are carried out by the driller in charge of the well or by the geologist in charge of the project. Their quality depends on the presence of recognizable indicators, such as a clay layer or sand layers, or by the presence of shells or paleo-indicators. The drilling of boreholes is often carried out using destructive techniques, which can lead to great uncertainty regarding the final assigned unit. The lithological logs can provide information on the type of sediment encountered at a given depth (sand, gravel or clay), but they cannot be used to infer the sedimentological facies of a deposit.

- Gamma-ray (GR). GR logging measures the natural radioactivity of the rocks/sediments produced by the 3 major radioactive elements that are the Potassium (K), the Thorium (Th) and the Uranium (U). The Potassium (feldspar or mica) and Thorium (zircon, tourmaline, rutile) are mostly found in clay deposits. The Uranium is mainly present in organic matter (shell and plant sediments) and characterizes the presence of clay in reducing environments. Gamma-ray measurements are directly correlated to the clay content of the sediment. Their value generally increases with decreasing grain size of the sediments (Fig. 2.4). It should be noted that a fluvial channel that is rich in potassium feldspar could produce a similar gamma-ray response as a clay rich environment. Therefore, gamma-ray interpretation is usually coupled with resistivity curves analysis to avoid errors during the facies interpretation process.

- Resistivity (Res). The resistivity value measures the electrical or magnetic signal response of a material. The resistivity value depends on several parameters. The percentage of liquid present in a material and the resistivity of the associated liquid affect the measured resistivity (an increase in dissolved minerals results in a decrease in resistivity). The clay content, or the percentage of conductive materials (clay is less resistive than gravel and sand), and the internal arrangement of the material (distribution of pores) also play a major role in the resistivity value.

- Spontaneous polarization (SP). SP logging records the potential difference between a moving electrode and the electrochemical signal of the rock. The signal is positive when the electrode faces clay sediments and is negative when the electrode faces more permeable units such as sand deposits.

- Neutron log. The neutron log is sensitive mainly to the amount of hydrogen atoms in a formation. Its main use is in the determination of the porosity of a formation. In formations with a large amount of hydrogen atoms, the neutrons are slowed down and absorbed very quickly and in a short distance. The count rate of slow neutrons or capture gamma-rays is therefor low. Hence, the count rate will be low in high porosity rocks.

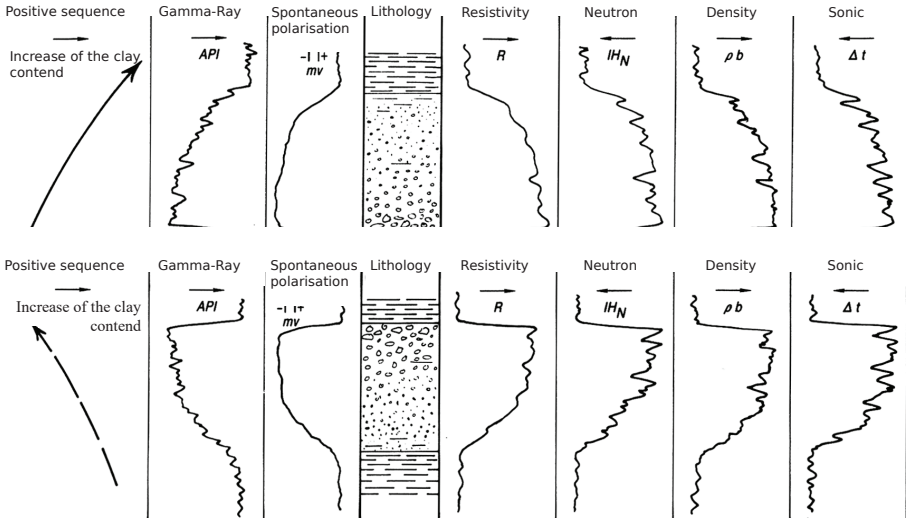

Figure 2.4: Typical response curves for two different sedimentation sequences. The curves must be interpreted together to avoid facies misinterpretation. Modified from Duvail [2008].

In addition to the geophysical database, two observation sites were installed for the Dem'Eaux project: one close to the shore (Dem'Mer) and one on land (Dem'Ter). At these sites, drill cores were extracted for interpretation along with the geophysical logs being acquired. These two sites are used to calibrate the geophysical responses to the sedimentological facies and to help define the sub-interfaces within the Continental Pliocene.

In this section and for the surface interpolation maps of the Continental Pliocene layer as well as for the facies interpretation of the sedimentological unit composing the Continental Pliocene aquifer, we focus on the interpretation of the GR, Res and SP geophysical logs, which carried out the most reliable information.

Geophysical logs interpretation

The gamma-ray and resistivity logs allowed to identify changes in sedimentary deposits and grain distribution along depth. Sand sediments have a low gamma-ray response, producing small peaks on the curve, whereas clay sediments produce high response peaks due to their high content of radioactive elements [Serra O. et al., 1975]. By analyzing the gamma-ray and resistivity responses at a given depth, coupled with their vertical evolution, it is possible to identify and assign a sedimentary litho-facies for a certain depth range. During the interpretation process, it is not only the measured value of resistivity or gamma-ray response that is critical for the characterization of the facies, but

also the coupled vertical evolution of these two curves. To facilitate the interpretation process, the gamma-ray curve is usually presented on the left of the resistivity curve. Figure 2.4 shows response curves for gamma-ray and resistivity logging and compares them to two deposit sequences. In his work, Duvail [2008] presents a description and an interpretation of the response curves for the different facies observed in the Pliocene's aquifer. These interpreted response curves served as an example for the interpretation process of the new geophysical data.

For this Ph.D. thesis, 101 geophysical logs have been interpreted, using the GOCAD software as visualization platform, to identify the facies at a given depth and to determine the elevation of the internal surfaces dividing the Continental Pliocene (UPC-1, UPC-12, and UPC-2). To facilitate the interpretation process, the geophysical logs are interpreted along different cross-sections, which facilitates the correlation of structures and helps to understand the vertical sequences. The interpretation of the sedimentary facies was carried out following two levels of description. The first level is the more complex or detailed. It describes as accurately as possible the different sedimentological facies of the Continental Pliocene layer. The second level is simplified and is composed of three facies. This description incorporate the alluvial fan, next to the massifs, and only differentiates the sand-like sediments from the clay-like sediments in the rest of the plain. The clay and sand sediments are differentiated based on their geophysical response curve and also based on their sedimentological grain description. These two levels of resolution are used for different geostatistical approaches during the modeling process. The facies composing the different data sets are shown in figure 2.5, along with some examples of geophysical logs facies interpretation.

The final facies selected to compose the Continental Pliocene, based on the interpretation of the geophysical logs, are:

- Alluvial fan. It corresponds to a mixture of coarse sediments such as gravel, sand, and smaller pieces of sediment such as silt. They are located close to the massif, where flowing water has interacted with mountains or hills, before spreading out as it meets the flat plain. They are often arranged in a triangular based or fan like shape.
- Alluvial channels. It corresponds to sandy deposits, and includes both braided and meander-like channels in the conceptual facies description of the Roussillon plain. The braided shape beds are located closer to the sediment sources. The meander-like beds appear as the energy source decreases, corresponding to a flattening of the sedimentological depositional environment. The meander beds are generally described as wider and thicker compared to the braided shape beds.

- Alluvial crevasse splay. It corresponds to a mixture of sandstone and some clayey deposits, thinner than the channel deposits, and is located on the side of the channel belts. These structures are associated with a flood event, when the bank deposits that define the channel beds suddenly break and create a fan-like deposit.

- Alluvial floodplain. It corresponds to clay, silt and sandy-clay sediments. Floodplain deposits are formed by the lateral movement of a stream and over bank deposition. It generally corresponds to the flat area of land separating river beds.

- Sandbars. It corresponds to the sandstone unit in the distal part of the system. It is composed of coarse deposits corresponding to a partially exposed ridge of sand formed by rivier's waves at the end of a river system.

- Marshy plain. It corresponds to the marshy fine sediment in the distal part of an alluvial system, where the coastal offshore marine system and the alluvial system meet.

Geological mapped data set

The second hard conditioning data set is based on the geological map of the Roussillon region (Fig. 2.6). As the Continental Pliocene layer is exposed and mapped, the geostatistical model must take this information into account. By creating and using a dense hard conditioning data set, based on the geological units of the exposed Continental Pliocene, the geostatistical models will respect the geological information during the simulation. The outcrop zones used as conditioning data for the Continental Pliocene conditioned the alluvial fan deposits in the proximal part of the alluvial system, close to the massifs bordering the plain. The other outcrop zones are not used as conditioning data, as they are only described as undifferentiated Continental Pliocene units.

2.4 Offshore seismic data set

We have seen that a large dataset of conditioning data benefits the onshore part of the model. While onshore data are usually easier to obtain than offshore data, the Roussillon Dem'Eaux project is fortunate to benefit from a large set of offshore seismic lines. These lines are mainly from old petroleum exploration campaigns and cover a large part of the actual hydrogeological offshore extent (Fig. 2.1). We can distinguish three main seismic sets, the ELF-LRM set with conventional seismic data, the MARION set acquired in 2000 with high seismic resolution, and the CALMAR set based on Sparker data. While the ELF-LRM and CALMAR sets have only been used for the surface interpolation, the MARION data set has also been used for facies identification in the offshore domain [Fioravanti et al., 2022].

a)

Interpretation	Facies	Code	Color
Simple	Floodplain	0	
	Channel	1	
	Alluvial fan	2	
Complex	Floodplain	0	
	Marshy deposit	1	
	Crevasse splay	2	
	Sandbar	3	
	Channel	4	
	Alluvial fan	5	

b)

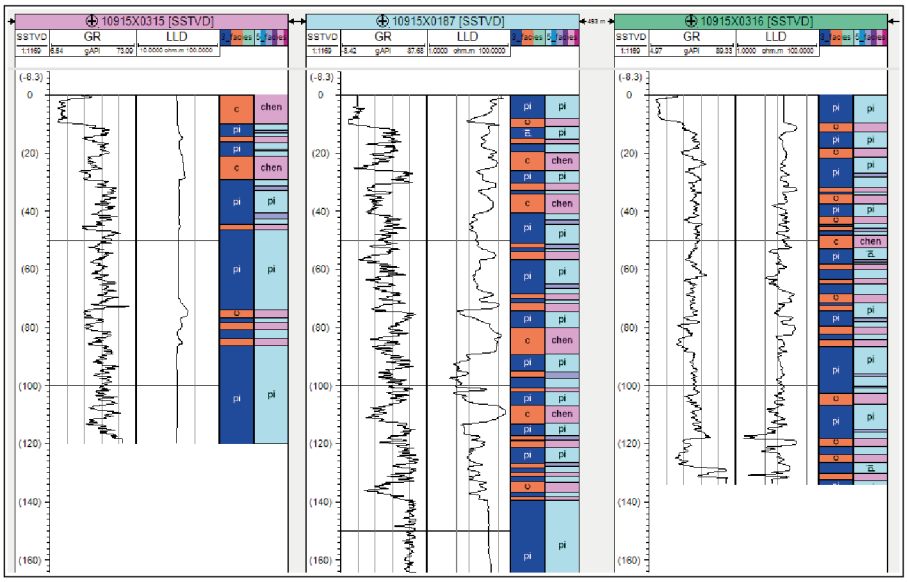

Figure 2.5: Litho-facies interpretation of the Roussillon data set. a) two approaches have been carried out, one with 3 facies and one more complex with 6 facies. b) 3 examples of facies interpretation, for each, the left column corresponds to the simpler model set and the right column to the complex model set.

These seismic lines served for the interpolation of the Roussillon main envelopes [Fioravanti et al., 2022]. Moreover, using onshore/offshore correlation, it was possible to identify the UPC surfaces (which divide the Continental Pliocene) on the different seismic cross-sections. This offshore data set is used as conditioning data during the interpolation process of the UPC surfaces.

Four of these lines were part of a special study that aimed at describing the sedimentological facies composing the offshore Continental Pliocene domain [Fioravanti et al., 2022]. Based on the interpretation of the wave travel time

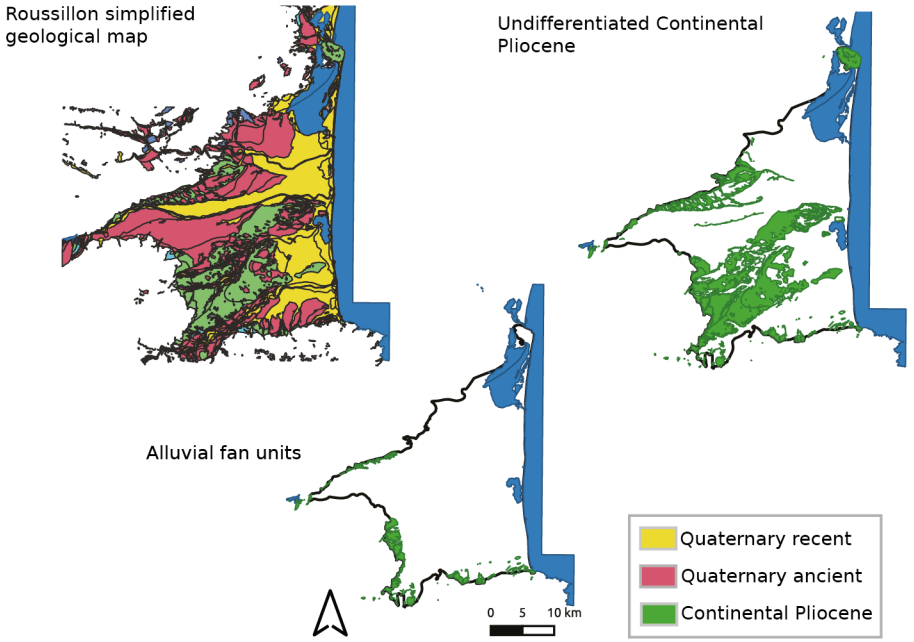

Figure 2.6: The geological hard data set is created from the Roussillon geological map, where the alluvial Pliocene units are identified and transformed to a conditioning data points set.

cross-sections, the visible sedimentological structures of these four seismic lines have been correlated with the sedimentological elements described in the onshore domain by the geophysical logs (Fig. 2.1 orange lines). Once interpreted, these maps have been transformed to conditioning data for the geostatistical simulations (Fig. 2.7). It is important to note that the density of information provided by a complete cross-section is much greater than what is provided by a set of interpreted boreholes. Depending on the orientation of a cross-section in the plain, this one can intersect along complete sedimentological structures. This type of data set is much appreciate during 3D simulation since it provides 3D information regarding the pattern spatial arrangements.

2.5 UPC surfaces creation

In order to interpolate the surfaces delimiting the sub-intervals of the Continental Pliocene, onshore and offshore data set have been compiled to create a suitable conditioning set for the interpolation process (Fig. 2.8).

In the onshore domain, it was possible to identify the elevation of the UPC surfaces based on interpreted stratigraphic cross-sections. These cross-sections are composed of geophysical logs spatially interpreted together. A total of

62 wells with the proper geophysical information was available to define the onshore database of the UPC surfaces elevation.

In the offshore domain, the seismic lines have been used. Based on the work of Fioravanti et al. [2022], the interpreted elevation of the UPC surfaces were collected as conditioning data (Fig. 2.1 blue seismic lines).

Finally, to create a model that respects the vertical stratigraphic pile of the main layers, we sampled points from the elevation map of the top Pliocene layer and of the bottom Pliocene layer all along the boundary of the hydrogeological domain (Fig. 2.8). Based on these points, we created three intermediate sets of conditioning data points separating evenly the Pliocene layers (top and bottom layer of the aquifer). Since no conditioning data are available at the boundary location of the simulation domain, these sets are created to ensure that the three UPC surfaces pass between the top and bottom surfaces of the Continental Pliocene layer.

The final elevation maps were generated using the Discrete Smooth Interpolation (DSI) method in GOCAD, and were visually inspected and locally corrected to remove major interpolation artifacts (Fig. 2.9).

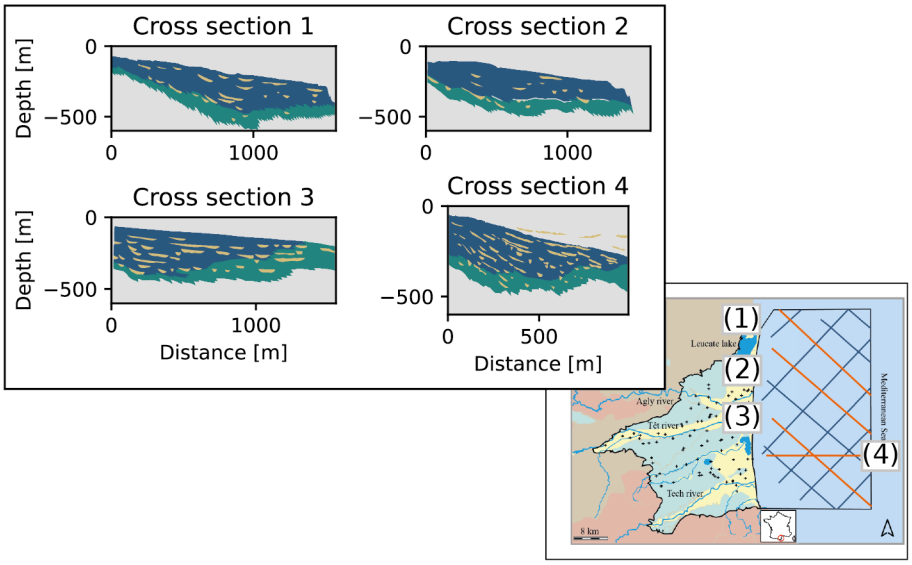

Figure 2.7: The interpreted seismic lines. Channels like structure are visible on these lines and will condition the offshore domain during geostatistical simulation.

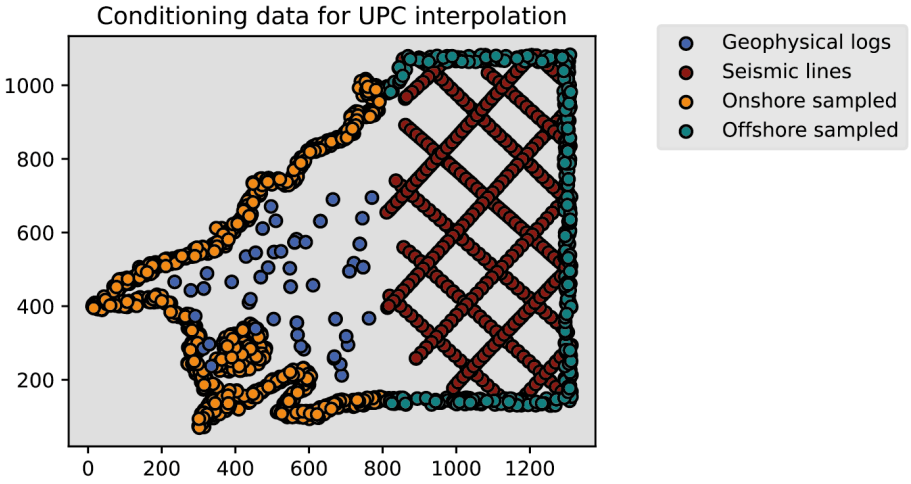

Figure 2.8: Conditioning data sets that are used for the interpolation of the UPC surfaces.

2.6 Continental Pliocene sub-intervals and conceptual description

This final section introduces the conceptual description of the four sub-intervals composing the Continental Pliocene layer. Following the analysis of the geophysical logs, seismic lines, and structural offshore cross-sections of the system, it appears that the Continental Pliocene layer presents different structures and stacking arrangements in the plain. These depositional sequences have been identified in the core log analysis of the two Roussillon study sites, Dem'Mer and Dem'Ter [Duvail et al., 2021; Issautier et al., 2021]. Figure 2.10 shows the core log description of the Dem'Mer study site, located close to the coast, and shows the four main sequences identified in the Continental Pliocene layer. These sub-intervals are separated by three interpolated UPC surfaces: starting from the top with the UPC-2, UPC-12, and UPC-1 surfaces.

Since we will use geostatistical methods to simulate the Continental Pliocene layer, it was decided to divide this layer into four sub-intervals in order to better constrain the internal location of the sedimentological facies. Geostatistical methods work best when applied to a single, simple, conceptual system that exhibits similar statistics. By subdividing the Continental Pliocene layer into four sub-intervals, corresponding to sub-layers where the horizontal spatial distribution of the facies follows a similar conceptual spatial description, we better represent the observed vertical trends along the boreholes.

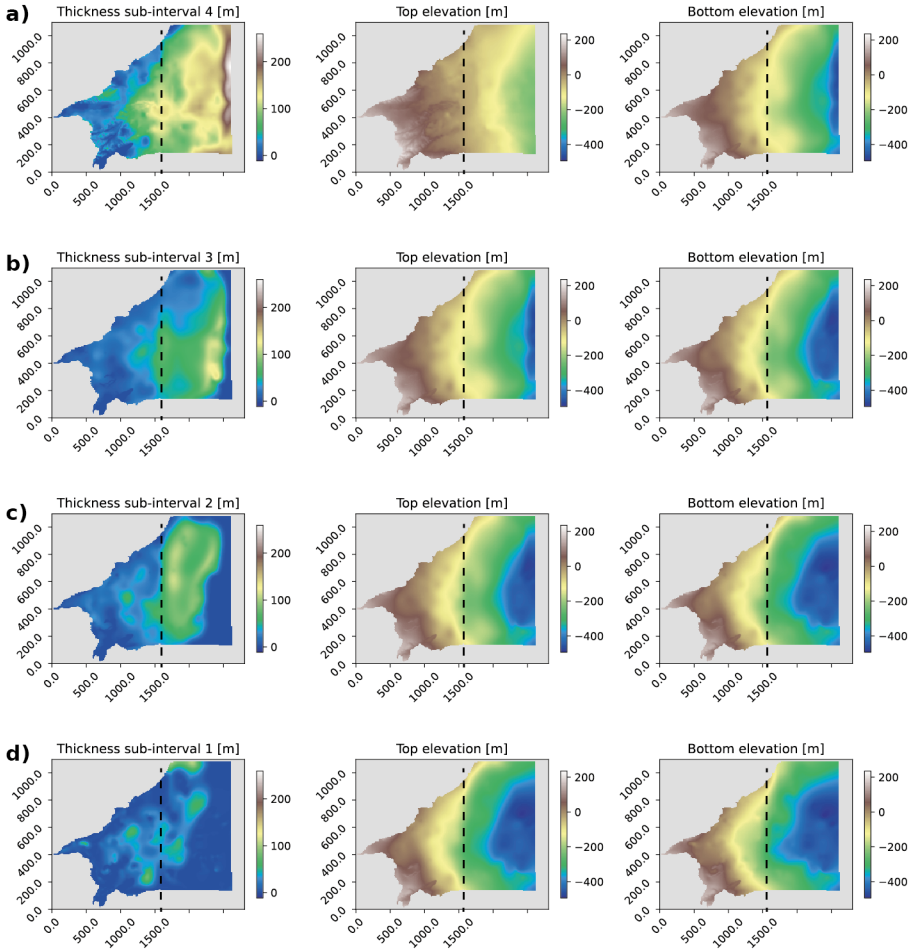

Figure 2.9: Thickness, top and bottom elevation maps of the interpolated sub-interfaces of the Continental Pliocene layer. Sub-interval 4 (a) is the top one, and Sub-interval 1 (d) is the bottom one. The black dashed line represents the actual coastline.

The use of multiple-point statistics to simulate the geological heterogeneity requires defining a conceptual geological model for the Continental Pliocene system. We base this description on the six sedimentary facies identified previously. The detailed description will be adapted to fit the observed differences in the sub-intervals. The geological concept will be described quantitatively in the next chapter by generating a training data set (TDS) representing the patterns and facies arrangements to be simulated.

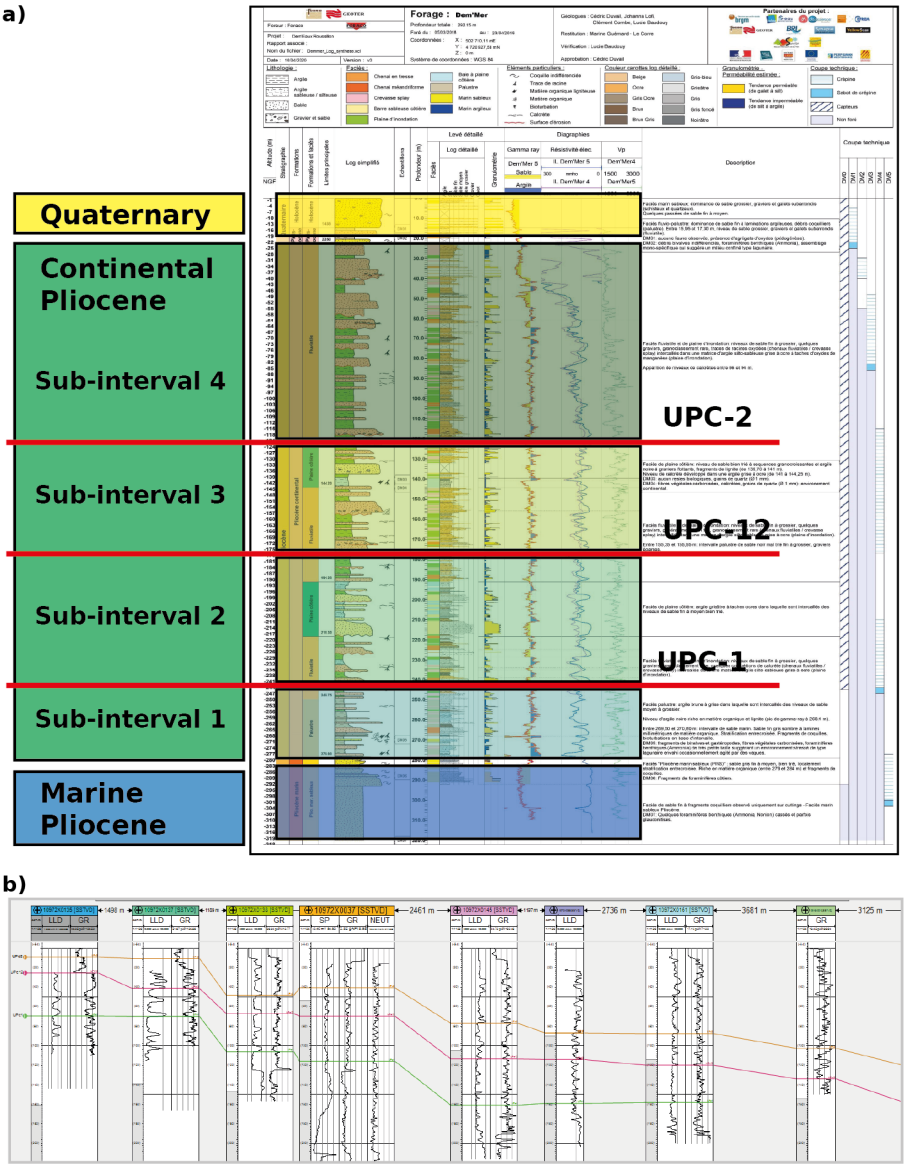

Figure 2.10: a) The four sub-intervals are defined on the Dem'Mer and Dem'Ter geophysical log (here Dem'Mer). b) The sub-intervals are then interpolated based on the geophysical logs of the Roussillon database.

In terms of data, we observe that there is a transition from the upstream part to the downstream of the catchment. In the upstream part, the alluvial fan facies dominates, then there is an evolution toward alluvial plain structures, and finally, in the distal part of the system, with the occurrence of marshy floodplain and sandbars deposits.

The main differences between the sub-intervals are the spatial location of the transition zones between the braided and meander-like rivers and between the alluvial and marshy deposits. By adjusting the location of these transition zones and making them specific to each sub-interval, the geostatistical methods are likely to reproduce the main spatial arrangement of the facies in both the horizontal and vertical direction. These differences in the depositional sequences between these sub-intervals are interpreted as mainly due to the variation in the eustatic sea level during the period of sedimentation. However, due to the lack of eustatic sea level curves for this precise period of time and location, it was not possible to derive a continuous variation in the location of the sedimentological structures. The four sub-intervals correspond therefore to the time of major shifts in the progradation and depositional sequence that we are able to map across the plain.

Figure 2.10 presents a schematic log delimiting the four sub-layers composing the Continental Pliocene layer. The main characteristic of the sub-intervals are:

- Sub-interval 4 (top one). In this interval, the alluvial system is fully developed and the stacking of large sandstone deposits is possible due to the maturity of the river belt location.
- Sub-interval 3. In this interval, the alluvial system is almost fully developed and the transition between the braided and meander river is located further away from the massif.
- Sub-interval 2. In this interval, the alluvial system from the northern massif is activated. The marshy environment is pushed forward in the offshore domain.
- Sub-interval 1 (bottom one). In this interval, the marshy deposits are located closer to the massif and cover the majority of the current offshore domain. The alluvial systems are only originated from the west location.

2.7 Results

This first chapter presents the interpretation processes that lead to the creation of the structural surfaces of the Roussillon aquifer, and to the creation of the sedimentological database that will be used later on for the geostatistical simulation of the Continental Pliocene layer.

A total of 101 wells and four interpreted offshore seismic cross-sections have been considered for the Continental Pliocene layer modeling. While the onshore well data are homogeneously distributed across the plain and correspond to more than 3'000 data points, they only describe a small fraction of the reality in comparison with the large extent of the onshore domain. In the offshore domain, the seismic data provide a unique insight into the 3D structural shape of the facies and cover a large area of the domain. On the downside, the seismic data are more complex to interpret and provide a lower resolution data set compared to the geophysical logs.

The second main result of this chapter, is the interpolation of the internal surfaces delimiting the Continental Pliocene layers (Figs. 2.9, 2.11, and 2.12). The interpolated surfaces differentiate important shifts in the location of the sedimentological structures that composed the Continental Pliocene layer. Three new surfaces (UPC-1, UPC-12 and UPC-2) have been interpolated based on the available data and on a created set of elevation data.

The final model of the Roussillon consists of six reservoirs. Looking at the cross-sections of these sub-intervals, we can see that the main potential reservoir of the Roussillon aquifer is located in the offshore domain, where the available space is much larger than in the onshore domain (Figs. 2.11 and 2.12). The UPC surfaces show a clipping in the offshore domain, corresponding to the end of the prograding structures.

2.8 Discussion and Conclusion

The geological model of the Roussillon is composed of three main geological units, starting with the Marine Pliocene formation at the bottom, topped by the Continental Pliocene unit and finishing with the Quaternary unit. The first phase of this thesis project consisted in the definition of the main sedimentary envelopes, and in the compilation of a geological database. Onshore and offshore data set, composed of geophysical logs, interpreted cross-sections and seismic lines, along with the general geological knowledge of this sedimentary basin acquired from previous studies. Clauzon et al. [2015]; Duvail [2012]; Aunay [2007]; Lofi et al. [2005], have yielded to the construction of a conceptual representation of the main structures composing the Roussillon aquifer.

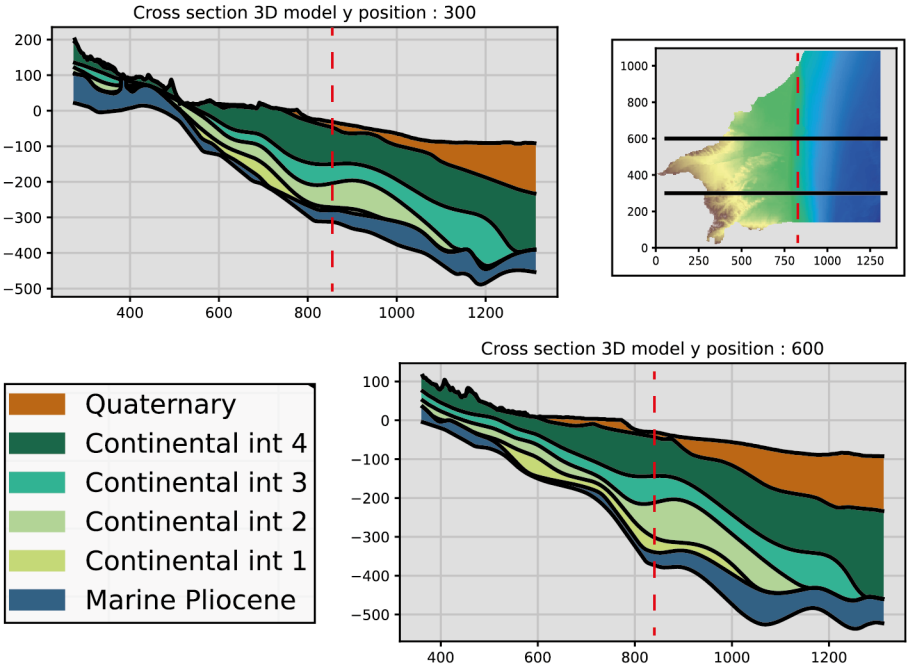

Figure 2.11: Cross-sections of the final 3D envelopes of the Roussillon geological model in the east-west direction. The Quaternary layer is small in comparison to the other main layers. The interpolated UPC surfaces divide the Continental Pliocene layer into four sub-intervals. The dashed red lines represent the approximate coastline.

After the analysis of the complete data sets, new sub-surfaces were defined for the Continental Pliocene. These surfaces delimit sub-intervals within the Continental Pliocene that are characterized by a different structural spatial arrangement of an identical sedimentological concept. The Continental Pliocene can be described as an alluvial system that evolved from alluvial fan deposits near the massif to alluvial plain and then to a marshy environment.

The transitions between these environments are mainly controlled by the eustatic level at the time of deposition. While defining a complete eustatic curve for a defined zone is challenging and requires a special type of geochemical or paleo graphical data, it was still possible to define important shifts in the depositional environment for the Continental Pliocene layer. Using the geophysical logs, interpreted in terms of depositional sequences, and the offshore data set, it was possible to map and interpolate the depth of the three surfaces that divide the Continental Pliocene layer.

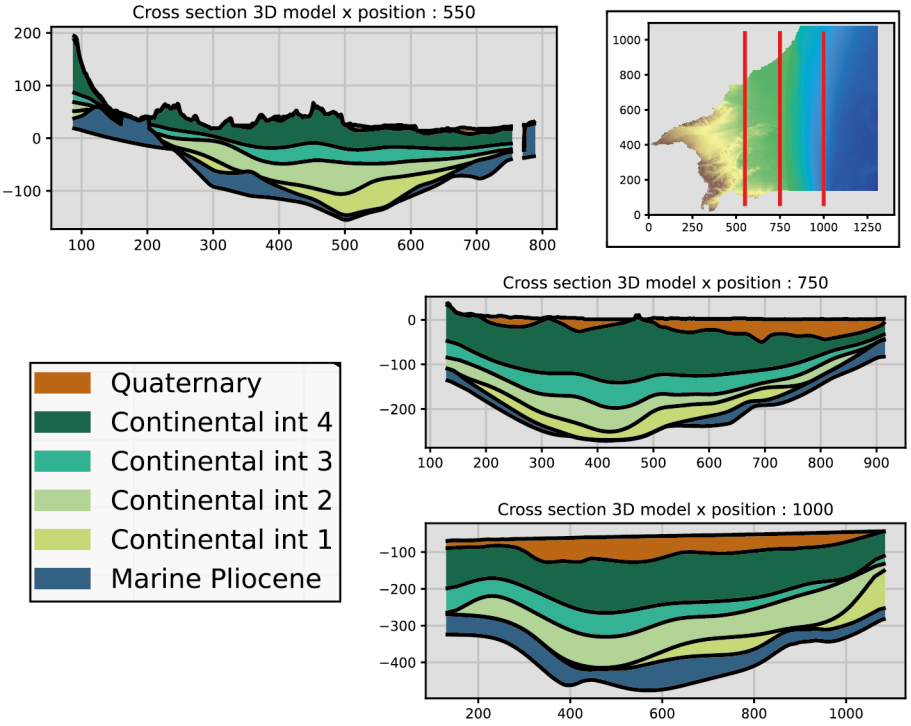

Figure 2.12: Cross-sections of the final 3D envelopes of the Roussillon geological model in the north-south direction. The different sub-intervals follow the base Miocene envelope shape. The quaternary layer thickness increases in the offshore domain.

The geological model of the Roussillon aquifer is composed of six surfaces delimiting the three main aquifers and the four sub-intervals of the Continental Pliocene. The hydrogeological model covers about 800 km^2 in the onshore part and extends for about 30 km in the marine domain. The hydrogeological offshore extent of the model is smaller than the actual geological offshore extent of the Roussillon basin. This limit was set to limit the number of active cells during the hydrogeological simulation.

The second use of the onshore and offshore geological data set will serve as conditioning data for the geostatistical simulation of the Continental Pliocene layer in the following chapters. The geophysical response curves have been interpreted in terms of six sedimentological facies identified in the 101 geophysical logs and in the four interpreted offshore seismic lines. These conditioning data will play an important role in geostatistical simulations, since they influence the spatial location of the facies during the geostatistical simulations. The Roussillon data set is well distributed in the onshore part, but one could argue that the number of interpreted wells is still small compared to the actual size

of the model. We also note that there is a potential to enlarge the offshore data set by pursuing the interpretation of the entire set of seismic lines.

Furthermore, although the Roussillon geological data set is sufficient to interpolate the main surfaces of the different aquifers, it suffers from heterogeneity in its resolution between the onshore and the offshore regions. Seismic data in the onshore domain would be extremely useful to better constrain the 3D surfaces and occurrence of the facies in the proximal part of the alluvial plain. Such large model generally benefits from larger geophysical data sets, which can be used as auxiliary variables during geostatistical simulations [Neven et al., 2022a].

Understanding and defining a geological and sedimentological concept is not an easy task. For such large model, it requires the expert knowledge of different specialists to compile and interpret the available data sets in a meaningful way. Another aspect is the transfer of the created sets and general knowledge from the geologists and sedimentologists to the hydrogeologists and the modelers. A model is always a conceptual description of the reality and is created to serve a specific purpose. This project is a good example of how important it is to involve as soon as possible all the specialists who will work with the geological model and the geological data in order to create the most suitable model, surfaces and data sets to be passed on to the different steps of the project. This chapter introduced the main steps and data that were required to create the structural model and the complete conditioning data set for the Roussillon aquifer, ready for the geostatistical modeling part.

Chapter 3

MPS simulations

Abstract

This chapter presents a revised version of the work presented in[4] [Dall'Alba et al., 2020] published during the beginning of thesis. Since then, the domain of the model has been extended to the offshore part and the geological concept has been improved, and therefore the workflow had to be adjusted.

The aim of this chapter is to describe the workflow used to create the multiple-point statistics (MPS) litho-facies models of the Continental Pliocene layer. When few direct observations are available, statistical inference from field data is difficult if not impossible, and traditional geostatistical approaches are of limited value. On the opposite, MPS simulations can rely on one or several alternative conceptual geological models provided using training data sets (TDS). But since the spatial arrangement of geological structures is often non-stationary and complex, there is a need for methods allowing to describe and account for the non-stationarity in a simple but efficient manner. The main goal of this chapter is therefore to propose a workflow using the direct sampling algorithm DeeSse, that aimed at integrating expert conceptual knowledge into non-stationary TDS for 2D complex MPS simulations. The conceptual model is provided by the geologist as a two-dimensional non-stationary TDS in map view, displaying the possible organization of the geological structures and their spatial evolution. To control the non-stationarity, 2D trend maps are obtained by solving numerically the diffusivity equation as a proxy to describe the spatial evolution of the sedimentary patterns, from the sources of the sediments to the outlet of the system. 2D continuous rotation maps are estimated from inferred paleo-orientations of the fluvial system. Both trend and orientation maps are derived from geological insights gathered from outcrops and general

[4]Dall'Alba, V., Renard, P., Straubhaar, J., Issautier, B., Duvail, C., Caballero, Y. (2020). 3D multiple-point statistics simulations of the Roussillon Continental Pliocene aquifer using DeeSse. Hydrology and Earth System Sciences, 24(10), 4997-5013.

knowledge of processes occurring in these types of sedimentary environments. Finally, the 3D model is obtained by stacking 2D simulations simulated from 2D training data sets. The vertical facies transition between successive 2D simulations is controlled partly by the borehole data used for conditioning and by a sampling strategy. This strategy accounts for the vertical probability of transitions, which are derived from the borehole observations, and works by simulating a set of conditional data points from one layer to the next. This process allows us to avoid the creation of a 3D training data set, which may be cumbersome, while honoring the observed vertical continuity.

3.1 Introduction

It has been shown, for example by Naranjo-Fernández et al. [2018], that accounting for heterogeneity is an important step in producing realistic hydrogeological models and properly managing the water resource, especially in the context of global climatic changes. The present study proposes a new multivariate workflow, using a multiple-point statistics (MPS) approach, to model the spatial heterogeneity of complex alluvial aquifers. The workflow is applied to the Roussillon aquifer, which is a multi-layered system composed of the Quaternary aquifer, the Continental Pliocene aquifer, and the Marine Pliocene aquifer (from top to bottom). Located along the southernmost part of the French Mediterranean coast, near the Spanish border, this system is used intensively both for drinkable water and irrigation [Aunay et al., 2006]. From its social and economic importance, understanding the aquifer is essential for the authorities to ensure long-term and sustainable management of the resource. Since one of the largest sources of uncertainty is the identification of the hydraulic conductivity field, it has been decided to focus on the modeling of the complex geological heterogeneity of the Continental Pliocene layer. This layer consists of alluvial deposits and presents a high level of internal heterogeneity.

To model the heterogeneity, different geostatistical methods have been developed and used in the last decades [Koltermann and Gorelick, 1996; de Marsily et al., 2005]. They were employed in different fields going from risk assessment, resources management, mining or petroleum engineering [Matheron, 1963; Strebelle et al., 2002; de Carvalho et al., 2017]. All these methods aim to model the variables of interest at locations where they have not been measured. Traditional geostatistical methods are based on covariance or variogram models inferred from the data. Kriging [Matheron, 1963] provides the best linear unbiased estimator, it is fast and produces a smooth interpolation. Multi-Gaussian simulation methods, such as the sequential Gaussian simulation approach (SGS) proposed by Deutsch and Journel [1998], are able to generate random fields, depicting the spatial variability of the variable of interest. Truncated or pluri-Gaussian simulation methods (TGS or PGS) allow generating discrete realizations where the spatial relations between the facies (categories) are derived from one or several underlying multi-Gaussian random fields [Matheron et al., 1987]. However, these methods are based on two-point statistics and

cannot reproduce some geological features such as the sinuosity of a channel or realistic sedimentological patterns. Hence, they are not always suitable for modeling the expected heterogeneity in geological reservoirs. On the contrary, object-based methods consist in placing directly in the simulation domain some random, predefined objects (e.g. channels) defined by their shapes (e.g. width, sinuosity, ...), which allows generating realistic realizations. However, such techniques suffer from the difficulty of conditioning the simulations on punctual data. Multiple-point statistics methods have been developed since the 90s to overcome these limitations. MPS techniques allow generating random fields reproducing the spatial statistics given in a training data set (TDS), which is a conceptual model that integrates the geological knowledge of the area of interest. Moreover, unlike traditional approaches, MPS does not require the definition of an analytical model to describe the statistical spatial distribution of the variable of interest, instead, it infers the model in an implicit way from the TDS provided by the user [Hu and Chugunova, 2008].

Many MPS algorithms have been developed over the years. The general principle consists in sequentially populating the simulation grid while reproducing the patterns (spatial statistics) present in the TDS. For example, in SNESIM [Strebelle et al., 2002], the statistics of patterns on a pre-defined geometry are stored in a tree shape database that is built by scanning the whole TDS before starting the simulation. Then, the simulation proceeds pixel by pixel, at each step a value is drawn randomly according to probabilities conditioned by the surrounding patterns and computed from the database. As a consequence, the method is memory-consuming and limited to the simulation of categorical variables. In IMPALA [Straubhaar et al., 2011, 2013], the limitation due to the memory is alleviated by using a list shape database, and non-stationary TDSs can also be handled with the use of auxiliary variables [Chugunova and Hu, 2008]. In other algorithms, such as FILTERSIM [Zhang et al., 2006], CCSIM [Tahmasebi et al., 2012] or IQSIM [Hoffimann et al., 2017], the simulation grid is filled by directly pasting or quilting patches, *i.e.* several pixels at a time. FILTERSIM uses a set of filters to reduce the dimension of the problem, whereas CCISM is based on cross-correlation between patches. IQSIM proposes a new approach that bypasses traditional ad-hoc weighting of auxiliary variables. The main drawback of patch-based methods is often their difficulty to honor conditioning data.

One of the most flexible MPS algorithms is the Direct Sampling [Mariethoz et al., 2010]. It is a pixel-based method, where the simulation of one pixel consists of randomly searching for a pattern in the TDS that is similar to the pattern centered on the considered pixel in the simulation grid, and then copying the value of the variable from the TDS. It has the advantage of making database creation unnecessary, does not require computing probability, and can handle patterns of varying geometry. By adapting the way of comparing the patterns in the TDS and in the simulation grid, the algorithm is able to deal with categorical and continuous variables, as well as with the joint simu-

lation of multiple variables. In this work, we use the direct sampling algorithm implemented in the DeeSse code [Straubhaar, 2019]. It is parallelized and offers many options to constrain the stochastic simulations, such as continuous rotation/scaling maps or proportion targets. Finally, by generating an ensemble of realizations, it is then possible to estimate any probability of interest from the different facies maps. More details about the features of the DeeSse code are provided in Meerschman et al. [2013]; Straubhaar et al. [2016, 2020a,b]; Straubhaar and Renard [2021].

The choice of a simulation technique to model an aquifer at a regional scale depends on different factors. One important aspect is the amount of data available. When the amount of data is large, it is possible to infer rather accurately the statistics describing the spatial variability from the data. Probability distributions about the different rock types, variograms, and spatial trends can be directly estimated and used in the simulation process. This situation often occurs in the mining industry, for example, where a very large number of drill holes are made during the exploitation of an ore deposit. The configuration is very different in other situations, such as the Roussillon plain, where only a few boreholes are available for a large study area. It becomes then difficult if not impossible to estimate accurately those statistical parameters from the data set. One has then to rely more heavily on indirect data, geological concepts, and analogy with other sites. In these situations, statistical distributions, variograms, and orders of magnitude of correlation lengths could be borrowed from databases of similar environments such as those developed by Colombera et al. [2012]. The issue with that approach is that the simulations may be constrained only by a few data points and therefore the final variability among the simulations will be excessively large, and the geological features will not be properly represented because the field data will not compensate for the lack of geological concept in a variogram based geostatistical approach. An object-based method would respect better the geological knowledge because the user will have to explicitly define the shape of the objects, and this approach could be an interesting solution for these situations with an important data gap. The object-based approach allows integrating directly geological knowledge in the stochastic simulation process. However, since conditioning poses difficulties for patch-based methods such as object-based, we prefer to use MPS, which allows the creation of complex and realistic geological features while handling conditioning on data points in a straightforward manner.

When using MPS, an important part of the process is the construction of the training data set. We first want to note that the conceptual sedimentological models are usually represented in 2D map views or block diagrams, and geologists are used to express their understanding of a system by drawing such maps and cross-sections. Furthermore, remote sensing data or geological maps are widely available and can be used to refine these 2D conceptual models. Accessing 2D training data sets is therefore easy and simple. However, the standard MPS workflow requires a 3D training data set to generate 3D simulations. Get-

ting the 3D training data set from 2D concepts is not a simple task. It may require a significant amount of tedious work to construct manually a 3D training data set from the 2D concepts. Therefore, previous research was devoted to the design of MPS algorithms able to use 2D training data sets directly as input for 3D simulations [Comunian et al., 2012; Cordua et al., 2016]. Here, we propose a simpler approach that allows the user to avoid the step of the 3D training data set construction. This is not mandatory. If a 3D training data set is available, it can easily be used in the workflow, but if it is not available it should not be a limitation, as we will illustrate in the chapter.

Another very important aspect to take into account at the regional scale is the statistical non-stationarity resulting from geological processes such as the location of the sources of the sediments, their transport, deposition, and so on. The application of MPS to a real case study requires more than just an efficient MPS code and a good training data set, it also requires the development of a methodology and a workflow to account for all those previously cited aspects.

The aim of this chapter is therefore to introduce a global workflow allowing the incorporation of most of the available geological knowledge into a plausible heterogeneity model, and to illustrate the method on the Roussillon plain. This approach is generic and can be applied to any other case where the available data are scarce compared to the geological knowledge. The workflow includes a series of steps that are described in detail in the chapter. Based on the borehole and geological knowledge of the site, a plan view non-stationary training data set displaying the main sedimentological features is designed. In this approach, we limit ourselves to the construction of a 2D training data set, since there are many situations in which the cross-sectional view at the scale of the aquifer is much less well-known than the expected spatial organization of the sedimentary layers on a 2D horizontal plane. The vertical transitions are controlled using the probability of transitions derived from the boreholes. To control the lateral transitions and non-stationarity, 2D auxiliary maps representing a proxy of the evolution of the system from the sources of the sediments to the output are modeled by solving a diffusivity equation. The boundary conditions imposed to the diffusivity equation allow accounting for the paleo-input zones and the lateral geometry of the aquifer. In addition, the proposed workflow accounts for the paleo-orientations of the sedimentary system and its related uncertainty as inferred from field observations. This work shows that such an approach can be efficient to simulate realistic alluvial systems matching the conceptual knowledge of the system.

3.2 Background information

Geology

As presented in the previous chapter (Chap. 2) the Roussillon aquifers is composed of three main layers, going from top to bottom as : Quaternary aquifer, Continental Pliocene aquifer and Marin Pliocene aquifer. This aquifer found its origin with the opening of the Golf of Lyon and the Messinian salinity crisis that created large space in the Miocene deposit for Pliocene and Quaternary deposits to accumulate afterward. The Pliocene layer is composed of different sandstone units separated by silt and clay layers of low permeability [Duvail, 2012; Aunay et al., 2006]. The main sources of sediments came from the weathering of the massifs surrounding the Roussillon's plain. Its depth increases towards the coastline, where its maximum thickness reaches 300 m [Duvail, 2012]. The best known and oldest systems in the Pliocene Basin are the Gilbert delta. These correspond to the post-Messinian detrital filling. They are extremely coarse deltaic structures that rework the crystalline and sedimentary substratum of the early Messinian. They correspond to sub-aquatic cones, set up on particularly steep slopes, explaining in great part their gravitational nature. On top of these deltaic formations, we found alluvial sediments composing the main aquifer reservoir known as the Continental Pliocene aquifer. This chapter focuses on the simulation of the internal structures of this second layer, the Continental Pliocene deposits, composed of interbedded alluvial deposits.

The Continental Pliocene aquifer is exposed inland where it is not covered by Quaternary deposits, and also extends for several kilometers in the offshore part of the domain. The exposed part of the domain and the extension of the domain are presented in more detail in the previous chapter (Chap. 2 Fig. 2.1). Its altitude ranges from -490 m in the offshore area to 230 m in the plain, with an average thickness of about 170 m for the defined simulated area. The sediments that compose it originate from the surrounding massifs and are distributed following the ancient alluvial system, where the coarse sediments are found near the massifs, forming alluvial fan deposits and followed by a mixture of sandstone and clay deposits as the system loses energy and evolves towards the seashore. This system ends in a marsh-like environment near the old coastline.

Based on field observations, the Continental Pliocene can be considered as a classical fluvial sedimentary system. Near the relief, the association of high energy systems and the large amount of available sediments created alluvial fan deposits, composed of sandstone conglomerates. These alluvial fans have an extent of 1-3 km radius and can be more than 10 m thick. Fans merge together, producing larger bodies of 3 to 6 km wide and over 60 m thick. The alluvial fans rapidly evolve to braided river deposits composed of coarse sands and sandstone conglomerates. These braided structures have generally

an extent of 100-150 m width and are 1-5 m thick. It appears that these networks can be laterally and vertically well-connected, forming very dense and large objects near their sources. With the decrease of the sedimentary slope, the structures tend to evolve toward meandering river structures. Their deposits are still relatively coarse, yet much more sorted, and well contained within a single channel, their width reaches up to 300 m and their thickness up to 12 m. The connectivity of the river bed deposits is hard to observe either in the vertical or in the horizontal directions. Three other sedimentary elements are also intrinsically developed within the alluvial plain. The first two are the crevasse splay deposits and the levees, which are both directly related to the river's banks flooding dynamic. The last element is the floodplain characterized by a fine-grained (silt to shale) sedimentation corresponding to the decanting process of flooding events. In the following, and because we do not consider the deeper Marine Pliocene formations in this paper, we refer to the Continental Pliocene layer/aquifer as Pliocene layer/aquifer.

An important feature to consider in the description of this aquifer is the vertical stacking of the alluvial channels, which shows different regimes of progradation and connection through the vertical axis. These different regimes are related to the variation of the sea level through time, which influences the depositional system. Although it is not possible to have a precise temporal evolution of the Pliocene eustasy level, making it complex to distinguish or create a historical progradation/aggradation curve of the system, it is possible to subdivide the Continental Pliocene aquifer into 4 sub-intervals. These sub-intervals are characterized by different stacking arrangements or horizontal facies spatial distributions. These sub-intervals are numbered from 1 to 4 from top to bottom. The three surfaces that encompass these sub-intervals, from top to bottom, are called UPC-2, UPC-12, UPC-1 and are presented in chapter 2.

In this chapter and for all the MPS models, the four layers of the Continental Pliocene are simulated following the same workflow and using the same TDS. However, for each sub-interval, the auxiliary variables are adjusted in order to take into account their spatial stacking differences, and the horizontal pattern spatial distribution.

Hydrogeology

From a hydrogeological perspective, the study area contains three main aquifers; the Quaternary aquifer located in the shallow alluvial deposits along the rivers (Agly, Têt and Tech), and the Continental and Marine Pliocene aquifer located deeper and covering the whole basin. These aquifers are exploited for agriculture and domestic use.

Due to its wide extension, both onshore and offshore, the Pliocene's aquifer represents a large water reservoir. However, due to uncertainties related to its properties and recharge processes, the management of this resource is difficult.

In the 1960s, the piezometric level was on average 8 m higher as compared to the 2012 data and even artesian at some locations. In recent years and close to the seashore, its exploitation has lowered the groundwater level below sea level during the summer months, when withdrawals are most intense. This situation raises concerns about seawater intrusion risk on the coastal part of the Pliocene aquifer.

As a consequence of climate change, groundwater reserves and recharge may decrease in the near future. For a scenario where the average annual temperature increases by 1.5 C° associated with a decrease in precipitation rate, rivers flow could drop by 40 % over the next 30 years [Chauveau et al., 2013], which will automatically create new stress on the groundwater resource. Considering that the multi-layer Plio-Quaternary Roussillon's aquifer accounts for almost 80 % of the resources used for drinking water, there is an urgent need to understand its behavior in order to manage this resource sustainably to face global change impacts [Caballero and Ladouche, 2015].

Multiple-point statistics and DeeSse

The method used to model the Pliocene Continental layer is the MPS approach. MPS allows flexible use of conditioning data, second auxiliary information, and overcomes the limitations of two-point statistical methods to model complex realistic patterns. The most essential ingredient of MPS approach is the TDS. The TDS is a conceptual model displaying the structures the user wants to simulate. The use of TDS gives flexibility and creativity to the modeler. Unlike some other geostatistical methods such as two-point statistics, utilization of training data sets allows specialists from different fields to discuss together about the geometry and the type of heterogeneity of a model.

A TDS can either be stationary or non-stationary. Stationary TDSs are easier to use, they display a repetition of patterns with a homogeneous spatial distribution, *i.e.* the same type of spatial features is present everywhere in the grid. On the opposite, non-stationary TDSs display different kinds of structures depending on the location, they generally include more information and are more complex. When working with non-stationary TDS, some rules must be observed in order to produce realistic simulations. Since the repetition of patterns is not homogeneous on such TDS, one or several auxiliary variables are required to describe the pattern's spatial distributions. In the simulation grid, corresponding auxiliary variables are defined to control the spatial location of the structures that have to be simulated [Chugunova and Hu, 2008]. With this information, patterns are not mixed together when simulated and trend characteristics can be reproduced. Auxiliary variables for the simulation grid are often called trend maps, because they allow to control the trends of the simulated structures.

The use of the direct sampling algorithm allows us to work with continuous rotation maps, defined for all the nodes of the grid [Mariethoz et al., 2010], whereas classical MPS techniques require the definition of rotation zones of unique value [de Carvalho et al., 2017]. Hence, the specific spatial features displayed in the TDS can follow the same orientation everywhere, which facilitates the construction of the conceptual model, whereas the rotation map defines the local orientation in the simulation grid. Such map, consists of rotation values defined on the simulation grid for each pixel, the given value specifying a rotation that must be applied to the TDS structures.

As previously mentioned, the DeeSse code is used in this project, which is an implementation of the direct sampling method proposed by Mariethoz et al. [2010]. The algorithm is controlled by three main parameters; n- number of neighboring nodes, f- scan fraction, t- distance threshold. The first one, n, defines the maximum number of nodes considered when comparing a pattern in the TDS and in the simulation grid. At the beginning of the simulation, these n closest points are likely to be located far away from the simulated point. As the simulation progresses, the density of simulated point increases and the n closest points are starting to be located closer to the central point. This feature enables DeeSse to reproduce structures of all sizes during the simulation, starting with large ones and finishing with small and fine structures [Mariethoz et al., 2010]. The second parameter is the threshold value t. When comparing patterns during the simulation, DeeSse calculates the pattern similarity between the TDS and the simulation grid with a distance value. A perfect match between the patterns represents a distance of zero, and completely different patterns correspond to a distance of one. If the distance calculated at the first random position in the TDS is larger than the threshold, another point is chosen randomly in the TDS and the distance is re-calculated. This is repeated until the value of the distance has reached the threshold or until a perfect match is found, then DeeSse copies the value of the central point found in the TDS into the simulation grid. The last parameter, f, allows limiting the simulation time while conserving realistic patterns reproduction. If a fraction f of the TDS is scanned without finding a pattern satisfying the threshold condition t, then the best node scanned so far (corresponding to the minimal distance between patterns) is retrieved. The same principles are used for categorical and continuous variables, with an adapted definition of the distance. For multivariate simulation, one pattern per variable is considered, with the same central node, and one n value and one threshold value (t) per variable.

Finally, the DeeSse code integrates the use of Gaussian pyramids for the simulation of complex patterns. The use of pyramids helps to better reproduce the different scales of the simulated structures. The Gaussian pyramids approach works by upscaling the simulation grid and the TDS to a coarser grid, this is repeated x numbers of time, resulting in several grid levels, with coarser and coarser resolution. The upscaling is done by applying a convolution kernel over the TDS. The MPS simulation starts at the coarsest resolution grid. The result

is then expanded (by convolution) onto the previous (finer) grid level and is used as auxiliary conditioning to guide a next MPS simulation at that resolution. This is repeated until the original grid (finest resolution) is simulated. The Gaussian pyramids approach has many advantages as in addition of improving the quality of the simulated structures at small and large scales, it can also, depending on the configuration, reduce the total simulation time process. More information is documented in Straubhaar et al. [2020a].

3.3 Materials and Methods

This section presents the various elements that constitute the proposed MPS workflow. The elements are presented in their chronological order. The section begins with an overview of the workflow before describing each of the steps more in detail.

Workflow

The first step of the workflow is to interpret the geophysical logs, seismic data and geological field observations, and to create, based on their interpretation, a sedimentological concept. More explanation on the data treatment of those data sets can be found in chapter 2.

The second step consists in transforming the conceptual sedimentological description into one or several training data sets. This step is an iterative task, the modeler works with the geologist, and they come up with one or several representative TDS(s) of the system. In the Roussillon case, the TDS used for the Pliocene, is a 2D non-stationary conceptual plan view of an alluvial system composed of 6 sedimentary facies. The TDS imposes constraints on the geometry of the simulation grid and on the auxiliary information that have to be incorporated into the model.

The third step is the creation of a suitable simulation grid and its associated auxiliary variables. The Roussillon simulation grid is created based on the upper and lower surfaces topography of the Continental Pliocene layer. This interval is then subdivided into four sub-intervals, delimited by three interpolated surfaces (from top to bottom, UPC-2, UPC-12, UPC-1). Each sub-interval is finally divided into stratigraphic layers, respectively going from top to bottom, into 48, 24, 18, 18 layers.

In order to deal with the generated TDSs that show non-stationarity in the spatial location of their patterns, two auxiliary variables have been created to inform the algorithm where each kind of patterns in the TDSs must be simulated in the simulation grid. For each of these auxiliary variables, one map is created for the TDS and one for the simulation grid.

The first auxiliary variable is constructed to represent the horizontal trend of the TDS, going from left to right in the training data set. This variable represents the continuous evolution of the conceptual sedimentary system, advancing from the sediments sources (left side of the TDS) to the seashore (right side of the TDS), from a top view perspective. The value of the auxiliary variable is simply the x coordinate of the TDS re-scaled between zero and one. In the simulation grid, we compute the auxiliary variable by solving numerically a diffusivity equation with proper boundary conditions allowing to mimic the general trend of sediments transport from the sediments sources, on the west of the basin, to the coast.

The second auxiliary variable is used to control the zones where the alluvial deposits should not be simulated. These zones correspond to the border of the simulation domain in the offshore part. Since no channels are known to be present in these areas, from both conceptual knowledge and borehole analysis, we want to "clean" these zones from the presence of any channel. For this purpose, we have created a second categorical auxiliary variable, where the value 1 corresponds to the presence of channel deposits and the value 0 to their absence.

Finally, we add to the model rotation maps, in order to guide the simulation of the alluvial channel in the simulation grid. Two continuous rotation maps are used to define the rotation limits for the simulations, adding a tolerance of +/- 10° on the rotation map obtained by kriging data that constrain the paleo-orientations of the main paleo-rivers.

The 3D model is then composed of stacked 2D simulations constrained by the 2D training data set composed of categorical facies map, auxiliary variables and rotation maps. As discussed in the introduction, this approach allows avoiding the construction of a 3D TDS that could be cumbersome. To compensate for this choice and to take advantage of the information available from the hard data set, the 3D grid is created with a rather fine resolution along the z axis. The vertical transition between facies is controlled by simulating data points from the previous 2D simulations and used them as additional conditioning data for the simulation in the next 2D layer. The values assigned to these sampled points are based on the vertical transition distribution of the facies, inferred from the hard data set. This process allows bypassing the creation of a 3D TDS and to simulate with 2D simulation, 3D objects with a realistic z dimension.

The final step in this workflow is to generate a set of simulations to characterize the uncertainties around the spatial locations of the channels. Probability and entropy maps are computed to summarize this information.

Flattened space simulation grid

With the creation of the TDS, the conceptual sedimentation process of the Roussillon's plain is now transferred into a conceptual model. The next step is to create a suitable simulation grid (SG) for the MPS simulation according to the sedimentation process expressed in the TDS. As mentioned before, it is decided to create the 3D model by stacking 2D simulations.

Regarding the MPS simulations, they are carried out in a 2D flatten space grid that does not take into account the volumetric facies scaling of the structural grid. This decision was made to facilitate the simulation process and the creation of the 3D auxiliary maps. The grid dimensions are in x, y, and z: $1404 \times 1097 \times 108$ cells, with a cell dimension of $50 \times 50 \times 1$ m. The x and y cell dimensions are defined to optimize the resolution of the modeled objects while keeping the computation time reasonable.

As presented in the previous chapter (Chap. 2), the simulation grid that is used for the MPS simulation is bounded by two main layers, the upper and lower layers of the Continental Pliocene aquifer. These digital elevation maps of the Pliocene [Duvail, 2012] are used to select the active domain of the 3D simulation grid. This grid is also subdivided in 4 sub-intervals delimited from bottom to top by the UPC-1, UPC-12, and UPC-2 surfaces. These sub-intervals represent specific sedimentological settings and are modeled individually in this study, using the same TDS but adapted auxiliary variables, and rotation maps. The simulation grid is defined as a structural grid, which means that the number of layers is fixed in all the domain for each sub-interval. However, the top and bottom altitude of each cell is free to vary spatially in the layers (Fig. 3.1). The number of layers composing each sub-interval was defined in order to avoid pinched cells and to assure a mean cell thickness above 0.5 m in each sub-interval. The number of layers for each sub-interval is from top to bottom composed of 48, 24, 18, and 18 layers.

Conditioning data set

Conditioning data sets, also called hard data, correspond to field observations, which are assigned to cell values in the simulation grid. The first hard data set of the Pliocene model consists of 101 geophysical logs (lithological, gamma-ray and resistivity logs) that have been described and interpreted in terms of sedimentary facies. The second hard data set contains facies information derived from the geological map of the Roussillon [Genna, 2009]. It consists of the mapped outcrop of the Pliocene alluvial fan. The final conditioning data set comes from the interpretation of seismic sections acquired in the offshore domain of the Roussillon plain. All these data sets are presented in chapter 2.

The final conditioning data set is composed of 187'320 interpreted points. These points are described as 6 different sedimentological facies, which are used as hard conditioning data during the simulation.

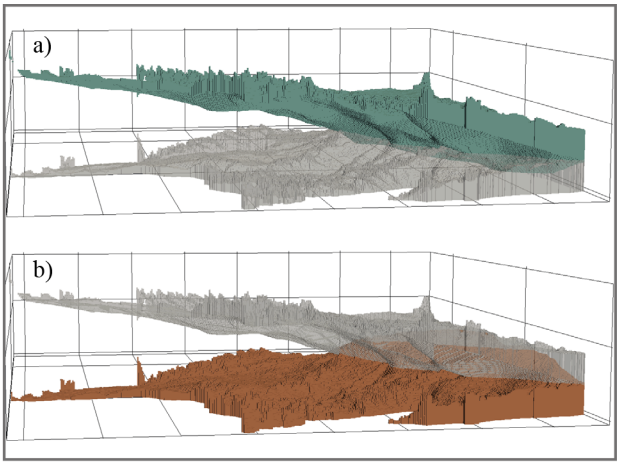

Figure 3.1: (a) In dark green, the 3D volume of the Continental Pliocene (the gray volume representing the transformed space). (b) In dark orange the transformed grid (flattened space) of the Continental Pliocene layers inside which the 2D simulations are simulated (the gray volume representing the original space). The vertical scale is exaggerated in this representation. View from the south of the area toward the north. The offshore domain is here not shown to simplify the representation.

Training data sets

Based on field observations, well logs analysis and the general understanding of the sedimentary processes composing the Pliocene, different TDSs were created and tested. We here present the main TDSs and their associated concepts (Fig. 3.2). These TDSs correspond to different possible conceptual representations of the Pliocene and were tested using 2D simulations. As discussed by Høyer et al. [2017], the creation of the TDS is an iterative task, and it is always preferable to compare TDSs not only on their structural aspects but also on their associated MPS simulation outputs. This is particularly important when the model includes non-stationary and uses complex auxiliary variables, making the simulated patterns difficult to predict from the TDSs alone. The TDS of the Roussillon MPS model consists of a categorical map describing the sedimentological patterns to be simulated and two auxiliary variable maps describing the spatialization of these patterns in the simulation grid. In addition, a rotation map is provided for the simulation grid in order to change the orientation of the patterns of the conceptual sedimentary map in the simulation grid during the simulation process.

The primary variable of the five TDSs, often called training images, presented in figure 3.2, describes alluvial systems composed of similar elements and spatial patterns of evolution: the systems start from the sediments sources on

the upstream side, with alluvial fan deposits, and gradually moves toward the output of the system on the coastal side. In all cases, the facies evolve from braided to meandering river deposits, it is only in the last TDS that the marshy environment is incorporated and tested. The five different training data sets are proposed to test different assumptions concerning the spatial arrangement of the facies at different scales. The simulations performed here and presented with figure 3.2, are designed to test the sedimentary map of the TDSs, and are not representative of the final modeled system. These simulations are run with very flexible parameters n, t and f, without incorporating the hard conditioning data or calibrating the auxiliary trends. For alleviating the time of simulation, only the first auxiliary information of the TDS is used in these simulations. Their sole purpose is to provide a visual understanding of the spatial distribution of patterns within the simulation grid.

The first TDS (Fig. 3.2a), was created based on a simple sketch. The TDS is simple as it is only composed of 3 different facies and does not incorporate complex shapes. The system starts with alluvial fans and rapidly evolves toward alluvial channels that are incorporated into a homogeneous floodplain. We can see that since the TDS is quite simple, the MPS algorithm succeeds in reproducing continuous patterns. Such a simple TDS allows to quickly generate suitable simulations and are informative as a first system approximation.

The second TDS (Fig. 3.2b), was created based on a more conventional conceptual representation of braided/meandering river systems. It includes complex braided structures and followed by meandering river beds. We can also see that crevasse splay are included in the TDS. The resulting simulation shows realistic meandering river deposits. However, these simulated patterns tend to be wider than those observed in the outcrops in the Roussillon plain and the braided structures are too laterally connected to each other compared to field observations. In addition, the alluvial fan deposits -gray facies- are underrepresented compared to the field observations.

The third TDS (Fig. 3.2c), was created based on an analogous case. It originates from the visual interpretation of satellite images of the Tagliamento River, which is located in northern Italy near the city of Udine, close to the Slovenia border. In this TDS, the entire channel belts of the braided part are connected, losing some complex structures compared to the previous one. This third TDS does not represent the small scale internal structures of the river deposits within the channel belts, nor the embankment structures. The output of the 2D MPS simulation using this TDS results in the creation of too many small meandering river deposits on the plain and to large braided structures.

The fourth TDS (Fig. 3.2d) was obtained by trial and error adjustments. It is composed of five sedimentary facies and shows the evolution of an alluvial system from the mountain (sediment sources) to the coast, excluding the estuary part [Nichols and Fisher, 2007]. In this TDS, meandering river channels are

represented by a straight shape, following the developed sedimentary concept, claiming that the TDS does not show the patterns that would be found in a snapshot of a fluvial system in surface, but rather represents an integrated view of the sedimentary system through time. This concept is illustrated in figure 3.2f. The associated simulation displays braided and meandering channels that are satisfactory regarding their general sizes and aspects. However, this TDS produces too many channel systems on the plain that are located too close to each other.

The last tested TDS (Fig. 3.2e) mixes some of the previous TDS's patterns. This TDS is composed of a unique facies code for both the braided and the meander deposits. The river systems are straight and develop into coastal deposits. The coastal aspect is new here and describes the end of the fluvial system as it transits toward the marine one. Two new facies make up these marshy deposits, one representing the swampy plain and the other the sandbank deposits. Note also that the dimension of the crevasse splay deposits increases with the decrease of the sedimentary slope (assuming that the sedimentary slope decreases as we move from the sediment sources to the seashore). It is this TDS that is used for the next modeling part of the workflow. As explained earlier, the fluvial system is also represented here following a straight structural direction, since the TDS does not show the patterns that would be found in a surface snapshot of a fluvial system, but rather represents an integrated view of the sedimentary system through time. This concept is illustrated in Fig. 3.2f, with the meandering river facies used as an example. At $t = 0$, the meandering river bed follows one path, controlled by the sedimentary slope and the topography. At $t = 1$, the bed would have migrated laterally, possibly cutting through the previous bed. Finally, at $t = 2$ it is possible to define an area of high river bed occurrence, where all meandering river bed facies would be located. The last one, $t = 3$, highlights the only possible location where crevasse splay could be located, on the borders of the river channel belt. This final TDS (Fig. 3.2e), is composed of 1'200×1'170 cells. The patterns are quite complex, but show satisfactory shapes and sizes once simulated.

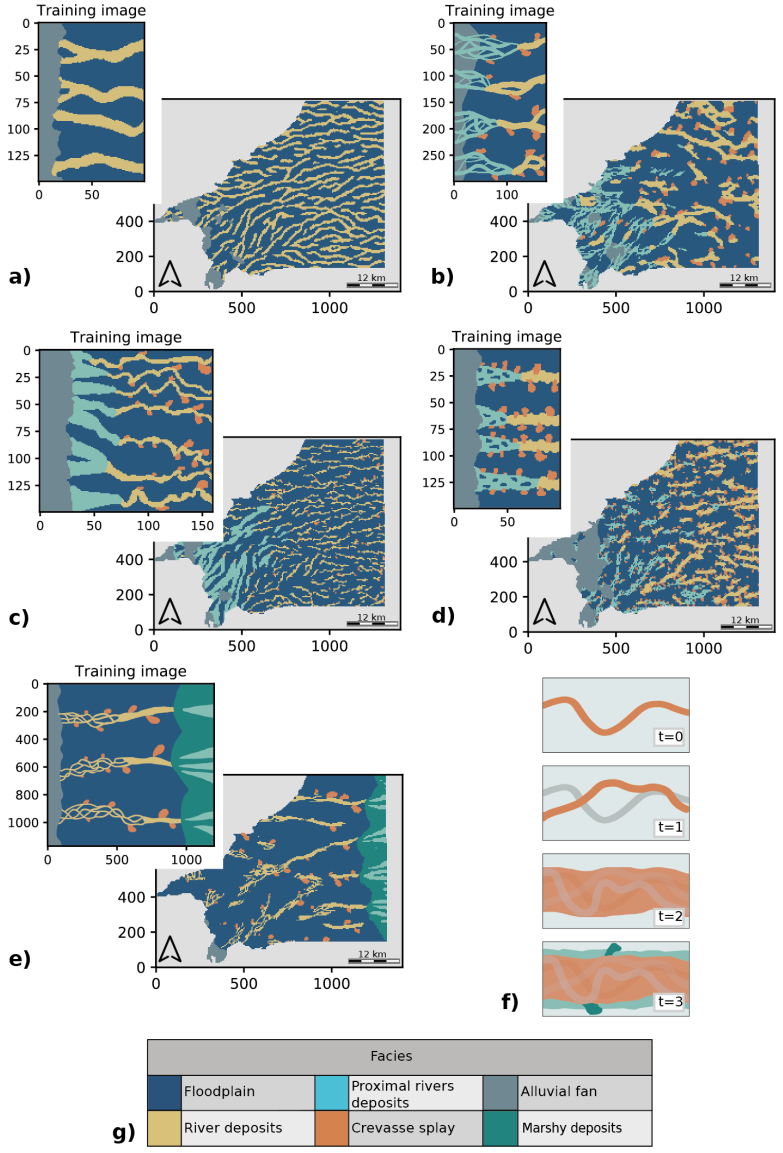

Figure 3.2: (a) First simple training data set. (b) Second TDS, using more complex shapes (braided and meandering parts are differentiated). (c) Analogous case. The patterns are more blocky and have a higher sinuosity. (d) A mixture of a sketchy TDS and an analogous TDS. The system shows some complexity. (e) The selected TDS, which incorporates the marshy part of the system. (f) The selected depositional concept, the meander facies does not represent a snapshot of its location at one defined time t, but the accumulation of all its locations through time. (g) The facies composing the TDSs.

Auxiliary variable 1: Trend Maps

In order to deal with the non-stationary of the TDS patterns distribution, the model has to be constrained with auxiliary information. This auxiliary information is essential to respect the TDS patterns distribution during the MPS simulation. An auxiliary variable (also called trend map) must be defined for the TDS and for the simulation grid. For the TDS, the trend map corresponds to the x coordinate rescaled between zero and one, corresponding to the lateral evolution of the fluvial system (Fig. 3.3b).

For each sub-interval, the first TDS auxiliary variable map associated with the conceptual sedimentological map is rescaled to move the position of the facies in the simulation grid. This TDS auxiliary variable is linked to an auxiliary field associated with the simulation grid. During the simulation, the MPS algorithm will only copy patterns present in the sedimentological map to locations in the simulation grid that match the associated auxiliary variable. It is this first trend map that controls the spatial reproduction of the patterns. By adjusting either the TDS variable or the corresponding auxiliary variable in the simulation grid, we can control the location of the patterns in the simulation. It is this auxiliary variable that constrains the distance between the beginning of the system with the alluvial fan, the transition to the braided channels and then to the meandering channels, and the final transition to the marshy deposits. By adjusting this auxiliary variable, we are able to expand or contract these different zones, thus shifting the transition between the different sedimentological environments in the simulation grid. By adjusting the trend of the TDS for each sub-interval that constitutes the continental Pliocene, we are able to simulate the evolution of the bathymetric level, corresponding to the evolution of the transition zone location, between the meandering channels and the marshy environment (Fig. 3.4), and matching the conceptual description of the system at different times. The auxiliary variable of the TDS for each sub-interval has been manually calibrated to match the conceptual geological description of these sub-intervals.

These auxiliary variables are created by linearly interpolating 10 points, of values incrementally fixed between zero and one, and located at manually calibrated x positions in the conceptual TDS grid map. This linear interpolation is then copied along the y axis of the TDS grid to create the auxiliary variable of the TDS (Fig. 3.3b).

During the simulation, these TDS auxiliary variables are slightly randomly modified for each simulated layer in the sub-intervals. For each sub-interval, we randomly shift the x location of each calibrated point by drawing a random value between -5 and 5 from a discrete uniform distribution, and adding it to the position of the interpolated points. Hence, during the simulation, each layer of a sub-interval uses a slightly modified version of the calibrated auxiliary map, changing the transition location of the different patterns in the simulation grid.

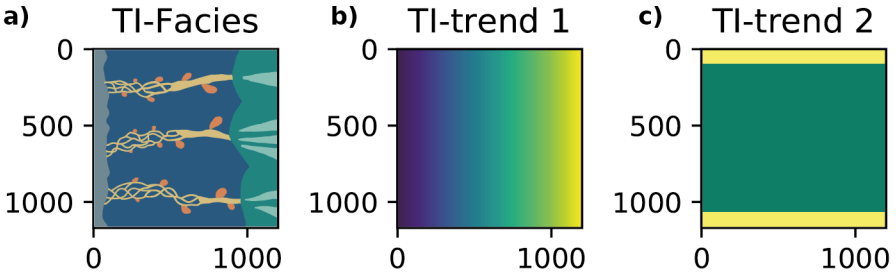

Figure 3.3: a) Selected training data set for the MPS simulations. This TDS is a top view representation of the evolution of an alluvial system, starting with alluvial fans deposits on the left side, evolving to alluvial braided and meander channels, sitting in flood plain deposits and ending with sandbars and marshy deposits on its right side. b) First auxiliary variable of the TDS, which controls the lateral distribution of the patterns in the simulation grid, going from the left side (sources of the system) toward the right side (end of the system, coastal side). c) Second auxiliary variable, which defines the border area of the grid domain where alluvial channels are not present.

This is done to allow for some freedom in the spatial locations of the patterns during the simulations; since the Pliocene bathymetric level evolution is not well known, we do not want to over-constrain the model with a fixed auxiliary variable.

This first trend map must be associated with another trend map with similar range values for the simulation grid. Creating a 3D trend map for the simulation grid is complex due to the geometry of the layers and requires the development of a new approach, different from the one used for the TDS. In the flattened space grid, the auxiliary variable, a trend map ranging between 0 and 1, is computed by numerically solving a diffusivity equation in steady state ($\Delta h = 0$, with Δ representing the Laplacian operator) for the 2D layer composing the 3D grid. The problem is solved using a finite element mesh following the exact geometry of the domain. The boundary conditions are prescribed values $h(x) = h_0$ on some parts of the boundary, and $\vec{\nabla} h(x) \cdot \vec{n}_x = 0$ on the rest ($\vec{n}_x$ being the unitary vector normal to the boundary at x), meaning that the gradient of h is parallel to the boundary on that part. This problem is similar to simulating hydraulic heads in a homogeneous confined aquifer for a steady state flow.

After setting the proper boundary conditions – four input zones set to $h_0 = 0$ and one output zone set to $h_1 = 1$ (Fig. 3.5a) – we obtain the desired trend map (values ranging between 0 and 1) by solving numerically the diffusivity equation. The resulting map is a proxy for describing the evolution of the sedimentary system in the SG (Fig. 3.5b). The four zones with values close to zero correspond to the major paleo-river entrances and the southern relief

zone, where alluvial fan deposits are known to be present. The output zone with values close to one corresponds to the most distal part. This method allows the creation of trend maps that respect the geometry of the SG and takes into account the paleo river locations. It mimics the general trend of sediment transport from the sediment sources to the coast, but it does not constitute an attempt to developing a physically-based model of sedimentation. Finally, two different maps are produced, using different paleo-river sources as boundary conditions. The first auxiliary map (Fig. 3.7a, left side) is used for the bottom sub-interval and does not include a possible paleo-river entrances coming out from the northern part of the domain, the Corbière Massif, while the second one (Fig. 3.7a, right side) includes this paleo-river entrance and is used for the three other sub-intervals.

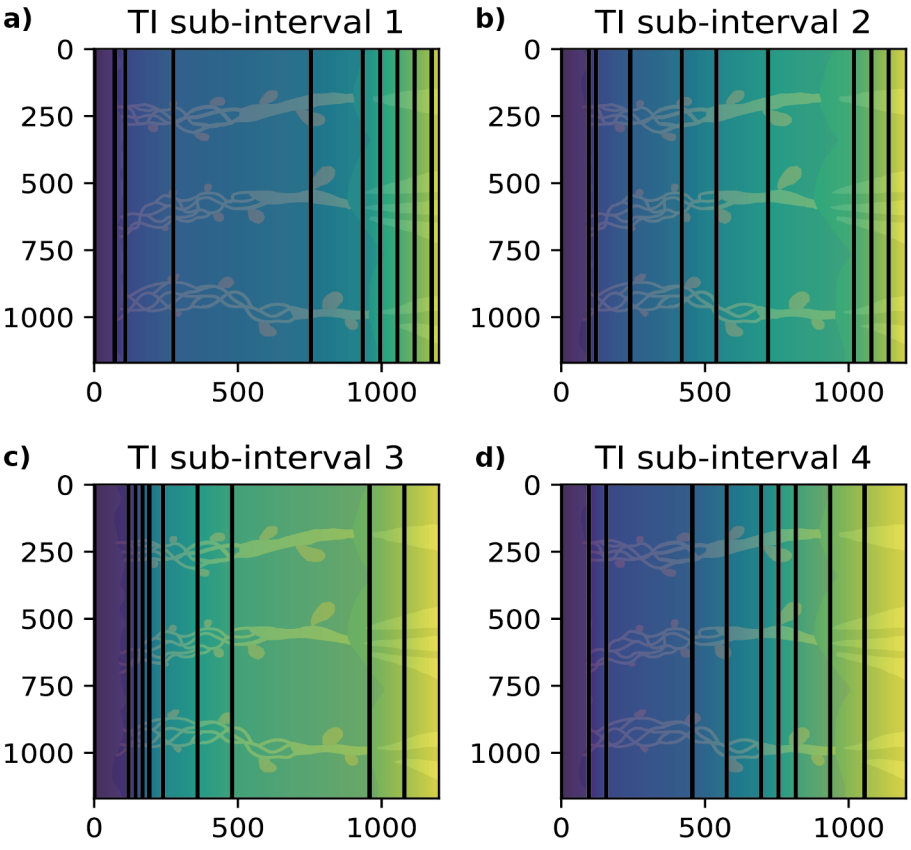

Figure 3.4: The adjusted first auxiliary variable of the training data sets. Each trend is adjusted to fit the depositional concept of each sub-interval, moving the location of the transition between alluvial and coastal deposits along the simulation grid.

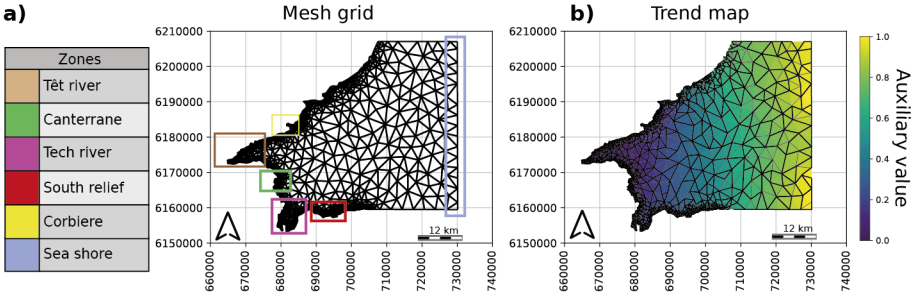

Figure 3.5: a) Boundary conditions are fixed on a grid, between assumed paleo-river entrances on the western side of the 2D simulation grid and the seashore located on the eastern side of the domain. b) Once the diffusivity equation is solved numerically, we use the output as an auxiliary variable map for the simulation grid. The values are matching the one of the TDS first auxiliary variable map, ranging from 0 to 1.

Auxiliary variable 2: Channels categorical location

As introduced in the subsection 3.3, a second auxiliary variable is added to the simulation data set. This second auxiliary variable is used to control the presence or absence of channels in the border locations of the offshore domain. From the seismic cross-sections and the general understanding of the system at hand, it was determined that no alluvial channels should originate or terminate in the lateral boundaries of the offshore domain. To do this, we created a categorical auxiliary variable, which takes the value of 0 in the area where the channels can be simulated and the value of 1 when only the floodplain is allowed to be simulated.

The areas where the channels should not be simulated are located on the border sides of the offshore domain in the simulation grid (Fig. 3.7b). As for the first trend map, two different auxiliary variable maps are created, the first one for the lowest sub-interval and the second one for the three other sub-intervals (Fig. 3.7b). Again, these auxiliary maps are slightly randomized for each simulated layer to avoid over-controlling the pattern location. The random set of auxiliary maps is created by applying a moving kernel to the original auxiliary information in the simulation grid. The original auxiliary variable consists of two zones, 0 and 1 values. Therefore, the averaged grid is composed of continuous values ranging between 0 and 1. The size of the kernel window is chosen randomly between 10 and 60 pixels, and a uniform weight is applied. Then, the new auxiliary variable maps are created using a threshold condition, where all averaged values below 1 are assigned a value of 0.

This process allow us to create a set where the position of the auxiliary variable is randomly moving in the simulation grid. The second auxiliary variable of the TDS is shown in figure 3.3b, with the corresponding grid information being displayed in figure 3.7b.

Rotation Maps

A 2D rotation map is created in order to rotate the orientation of the structures in the simulation grid relatively to their orientations in the TDS. This map is built based on data gathered from field observations and interpretations of assumed rivers' paleo-orientations (Fig. 3.6a). The main river influx came from the Têt river in the central part of the basin and from the Tech river in the south-west part. Based on these orientations, a fictive rotation point set is created and interpolated using kriging.

The orientation map is based on interpretation and is therefore uncertain. DeeSse allows accounting for this uncertainty. A tolerance of +/- 10° is considered and added/subtracted to the kriged map to obtain two rotation maps: one with the minimal angle values and one with the maximal angle values (Fig. 3.6b).

As for the trend maps, two different rotation maps were used (Fig. 3.7c). The first one is used for the lowest sub-interval and the second one for the other three sub-intervals. The main difference between these maps is the assigned rotation near the northern zone, related to the Corbière massif. Since this zone was assumed to be inactive as a source zone during the first part of the Pliocene, corresponding to the sub-interval 1, the channels cannot originate from this zone during the simulation and therefore the rotation value has to be modified to take this information into account and to simulate the alluvial patterns correctly.

The same 2D rotation maps are used in the sub-intervals, along the z-axis, assuming that the variation of the paleo-orientations through time is encompassed within the tolerance values.

Vertical transition

Sampling approach

To control the vertical transition from one layer to the next one, we developed a simple sampling approach, illustrated in figure 3.8. The approach starts by simulating the first layer of the transformed grid (layer 0/bottom layer) using only the hard data set as conditioning data. Once this layer is simulated, points are sampled from this layer and propagated as additional (or secondary) hard data for the next layer. The facies value assigned to these points is drawn accordingly to the vertical transition probability between two facies, calculated from the boreholes hard data set.

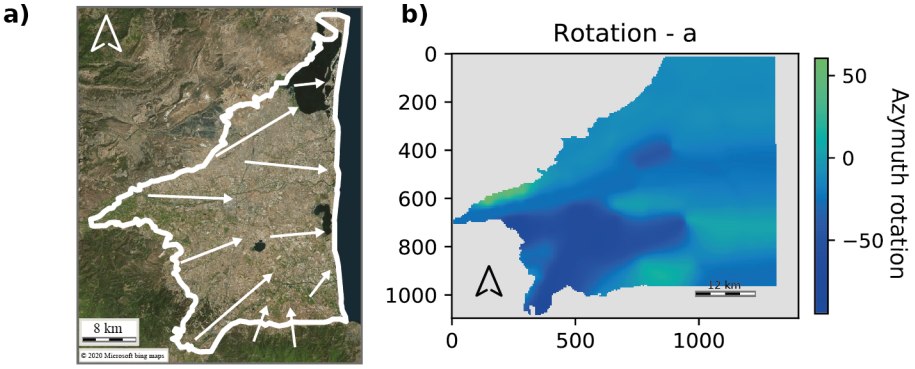

Figure 3.6: a) The main direction of the paleo river-orientations. b) An example of associated kriged map.

Three parameters control this method, the first one defines which facies have to be sampled. After some tests, it appears that concerning the Roussillon case, the best way to control the vertical continuity of the objects of interest is to sample only from three facies: the alluvial fan, the river and the sandbar facies. Since the floodplain facies is the most frequent one, sampling this facies at random location leads to an over-representation of the flood plain and tends to bias the MPS simulations. The crevasse splay facies is not sampled in order to avoid to over constrain the structure of the fluvial objects. The second parameter is the sampling rate. It is here fixed at 0.0075% of the number of simulated cells for each of the three facies. The last parameter controls the maximum number of successive layers that are simulated using the sampling approach. This mechanism allows controlling indirectly the maximal vertical size of the objects. This last parameter is set to 6 for the Roussillon case, meaning that after six successive layers simulated using the approach, the next one will not use secondary sampled hard data.

Without this approach the vertical transition between facies would only be controlled by the hard conditioning data which are scarce compared to the size of the SG and the number of active cells that compose it.

Vertical transition statistic and facies proportion

To validate the vertical sampling approach, two simulation sets have been created, one using the sampling approach and the second one not using it. Both sets are composed of 50 simulations, use the same training data set, the same auxiliary variables, and the same conditioning data. For the purpose of saving computational time, the two tests sets used to test the influence of the sampling approach use a simpler training data set and a simpler grid, with the marshy domain of the TDS and the offshore domain of the simulation grid being not simulated. Figure 3.9a compares the proportion of facies from the TDS, the

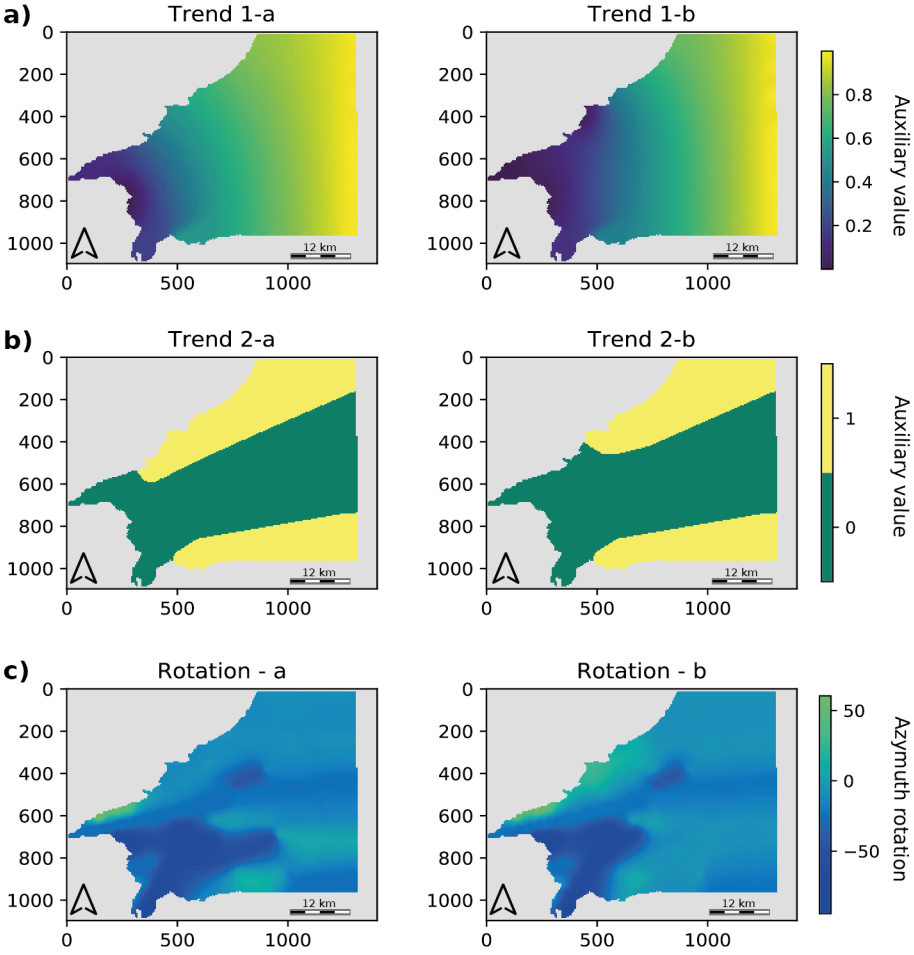

Figure 3.7: This figure shows the different auxiliary and rotation maps of the simulation grid that are used for the MPS simulations. The left column corresponds to the lowest sub-interval (sub-interval 1), which is characterized by the absence of the northern massif paleo source. The right column corresponds to the auxiliary maps of the other three sub-intervals (sub-intervals 2, 3, and 4). All of these maps are presented as a top view of the plain. a) The auxiliary maps describing the lateral distribution of the TDS patterns. b) The trend maps controlling the presence or absence of the alluvial channels. c) The rotation maps correspond to the azimuthal rotation applied to the patterns of the TDS in the simulation grid.

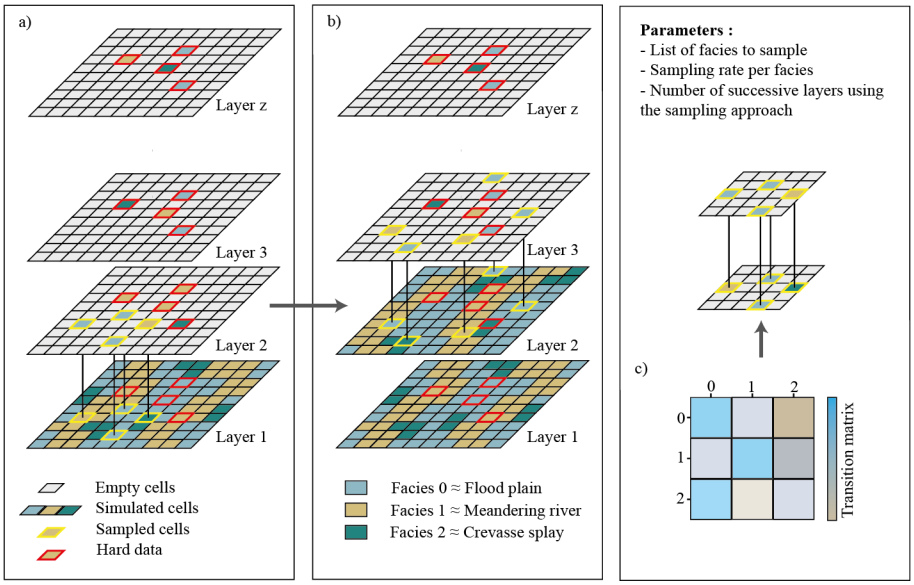

Figure 3.8: a) The first simulation takes place with only the hard data set as conditioning data. Then a set of cells is sampled (in yellow) and used as new conditioning data for the next simulation. b) The process is repeated until the defined number of successive layers is reached. Once reached, a simulation takes place without a sampling set. c) The value of the sampled cell is drawn based on the vertical transition matrix, calculated from the borehole data set.

hard conditioning data set and two simulation sets. Overall, the proportion of simulated facies is satisfactorily reproduced when we compare the proportion of the simulation sets against the proportion of the hard data. It appears that the facies proportions are controlled by both the TDS and hard data, with the hard data set having a slightly larger influence. This is reflected with the alluvial fan facies, which is less represented in the hard data set - mostly due to the central location on the plain of the majority of the boreholes - and less represented in the model compared to the TDS proportion. These facies proportion show the importance of the hard data on the simulation output and the consequence that can arise from a biased hard data set.

To quantify the impact of the vertical sampling strategy, following previous authors, we compared the distributions of the vertical runs [Mood, 1940; Boisvert et al., 2007]. To compute this indicator, the 3D grid is decomposed as a set of vertical columns of voxels. A vertical run is then defined as the length of a succession of the same facies values preceded and succeeded by a different facies. By computing the run length on all the columns for a given facies, one can compute the empirical distribution of runs for this facies. These empirical distributions are computed for the simulation sets and for the borehole data

set. We then compute dissimilarity indices between the simulated and observed distributions for all the facies using a normalized Euclidean distance. The closest to zero the dissimilarity value is, the more identical the distributions are and reciprocally (Fig. 3.9b). The alluvial fan facies is here not represented, because it is under-represented in the hard data set, and a reference distribution cannot be inferred from it.

Overall, the simulation set using the vertical sampling strategy possesses distributions closer to the conditioning data (smaller dissimilarity values) and produces vertically connected objects. The set using the vertical sampling strategy is composed of a larger number of thick objects as compared to the simulations set not using the sampling approach. Figure 3.9b show the beneficial impact of the vertical sampling approach on the simulation outputs.

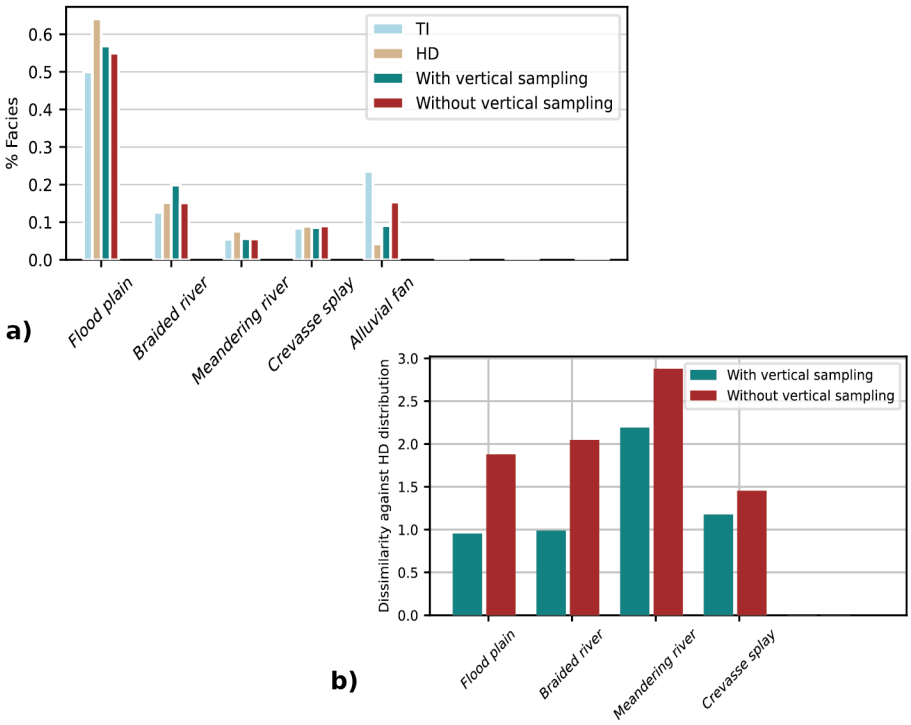

Figure 3.9: a) Facies proportion in the training data set, the hard data set, 3D simulation with vertical sampling and 3D simulation without vertical sampling. b) The dissimilarity values of the two simulation sets. The dissimilarity values are calculated against the vertical size distribution of the hard conditioning data.

DeeSse parameters

The main parameters used for the MPS simulation with DeeSse are tested and chosen in order to minimize the simulation time without impairing the quality of the outputs. Three variables are considered: the facies (categorical) and the two trend maps (defined as continuous). The parameters defined for these three properties are the search ellipsoid which allows limiting the size of the pattern, the maximal number of pattern nodes (n), the acceptance threshold (t) and the scan fraction (f).

To select the best parameters for the simulation of the Roussillon, we used the k-fold cross-validation approach proposed by Juda et al. [2020], to test and select the most appropriate ensemble of parameter sets. In this approach, the conditioning data is divided into k random clusters. One cluster is selected and removed from the conditioning data. The MPS simulation is then performed, and the removed cluster is used as a validation set from which a quadratic score is calculated. The approach then replaces the validation set by another one and re-simulates the new validation points to calculate another score. Once all the clusters have been tested, a final averaged score is calculated. Each parameter combination is tested using this framework, and the global ranking of the parameter sets allows the selection of the most suitable parameter sets.

Due to the lack of conditioning data regarding the number of simulated cells, the calibration of the MPS parameters was performed in a 2D simulation. We selected the simulated layer with the maximum number of conditioning data and used it to calibrate the MPS parameters. Using a 2D simulation also reduces the simulation cost of the calibration approach. In this case, the search ellipsoid for the facies variable is defined by a radius of 500 cells in x, and y axis directions and 1 along z because 2D simulations are performed. The maximal number of nodes is set to 24 for the facies variable and to 1 node for the trend variables. The larger number of neighboring nodes for the facies is defined to ensure a proper pattern reproduction during the simulation at both large and fine scales. The search ellipsoid of the two secondary variables is not relevant here, since the variable are informed for the whole grid. Moreover, there is no need to define more than one node for the n parameter of these variables, and is therefore fixed to 1. The threshold parameter t that controls the pattern quality reproduction is set to 0.0025 for the facies property and respectively to 0.01 and 0.005 for the trend properties. Finally, the scanned fraction of the TDS is set to 0.5.

Once satisfied with the 3D simulation output, the last step of the approach consists in producing numerous simulations in order to compare them and to study the uncertainty of the model. The simulations are run on a CPU cluster, allowing to parallelize the computational load between different CPUs.

3.4 Simulation results

The following section presents the results of the workflow and the models obtained with DeeSse. The general aspect of the simulation is discussed first, before focusing on the ensemble statistics results calculated from the 50 simulations set.

Note that MPS validation is still an active research topic. Some tests and approaches are discussed, for example, by Mariethoz and Caers [2014] or Juda et al. [2020]. However, due to the relatively small amount of hard conditioning data compared to the number of simulated cells in our 3D grid, we limit ourselves in this work to analyzing the plausibility of the geological patterns in the simulations with respect to the conceptual model, and the final geological uncertainty resulting from the model.

3D simulation

The results of the simulation process are presented in figure 3.10, figure 3.11 and figure 3.12. Figure 3.10 presents one 2D top view of a simulations layer for each sub-interval composing the Continental Pliocene, while figures 3.11 and 3.12 shows 2D cross-sections of the simulated facies in the stratified grid.

Regarding the 2D top view simulation (Fig. 3.10), the first observation is that the model reproduces well the training data set patterns. All the main features of the TDS are well reproduced, and the different patterns are not mixed between each others. Some discontinuities can be observed between the braided and meandering river deposits. These discontinuities are caused by the presence of hard conditioning data that do not match the pattern locations imposed by the trend map of the simulation grid. The second observation concerns the control of the non-stationarity. We can observe that the simulated structures successfully follow the trend imposed by the (first) auxiliary variable. Moreover, the trend deformation method applied to each TDS sub-interval succeeds to move along the patterns' location within the plain, and successfully creates different sedimentological horizons, matching the conceptual descriptions. Another observation is that, the continuous rotation maps produce the desired smooth pattern rotations, which could not be obtained with classical zonal rotation approaches. The use of these rotation maps enable the creation of realistically oriented channels along the plain. Finally, we can observe that the secondary trend, used for the "cleaning" of the offshore boundaries, works properly and avoids the creation of degenerated patterns on the border locations where sediment sources are absent.

If we look at the corresponding cross-sections (Figs. 3.11 and 3.12), we can see that the spatial patterns are different for each sub-interval. This is due to the variation of the horizontal pattern distribution imposed by the first trend variable, which manages to create zones of different connectivity at different

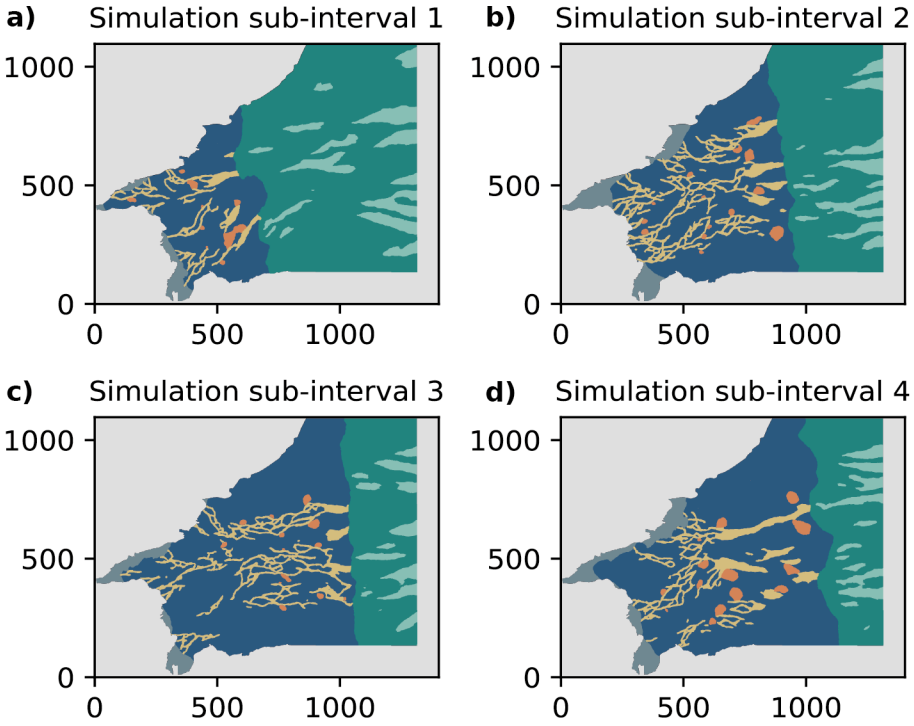

Figure 3.10: 2D top view representation of the MPS simulations going from bottom to top as a) the first sub-interval, b) the second sub-interval, c) the third sub-interval, and d) the last sub-interval. The patterns of the TDS are well reproduced in the simulation grid, and have realistic shapes, orientations and distributions in the simulation grid thanks to the use of multiple auxiliary variables and rotation maps. For each one of the sub-intervals, we can see that the seashore location varies between the sub-intervals (transition between blue and greenish facies). This is done by modifying the first trend variable of each TDS's sub-interval, and is consistent with the conceptual sedimentological evolution of the Roussillon alluvial continental system.

locations in the alluvial plain. The last visual observation concerns the stacking of the channels, which is controlled by the hard conditioning data, the sampling process, and the vertical facies transition probability. Without creating realistic channel like 3D structures, the proposed approach manages to stack the channel facies along a central position in the vertical axis, improving the global realism of the 3D simulations.

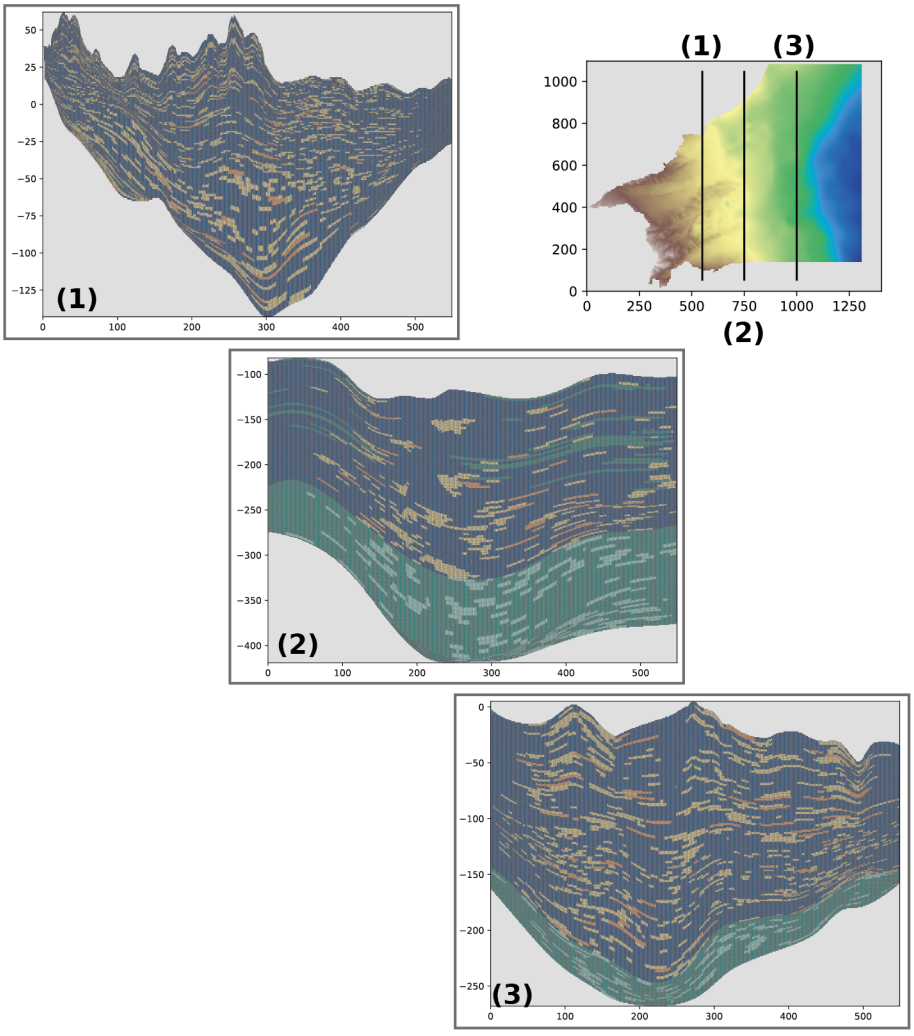

Figure 3.11: 2D cross-sections of a MPS simulation in the stratified grid. The cross-sections are along the y axis. The different sub-intervals are visible with different stacking arrangements and facies proportions.

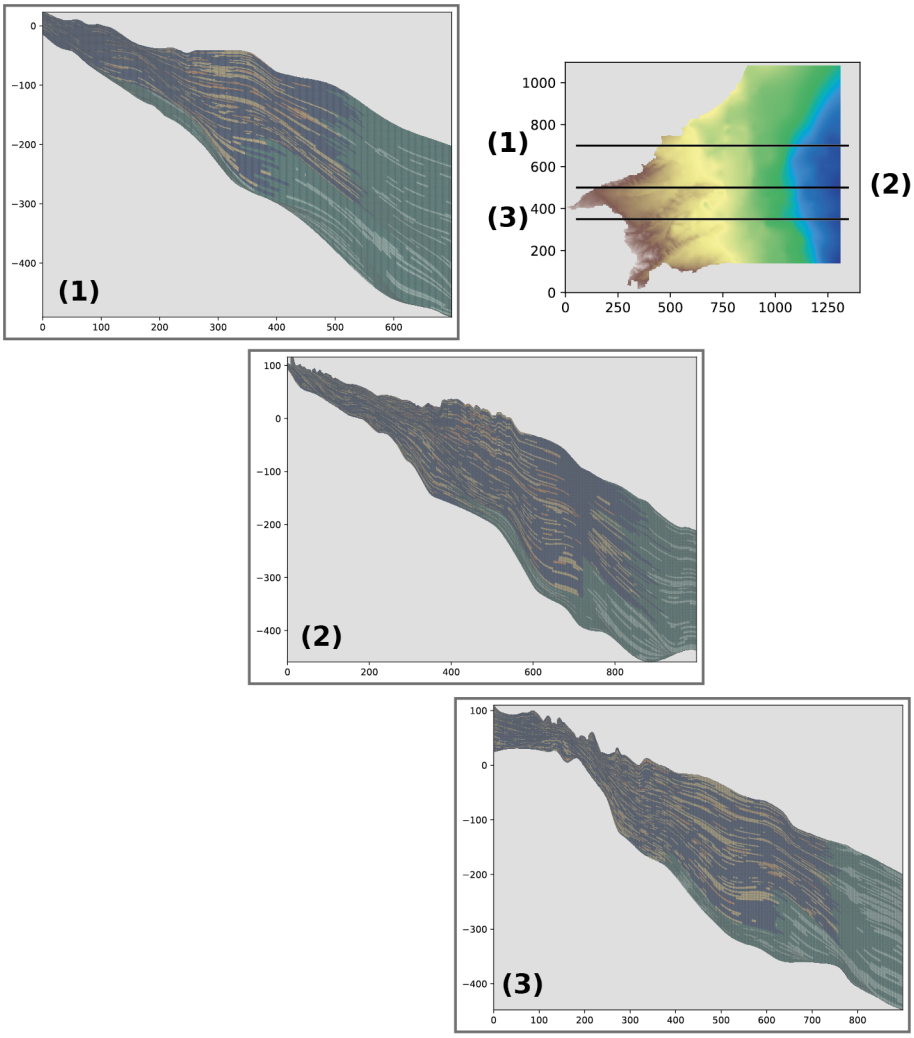

Figure 3.12: 2D cross-sections of a MPS simulation in the stratified grid. The cross-sections are along the x axis. The different sub-intervals are visible with different stacking arrangements and facies proportions.

Finally, the percentage of simulated facies through the 50 simulations set is calculated and compared to the TDS and hard conditioning data sets (Fig. 3.13). We can see that both the TDS facies proportion and the conditioning data facies proportion influence the output set of simulations. If we focus the analysis on the alluvial channel and sandbars deposits, which represent the potential main water bearing facies, the simulations set appear to correctly reproduce the proportion of these two facies. Some differences are still visible between the facies proportions of the MPS simulations and the facies proportion of the hard conditioning data set, mainly due to the influence of the facies proportion of the TDS. Globally, the proportions of simulated facies are satisfying and reproduce the qualitative information of the conceptual description of the system (the training data set), and the quantitative facies proportions of the conditioning data.

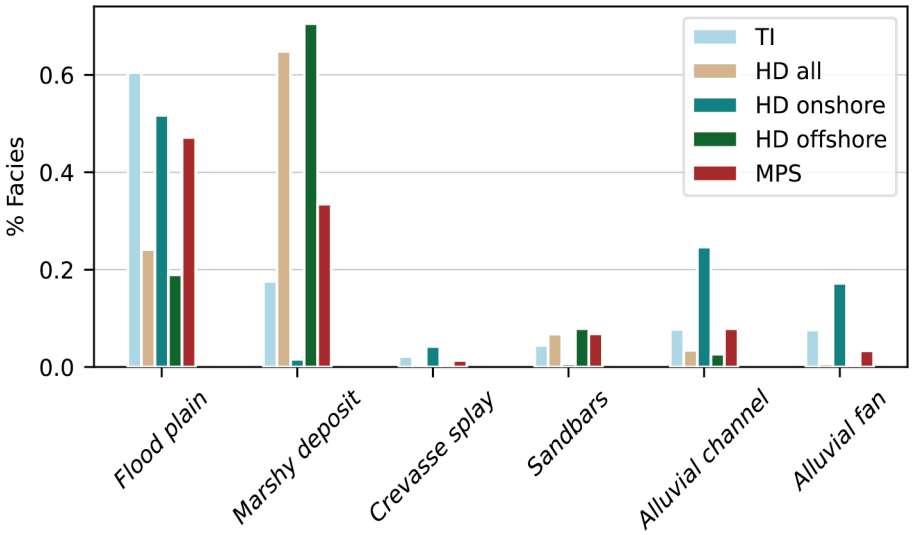

Figure 3.13: Facies proportions present in the training data set, the hard data set, the onshore data set, the offshore data set, and the 50 simulations set with vertical sampling.

Probability Maps

Simulating numerous realizations enables us to calculate probability maps (Fig. 3.14) and the pixel wise entropy of the simulations set (Fig. 3.15).

The probability maps show the probability of facies occurrence at each grid location based on 50 simulations, if a facies is highly constrained at a spatial location, it is likely that all the simulations will simulate that facies at the same location and thus the probability map will show either very high or very low value at that spatial location. On the contrary, if a facies is less constrained, its probability map will show larger zones of occurrence through the simulations

with more moderate values. The zones of extreme values are generally located around hard conditioning data locations, which induce zones of low variability near them.

In this case, we are focusing on the uncertainty regarding the shape of the alluvial systems and the uncertainties associated with their spatial location, with the probability maps shown in figure 3.14 corresponding to the facies probability of occurrence of the alluvial channels and of the sandbars. Figure 3.14a shows that the facies variability is not affected by the depth of the simulated layer, and that the channels and sandbars represent continuous structures that are located around the conditioning data locations. These top view maps also highlight the fact that the models are not overly constrained by neither the TDS nor the hard data. The probability of having a channel deposit is fixed at the conditioning data location and then progressively diffuses from these locations, which demonstrates that the model is not over-constrained by the conditioning data. Moreover, even when a river bed location is constrained with a hard data, the associated spacing with other river bed is not fixed and can fluctuate through the simulations set, which indicates that the TDS does not lock the locations of the pattern through the ensemble of simulations. The offshore seismic lines appear to have a strong influence in the sandbar locations. These conditioning data also appear to cut through some continuous systems at some

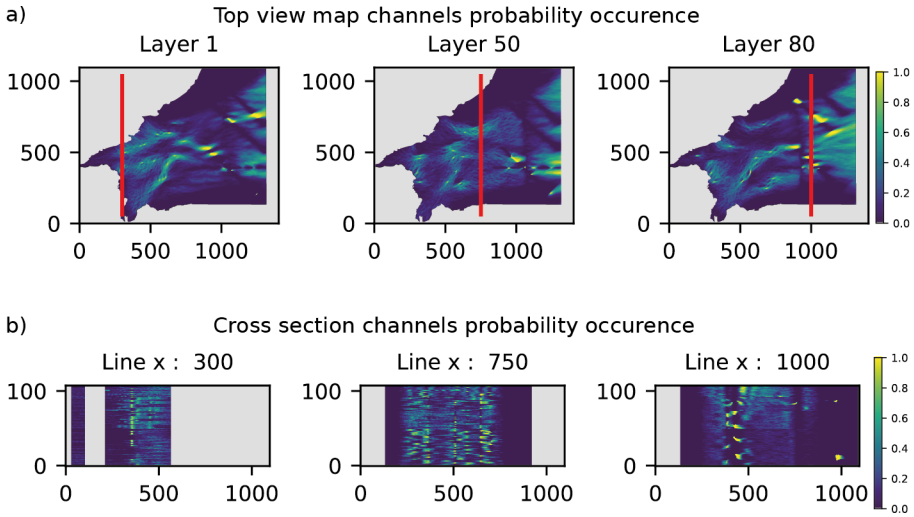

Figure 3.14: a) 2D top view of the MPS probability maps for the location of alluvial channels and sandbars (representing the potential main aquifer reservoirs) and b) 2D cross-sections. These probability maps show that through the ensemble of simulations the alluvial systems are simulated around the conditioning data and correctly explore the different probable systems that match the hard data sets and the conceptual models.

offshore locations. This issue is mainly due to the conditioning cross-sections that are uniquely interpreted, and cross large areas of the model grid.

Looking at the cross-sections of the probability maps of alluvial channels and sandbars occurrence (Fig. 3.14b) we can see that the sampling process succeeds in creating continuity in the alluvial system and in the channels locations during the simulation. Realistic channels are shown in the probability cross-sections. We can see that in the offshore domain the use of full cross-sections as conditioning data tends to over constrain the simulation but produces plausible channel-like structures.

Finally, this analysis of the probability maps shows that the models respect the depositional concepts expressed by the TDS and the trend maps for the different sub-intervals. There is a shift between the simulation concepts, the top facies location and the facies stacking arrangement between the four sub-intervals, that is clearly visible both in the top views and in the cross-sections maps, validating the developed workflow approach.

Entropy Map

The probability maps are used to calculate the information entropy. The Shannon Entropy was introduced in the theory of information developed by Shannon in the middle of the 20th century [Shannon, 1948] and represents the amount of information carried within a probabilistic distribution. As proposed for example by Wellmann and Regenauer-lieb [2012], information entropy is an effective tool to visualize uncertainties in a spatial context. The main advantage of the entropy is that it summaries the overall uncertainty contained in a probability distribution with a single number. The entropy is defined as:

$$H = -\sum_{i=1}^{n} p_i \log_n(p_i) \tag{3.1}$$

where log_n represents the logarithm in base n (or the number of facies in our case, six), and p_i the probability of occurrence of the i-th category. The entropy is maximal and equal to one when all the outcomes have identical probabilities, and is equal to zero when there is a perfect certainty of the outcome.

The entropy map (Fig. 3.15) shows that there is little geological uncertainty in the upstream part of the plain, on the border of the domain, where the alluvial fan dominates. The entropy maps, whether in plan view or cross-sections, allow one to effectively see all the conditioning data locations where the calculated entropy is zero. The alluvial channel facies are mostly constrained around the conditioning data. Moreover, the entropy values rapidly increase with the distance to the conditioning data. These maps show that the entropy is high

where the conditioning data are absent and that the simulations explore different alluvial configurations, which is a good thing since the stochastic approach is used to sample all the geological uncertainty of the model.

Finally, the entropy top view maps (Fig. 3.15a) show the effect of the randomized process used for the first auxiliary variable of the training data set. In each 2D simulation, the transitions between the continental system and the marshy environment is controlled by the first auxiliary variable, which was calibrated for each sub-interval, but randomly modified at each iteration. The auxiliary data were slightly modified to take into account the uncertainty on the exact transition location, which creates the vertical lines of high entropy visible in the entropy maps.

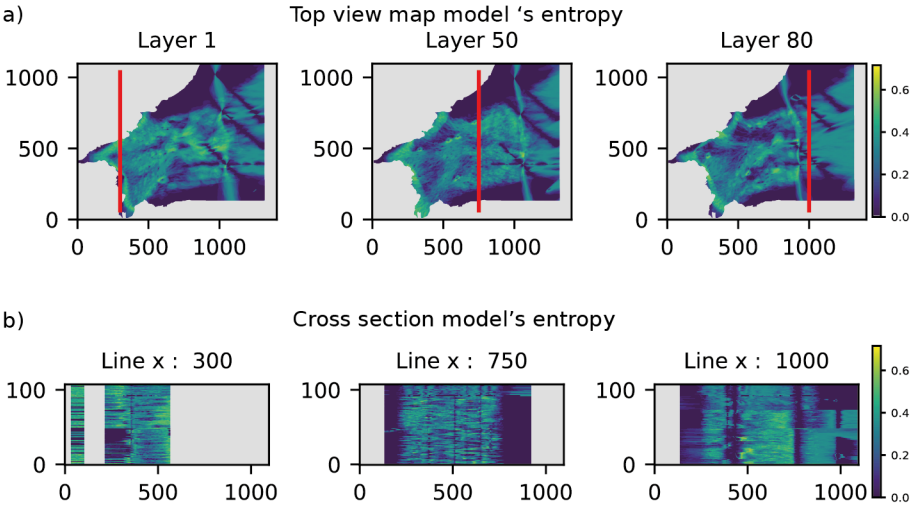

Figure 3.15: a) 2D top view of the entropy maps at different depths, and b) 2D entropy cross-sections. The lines and points where the entropy is zero correspond to the presence of conditioning data. The higher the entropy value is, the more uncertain is the prediction of the facies at that location.

3.5 Discussion and Conclusion

This study proposes a new workflow for the simulation of complex heterogeneous aquifers. Unlike more classical MPS studies, which rely on large primary or secondary hard data sets such as geophysics [Strebelle et al., 2002; Barfod et al., 2018; Høyer et al., 2017], this work relies on conceptual knowledge and auxiliary information.

A main novelty within this workflow is the creation of 2D non-stationary simulations accounting for trends computed by solving a diffusion equation, the use of two continuous maps of rotation angles to account for the uncertainty on

the paleo-orientations, and the transfer of conditioning data from one layer to the next one, in order to constrain the vertical transitions between the facies.

Solving numerically the diffusion equation allows accounting easily for the complex geometry of the extension of the sedimentary basin when computing the trend map. Using that technique, it is straightforward to impose prescribed values of the trend on certain parts of the boundary and to ensure that the gradient of the trend will remain perpendicular to the borders of the domain.

The proposed approach is simpler and faster than one based on 3D TDS. It has the advantage of being more flexible during the development of the model, where all the elements can be easily adapted to the specific case and tested. In particular, the possibility of using auxiliary information allows the modeler to approach each problem with a different angle making MPS, and especially DeeSse, a very flexible method.

The study of the Roussillon plain shows the importance of testing different TDSs to obtain acceptable structures. The TDS must be created to reflect the general geological knowledge available for the study site, and it must respect the interpreted data. One of the strengths of the MPS method is that it allows to test rapidly different concepts that can be discussed and adapted. Moreover, the use of complex auxiliary variable(s) and continuous rotation maps allow the final model to account for that information while honoring the borehole data.

The robustness of the proposed methodology has been tested with two sets of 50 simulations, one set with the vertical sampling approach and the other one without it. Despite its relatively simplicity, the vertical sampling improves the vertical object size reproduction. The simulation without vertical sampling misses creating the large vertically connected objects, whereas the simulations with vertical sampling have a distribution more comparable to the hard data set distribution (Fig. 3.9b). These improvements, regarding the vertical objects size reproduction, are important, since the meandering river deposits and the braided river deposits are known to have high aquifer potentials. It is important to note that the proposed statistical benefits of the sampling approach are based on a simplified training data set, limiting the real appreciation of the benefit of the methods on the final TDS and models.

The impact of the sampling method could also be characterized with other statistical descriptions, such as the calculation of the statistical connected body size of the meandering facies, which could be used to compare the sampling set against simulation that does not use the sampling approach. Yet, the role of these statistical descriptions are limited due to the lack of true/representative sets to be compared against. Recreating the vertical connectivity and the 3D shapes of these complex objects is a key parameter for the future use of the geological model for the hydro-characterization of aquifers and is a global challenge in MPS simulations where 3D training data sets are not available

[Comunian et al., 2012].

The probability and the entropy maps, as well as the facies proportion reproduction (Fig. 3.14, 3.15, and 3.13), show that the important sedimentary concepts have been well integrated into the model. The facies proportion of the different objects are satisfactorily reproduced and are constrained by both the boreholes' facies distribution and the TDS distribution. The probability and the entropy maps also show a lack of hard data. Indeed, the hard data set used may not be fully representative of the facies distribution of the Pliocene, and the simulation can suffer from this bias. Regarding the vertical sampling approach, even if it improves the realism of the simulated objects, the simulated shapes would benefit from additional constraints. The vertical transition matrix inferred from the boreholes can also present a bias due to their location or their non-representativeness of the real transition matrix.

Therefore, the model of the Roussillon plain would clearly benefit from additional boreholes with gamma ray and larger onshore geophysical data. A denser data set would permit to conduct a meaningful 3D cross validation exercise, as suggested by Juda et al. [2020]. At present, the data are not sufficient to really test carefully the predictive power of the MPS model. The model of the Roussillon plain would also benefit from additional information regarding the geometry of the sedimentological objects (their width, their lateral distribution...). Analogue data or geophysical inputs could help to better understand these geometries and could help in characterizing the transition zone between braided and meandering river deposits.

Finally, despite these possible improvements, this work demonstrates the applicability of DeeSse and of the proposed workflow to simulate complex internal aquifer heterogeneity at a regional scale.

Chapter 4

Aquifer properties

Abstract

Hydraulic conductivity and storativity are two of the most important parameters that describe the properties of an aquifer. These two parameters define the ability of a fluid to move through the material and the ease with which an aquifer can store and release water for a given pressure drop. Setting these parameters is a critical step in hydrodynamical simulations to reproduce the piezometric signals from observations and to correctly estimate the different flux in a hydrodynamical model. These hydrodynamical parameters are often derived from literature reviews, measured in laboratory experiments, or calculated after interpretation of hydraulic tests.

This chapter discusses the different approaches used to create hydraulic conductivity and storativity/specific storage fields for the hydrodynamical simulations in the Roussillon Basin. Different sets of approaches are presented and used to compare the influence of different hydraulic conductivity fields on the hydrodynamical simulation results.

The first concept is based on the interpretation of hydraulic pumping tests conducted in the Roussillon basin. This approach, which we called the depth-related approach, utilizes calculated values of hydraulic conductivity and storativity, which are assigned to specific depth ranges, to generate the hydraulic fields. The second concept is a stochastic approach that uses Sequential Indicator Simulations (SIS) to create an ensemble of 50 simulations based on variogram analysis of geological conditioning data. This is a classic approach that is easy to set up but often fails to reproduce complex realistic patterns. The final approach is the one based on MPS simulations (Chap. 3). It consists of an ensemble of 50 models generated by the DeeSse algorithm. This approach is the more complex and requires a lot of data and conceptual knowledge in order to be correctly set up and to produce satisfactory results.

The SIS and MPS approaches do not directly simulate the physical property of interest, but simulate categorical sedimentological facies. Sequential Gaussian Simulation (SGS) are therefore used to assign cell-wise physical properties to the simulated categorical facies of these two stochastic approaches.

This chapter also introduces the upscaling process used to transfer the physical properties of the stochastic simulations to the lower-resolution grid used in the hydrodynamical simulations. This upscaling process is necessary since the original number of cells composing the MPS and SIS grid is too large to be used directly into hydrodynamical software (more than 90 Million of active cells).

The upscaled hydraulic conductivity and storage fields of the three conceptual approaches are presented at the end of this chapter.

4.1 Introduction

Hydrodynamical modeling plays a critical role in understanding the behavior of groundwater systems. Two essential parameters of such models are the hydraulic conductivity and storativity, which have a large impact on the modeling results and can greatly influence the accuracy of a model. This chapter serves as a transition between the geological model and the hydrodynamical model and proposes to present the hydraulic conductivity and storativity fields of the three selected geological approaches used to represent the internal sedimentary organization of the Roussillon aquifer.

The aim of the chapter 2 was to introduce the geological aspect of the Roussillon basin, to present the different geological data sets available for modeling both the main surfaces composing the geological model and the sedimentological Continental Pliocene layer. These data and the interpolated surfaces were then used in the chapter 3 as elementary information for the construction of the geostatistical model of the Continental Pliocene sub-intervals using the multi-point statistical approach. An ensemble of 50 3D models composed of six sedimentological facies were generated using the MPS simulation approach. These fields constitute the MPS stochastic set and represent a complex conceptual representation of the Roussillon sedimentological model.

In addition to the MPS set, this chapter presents two other sets of hydraulic conductivity and storativity fields. These two sets are generated using more classical hydrogeological and geostatistical approaches. The first approach consists of one deterministic model and proposes to create a depth-related model of the Continental Pliocene hydraulic conductivity field. This field is based on the study of hydraulic pumping tests conducted in the Continental Pliocene layer [Dewandel et al., 2022]. The second approach is stochastic and uses Sequential Indicator Simulations (SIS) to create an ensemble of simulations based on variogram analysis of the geological conditioning data [Deutsch and Journel, 1998]. The SIS approach considers only three sedimentological facies, namely

alluvial, sandy and clay deposits, and is therefore less complex than the MPS approach. These three approaches and their corresponding fields will be used in the following chapters of this thesis as hydraulic conductivity and storativity fields for the hydrodynamical simulation. The final goal is to compare the advantages of using complex or simple sedimentary fields for hydrodynamical simulations.

The MPS and SIS sets do not directly simulate the physical properties of the aquifer, but rather categorical sedimentary facies that represent a particular type of environment or material. Therefore, it is necessary to assign physical properties to the categorical facies. Different approaches can be used to assign the physical properties to the sedimentological facies. The simplest is to assign a homogeneous value to each of the simulated categories. A more complex approach could use local geophysical properties derived from geophysical logging and locally interpreted hydraulic tests to correlate the permeability information with the depth and spatial location of the simulated facies [Neven et al., 2022a,b]. Here we decided to use Sequential Gaussian Simulation (SGS) to assign cell-wise physical properties, based on literature values, to the simulated facies [Deutsch and Journel, 1998]. This approach allows the generation of internal heterogeneity within the different facies, centered around a defined mean value. Since there is no conditioning data available to assign the physical properties, the variogram models and the mean values used for the SGS simulation of the permeability fields are manually determined. The mean values of the facies permeability field, simulated with the SGS approach, will then be calibrated using steady-state simulation, as presented in the following chapters of this work.

Since the grid used for the hydrodynamical simulation has a coarser resolution than the grid used for the geostatistical facies simulation, the associated hydraulic conductivity fields (either MPS or SIS simulation sets) must be upscaled. This process of upscaling is required because the initial number of cells in the MPS and SIS grid is too large to be directly used in hydrodynamic software, with over 90 million active cells. On the one hand, geostatistical simulations are often performed with a rather fine simulation grid in order to take advantage of local conditioning data or to simulate complex, fine-scale realistic patterns. On the other hand, hydrodynamical simulations rely on a complex system of equations, are composed of numerous boundary conditions, are often run in a transient state, and use therefore a coarser grid to limit the computational resources needed to solve the flow equations. This difference in grid resolution is present for the Roussilon case, where the geostatistical simulation grid of the Continental Pliocene is composed of 50 m cells resolution and 110 layers, and its corresponding hydrodynamical grid is composed of 200 m cells resolution and a total of 18 layers.

A homogeneous upscaled bloc is considered to be equivalent to a heterogeneous one if the homogeneous medium carries the same flow as the real heterogeneous medium when identical boundary conditions are prescribed on the two media. The upscaling process of additive physical properties such as porosity is easy to implement since it only requires calculating the arithmetic mean of the property. However, the upscaling process of non-additive properties such as hydraulic conductivity is less straightforward. Much research has been done to develop mathematical approximations of the upscaled hydraulic conductivity [Renard and de Marsily, 1997; Wen and Gómez-Hernández, 1996; Renard and Ababou, 2022]. Analytical formulations have been proposed as well as numerical approaches.

Approaches such as the Wiener bounds, Cardwell and Parsons bounds, or the Kruel-Romeu approach, are all based on different arrangement of the harmonic and arithmetic mean of the upscaled cells and are often used as first approximation for the calculation of upscaled hydraulic conductivity [Renard and de Marsily, 1997]. Numerical approaches calculate the equivalent hydraulic conductivity field by solving the flow equation on the heterogeneous medium under different types of boundary conditions and apply an equivalence criterion (equality of the flux, or equality of the total dissipated energy for example) so that the upscaled permeability matches the criterion defined for the heterogeneous medium [Renard and Ababou, 2022]. Recently, new geostatistical approaches have also been developed to simulate the upscaled properties directly on unstructured grids having a wide range of grid cell sizes [Mourlanette et al., 2020].

Here, the simulation grid and the upscaled grid are both regular Cartesian grids, which facilitates the upscaling approach. We then decided to apply the method proposed by Kruel Romeu [1994] to upscale the simulated hydraulic conductivity fields of the MPS and SIS sets. This approach is simple enough to be applied quickly, which facilitates its use during an inverse calibration process when the hydraulic conductivity fields have to be upscaled a numerous number of time. A comparison of this method with other fast techniques has shown that it provides reasonably accurate results [Renard et al., 2000].

The last aspect covered in this chapter concerns the different storativity fields associated with each of the three approaches (depth-related, SIS, and MPS approaches). The storativity parameter controls the ability of a material to store and release a liquid under a defined variation of pressure.

Regarding the depth-related model, the storativity field is based on storativity values and maps that have been compiled and created from the interpretation of hydraulic pumping tests conducted on the Roussillon plain [Dewandel et al., 2022]. The 2D storativity maps interpolated from the hydraulic pumping test interpretation are used to create the 3D storage fields based on the thickness of each layer that make up the depth-related model.

For the other two stochastic approaches, the storativity fields are directly linked to the categorical facies simulations. Based on the stochastic simulations, the facies are upscaled directly to the hydrodynamical grid using their indicator variables. Based on the percentage of different facies that make up the upscaled cells, rules were created to assign new categorical upscaled facies. These new upscaled facies take into account the potential mixing of sedimentary facies. Each of these upscaled facies is then assigned a storativity value based on literature values [Barthélemy and Seguin, 2016; de Marsily, 2004]. These storativity fields will be calibrated in a second part using transient hydrodynamical simulations.

Finally, the hydraulic conductivity and storativity values of the Quaternary, Intermediate and Marine Pliocene layers are fixed from literature and precalibration and are assumed to be homogeneous.

This chapter begins by summarizing important information about the hydraulic conductivity and storage parameters. The same section also introduces the Sequential Indicator Simulation (SIS) approach used to simulate a simpler three facies stochastic model, the Sequential Gaussian Simulation (SGS) used to populate the facies field with hydraulic conductivity values, and describes the upscaling approach. The results section presents the hydraulic conductivity and storativity fields of the depth-based approach, the SIS approach, and the MPS approach.

4.2 Methods

After presenting an overview of hydraulic conductivity and storativity physical properties, this section will review the SGS and SIS geostatistical methods. The SIS approach is used to create simpler, three facies, sedimentological stochastic models of the plain, while the SGS are used to simulate hydraulic conductivity within each facies of the MPS and SIS simulations. As mentioned above, geostatistical simulations and hydrodynamical simulations are often performed in grids of different resolutions, requiring upscaling of properties from one grid to another. This section also presents the selected upscaling method used for the transfer of the physical properties to the hydrodynamical grid.

Physical parameters

Hydraulic conductivity

Hydraulic conductivity is an important parameter in many fields, including hydrology, geology, and civil engineering. It is used to predict the movement of groundwater through soil and rock formations, to design drainage systems, and to assess the potential for contamination of groundwater resources.

In hydrology, hydraulic conductivity is a parameter that defines how easily a given fluid can flow through a given soil or rock formation. The hydraulic conductivity depends on the medium in which the fluid evolves, as well as the properties of the fluid (saturation, viscosity, temperature, and density). It is defined as the volume of fluid that can pass through a unit area of the medium in a unit time under a unit hydraulic gradient, and is directly related to the permeability of the material. Permeability is an intrinsic property of a porous material (depending only on properties such as pore size, tortuosity, and surface area) and represents the ability of the material to allow fluids to flow through it. In an isotropic saturated granular material, the permeability can be estimated with the Kozeny-Carman law [Carman, 1937] as

$$k = \phi \frac{m^2}{F\tau^2}, \tag{4.1}$$

where k is the permeability, ϕ is the porosity of the material, m is the hydraulic radius, τ is the tortuosity, and F is a shape factor depending on the material structural arrangement. The permeability is usually expressed in m^2.

The hydraulic conductivity is linked to the permeability by the relation:

$$K = k \frac{\rho g}{\mu}, \tag{4.2}$$

where K is the hydraulic conductivity, k corresponds to the permeability, ρ is the density of the fluid, g the gravitational constant, μ the fluid viscosity. The hydraulic conductivity is generally expressed in m/s.

Hydraulic conductivity can be measured or determined in several ways, depending on the size and complexity of the system being studied. Common methods include laboratory measurements using a permeameter, which allows water to flow through a small sample of the porous medium under controlled conditions. This method can provide accurate measurements of hydraulic conductivity for a given sample, but may not represent the variability of the material in the field. Hydraulic parameters can also be calculated from field measurements using various hydraulic tests. These methods involve measuring the response of the system to changes in water pressure or flow, and can provide information about the average hydraulic conductivity of the material over a larger area. Finally, literature values can be selected from analog sites or for analog materials. Overall, the choice of the method for measuring or determining hydraulic conductivity depends on the objectives of the study, the resources available, and the characteristics of the system being studied.

Hydraulic conductivity is not an additive property, meaning that the hydraulic conductivity of a mixture of two materials with different hydraulic conductivity values is not equal to the average of the two values. This is mainly because the flow of fluid through the mixture depends on the way the different materials are arranged and how the pores in each material are interconnected.

Storativity and specific storage

Storativity is another key parameter in any transient modeling effort. Storativity represents the ability of the formation to store and release water.

The specific storage or specific storativity is defined as the volume of water released from a unit volume of saturated aquifer for a unit decrease in pressure head:

$$S_s = \frac{1}{\rho} \frac{\partial(\rho\phi)}{\partial h} \tag{4.3}$$

where S_s is the specific storage, ρ the fluid density, ϕ the porosity, and h the pressure head.

The specific storage is expressed in m^{-1}. This parameter depends on several factors such as the porosity, compressibility, and internal geometry of the material. Since the water and the matrix of the media are both compressible, the change in head induces the water to be stored or released. Under the assumption that the total stress remains constant and that the porous medium deforms only in the vertical direction, the specific storage is related to the porosity and the compressibility of the liquid and medium by:

$$S_s = \rho(\alpha + \omega\beta) \tag{4.4}$$

where ω is the porosity of the rock, and α and β are respectively the volumetric medium and liquid compressibility.

In a confined aquifer, the storativity is the integral of the specific storage over the saturated thickness of the aquifer:

$$S = \int_0^e S_s \mathrm{d}e, \tag{4.5}$$

with e the saturated thickness of the aquifer. The storativity is a dimensionless parameter, and it can be estimated from pumping test data or by inversion of a transient hydraulic head data using a numerical model.

In an unconfined aquifer, the specific yield of the formation plays the same role as the storativity. It is defined as the ratio of the volume of a liquid drained by gravity over its total void volume:

$$S_y = \frac{V_{gravity}}{V_{total}}. \tag{4.6}$$

The upscaling of storativity fields is less complicated than the upscaling of the hydraulic conductivity, since this parameter is based on the porosity value of the material, which can be added arithmetically [de Marsily et al., 2005].

Depth-related assignation

The first model is created using estimated hydraulic conductivity from pumping tests and elevation maps of the UPC and Continental Pliocene envelope to generate the hydraulic conductivity field. This approach is based on the interpretation of pumping tests in the Roussillon plain [Dewandel et al., 2022].

First, depth-related hydraulic conductivity statistics are calculated from the interpreted transmissivity of the hydraulic tests. These statistics are based on the transmissivity values and the depth location of the screen portion of each interpreted well. Hydraulic conductivity is calculated for 50 m depth intervals.

The model is then divided into four layers bounded by the UPC surfaces and the top and bottom of the Continental Pliocene layer, as described in chapter 2. The hydraulic conductivity values of each cell in these layers are assigned based on the depth of the cells and the corresponding hydraulic conductivity values on the layer.

Sequential Indicator Simulation for facies simulation

Stochastic simulation is the process of generating a set of equally probable models of a given spatial distribution for a variable of interest. The simulation is either conditional, where the simulation considers data values at their grid location, or unconditional, where no data set is used as a starting point for the realization. Depending on the simulation approach chosen, the simulated variable may be continuous (e.g. a permeability field) or categorical (e.g. a defined material type) [Journel and Alabert, 1989; Gómez-Hernández and Srivastava, 1990; Deutsch and Journel, 1998]. The previous chapter introduced the Multiple-Point Statistics (MPS) simulation approach, a more recent geostatistical method that relies on the use of a training data set and can be quite complex to implement. Apart from the MPS approach, this work proposes to use Sequential Indicator Simulation (SIS), another geostatistical approach, to simulate the spatial location of sedimentological facies for the Roussillon plain.

Sequential Indicator Simulation (SIS) is a stochastic simulation technique used to model categorical variables, such as the presence or absence of a geological feature at a given location [Journel and Alabert, 1989]. The SIS method is widely used in various fields including geology, hydrogeology and environmental engineering to simulate categorical variables such as lithology, soil type or the presence/absence of a contaminant at a given location. This method is particularly useful in situations where insight can be gained into the uncertainty associated with the estimation of categorical variables. This method is a variogram-based approach; it relies on indicator kriging, and is therefore a two-point statistical approach [Deutsch and Journel, 1998]. It can also be combined with rotation information and proportion maps to control the spatial pattern locations during the simulation.

The basic principle behind SIS is to simulate each cell of the simulation domain sequentially, conditionally to its surrounding cells. The first step is to define the classes to be simulated (e.g. sand, clay, etc.) and treat them as binary indicator variables. This means that each class is simulated independently, with the simulated value for each variable corresponding to the probability of the cell belonging to that class. The second step is to define a variogram model for all the different classes. These variograms represent the expected spatial correlation that will be simulated for the different classes. The next step is to assign the existing information (conditioning data) to the grid. If a facies is present at a location, a value of one is encoded in the corresponding indicator simulation grid and a value of zero is placed in the other indicator simulation grids. This means that there is a probability of one that this facies belongs to the first class, and zero in the other classes. The fourth step is the simulation itself, and begins by randomly selecting an unassigned cell to simulate. At this point, the conditional probabilities for each class are estimated using indicator kriging and the surrounding informed cells. These informed cells are composed of the original conditioning data and the previously simulated points. A class is randomly drawn according to these probabilities and assign to the simulated cell. Then, the algorithm randomly selects a new uninformed cell and repeats the previous steps until the entire grid is simulated. This process can then be repeated several times to generate a set of realizations that can be used for uncertainty quantification.

We use the SIS approach to generate a three facies categorical set of 50 3D models of the Roussillon continental Pliocene layer. The three facies represent the sandy alluvial deposits, the clayey floodplain deposits, and the alluvial fan deposits. The conditioning data set used for this approach is larger than the one used for the MPS approach, since it regroups the 101 geophysical logs, interpreted according to their sedimentological description, the four interpreted offshore seismic lines presented in chapter 2, and also a classical borehole log database, which consists of more than 500 logs interpreted in terms of sand, clay and alluvial deposits and located all over the plain.

The SIS approach directly simulates the 3D facies fields and re-uses the rotation maps as local azimuth information, as well as the auxiliary trend maps used in the MPS approach (chapter 3) to constrain the facies position during the simulation. The auxiliary trend maps are here converted to facies probability maps. The first auxiliary map, evolving from west to east, is used to control the alluvial fan location during simulation. In the west part of the domain, where the trend values are ranging from 0 to 0.1, we fixed the probability of simulating alluvial fan to 1 and the two other facies to 0. In the rest of the domain the probability of simulating the two other facies is set to 0.5, except in the offshore border side of the domain, characterize by the second auxiliary variable of the MPS approach, where the probability of having sand channel is fixed to 0.

The variogram models of each facies are determined for each sub-interval based on a random sub-set of the conditioning data to alleviate the computational coast of computing the experimental variogram models. The variogram models are automatically optimized to match the experimental variogram of the selected data, directly in the code. The geone package [5] is used for both the variogram analysis and the SIS simulations.

Sequential Gaussian Simulation for hydraulic conductivity fields assignation

Sequential Gaussian Simulation (SGS) is a geostatistical technique used to model spatial variability in natural systems, particularly in earth sciences such as hydrogeology, geology and environmental science [Journel, 1983; Neven et al., 2021; Schorpp et al., 2022]. Deutsch and Journel [1998] developed SGS to produce individual realizations of the dispersion of grades in a three-dimensional ore body. This stochastic approach is used to generate multiple realizations of a variable of interest based on a set of data and a variogram model.

The idea behind stochastic Gaussian simulation is to use a kriging estimator (generally simple kriging) to determine, in each cell, the parameters (mean and variance) of the Gaussian density from which a value is drawn for the variable to be simulated. This method is based on the two-point statistical variogram approach, where the variogram describes the spatial correlation of the variable of interest across the study area. The resulting set of realizations can be used to estimate the uncertainty and variability of the variable of interest and to make predictions or simulations of the system under study.

This requires the definition of a variogram model that can be inferred from the data or estimated by the modeler if there is an insufficient amount of data points. During the simulation, conditioning data are selected within a defined neighborhood close to the current simulated cell, which includes the original

[5] https://github.com/randlab/geone

data and all previously simulated cells. Once the mean and variance have been calculated, a value is drawn from the corresponding Gaussian distribution and assigned to the simulated cell. This process is repeated sequentially for all the different cells of interest, following a random path. It is important to note that since this method draws values from a normal distribution, the simulated variable of interest will also be normally distributed. If the actual variable follows a different distribution, it is necessary to transform the data so that it follows a normal distribution. If this is the case, the resulting Gaussian simulations must then be transformed back to follow the original data distribution.

In this work, the SGS approach is used to simulate the log_{10} of the hydraulic conductivity fields within each of the simulated facies of the SIS and MPS approaches. The variogram models are based on expert judgement to match the general object size and to create a realistic parameter distribution within each facies. Simple kriging is used for the simulation, with the mean value of the simulated facies hydraulic conductivity fields taken from the literature. Once again, we used the geone package for the SGS simulations.

Upscaling process

The term upscaling refers to the process of averaging a property from a smaller scale to a larger scale. In hydrogeology, upscaling is the process of modeling the behavior of a large-scale aquifer system based on the properties and behavior of smaller-scale components. Typical geological or sedimentological models are composed of tens or hundreds of millions of cells, which is far too many to use directly as an input grid for a flow model [de Marsily et al., 2005]. The properties and behavior of a large-scale system can be estimated by aggregating information about its smaller-scale components, such as individual pores, fractures, or rock layers.

We can distinguish two classes of property behavior with respect to the upscaling problem, the additive and the non-additive properties. Additive properties are physical properties that can simply be summed when two or more materials are combined. This means that the total value of the property in a mixture is equal to the sum of the values of the property in each component of the mixture, weighted by the proportion of each component. In hydrogeology, porosity is an example of an additive property because one can add the volumes of pore space to get the total pore space in order to get the total porosity of the sample. Non-additive properties are those that do not follow the principle of additivity. In other words, the total value of a system with non-additive properties cannot be obtained by simply adding the values of its individual components. Hydraulic conductivity is a non-additive property. Non-additive properties are often complex and may require specialized methods or models to fully understand and describe them [Renard and Ababou, 2022; Mourlanette et al., 2020].

Regarding the upscaling process of the hydraulic conductivity fields derived from the stochastic MPS and SIS sets, which are assigned using SGS simulations, in this work we used the approach proposed by Kruel Romeu [1994]. This approach first computes different combinations of arithmetic and harmonic means of the cells to be upscaled. The second step is to compute a geometric weighted mean based on these upscaled first approximations (Fig. 4.1). The weights are calculated based on anisotropic coefficients, which are obtained from coefficients describing the space dilatation in the x, y and z directions between the original and the upscaled grid.

This approach employs the Cardwell and Parsons bounds, which are an improvement of the Wiener bounds and tighten these upscaled approximations (Fig. 4.1). These bounds are defined as follows for a 3D block and a flow in the x direction:

$$K1 = \mu_h^x(\mu_a^z(\mu_a^y)) \geq K_{equi} \geq \mu_a^z(\mu_a^y(\mu_h^x)) = K2, \tag{4.7}$$

where μ_h is the harmonic mean, μ_a the arithmetic mean, calculated in the x, y, and z block direction. K_{equi} is the true upscaled hydraulic block conductivity. Kruel-Romeu introduce intermediate values $K3$, and $K4$ to take into account the anisotropic effect between the original grid resolution and the upscaled grid resolution. These new coefficients are:

$$K3 = \mu_a^y(\mu_h^x(\mu_a^z)) \quad K4 = \mu_a^z(\mu_h^x(\mu_a^y)) \tag{4.8}$$

In the final combination of these bounds, power exponents are used to control the geometric anisotropies of the upscaled process:

$$K_{equi}^{xx} = K1^{\theta_{y2}\theta_{x3}+\theta_{z2}\theta_{y3}} K2^{1-\theta_{y3}-\theta_{x3}} K3^{(1-\theta_{y2})\theta_{x3}} K4^{(1-\theta_{x2})\theta_{y3}} \tag{4.9}$$

with the exponents being defined as:

$$\theta_{y2} = \frac{arctan(\sqrt{a_y})}{\pi/2} \quad \theta_{z2} = \frac{arctan(\sqrt{a_z})}{\pi/2} \tag{4.10}$$

$$\theta_{y3} = \frac{\theta_{y2}(1-\theta_{z2})}{1-\theta_{y2}\theta_{z2}} \quad \theta_{z3} = \frac{\theta_{z2}(1-\theta_{y2})}{1-\theta_{y2}\theta_{z2}} \tag{4.11}$$

with:

$$a_y = \frac{k^{yy}}{k^{zz}} \left(\frac{dx}{dy}\right)^2 \quad az = \frac{k^{zz}}{k^{xx}} \left(\frac{dx}{dz}\right)^2, \tag{4.12}$$

where a_y and a_z are the anisotropy factors that account for the local directional permeability anisotropy. In our case, the local permeability is assumed to be isotropic (the local k^{xx}, k^{yy}, and k^{yy} are identical in each cell).

The upscaling process used to generate the specific storage fields is different from the one used for the hydraulic conductivity field. Since the specific storage, and therefore the storativity, depends mainly on the porosity of the material, we can consider it as an additive property as a simple approximation. We decided to directly upscale the categorical simulated facies to the upscaled grid and then assign homogeneous specific storage values to each facies. To account for the potential mixing of facies during upscaling, new mixing facies are introduced based on the fraction of facies composing the upscaled cells. For example, if an upscaled cell is composed of more than 50% sand, the upscaled cell is coded as sand, but if the upscaled cell is composed of 25% to 50% sand, the upscaled cell is coded as sand mix. The priority of this facies assignment is toward the sandy deposit, meaning that the percentage of sand in the upscaled cell is tested before the percentage of clay in the upscaled cell. The classes have been selected in order to keep the number of the upscaled facies small, while

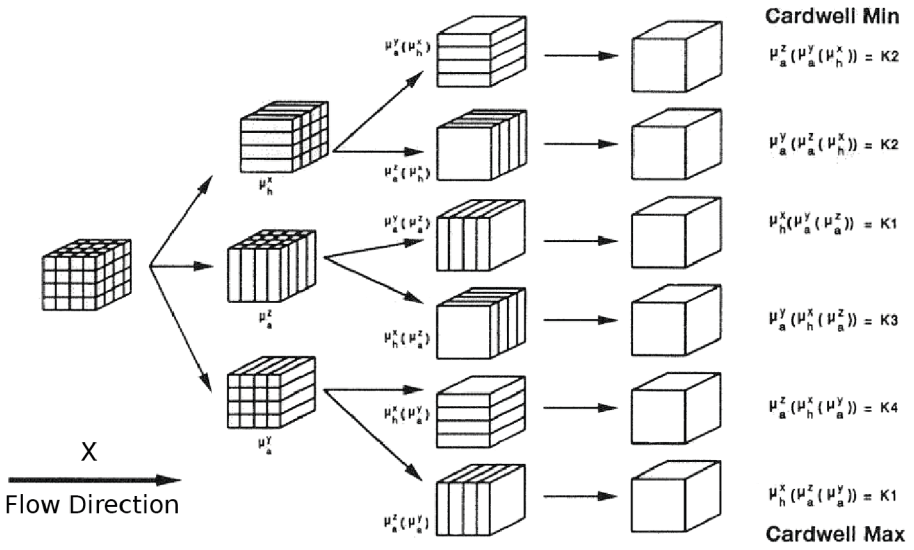

Figure 4.1: Cardwell and Parsons bounds, and intermediate $K3$ and $K4$ calculation approach. Modified from Renard and de Marsily [1997]

still taking into account the mixing process of the facies during the upscaling. This process is used to promote the sandy facies over the clay facies during upscaling and to preserve the potential geologic reservoir bodies. The same approach is used for the MPS simulation set.

Table 4.1 summarizes the rules used for upscaled facies assignment and the homogeneous specific storage values assigned to each upscaled facies. The specific storage values are derived from the literature [de Marsily, 2004; Barthélemy and Seguin, 2016; Kuang et al., 2020] and are used as a first approximation. A total of 10 upscaled facies are generated from the MPS approach and five upscaled facies are generated from the SIS simulation sets.

Table 4.1: This table shows the conditioning rules for the upscaled facies assignment with respect to the storativity fields. The percentage of sand is always check first for the upscaling assignation process. Homogeneous specific storage values are assigned to the upscaled facies.

Set	Upscaled facies	Composition	Storativity [-]
MPS	Floodplain	>50% floodplain	10^{-3}
	Marshy deposit	>50% marshy deposit	10^{-3}
	Crevasse splay	>50% crevasse fan	10^{-5}
	Sandbars low	>20% sandbars	$10^{-3.5}$
	Sandbars mix	>30% sandbars	10^{-4}
	Sandbars High	>40% sandbars	10^{-5}
	Channel low	>20% channel	$10^{-3.5}$
	Channel mix	>30% channel	10^{-4}
	Channel high	>40% channel	10^{-5}
	Alluvial fan	>50% alluvial fan	10^{-5}
SIS	Alluvial fan	>50% alluvial fan	10^{-5}
	Sand mix	>25% sand	$10^{-4.5}$
	Sand high	>50% sand	10^{-5}
	Clay mix	>25% clay	$10^{-3.5}$
	Clay high	>50% clay	10^{-3}

4.3 Results

This section presents the hydraulic conductivity and specific storage fields generated for the three selected hydrogeological approaches, as well as the physical parameters fields of the Quaternary and Marine Pliocene layers. The values of these fields are either simulated using the SGS simulation or homogeneously assigned for each facies. It is important to note that the hydraulic conductivity and storativity values are derived from the literature and represent a first approximation of the hydraulic parameters. These parameters will be calibrated in the following chapters of this thesis.

Quaternary and homogeneous layer

The Quaternary and Marine Pliocene layers are used in all the different approaches and are assumed to be homogeneous. In addition to these two layers, two intermediate layers are also present in all the different approaches. These two layers are considered as buffer zones between different parts of the simulated domain. The first buffer layer is placed on top of the pile, and cover the offshore extension of the quaternary layer. This buffer layer is defined as a 2 m thick unit. The second buffer layer is set between the Quaternary and the upper continental layer, and is defined as a 1 m thick unit.

Regarding the Quaternary layer, the hydraulic conductivity fields are derived from the synthesis of Caballero et al. [2022b], Dewandel et al. [2022], and Lanini et al. [2022]. We distinguish two homogeneous zones within this layer (Fig. 4.2a), corresponding to ancient and recent alluvial plains. The homogeneous hydraulic conductivity of these zones is set to $8 \cdot 10^{-4}$, and $2 \cdot 10^{-3}$ m/s, respectively. Based on the average storativity values of the formation in Dewandel et al. [2022], the storativity is first assumed to be homogeneous and is set to $6.8 \cdot 10^{-3}$. This value is simply divided by the thickness of the layer to generate the specific storage field of the Quaternary layer (Fig. 4.2b).

The Marine Pliocene aquifer is defined as homogeneous in this study. Since there is not much information available for this layer and that it is not so much exploited as a water resource, this layer is set to act as a potential reservoir from which interactions with the Continental Pliocene layer can occur. Since it consists mainly of a sand mixture with interbedded clayey deposits, the hydraulic conductivity of this layer is set to 10^{-4} m/s (Fig. 4.2c). The corresponding first integrated storativity of the layer is set to 10^{-4}. The specific storage field is generated by dividing the storativity by the cell thickness of the layer (Fig. 4.2d).

The buffer layers are established to buffer the potential interaction between the different aquifers. These layers should be permeable enough to conduct water, but should not represent a significant water stock. Their hydraulic conductivity and storativity values are both set to 10^{-3} m/s and 10^{-4} and are assumed to be homogeneous as a first approximation.

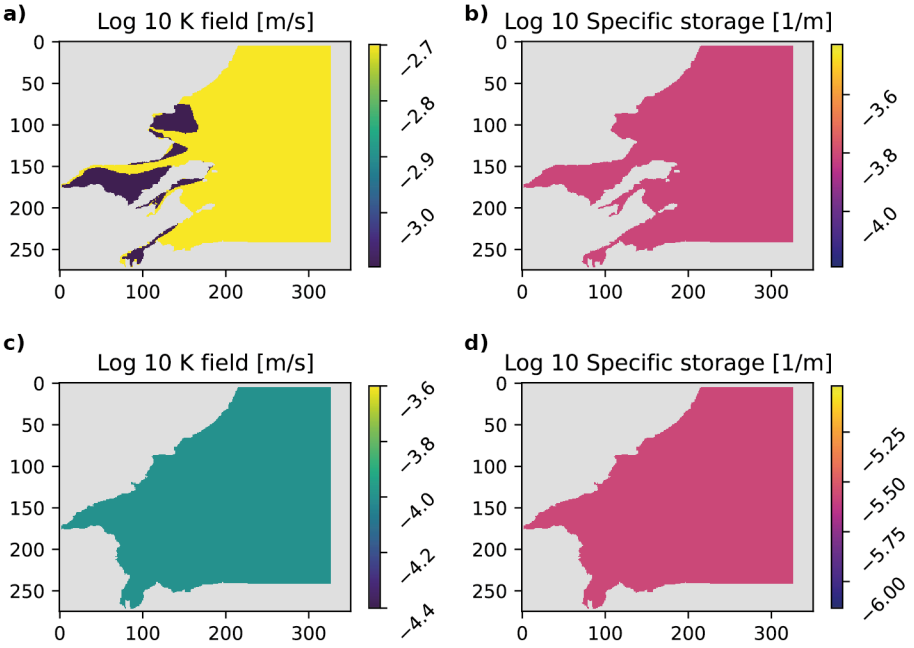

Figure 4.2: a) The hydraulic conductivity field of the Quaternary layer, composed of two homogeneous zones. b) The specific storage of the Quaternary layer. c) The homogeneous hydraulic conductivity field of the Marine Pliocene layer and d) its associated specific storage field.

Depth-related approach

We now present the hydraulic fields corresponding to the Continental Pliocene layer of the depth-related approach. The interpreted hydraulic conductivity values are compiled in table 4.2 and are assigned to the grid cells based on their altitude (Fig. 4.3).

Table 4.2: Hydraulic conductivity for 50 m intervals, used to create the hydraulic fields of the depth-related approach.

Depth interval [m]	K [m/s]
0-50	$1 \cdot 10^{-4}$
50-100	$4 \cdot 10^{-5}$
100-150	$3 \cdot 10^{-5}$
150-200	$2 \cdot 10^{-5}$
200-250	$1.5 \cdot 10^{-5}$
>240	$1 \cdot 10^{-5}$

In their work, Dewandel et al. [2022] also calculated the mean storativity value of the Continental Pliocene layer. The specific storage is distributed with respect to the cell thickness and the integrated mean storativity of the layer, fixed at $3 \cdot 10^{-4}$, by Dewandel et al. [2022] (Fig. 4.4).

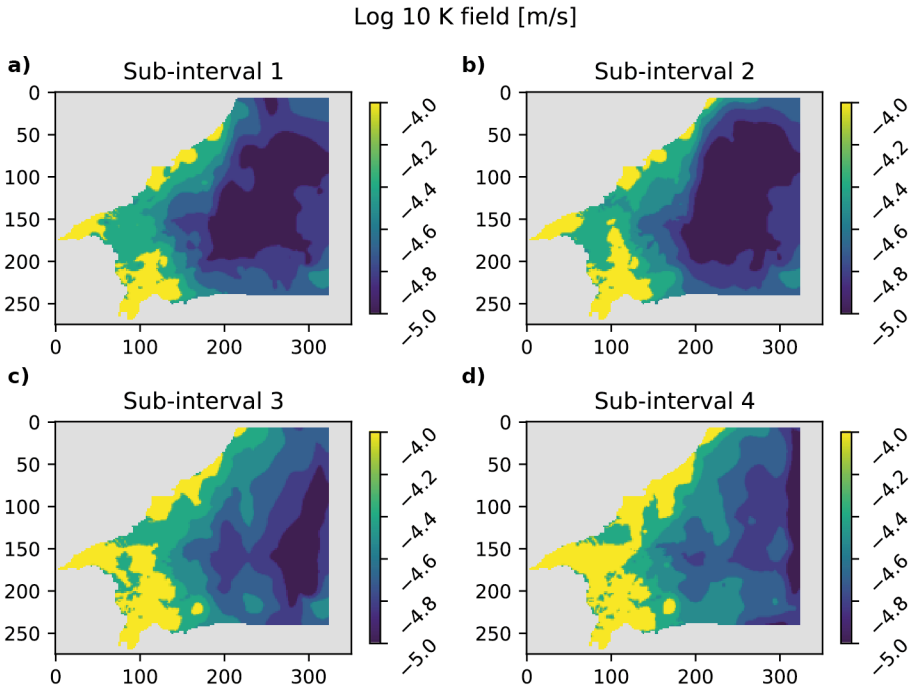

Figure 4.3: Log 10 of the hydraulic conductivity fields of the depth-related approaches. The Continental Pliocene layer is split in four sub-intervals (the sub-interval one is the bottom one and the sub-interval four is the top one).

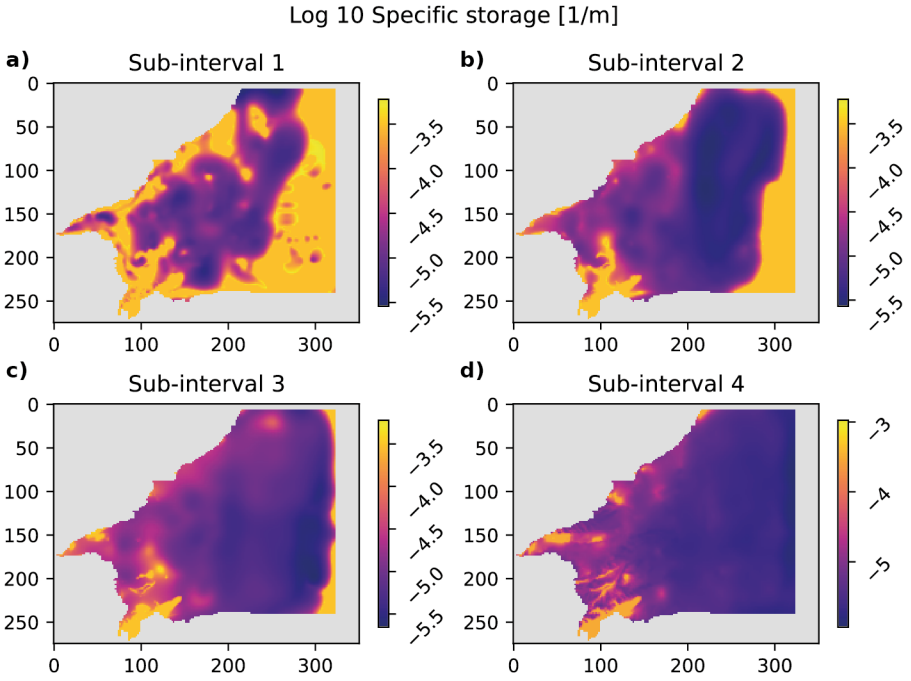

Figure 4.4: Log 10 of the specific storage fields of the four sub-intervals composing the Continental Pliocene layer of the depth-related approach. The specific storage values are based on the mean storativity of the Continental Pliocene layer (the sub-interval one is the bottom one and the sub-interval four is the top one).

SIS

In this second approach, we use sequential indicator simulation to simulate categorical facies. Three facies are simulated in this approach, corresponding to sand type deposits, clay type deposits, and alluvial fan deposits. As presented in chapter 2, the four sub-intervals of the Continental Pliocene layer are simulated independently. The calibrated variogram models used for the SIS facies simulations are presented in table 4.3.

Table 4.3: Variogram model derived for the SIS facies simulations. The variogram models are automatically adjusted based on a subset of data and their corresponding experimental variogram. The range are cell based unit. The range values are expressed in number of pixel/cell in the simulation grid.

Interval	Facies	Model	Sill	Range x	Range y	Range z
4	Clay	Spherical	0.23	12	15	2
	Sand	Spherical	0.237	16	12	2
	Alluvial fan	Spherical	0.237	16	12	2
3	Clay	Spherical	0.225	14	12	1.75
	Sand	Spherical	0.23	16	12	2
	Alluvial fan	Spherical	0.23	16	12	2
2	Clay	Spherical	0.237	16	12	2
	Sand	Spherical	0.237	16	12	2
	Alluvial fan	Spherical	0.237	16	12	2
1	Clay	Spherical	0.227	23	12	3
	Sand	Spherical	0.227	21	12	3
	Alluvial fan	Spherical	0.227	21	12	3

Figure 4.5 presents a SIS simulation, on top view map, for each one of the sub-intervals composing the Continental Pliocene. The resulting SIS simulations are not as realistic as the MPS simulations, but respect the spatial correlation of the data set. Furthermore, by using the rotation maps and the auxiliary variable created for each sub-interval of the Continental Pliocene, the SIS simulation accounts for the conceptual description of the plain and the general spatial distribution of sand deposits (Fig. 4.5). A total of 50 simulations are performed using the SIS approach.

Once simulated, the hydraulic conductivity values are simulated within each of the three facies and upscaled to the hydrodynamical simulation grid (Fig. 4.6). Hydraulic conductivity is first simulated using the SGS algorithm of the geone package, before being upscaled with the Kruel and Romeu approach. The variogram models are presented in table 4.4 along with the mean fixed hydraulic conductivities, simulated using the SGS approach. These parameters are selected to represent the different hydraulic behaviors of the simulated facies.

Figure 4.6 shows the upscaled simulated hydraulic conductivity fields of the SIS approach. The structures present in the SIS simulations (Fig. 4.5) are blurred during the upscaling process. The central part of the plain appears more homogeneous than in the original categorical simulations. The simulated facies patterns are less recognizable as they are aggregated in both the vertical and horizontal directions. The upscaled grid resolution is four times that of the original grid, which explains the general mixing of patterns, but the main aggregation influence is on the vertical axis, where the number of layers goes from 108 layers to 18 layers, meaning that six layers are aggregated together, which greatly influences the resulting upscaled fields (Fig. 4.6). Despite the upscaling process, it is still possible to distinguish the sub-intervals from one another. The density of the zones and their intensity (difference between low and high conductivity) are different between the sub-intervals, which validates the approach of simulating the sub-intervals separately.

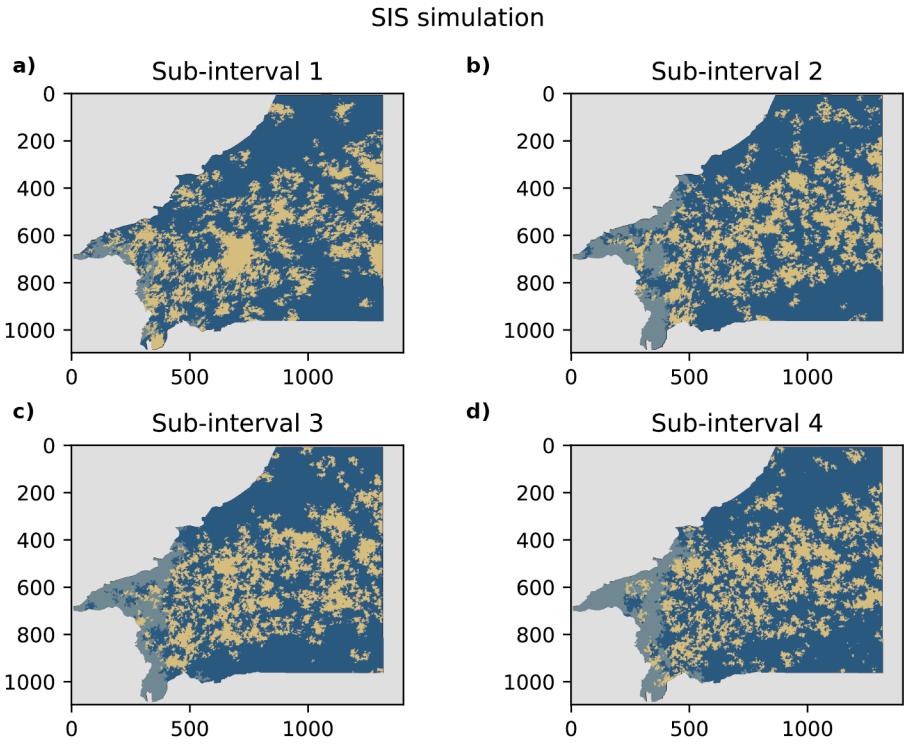

Figure 4.5: SIS simulations of the continental Pliocene layer. The gray sediments correspond to the alluvial fan, the brown sediments to the sandy sediments, and the blue sediments to the alluvial plain/clay sediments. Some aspects of the conceptual description of the sub-intervals described in chapter 2 are visible, such as the absence of the alluvial fan in the northern part of the model for the sub-interval one of the Continental Pliocene (d).

Table 4.4: Variogram models and mean hydraulic conductivity values used for the SGS of the SIS facies hydraulic conductivity parameter. The range values (R_x, R_y, and R_z) are expressed in number of pixels/cells in the simulation grid.

Facies	Model	Sill ($log_{10}(K)$)	R_x	R_y	R_z	K mean [m/s]
Alluvial fan	Spherical	0.227	21	12	3	10^{-4}
Sand	Spherical	0.227	21	12	3	10^{-3}
Clay	Spherical	0.227	23	12	3	10^{-6}

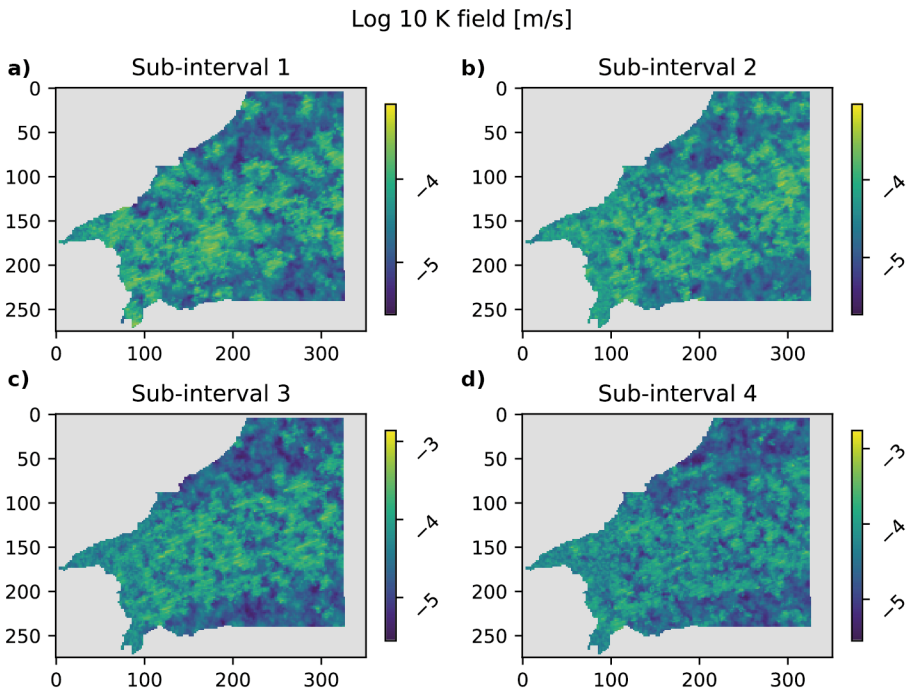

Figure 4.6: Upscaled hydraulic conductivity fields of the SIS approach for the Continental Pliocene layer. Four layers are here presented. The total upscaled grid of the Continental Pliocene layer is composed of 18 layers. The simulated patterns are mixed together during the upscaling.

The final component of this approach is shown in figure 4.7 and represents the upscaled specific storage fields derived directly from the SIS simulated facies. The three upscaled facies are directly upscaled into five facies fields that represent a potential mixture of facies properties. Within these upscaled facies, homogeneous specific storage values are directly assigned. This method better preserves the difference between sand and clay zones in the plain and results in a much more detailed field compared to the upscaled hydraulic conductivity fields.

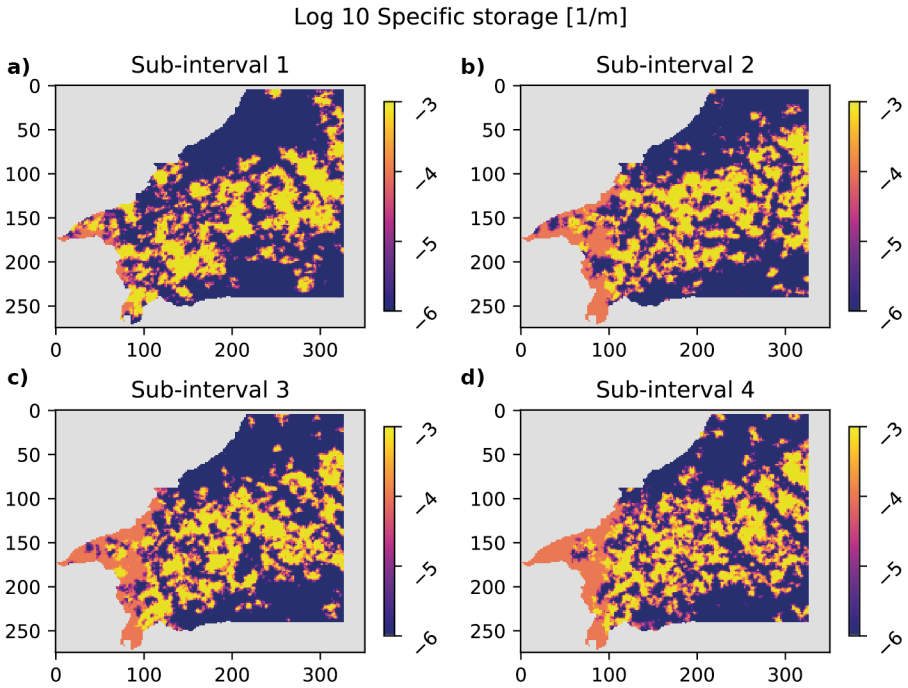

Figure 4.7: Upscaled specific storage fields of the SIS approach. The simulated facies are upscaled to a five facies model, where homogeneous specific storage values are directly assigned.

MPS

The last hydraulic parameters set is based on the MPS simulations presented in chapter 3. This set is the one that incorporates the more conceptual knowledge through the use of the training data set and the MPS stochastic approach. The same method is used here as for the SIS hydraulic conductivity assignment. The variogram models and the mean hydraulic conductivity values used for the SGS simulation are presented in table 4.5.

Table 4.5: Variogram model used for the SGS simulation of the hydraulic conductivity parameter of the different facies composing the MPS simulations set. The range values are expressed in number of pixel/cell in the simulation grid.

Facies	Model	Sill	Range x	R y	R z	K [m/s]
Alluvial fan	Spherical	0.227	21	12	3	10^{-4}
Channel	Spherical	0.227	21	12	3	10^{-3}
Crevasse splay	Spherical	0.227	23	12	3	10^{-3}
Floodplain	Spherical	0.227	23	12	3	10^{-6}
Sandbars	Spherical	0.227	23	12	3	10^{-3}
Marshy deposit	Spherical	0.228	23	12	3	10^{-5}

Once assigned, these hydraulic conductivity fields are upscaled to the hydraulic simulation grid using the same process as presented in the SIS section. Regarding the vertical view of the upscaled MPS field, we find the same aggregation pattern as presented in the SIS. The central part of the plane represents aggregated zones of channels. The different transition zones between the different environments are still visible between the different sub-intervals that make up the Continental Pliocene layer. The density of the aggregated zones also varies through the different sub-intervals, demonstrating that the conceptual description of the sub-intervals and their differences are carried out through the upscaled hydraulic conductivity fields (Fig. 4.8).

The specific storage fields of the MPS approach follows the same construction method as those generated for the SIS approach. The sedimentary MPS facies are directly upscaled, and homogeneous specific storage values are directly assigned to the upscaled facies. A total of 10 facies make up the upscaled field of storage MPS parameters. In the upscaled fields, the channel beds are clearly visible, and their shapes and connectivity are preserved by the upscaling. The different sedimentological concepts of the different sub-intervals are respected and transferred to the specific storage fields (Fig. 4.9).

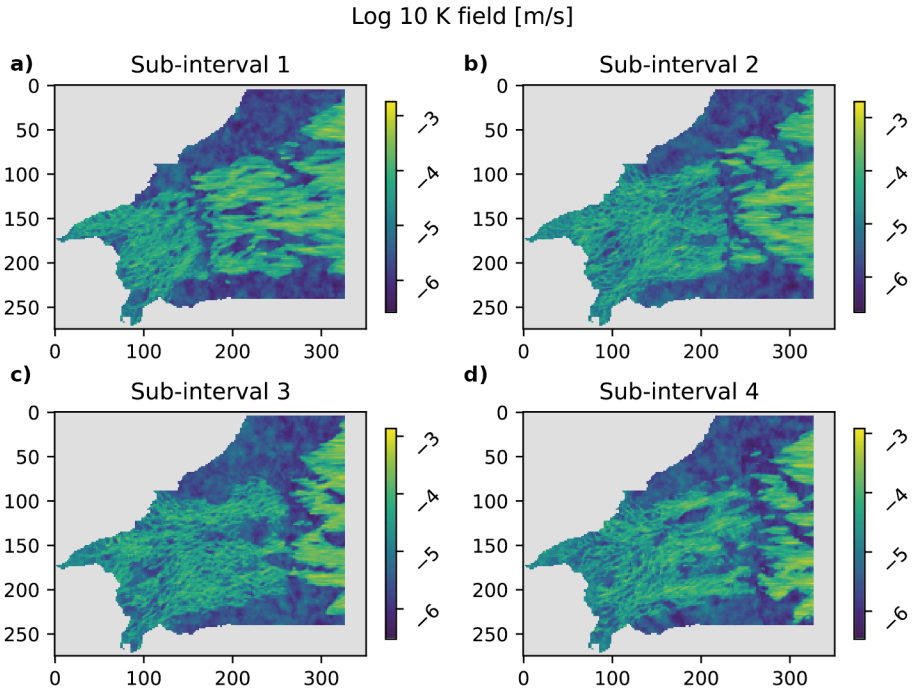

Figure 4.8: Upscaled hydraulic conductivity fields of the MPS approach. The sub-interval one is the bottom one, and the sub-interval four is the top one.

4.4 Discussion and Conclusion

This chapter presented the three approaches used for the simulation of the hydro-physical property fields of the Roussillon aquifer. These three approaches represent different conceptual approaches to the problem at hand. The first one, the depth-related one, is a deterministic approach, based on the interpretation of hydraulic pumping tests, and does not include any conceptual information during its creation process. Hydraulic conductivity and storage fields are based only on interpreted measurements and the geological map. The second approach, the SIS approach, is a stochastic simulation method based on indicator variograms. This approach incorporates some descriptive conceptual information of the system through the use of rotation and auxiliary maps that spatially describe the facies location on the plain. The use of a variogram model describes the two-point spatial correlation. However, the use of the variogram method is not able to simulate complex realistic shapes and simulates only patches of zones that are likely to be composed of sand or clay deposits. The last approach is the MPS method, which is complex to set up and requires expert knowledge in order to create the required training data set. By using a complex training data set, this approach is able to reproduce realistic patterns that make up an alluvial system and its associated hydro-physical fields.

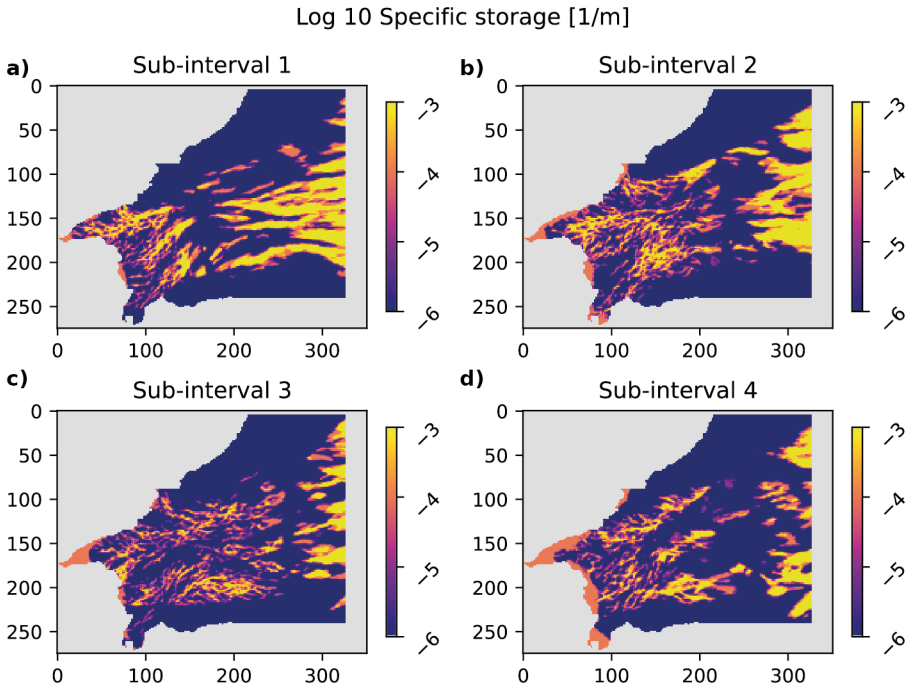

Figure 4.9: Upscaled specific storage fields of the MPS approach. A total of 10 facies make up these upscaled fields, each of which is assigned a homogeneous value. Depending on the sub-interval, the shapes and connectivity of the high storage zones are controlled by the original MPS simulation and the location of the simulated channel beds.

The final objective of this work will be to compare the performance of the three presented approaches when simulating groundwater flow in order, first, to estimate the geological uncertainty introduced in the hydrodynamical simulation and, second, to compare the benefit of incorporating more or less complex geological structures in the parameter fields.

One important limitations of the approach that we used in this work is the difference in resolution between the litho-facies simulation grid and the hydrodynamical grid, the latter being coarser/larger than the former. This difference in resolution requires the use of an upscaling step to transfer the physical hydrodynamical parameters to the hydrodynamical simulation grid. The upscaling process tends to aggregate the properties of the fields. Moreover, the upscaling process can be an important source of inaccuracy during the modeling approach, since the upscaled field here is an analytical approximation of the correct upscaled hydraulic conductivity parameters. After the upscaling, the detailed simulated patterns of the MPS simulations are lost and the upscaled fields tend to produce more homogeneous hydraulic conductivity zones

compared to the one originally simulated.

The process used to upscale the specific storage field better preserves patterns, but cannot be applied to the hydraulic conductivity fields due to the non-additive nature of the hydraulic conductivity fields. By creating intermediate mixed facies, the proposed approach preserves the main spatial link of the categorical simulation while taking into account the transition zone between lower and higher storage facies at the floodplain/channel interface.

Another important drawback of using fine-scale grid for the stochastic simulations and another coarser one for the hydrodynamical simulations is that it requires a large computing time to simulate and transfer the properties between one to another. The generation of MPS or SIS simulations followed by SGS simulation for hydraulic conductivity assignment is demanding in terms of computational resources, this can be an important limiting factor during the calibration process of these fields.

While the simulation process of MPS are numerically demanding, it still favors the creation of more realistic categorical fields conditioned by field data. In addition, the MPS simulation approach also includes the expert knowledge in the simulation process of these property fields. The SIS simulations, are in between the two other approaches, since they still use some conceptual knowledge, through the use of probability and rotation maps, and are constrained by a hard data set, but miss the simulation of realistic patterns. These two approaches can better represent local complexity, which can be important for the hydrodynamical approach. Finally, the MPS/SIS sets are stochastic processes that produce two ensembles of realizations that permit to study the uncertainty of the geological model on the hydrodynamical simulation. The number of members within these two simulation sets could also be increased during the SGS simulations of their hydraulic conductivity properties, since this process is also a stochastic process and could generate from one MPS/SIS simulation different hydraulic conductivity parameter fields.

We believe that the three approaches are representative of realistic levels of care that can be found in different hydrogeological projects and will be useful to characterize the effect of the selected sedimentological modeling approach on the simulation and will be able to describe the geological uncertainty derived from the conceptual model of the Roussillon aquifer. These fields will be used during the hydrodynamical simulation in both steady state and transient state in next chapters.

Chapter 5

Hydrodynamical concept, measurements, and model setup

Abstract

Numerical groundwater modeling is a powerful tool that allows hydrogeologists to simulate groundwater flow and gain insight into the behavior and characteristics of groundwater systems. However, no model can simulate a groundwater system without proper input, conceptualization of the aquifer system, selection of appropriate numerical methods, model calibration, sensitivity, and uncertainty analysis. The hydrodynamical input parameters are essential components that interact within the model, including no flow boundaries, constant head zones, or wells, and are linked to physical activities such as agricultural land use, drinking water supply, or recharge processes occurring from surrounding massifs. These components are associated with physical values and time series that can be defined as constant over time or associated with transient time series.

Over the past 20 years, the water level of the system has declined in most parts of the plain. The responses of the system to its various stresses are not easy to understand, as they result from a combination of local and global recharge and discharge processes. In order to constrain the model of the Roussillon groundwater system, this chapter presents the conceptual hydrodynamical description of the system and highlights its hydrogeological components. The Roussillon system is composed of five major rivers that, depending on the conditions, can participate to recharge the underlying aquifer. In addition to precipitation recharge, several anthropogenic recharge zones have been identified. This recharge process results from agricultural irrigation activities in the plain. The Roussillon aquifer also receives water from the surrounding massifs, from fault or contact zones, or karstic conduits systems. To represent this recharge, three recharge zones have been described, two in the north and one in the south of the domain. 264 wells make up the drinking and industrial data set, representing

about 40 Mm^3 of water abstraction per year. The agricultural data set, represented by the 2018 data set, consists of more than 1,350 wells and represents a total water withdrawal of about 20 Mm^3 per year. This chapter also presents the available groundwater level observations for the simulation period, which are used as a validation and calibration data set for the numerical models.

Finally, this chapter presents the numerical model of the Roussillon, built using the MODFLOW 6 software and the FloPy Python package. The grid discretization as well as the temporal discretization of the numerical model are presented.

5.1 Introduction

The construction of a hydrodynamical numerical model requires the collection, assembly, and analysis of a large amount of data. This includes data describing the geographical and geological information of the site, such as topographic maps, geological models, hydrogeological parameter fields, and data describing its hydrodynamical behavior, such as boundary conditions, precipitation time series, or the annual amount of water withdrawn for agricultural use or drinking water supply. One of the main differences between the construction of a black box model and a discretized model is the spatial representation of the information. In such numerical models, the interactions between the different components are no longer considered globally, but locally. Numerical models are used to analyze the potential effects of groundwater pumping, land use changes, or climate change on water resources. Only such numerical models are able to answer specific questions, such as the evolution of water levels in a given area or the variation of fluxes between a river and an underlying aquifer. These predictions are essential for regional or local management, and are even more important given the impact of climate change on water resources [IPCC, 2022]. By accurately simulating these vital underground systems, it is likely that they can be managed in a more sustainable manner.

One of the key factors for a robust groundwater simulation is the proper description of the internal variability of the hydrodynamical properties of the aquifer. The hydrodynamical properties are generally linked to the spatial organization of the sedimentological facies, which generally requires specific simulation methods to be created [Dall'Alba et al., 2020; Micallef et al., 2020]. The various components that make up the geological and hydrodynamical parameters of the Roussillon aquifer have been presented in chapters 2 and 4. The hydrodynamical fields constructed using the three selected approaches are used during the steady-state and transient simulations in the following chapters.

Once the geometry of the system has been defined, and that the main physical properties have been assigned, it is essential to clearly identify the main hydrodynamical limits of the system. These limits can be defined by no-flow boundaries, constant head zones, or constant flux zones, and are often called

hydrodynamical stresses.

Another important component of any hydrodynamical model is the set of hydrodynamical stress factors. It is important to clearly identify the various stresses and components that interact within the model and to understand their key interactions and behaviors. Within the domain, other stress factors may be present and interact with the water resource, such as the presence of wells that can withdraw water from the system. Once the major components are identified, the next step is to associate physical values and time series for each of these conditions.

The stresses data can be defined as constant over time or associated with transient time series, depending on the state of the simulation and the type of data/records available. These input data can be obtained manually in the field, or can be automatically collected from automatic data loggers, or can be derived from local hydrodynamical studies. Once collected, these data are subjected to pre-processing before being used in the model. Errors and biases can occur during data collection and pre-processing, so it is important to identify these potential sources of uncertainty for a robust uncertainty analysis of the model.

Finally, it is essential for a model to be confronted to historical observations to assess the quality of the model. These data can be punctual piezometric water levels, piezometric water level chronicles, river stage measurements, or river flux chronicles.

A correct conceptual description of the system under consideration and a rigorous identification of the main sources of uncertainty are always challenging steps in any hydrogeological study and influence the final reliability of the simulated output.

Depending on the focus of the project, different software and modeling approaches can be selected. The numerical modeling approaches used in hydrogeology are used to solve the groundwater flow equation, also known as Darcy's Law [Manning, 2016]. Darcy's Law is a fundamental equation that describes the flow of groundwater through porous media. It states that the flow rate of groundwater through a porous medium is proportional to the hydraulic gradient and the hydraulic conductivity of the medium. For numerical modeling, this equation is combined with the conservation of mass, which states that the rate of change of groundwater storage in a given volume of porous medium is equal to the difference between the groundwater inflow and outflow rates.

The numerical modeling approaches used in hydrogeology solve the groundwater flow equation by discretizing the domain into a mesh of nodes or elements and using iterative numerical methods to solve the resulting system of equations. The goal is to obtain a solution that accurately represents the flow of groundwater through the porous medium and the effects of various factors,

such as pumping or recharge, on the groundwater flow regime. There are several numerical modeling approaches used in hydrogeology, including the finite difference method (FDM) [Langevin et al., 2017], the finite element method (FEM) [Diersch, 2013], or the control volume finite element method (CVFEM) [Donea and Huerta, 2003]. Each method has its advantages and disadvantages and is suitable for different types of hydrogeological problems. The appropriate method depends on several factors such as the complexity of the problem, available data, and computational resources.

The Roussillon aquifer has experienced a continuous decline in groundwater levels over the last few decades, with local declines of up to several meters, as demonstrated by several studies [Chabart, 1996; Aunay, 2007; Caballero and Ladouche, 2015]. This trend is of particular concern given that global freshwater demand is expected to increase, or at best stabilize, in the coming decades, driven by agricultural activities, land use changes, and continued tourism development. In addition, there is an increased risk of seawater intrusion into the aquifer due to rising sea levels [Galassi and Spada, 2014] and changing climatic conditions [IPCC, 2022].

To address these challenges and evaluate the impact of these changes on water resources, we developed a 3D groundwater model using MODFLOW 6 [Langevin et al., 2017]. This modeling software uses the finite difference method (FDM) to solve the groundwater flow equation, allowing us to study the complex dynamics of water flow in the aquifer. This software is widely used in many environmental agencies and is considered a robust tool for many hydrogeological setups. Furthermore, this software, which is distributed by the USGS[6], is free and can be easily set up to work on a cluster when coupled with the open Python FloPy library[7].

Compared to previous modeling work in the region, our model incorporates new elements, such as the influence of irrigation canals, and provides a more rigorous quantification of prediction uncertainties. This work is a crucial step in improving our understanding of the vulnerability of the Roussillon aquifer to external stresses, and opens up new possibilities such as coupling the groundwater model with a novel economic model to develop more effective strategies for managing this critical resource [Neverre and Mathey, 2022] .

This chapter consists of four main sections. The first section introduces general information about the Roussillon aquifer system and presents the main conceptual elements of the model, its boundaries, fluxes and the hydrogeological assumptions made for the construction of the hydrogeological model. The second section introduces the MODFLOW grids, and the spatial and temporal discretization of the numerical setup. The third section presents the time series

[6]https://water.usgs.gov/water-resources/software/MODFLOW-6/

[7]https://github.com/modflowpy/flopy

of the various elements that make up the model (recharge processes, pumping wells sets, constant head boundaries and constant flux zones). These data span 20 years, from January 2000 to December 2019. The last section presents the available observational data that will be used to test and validate the robustness of the different models. This validation and calibration data sets is composed of 22 observation series for the transient-state data set, and is composed of 123 observation points for the steady-state data set (August 2012). This chapter ends with a brief discussion of the conceptual hydrogeological model of the Roussillon system.

5.2 Conceptual model

Hydrogeological setting

As previously described in detail in chapter 2, the Roussillon aquifer is located on the western border of the Mediterranean Sea, in the Pyrénées-Orientales region of southern France. The extent of the aquifer covers more than 800 km^2, a quarter of which is below 10 m.a.s.l. The relief slopes slightly from west to east, with maximum heights of about 200 m.a.s.l. at the western limit. This aquifer is bordered on the east by the Mediterranean Sea (Fig. 5.1).

Massifs are bordering the plain, with the south and east side composed of granitic Pyrenean mountains and with the karstic Corbières formation in the northern part of the plain. The Roussillon plain is a multilayered basin in which three aquifer units can be identified: the Quaternary, the continental Pliocene and the marine Pliocene.

The Quaternary aquifer generally follows the actual riverbeds of the plain and consists mainly of terraces, alluvial channels and floodplain deposits. This Quaternary layer extends offshore, but the evolution of its sediments and the structural spatial disposition are poorly documented due to the lack of data. This aquifer is considered unconfined in most of its onshore extension, but is considered confined in its offshore extension due to the presence of a silt cover composed of deglacial sediments [Duvail et al., 2022]. During the modeling phase, this aquifer is set has an unconfined unit.

The second aquifer is the Continental Pliocene. It is known to be highly heterogeneous, with sandy deposits of various sizes alternating with more or less clayey layers over thicknesses of several meters. The Continental Pliocene aquifer appears to be confined over most of the plain because its permeable layers are generally embedded in clayey formations with low vertical permeability [Chabart, 1996; Aunay et al., 2004]. This aquifer outcrops only on some western parts of the plain. For simplicity, and because the zones where the aquifer is unconfined are not well known, we assume this layer to be confined everywhere during the simulation. This layer can be described as a formation composed of highly permeable, heterogeneously distributed paleo-channels, em-

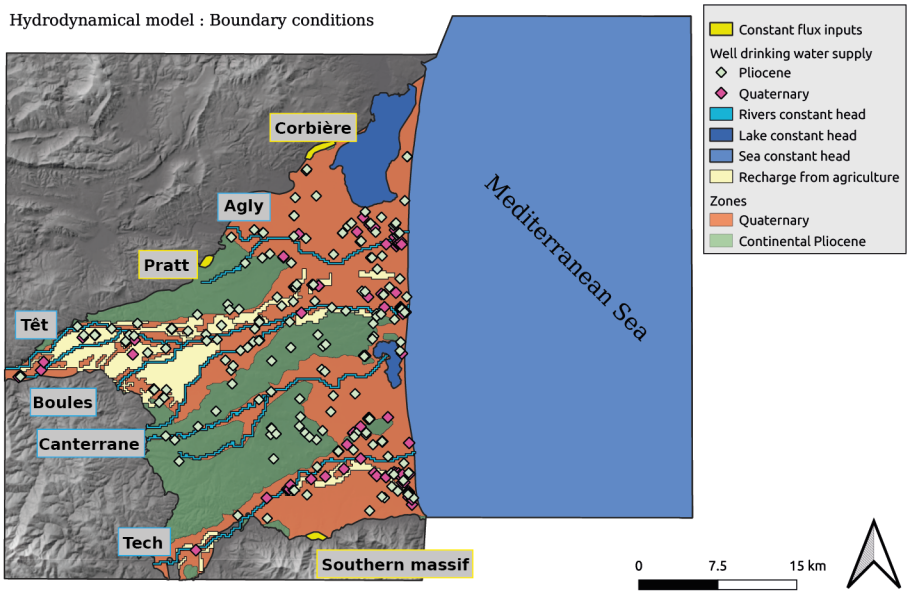

Figure 5.1: Conceptual hydrological model of the Roussillon plain and its associated hydrodynamical components. Here, the domain extent corresponds to the extent of the hydrodynamical domain, but does not correspond to the true extent of the Roussillon layers.

bedded in a lower permeability floodplain matrix.

The third aquifer is the Marine Pliocene bottom formation. It is generally considered to be a rather homogeneous and permeable unit, as it is mainly composed of prograding sandy formation. This formation is considered to be confined.

Hydrodynamical conditions

From a hydrological point of view, the plain is crossed by four main rivers (Fig. 5.1): the Agly, the Têt, the Réart and the Tech, most of which have their sources in the surrounding massifs. The catchment areas of these rivers range from 700 to 1300 km^2, except for the Réart (160 km^2). There are two other smaller rivers in the plain, the Boulès, a main tributary of the Têt, and the Canterrane, a main tributary of the Réart. These two rivers are less important than the four main ones. It is also important to note the presence of two large lagoons, the Canet lagoons in the central coastal part of the plain (7.82 km^2) and the Leucate one, in the north (54 km^2).

The main component of the water system of the Roussillon plain is the recharge from precipitation. With an average rainfall of 600 mm per year (2000-2019) and an average temperature of 15.3℃ (2000-2019), the Roussillon is considered a temperate Mediterranean region. The rainfall is not homogeneously distributed on the plain and the actual recharge reaching the aquifer depends largely on the infiltration factor of the soil, which can also strongly influence the actual recharge spatial distribution.

Most of the boundaries of the study area are considered as no flow boundaries, except for some small input zones known to contribute to the recharge of the system. The Corbières karstic massif (northwest) is estimated to supply nearly 200 l/s to the Quaternary and continental Pliocene layer [Ladouche and Dörflinger, 2016; Lanini et al., 2022]. Further to the northeast, the Pratt fault zone is also thought to supply water to the system [Lanini et al., 2022] (Fig. 5.1). Other massifs, such as the Aspres, located to the southwest of the area, are also suspected of feeding the aquifer, but the associated flows are not well-defined due to the lack of specific studies in the area. These three input zones are shown in yellow zones in figure 5.1.

Another major component of the hydrological balance is the large water extraction and infiltration from the agricultural systems present in the plain. The agricultural areas are mainly located along the Têt river and in the central part of the plain. The agricultural irrigation system of the Roussillon is based on the use of anthropogenic canals that divert water from the main rivers and redistribute it along the crops, and on direct withdrawals using wells. The agricultural canal system is complex and has greatly influenced the behavior of the aquifer water system, as it is now considered an essential water recharge process for the Quaternary and Pliocene aquifers in some areas (Fig. 5.1). Regarding the water abstraction from the agricultural well system, the total amount of water withdrawn from agriculture has reached 20 Mm^3 in 2018.

The last main component of this hydrodynamical system is the extraction of water for drinking and industrial use. The amount of water withdrawn annually for drinking and industrial purposes is estimated at 40 Mm^3 per year.

5.3 Numerical model setup and discretization

Modeling software

This work aims to simulate the main temporal evolution of the piezometric level of the groundwater resource of the plain, as well as to calculate the evolution of the different fluxes that happen between the different zones of interest. The main concern is the potential risk of saline water intrusion from the Mediterranean Sea. The MODFLOW groundwater software has been chosen to build this model. MODFLOW is widely used and recognized in groundwater studies. In this work, we use the MODFLOW 6 version [Langevin et al., 2017], and the

open source Python package FloPy to build the model, run it, and analyze the results [Bakker et al., 2016].

MODFLOW 6 uses a block-centered finite difference method (FDM) to solve its governing equations. It can accommodate structured and unstructured grids with local mesh refinement. The MODFLOW software is built around a groundwater model, to which various hydrogeological packages representing hydrodynamical stress conditions are added. These packages represent recharge parameters, constant head properties, pumping wells, rivers, drains, and all other types of hydrogeological elements. Several packages of the same type can be used for a single model, since all packages are independent of each other. Moreover, it is possible to couple different groundwater models, each characterized by its own set of packages. With this framework, this software is capable of solving multiple coupled numerical models in a single system of equations. The possibility to add and remove packages to a groundwater model, and to modify these packages even once created, makes MODFLOW 6 a very flexible software for the creation of hydrodynamical models [Langevin et al., 2017].

Numerical grid

Based on the geological analysis previously described, the model grid includes seven surfaces that define the internal geometry of the aquifers (from top to bottom):

- Digital Terrain Model (DTM)
- Quaternary base surface
- UPC-2 (interval Continental Pliocene surface)
- UPC-12 (interval Continent Pliocene surface)
- UPC-1 (interval Continental Pliocene surface)
- Continental Pliocene base surface
- Marine Pliocene base surface

Using these surfaces, two different model grids have then been created. They have the same horizontal extent, but differ in the number of layers representing the Continental Pliocene.

Figure 5.1 shows the horizontal extent of these grids. The onshore boundary is fixed by the adjacent mountains, while the offshore boundary is fixed to include the offshore extension of the domain, which represents a potentially important groundwater resource, and far enough to avoid simulating boundary effects.

The horizontal resolution of the model is set to 200 × 200m (351 rows and 275 columns).

The first grid is used for the depth-related approach presented in chapter 4. It consists of eight layers that follow the major geologic-topographic envelopes of the three aquifers. For this approach, the Continental Pliocene layer is divided into four sub-intervals, bounded by the three UPC interpolated surfaces (chapter 2). This results in a model grid with a total of 382'535 active cells.

The second grid is used for the other two stochastic approaches: SIS and MPS simulations used to model the hydraulic conductivity fields. This grid is composed of 22 layers. The Continental Pliocene layer is divided into 18 layers. It results in a total of 1'114'861 active cells. Note that the minimum cell thickness is set to 1m to avoid numerical problems.

Temporal discretization

The temporal discretization of the model covers the time span from January 1, 2000, to December 31, 2019. The temporal resolution of the transient model is set daily to match the smaller temporal resolution of the data set corresponding to the precipitation data.

5.4 Boundary conditions

The type and locations of the prescribed boundary conditions (BC) have been introduced in the conceptual model section and are shown in figure 5.1. Here, in this section, we explain how the values of the BC were estimated for each component of the model.

Constant head boundaries

Sea extension

A constant head BC is prescribed in the model area covered by the sea using the constant head package (CHD) of MODFLOW 6. Since no significant data are available offshore, and we are mainly interested in the risk of intrusion near the coast, we kept the offshore part of the model very simple. A constant head value of water depth$\times$0.025 (equivalent freshwater head) is prescribed for the offshore region. This choice allows us to mimic groundwater flow circulation in the offshore part of the model without explicitly representing the density dependent flow. The type of boundary to apply on such condition is not resolved through the literature and should be treated with care.

Lagoons

Two lagoons are implemented using the MODFLOW 6 Drain package (DRN). Caballero et al. [2022b] indicates that no flow from the lagoons to the aquifer can be observed under the current piezometric conditions of the Quaternary and Pliocene layers. The Drain package allows us to simulate that these water bodies only act as outlets for the aquifer, based on a fixed head value. The fixed head is set to 0.1 m with a conductance value of 1 m^2/s.

Rivers

Six rivers (Agly, Têt, Boulès, Reart, Canterrane and Tech) are included using a Cauchy boundary condition implemented in the River MODFLOW 6 package (RIV). Rivers and streams contribute or drain water from the groundwater system, depending on the head gradient between the river and the groundwater regime. The River Package does not simulate surface water flow in the river, only river/aquifer seepage. The River Package allows flow between the river and the aquifer, depending on the head gradient between the river and the underlying groundwater unit. If the cell below the river is disconnected from the river bed, a seepage flux is calculated using the head difference between the river stage and the bottom of the river bed, which limits unrealistic recharge from the disconnected river to the unsaturated groundwater unit [Langevin et al., 2017].

This package requires the definition of river bottom elevation, river stage elevation, and river bottom conductance. The river stage is defined according to the DEM, and the river bed is initially set to 0.5 m below the river stage in the upper part of the plain, and to 0.7 m in the lower part of the plain. These two values are set based on expert knowledge of the plain and are not intended to be an exact description of the riverbed thickness. The initial conductance parameter for all riverbeds is first set to 0.005 m^2/s. This value is calculated based on the conductance equation, which combines the geometry (width, thickness and length) and the hydraulic conductivity of the river bed [Langevin et al., 2017]. The conductance value will be calibrated in a subsequent step.

The main rivers of the plain (the Agly, the Têt, the Boules and the Tech) are assumed to have a constant water level throughout the simulation, as they are assumed to be perennial. The Canteranne and the Reart are assumed to be dry during the summer period. Their river stage is set as transient for the simulation, assuming an inverse bell-shaped curve. The distribution is created using a normal pdf curve from 0 to 12 on the x axis, representing the 12 months of the year (mean pdf of 6 and standard deviation of 1.8). We then roll the pdf along the x axis to have its maximum values located between December (12) and January (0) and its minimum value in June (6). The values of the pdf, on the y axis, are finally rescaled between 0 and 1 and used as a multiplier coefficient for the river stage throughout the year.

Flux conditions

A Neumann BC imposing a fixed flux value is set in three zones (Fig. 5.1, yellow zones). These zones correspond to the flow from the surrounding massifs, and are defined using the well packages (WEL), which allow fixing a constant flux value as BC. Near the Corbières massif (north of the Roussillon plain), a fixed annual flux of 150l/s is set, corresponding to the recharge of the karstic massif to the Roussillon formation [Ladouche and Dörflinger, 2016; Lanini et al., 2022; Schorpp et al., 2023]. The second zone corresponds to the presence of the Pratt fault zone (north-west), which is supposed to feed the Roussillon North Pliocene formation (Tab. 5.1). The last zone corresponds to the input from the Aspres massif, where a constant flux has been estimated manually and is assumed to be fixed and constant (Tab. 5.1) [Lanini et al., 2022; Schorpp et al., 2023]. This flux is distributed between the Quaternary and Continental Pliocene strata.

A no-flow condition is imposed along the other lateral boundaries of the model, since the Miocene bottom layer is assumed to act has a hydrodynamical barrier, and that no other contact zones were identified on the plain.

Table 5.1: Boundary flux conditions.

Zone	Flux [m3/s]
Corbière massif	0,15
Pratt fault	0,024
Southern massif	0,6

Recharge

The recharge is composed of two parts; one takes into account the precipitation and the other takes into account the water coming from the irrigation of the agricultural parcels and their irrigation channels. The two recharges are defined through the use of the recharge package (RCH), which define an input flow in [[L/T]] that is assigned to a specific cell or group of cells. The charge is then calculated by the software, taking into account the area of the assigned cells.

Recharge from precipitation

The effective precipitation is estimated using a simple soil water budget. The initial precipitation data come from the SAFRAN meteorological data service, which provides daily precipitation data in a grid of 8×8 km cells (mean annual precipitation of the Safran cell of the Roussillon in Fig. 5.2a) [Vidal et al., 2009]. The effective precipitation is calculated using the approach of Edijatno and Michel [Edijatno & Michel, 1989], which uses as parameters the RU max parameter (Fig. 5.2d), daily precipitation, temperature, snow cover, evapotranspiration (ETP) and a vegetation index. The precipitation, temperature, snow cover, and ETP are obtained from the SAFRAN data at a daily time

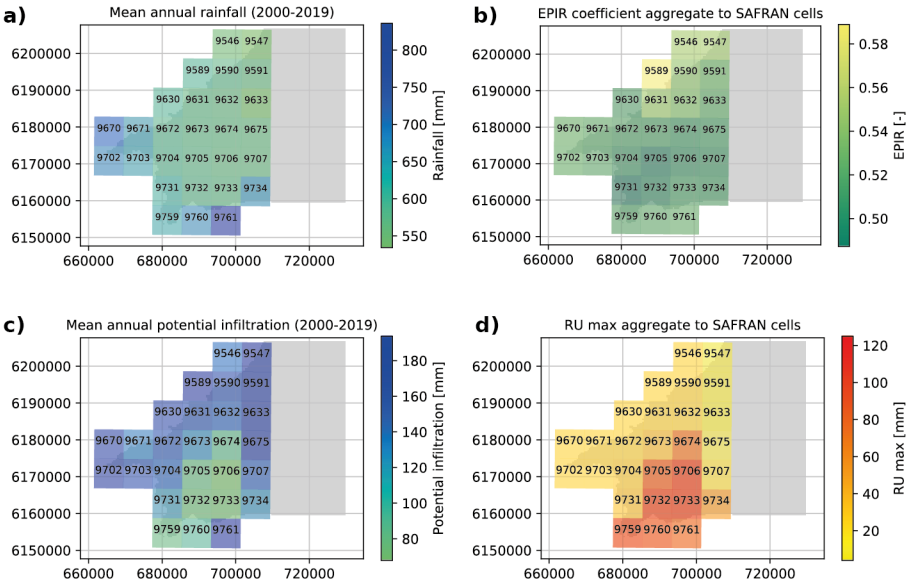

Figure 5.2: The main component of the potential infiltration calculation approach. The cell numbers correspond to the identification number of the SAFRAN cells (8×8 km cells). a) represents the mean annual precipitation per cell, b) the EPIR coefficient, corresponding to an infiltration/precipitation ratio, c) the calculated mean annual recharge, and d) the RU max coefficient, corresponding to the maximal soil water content for the water balance computation.

step, while the vegetation index is fixed at 1 to ignore the effect of vegetation on evapotranspiration. The RU max, which represents the maximum soil capacity of the reservoir, was calculated for the region using Caballero et al. [2021] data (Fig. 5.2d)) [Martinsen et al., 2022].

The potential infiltration is then estimated by multiplying the calculated effective precipitation by the EPIR (effective precipitation infiltration ratio) coefficient of the SAFRAN cells. The EPIR is obtained for each geological formation based on a calibrated relationship estimated between the EPIR and the IDPR (index of development and persistence of river networks), where the EPIR is assumed to be equivalent to the base flow index (BFI) (Fig. 5.2b) [Martinsen et al., 2022].

After calculating the potential infiltration, the effective infiltration is estimated using a convolution method. This is used to represent the transfer from the topographic surface to the aquifer through the unsaturated zone and to calculate the final effective infiltration component of the model. This approach, proposed by Besbes and de Marsily [1984], is able to represent the delay between

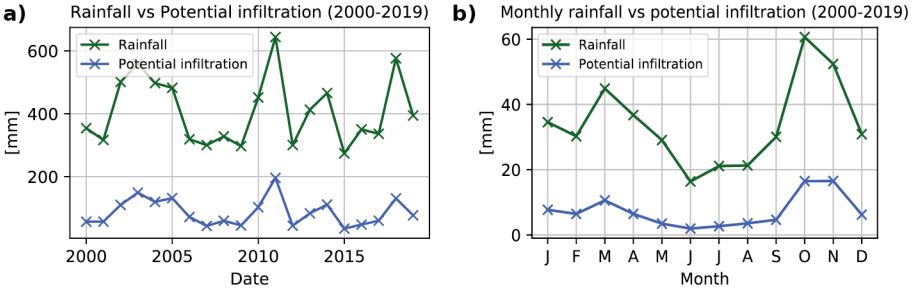

Figure 5.3: a) Annual precipitation and recharge for the Roussilon plain. b) Monthly mean precipitation and recharge. Both statistics are calculated for the period 2000-2019.

infiltration from the soil to the actual groundwater reservoir. These authors show that the gamma transfer function is sufficiently flexible to represent a wide range of recharge dynamics. The impulse response gamma function used for the convolution is:

$$\theta(t, \alpha) = \frac{t^{\alpha-1} e^{-t}}{\Gamma(\alpha)} \tag{5.1}$$

where α is the shape parameter, and Γ is the Gamma function.

The gamma function is estimated using the SciPy python package [8]. The parameters of this function are fixed to; $\alpha = 1.5$, loc=1 and scale=3.5. The loc and the scale parameters characterized the shape of the function within the SciPy package.

Figure 5.4 shows the effect of different α parameters on an infiltration time series. The larger the α coefficient is, the longer the curve is delayed by the convolution. The daily effective infiltration is then estimated by computing the convolution of the infiltration $I(\tau)$ with the transfer function:

$$R(t) = \int_{-\infty}^{t} I(\tau)\theta(t-\tau)d\tau \tag{5.2}$$

Figure 5.3a shows the average annual precipitation of the Roussillon plain, which is mainly homogeneous. It is only in the SAFRAN cells located near the massif, on the border of the domain, that the precipitation values are more important, going up to more than 800 mm/year in the southern area

[8] https://docs.scipy.org/doc/scipy/reference/generated/scipy.stats.gamma.html

(Fig. 5.2a). Once calculated, we can see that the combined effect of the Mediterranean climate and the infiltration coefficients on the estimated mean annual potential infiltration tends to reverse the spatial trend (Fig. 5.2c). The central part of the plain is where the potential infiltration from precipitation is estimated to be the lowest, with average annual values ranging from 80-100 mm/year.

Figure 5.3a shows the temporal annual evolution of the annual precipitation and associated recharge over the simulation period. We notice some large differences in the annual precipitation values. If we look at the mean monthly precipitation and recharge shown in figure 5.3b, we notice that the main peak in recharge occurs during the months of October and November.

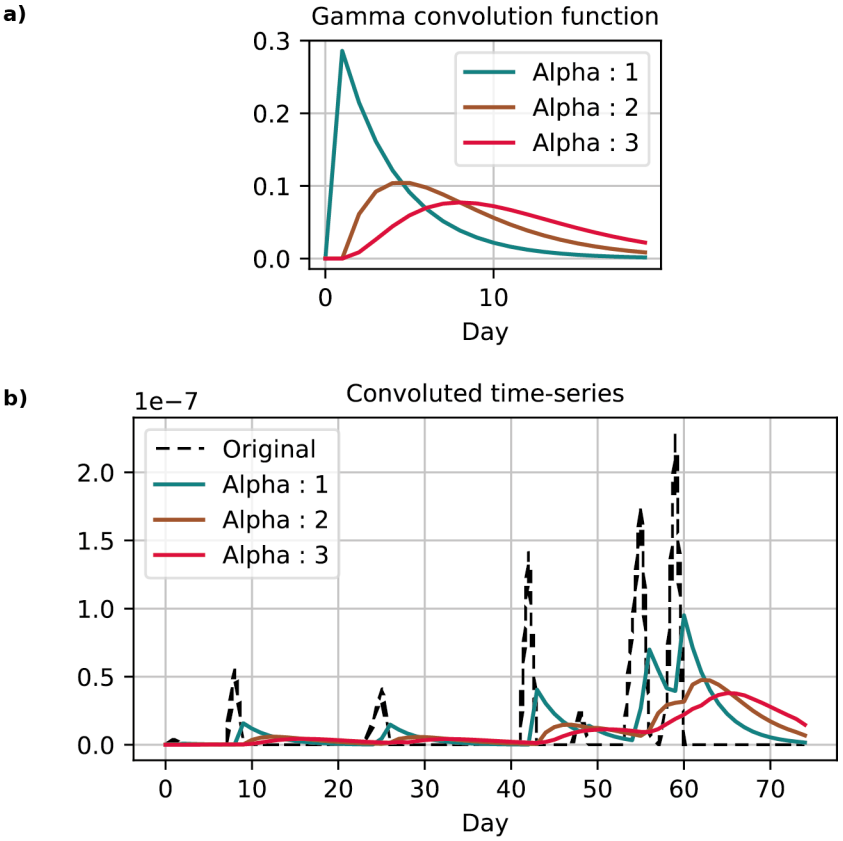

Figure 5.4: a) Convolution gamma functions, where only the α shape parameter is modified, and where the mean is fixed to 1 and the scale to 3.5. b) Modified time-series, from a potential infiltration data set.

To summarize, the main steps for the estimation of the effective infiltration are the following:

$$EffectivePrecipitation = f_{Edijatno}(DailyPrecipitation, RU_{max}, ...) \quad (5.3)$$

$$PotentialInfiltration = EffectivePrecipitation \times EPIR_{coeff} \quad (5.4)$$

$$EffectiveInfiltration = PotentielInfiltration * \theta(t, \alpha) \quad (5.5)$$

Recharge from anthropogenic agricultural canals

[Recharge from canal] The second recharge component is linked to the system of anthropogenic canals used for irrigation. Seepage from agricultural canals has been shown to be very important (2 to 5 m^3/s) and can locally exceed several times the recharge from precipitation [BRLI, 2018b].

The recharge of the canals is estimated by zones and is based on the water demand (depending on the type of crop and the local climatic conditions), the irrigation rate of the canals (irrigation water share of the canal origin) and a multiplication coefficient representing the efficiency of the canals estimated by a previous technical study [BRLI, 2018b,a].

Table 5.2 presents the resulting annual recharge values associated to the different recharge zones of the system of these canals (Fig. 5.5). These values are distributed along the year, following the estimated distribution provided by BRLI [2018b] and presented in figure 5.5.

Table 5.2: Annual recharge values associated with the recharge zones of the canal irrigation system, shown in figure 5.5.

Zone	Recharge [mm]
Têt river south	150
Têt river north	50
Tech river South	500
Thuir zone	200

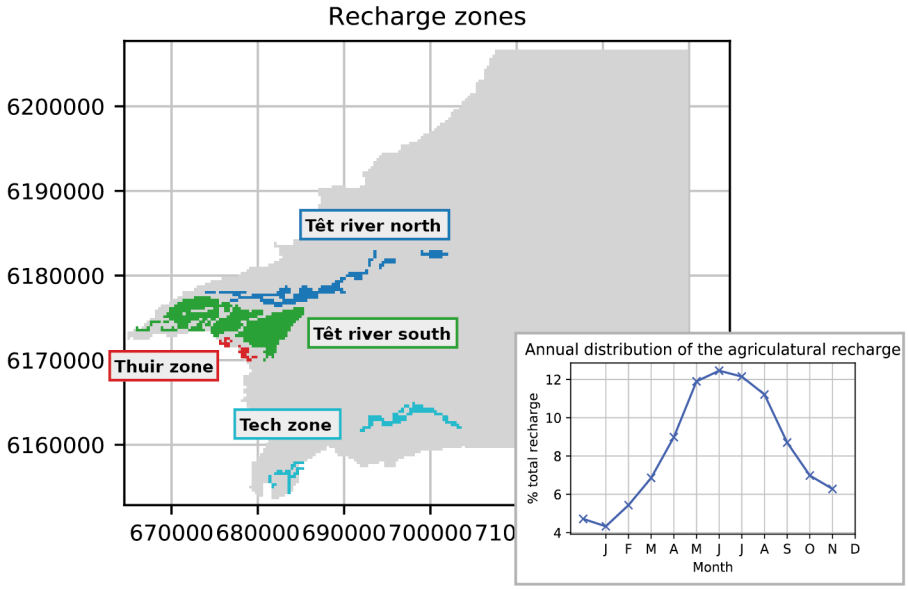

Figure 5.5: Recharge zones of the irrigation system from the agricultural canals and the associated annual temporal distribution.

Pumping wells

The main withdrawals in the plain can be divided into two parts, one for agricultural purposes and the other for drinking water supply and industrial uses. These two groups of conditions are implemented using the well package (WEL). This package works by defining a flow to a particular cell. This flux can be either defined as constant or associated to a transient time series. If multiple wells are defined in the same cell, the final intake is defined as the sum of wells' intakes in this cell. This package is a simple implementation and does not take into account the more complex well processes, such as quadratic pressure drop, that may occur within the pumped cell.

Withdrawals for agriculture purpose

[Agriculture water abstraction] For agricultural withdrawals, the choice is made to integrate each of the wells individually into the models (Fig. 5.6). More than 1'350 wells and their respective annual withdrawals are included in the database. Most of these are taping the Quaternary aquifer. The annual distribution of the withdrawals is not recorded and therefore, we had to distribute them using a distribution curve proposed by BRLI [2018b] and shown in Figure 5.6. Most of the water pumped for agricultural purposes is extracted during the summer period, when river levels and precipitation are low.

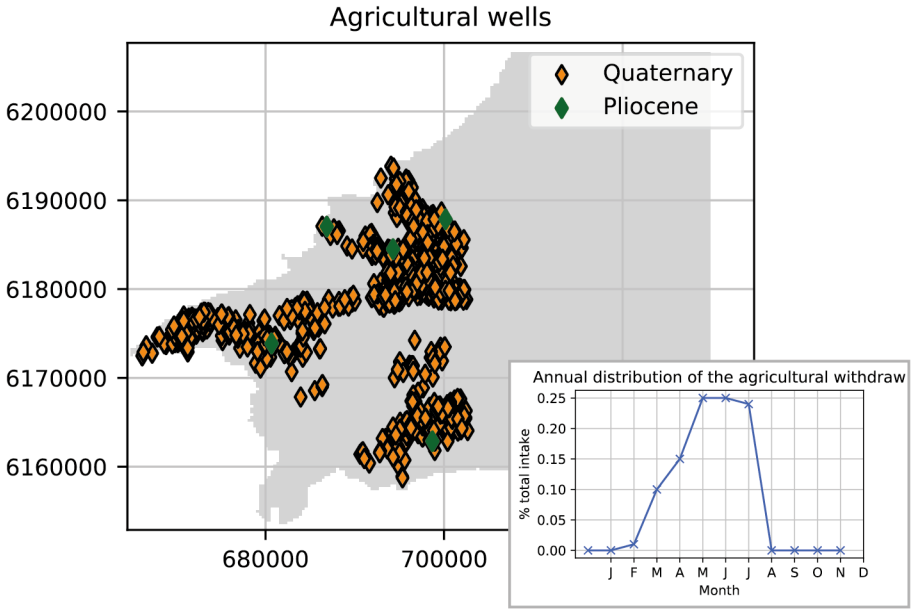

Figure 5.6: Map of agricultural wells and their annual monthly distribution. Most of the wells pump directly into the Quaternary aquifer. The wells are located along the main river valley, where the agricultural exploitation is denser.

One of the issue that we encountered with the agricultural pumping is that the declaration of the active wells was incomplete. The original available data set showed a significant increase in the number of wells, and in the corresponding abstraction, in 2018 (Fig. 5.7a and b). Based on available reports and discussions with water management authorities in the region, it was assumed that the 2018 intake value was more realistic than the rest of the data set. The larger number of declared wells corresponds to a new application of a water regulation that lead to a new survey of the active wells. Therefore, we corrected the data set based on the 2018 annual intake values and used the values shown in figure 5.8a and b in the model. To correct the data set we added the newly 2018 declared wells, and their corresponding abstraction to the previous years, to the rest span that cover the data set. The estimated total intake of the agricultural sector is estimated to be about 20 Mm^3 per year, most of which is pumped from the Quaternary aquifer (Fig. 5.8b).

Withdrawals for drinking water and industrial purposes

[Drinking water abstraction] The last element of the model corresponds to groundwater withdrawals for drinking water supply and industrial use. This database contains all registered annual withdrawals from 2000 to 2019 (Fig. 5.9a). A total of 264 wells formed this data set (Fig. 5.9c). Most of the water

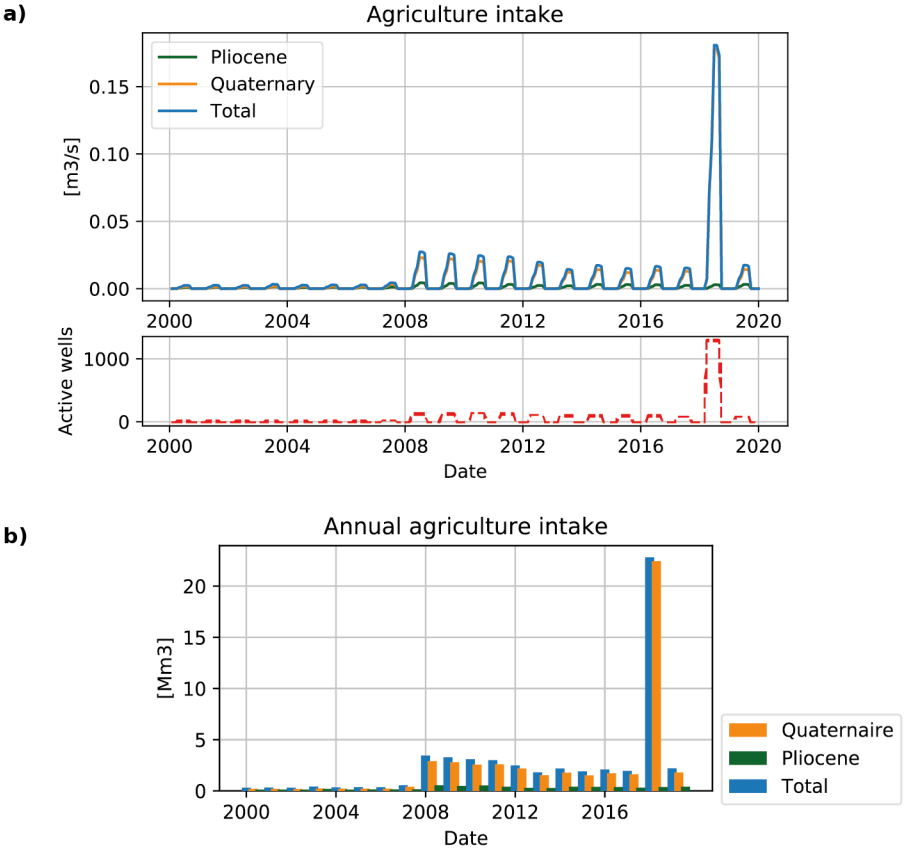

Figure 5.7: Original data set of annual agricultural intake values. This data set shows an unlikely peak in 2018. This peak is likely to be the actual amount of water pumped. The other years probably have missing data.

withdrawals were from the Pliocene. The total withdrawal for drinking water and industrial uses is about 40 Mm^3.

The annual distribution of inflow is estimated based on the well location on the plain and its URD (Unit homogeneous Resources-Demand) affiliation (Fig. 5.10). Each URD zone is characterized by a different distribution curve. The distribution curve of the URD zone is based on a socio-economic analysis presented in Neverre and Mathey [2022] and Caballero et al. [2022b]. These authors analyzed the water consumption of the zone and the different types of industry, housing, or infrastructure present in the sector.

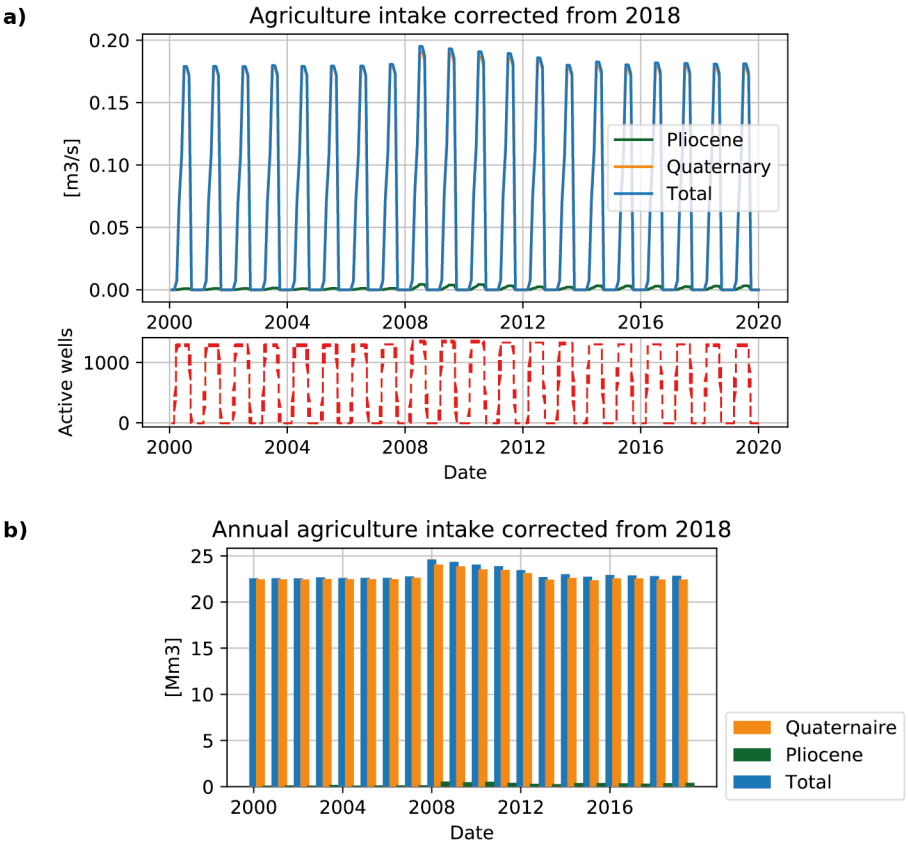

Figure 5.8: The corrected annual agricultural intake values, based on the 2018 value.

5.5 Observation wells

Transient data set

A total of 22 observation wells constitute the calibration and validation data set in transient regime (Fig. 5.11). Six of them are located in the Quaternary layer and the rest in the Continental Pliocene layer. The wells are not uniformly distributed across the plain. Most of the Pliocene observation wells are located near the coast, and many of them are grouped close to each other. Some regions, such as the upper part of the Têt River valley, are covered by only two Quaternary boreholes, while others have no data at all.

If we look at the temporal data availability in the time series (Fig. 5.11b), we can see that the whole span of the simulation is covered, but with large discrepancies in the density of available observation data depending on the period. Some observations cover only a two-year span, while others cover the

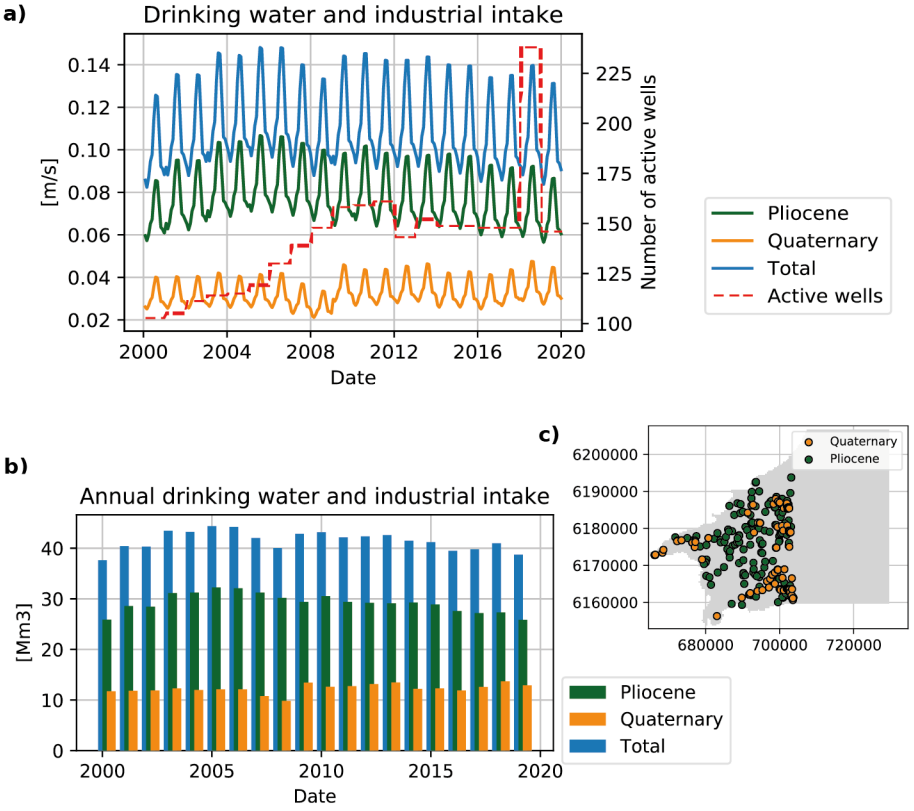

Figure 5.9: a) Annual temporal evolution of the drinking and industrial water withdrawals. b) Total annual water withdrawals. c) the location of the pumping wells that make up the drinking and industrial water data set.

entire simulation span from 2000 to 2019. The full names, and coordinates of the observations are detailed in the supplementary material A.1, table A.1.

Fig. 5.12 shows the data from all the observation wells. Different behaviors are visible. Some monitoring wells (e.g. 12, 13, 24) show an annual cycle with a minimum piezometric level at the end of the summer that is interpreted as resulting from the influence of heavy pumping in nearby wells. Other monitoring wells (e.g. 6, 25 or 31) show a more natural hydrodynamical signal. The Quaternary signals also look more natural and less influenced by seasonal pumping.

Finally, different trends in the global mean groundwater level are visible. Some observations tend to show a global decrease in water level (e.g. 2, 12, and 23), while other observations tend to show a static groundwater trend or even an increase in the mean groundwater level, which might be due to the water man-

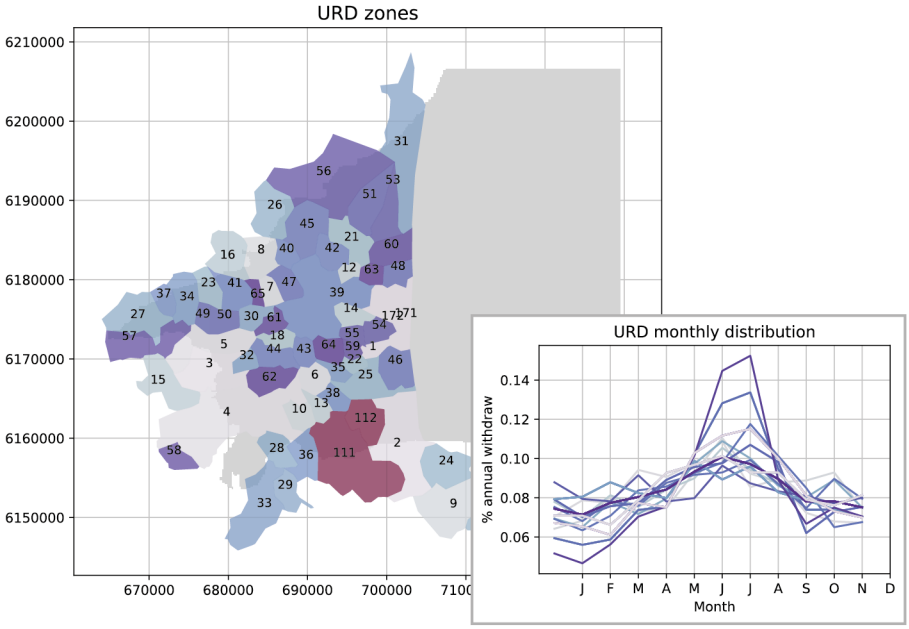

Figure 5.10: URD zone and associated annual water allocation. The URD zone is defined on the basis of socio-economic criteria.

agers actions to reduce the pumping on some sectors over the last 10 years (e.g. 19 and 27). It is important to note that the water head levels in the coastal area have not been corrected, based on their salinity values, in equivalent freshwater head levels.

Steady-state data set

While the number of observations with long time series is limited, there is a much larger number of wells in the plain that record piezometric data at specific times. During some calibration approaches presented in the next chapter, we will use steady-state simulation to calibrate some hydrodynamical parameters of the model. During these steady-state calibrations, we will use a specific data set containing 123 piezometric observations (Fig. 5.13). This steady-state data set corresponds to the month of August 2012. A larger data set can often be found for a specific time period. This data set, which is denser and more homogeneously distributed over the plain, will be helpful to calibrate localized spatial hydrodynamical parameters of the model.

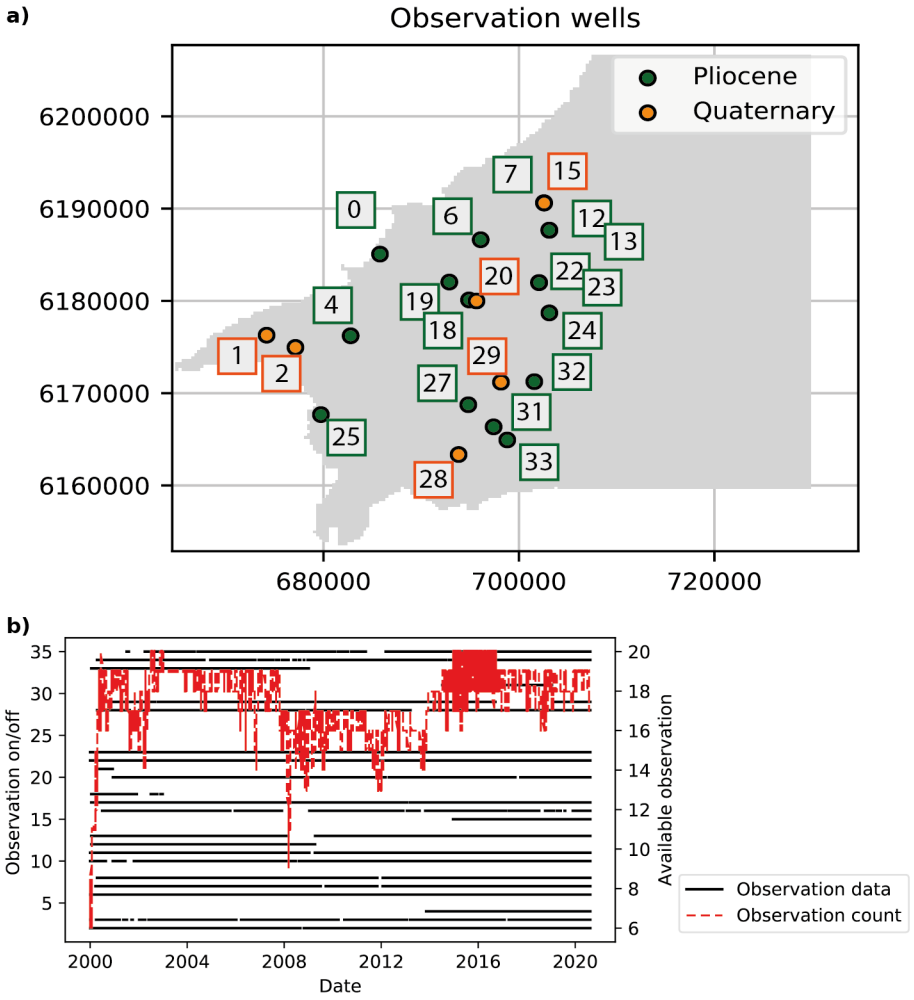

Figure 5.11: a) the location and name of the observation wells. b) an analysis of the temporal density of the available observation data.

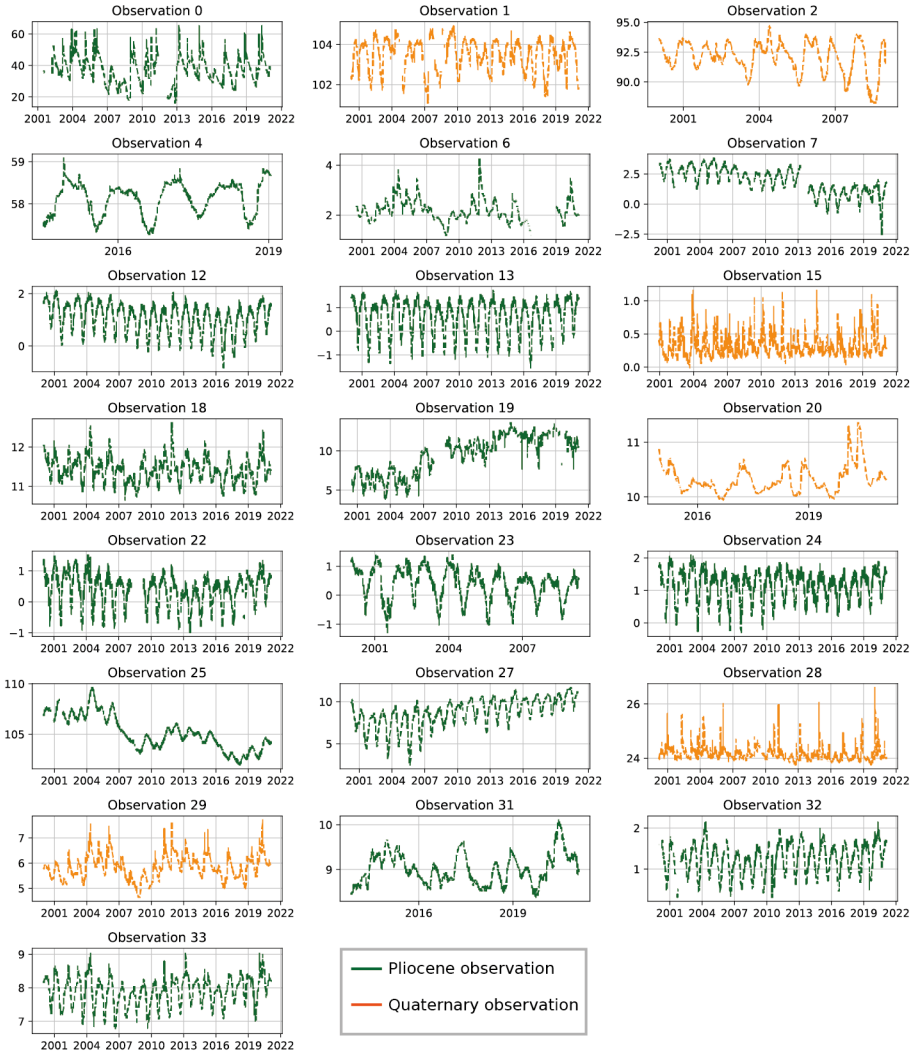

Figure 5.12: Observation data from the observation wells. Different behaviors are present in the data sets.

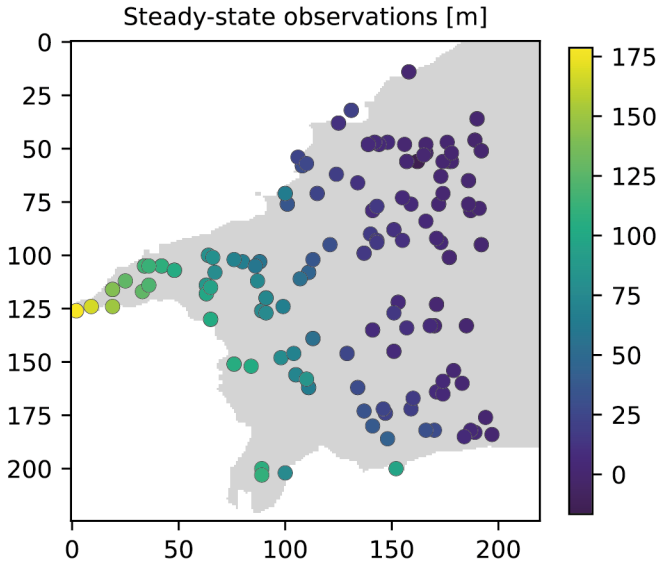

Figure 5.13: Steady-state observation data set. This set corresponds to the month of August 2012. The set is denser and the points are more homogeneously distributed on the plain, comparing to the transient data set.

5.6 Discussion and Conclusion

In this chapter, we presented and summarized the information that we used to establish the conceptual model of the Roussillon aquifer. This task is challenging due to the complex and dynamic nature of subsurface hydrologic systems, limited data availability, and the need to account for various sources of uncertainty.

As a consequence, one of the main limitations of our conceptual and numerical model is that the river systems are highly simplified. It was decided to represent them using the MODFLOW RIV package, which can handle the rivers as a relatively simple boundary condition. The package accounts for the fact that the flow can be limited when the groundwater level falls below the riverbed (instead of rising continuously), but it cannot dry up the river and stopping the recharge completely. The flow along the rivers are not computed in the model with this package, and therefore the amount of water available in the river at a certain time is not computed. The choice of this approach is based on the lack of readily available data to represent properly that part of the system, the numerical complexity that a more detailed approach would add to the hydrodynamical model, and the fact that for this PhD thesis we are already facing a high level of complexity with the geostatistical representation of the geological heterogeneity. Therefore, a possible future improvement could be the use of the more advanced package SFR [Leaf et al., 2021], which allows

the implementation of rivers in a more realistic way, or the use of a different type of numerical model including directly the coupling between surface and groundwater [Brunner and Simmons, 2012].

We also note important uncertainties regarding the annual volumetric amount of water, withdrawn for agriculture purposes. The 2018 data clearly show that past water withdrawals are not well recorded and that there may be even more undeclared wells on the plains, increasing the actual total amount of water pumped out of the system. Beyond the total number of wells and the total amount of groundwater pumping, we are also facing a high uncertainty in terms of seasonality of the pumping. Detailed data are not available over the whole simulation period, and we had to rely on indirect approaches. This leads to the use of a typical seasonal curve that is repeated every year, which is obviously a strong simplification of reality.

Another important uncertainty is related to the calculated effective infiltration from precipitation. In this work, we used the SAFRAN meteorological data and applied classical techniques of water balance in the soil, taking into account the main factors affecting recharge. We coupled this calculation with a transfer function to represent the transfer of water through the unsaturated zone. However, we had little data to calibrate the parameters of the transfer function. At this stage of the work, it is unclear whether these estimates are sufficient or whether additional research using, for example, remote sensing or alternative recharge calculation methods and models should be considered to better constrain the recharge time series. We will test these issues as we implement these time series as input to the groundwater model in chapter 7.

Finally, historical data are essential in the calibration and validation process of any numerical hydrogeological models, as they provide a means of comparing model outputs with actual field measurements. In the case of Roussillon, the transient historical observation data set is sparse compared to the size of the study area, and the observation points are not homogeneously distributed over the plain. Moreover, the observation data set shows different types of behavior, indicating that the aquifer is locally controlled by different components and cannot be reduced to a global homogeneous system, complicating the calibration process. Reproducing these signals, which show such a variety of behavior, will be a challenging task for the numerical modeling approach.

Creating a good conceptual model for hydrodynamical numerical modeling in hydrogeology is critical for accurately simulating groundwater flow and providing insight into the behavior of subsurface water systems. This can be a complicated task depending on the system at hand and the data available. Regarding the Roussillon model, we are confident in the fact that the conceptual model integrates most of the important elements of the system. However, some hydrodynamical components can contain uncertainties or errors, both in their conceptual description and in their transient series, when they estimate

or generalize important features.

Chapter 6

Initial parameters identification in steady-state

Abstract

Once the major elements of the model have been described and integrated, accurate modeling of complex hydrologic systems, such as groundwater flow, often requires the use of numerical models and a robust calibration process to ensure reliable predictions of system behavior. Calibration is a critical step in the modeling process that adjusts model parameters to reproduce observed piezometric level responses. During the calibration process, we attempt to minimize a defined objective function by adjusting the input parameters of the models. In groundwater modeling, the general main parameters that we want to calibrate are either the hydraulic field properties of the aquifer or the hydrodynamical model inputs.

This chapter presents the steady-state calibration process of the mean hydraulic conductivity values, used for the Sequential Gaussian Simulation of the corresponding property, of the sedimentological facies for the SIS and MPS simulations. This chapter also presents the identification of the river's hydraulic properties of the Roussillon model. These parameters are calibrated using a combination of a Monte Carlo approach and a more traditional optimization. Using these methods, we were able to identify parameter sets that minimize the root mean square error (RMSE) between the calculated groundwater levels and the 123 piezometric observations corresponding to the period of August 2012. We find that the relationship between the parameter values and the RMSE is very unstable, with many different parameter sets able to provide a reasonable fit. It appears that small variations in the parameters can really degrade the model outputs, or can lead to the non-convergence of the model. The calibration is conducted for three conceptual geological models: depth-related, SIS, and MPS, which are then compared against each other using RMSE, mean absolute error (MAE), and the continuous ranked probability score (CRPS).

The results show that we get a slightly better fit with the MPS models set. The main result of this chapter is an ensemble of pre-calibrated models that we will use in the following chapter for transient model calibration.

6.1 Introduction

Numerical models are an indispensable tool for studying the behavior of complex systems when the interaction of many components are nonlinear and not easily understood. One of the key aspect for robust simulation in groundwater modeling is a proper description of the system and its various hydrological components. Another key aspect is the description of the internal variability of the hydrodynamical properties of the aquifer. The values of these properties, whether described homogeneously or spatially varying, are often obtained from in situ measurements, interpreted from hydraulic tests, derived from literature studies, or fixed at constant values as a first approximation. In this process, the hydrodynamical properties may contain sampling bias or measurement errors, which may limit the ability of the model to produce reasonable forecasts. The data may also be very scarce and not covering well the region of interest. Therefore, there is a need to adjust these parameters for the system being modeled. This parameter estimation, or calibration, step is often required in most hydrogeological applications. Once calibrated, scores can be calculated to assess the validity of the model.

In hydrogeological modeling, calibration is the process of adjusting model parameters to reproduce an observed hydraulic response. The two main approaches to calibration are manual and automatic calibration, with manual calibration often preceding automatic calibration. Manual calibration is a trial-and-error process in which parameters are adjusted based on the conceptual knowledge of the modeler or as an initial guess to better understand the behavior of the numerical model until the simulated results reasonably match the observed data.

Automatic calibration often uses optimization algorithms to iteratively adjust the parameters and minimize an objective function, which represents the difference between the observed and simulated data. In the context of optimization, an objective function is a mathematical function that defines the quantity to be maximized or minimized by the optimization algorithm. The objective function takes one or more input variables and produces a single output value that represents the quality of the solution. The input variables are the parameters to be calibrated, such as hydraulic conductivity or storage capacity. The output value of the objective function represents the goodness of the fit between the model predictions and the observations. Except for some stochastic approaches that aim at sampling the parameter space, calibration methods generally compute or approximate the objective function at each iteration and estimate the gradient of the objective function to search efficiently for the parameter val-

ues that minimize the difference between the simulated and observed data sets [Doherty, 2015].

The most commonly used optimization methods are nonlinear least-squares algorithms that employ the Gauss-Newton method or the Levenberg-Marquardt algorithm to identify the optimal parameter set. Heuristic algorithms such as the Genetic Algorithm or the Nelder-Mead algorithm are also employed. They are more robust and less prone to be stuck in a local minimum of the objective function.

Automatic stochastic optimization algorithms are another important group of automatic calibration methods used in hydrogeology. These methods are often based on the Monte Carlo method. It involves running the model multiple times with different sets of input parameters that are randomly generated based on statistical distributions assigned to each parameter [Tarantola, 2005]. The output of each run is then compared to the observed data, and the results are statistically analyzed to determine the range of possible outcomes for the model. A very simple approach consists then in identifying the best models from the ensemble. There are more advanced parameter estimation methods based on the Monte Carlo approach, such as the Markov Chain Monte Carlo (MCMC) method. It uses a Bayesian mathematical framework to express the solution of the inverse problem as a posterior probability distribution. In general, that probability cannot be defined analytically and the MCMC method proceeds by sampling the parameter space in an iterative manner. At each iteration, model candidates are accepted or rejected in order to obtain finally a set of models describing the posterior distribution of the parameters. Other approaches, still based on the Monte Carlo scheme, are specifically designed to work for the calibration of categorical fields [Jäggli et al., 2017]. The advantage of the stochastic approaches is that they account for uncertainties and variability in the input parameters, which can lead to more realistic predictions and better decision-making in groundwater management. However, Monte Carlo methods can be computationally intensive and time-consuming, especially when dealing with complex models and large data sets.

One of the main challenges in hydrogeological modeling is how to integrate geological complexity with hydrological processes [Meyer et al., 2018; Blouin et al., 2012; Huysmans and Dassargues, 2009]. This is especially true in the case of regional scale models, where the geological structure is often complex and heterogeneous. In recent years, there have been advances in geostatistical methods such as multiple-point statistics (MPS), which can incorporate geological heterogeneity in a more realistic way. However, few studies have investigated the calibration of regional MPS models for hydrological applications.

The challenge of this work is to develop a calibration methodology that can reconcile the geological complexity, represented by the MPS models, with the hydrological data. While inverse methods have been used for hydrological

model calibration [Linde et al., 2015; Juda et al., 2022], there are very few non-synthetic applications that have used these methods with MPS models, and fewer with a model as complex as the Roussillon aquifer that incorporate many hydrodynamical boundaries. The calibration processes often focus on reproducing the target observation without taking into account the underlying geological structural elements. In this work, we want to develop a calibration methodology that can try to preserve the geological complexity of the MPS fields, while calibrating the hydraulic conductivity parameters to work with the hydrodynamical data of this regional scale model for the reproduction of piezometric observations.

In this chapter, we present how the hydrodynamic fields and river parameters have been identified in steady state for the Roussillon aquifer. As often done for complex models, we divided the parameter estimation approach in two steps. The first, presented in this chapter, corresponds to the preliminary calibration of the hydraulic parameters of the rivers, and the calibration of the mean hydraulic conductivity values of the MPS and SIS facies. This first step uses steady-state groundwater flow simulations to estimate these parameters. The second step, presented in the next chapter, uses transient simulations and an ensemble method to calibrate the hydraulic conductivity and storage fields more locally.

The first calibration approach is focused on the rivers parameters. We need to estimate the conductance of the river bed and the constant river stage. Due to the lack of available observations in the simulation period, these parameters are considered as constant in time, but they vary in space along all the grid cells representing the rivers. The riverbed conductance and the river stage were both calibrated independently and simultaneously using the Nelder-Mead optimization algorithm. The calibration process of these parameters was carried out using the simplest grid model (the depth-related approach), consisting of eight layers. We made the assumption that since most of the rivers are located on the top layer of the grid, the behavior of the calibrated parameters in the Pliocene formation, which is deeper, will not be too dependent on the simulation approach (SIS simulation set, MPS simulation set, or depth-related model), and hence used this last and simplest model.

For the mean hydraulic conductivity of the simulated facies, the SIS and MPS categorical simulations are populated using the Sequential Gaussian Simulation (SGS) method with a constant mean hydraulic conductivity. We calibrate the mean hydraulic conductivity values using a steady-state flow model. This calibration workflow is numerically demanding, involving SGS simulations and upscaling at each iteration. Therefore, it was decided to calibrate these parameters in steady-state to keep the numerical effort manageable. It would have been much more time-consuming if transient simulations had been used. Moreover, by doing a steady-state simulation we can use the steady-state observation set for the calibration approach, which is denser and more homogeneously dis-

tributed in the plain compared to the transient observation set. During this calibration phase, we also calibrate the homogeneous hydraulic conductivity values of the buffer layers of the models, located at the top of the model, between the Quaternary and the Continental Pliocene layer, and at the bottom of the model, representing the Marine Pliocene layer. We use a Monte Carlo approach for this step.

Once these two sets of parameters have been calibrated, this chapter briefly compares the results of the three model sets (depth-related, MPS, and SIS model sets), using the steady-state observation data. We also calculate the ensemble of responses of the MPS and SIS ensemble of simulations. This allows to quantify the uncertainty of these models sets on the prevision. To evaluate the performance of the calibrated models, we used three different evaluations: the root mean square error (RMSE), the mean absolute error (MAE), and the continuous ranked probability score (CRPS), which are used for comparing the output distributions of the stochastic sets against the observation values.

This chapter starts by presenting the different approaches and the workflow that we followed to calibrate the different parameters. The second section presents the results of the different calibration approaches and compares the performance of the calibrated sets in the steady-state simulation. The three sets tested are the depth-related model, the SIS simulation set, and the MPS simulation set. The chapter concludes with a discussion.

6.2 Methods

This section first introduces the target data and objective function, then it presents the two calibration approaches used to calibrate the mean hydraulic conductivity parameters and the hydraulic parameters of the rivers. We first calibrated the rivers parameters, and then used the calibrated values for the calibration of the hydraulic conductivity parameters. Finally, it presents the scores that we use to compare the quality of the models. The boundary conditions used for the steady-state model calibration approach correspond to the averaged values of the transient data, presented in the previous chapter (Chap. 5), averaged over the period of August 2012.

Target data and objective function

The aim of the steady-state calibration step, is to identify the parameters that ensure that the model reproduces as well as possible the 123 piezometric data measured in August 2012. For this purpose, the objective function that is employed in this chapter is the Root Mean Square Error (RMSE). It is defined as the square root of the mean squared differences between the simulated and observed piezometric values:

$$RMSE = \sqrt{\frac{\sum_{i=1}^{N}(\tilde{y}_i - y_i)^2}{N}} \tag{6.1}$$

with $\tilde{y}_i$ the i^{th} piezometric observation and y_i the corresponding i^{th} simulated value, and N the total number of observations. The lower the RMSE, the better the model fits the data.

River parameters calibration

The rivers parameters that we calibrated, are cell-based parameters that follow the path of the actual rivers of the plain. For each one of these cells, a river bed conductivity and a river stage has to be defined. A total of 1'082 cells composed the river sets, for a total of 2'164 parameters to be calibrated. The initial river conductance is fixed at 0.005 m/s. The initial river stage is fixed at 0.5 m in the upper part of the systems, and to 0.7 m in the lower part of the river systems, closer to the coast. This calibration step is performed using the depth-related model, which is the simplest of the three approaches.

To calibrate these parameters, we used the SciPy[9] Python package and the minimize function to find the best fitting river parameters. The SciPy minimize function minimizes a given objective function with optional constraints using various optimization algorithms. The input to the function is the objective function to be minimized, the initial guess for the optimization variables, and the parameters of the different algorithms. The output is a solution object containing the optimized variables and the corresponding minimum value of the objective function. The function uses numerical optimization methods such as gradient descent or the Nelder-Mead algorithm to find the minimum.

We decided to use the Nelder-Mead algorithm for the optimization. The Nelder-Mead algorithm is a direct search method commonly used for optimization problems where derivatives may not exist or may be difficult to compute. It is also known as the downhill simplex method. The Nelder-Mead algorithm is a heuristic algorithm, which means that it does not guarantee to find the global optimum of the objective function. In the Nelder-Mead algorithm, a simplex (a geometric shape consisting of N+1 points in N-dimensional space) is constructed around the initial set of model parameters. The simplex is then modified iteratively by performing a series of reflections, expansions, contractions, and shrinkage, which move the simplex towards the minimum of the objective function. At each iteration, the objective function is evaluated at the simplex vertices, and the simplex is modified based on the results of these evaluations.

[9] https://docs.scipy.org/doc/scipy/reference/optimize.minimize-neldermead.html

This method is relatively easy to implement and is known to be effective for a wide range of optimization problems. In our case, we set the maximum number of iterations to 50 and use the RMSE values as the performance indicator for minimization. The Nelder-Mead initial parameters proposed by the algorithm were kept unchanged. In our specific case, the optimization process is set to minimize the mean RMSE score calculated between the steady-state observation data set, composed of 123 piezometric level measurements, against the corresponding simulated piezometric level of the steady-state model.

This method was selected, due to its simplicity of implementation, and the good results that we get from the calibrated parameters. We also tested other optimization algorithms proposed in the SciPy library, which did not perform better, and did not reach convergence.

Three calibration strategies were tested. The first one was to consider the initial conductance values of the rivers bed as fixed and to calibrate only the river stage elevation parameters. The second test did the opposite, we fixed the river stage and calibrated the conductance parameters. The final calibration, tried to calibrate both the river conductance parameters and the river stages. The initial parameters were fixed based on expert knowledge of the system and were set to represent a general averaged state of the system. By testing different calibration sets, we investigate the best combination of expert knowledge and automatic calibration. Finally, we compare the results of the calibration sets and select the best one as the final parameter for the rest of the study.

Mean hydraulic conductivities calibration

The second calibration step concerns the mean hydraulic conductivity values used to simulate the hydraulic conductivity parameter within each of the categorical facies. Along with the mean hydraulic conductivity of the facies, we also calibrate the homogeneous hydraulic conductivity values of the two buffer layers between the marine extension and the Quaternary, and between the Quaternary and the Continental Pliocene, as well as the homogeneous marine Pliocene layer. This calibration step is repeated twice, once for the MPS approach and once for the SIS approach. The number of calibrated parameters is nine for the MPS approach and six for the SIS approach.

For the calibration of the mean hydraulic conductivity values, we used a Monte Carlo approach. After some preliminary tests, it appeared that the groundwater model is very sensitive to the mean K values, with some models not being able to converge if the K values were too different from the original ones taken from the literature. We therefore designed the Monte Carlo approach presented below to account for this sensitivity. At each iteration, the parameters are only slightly modified by the step values in order to preserve the range of the working parameters. The algorithm is always applied to the $\log_{10}(K)$ values of the hydraulic conductivity values, but will refer to them as the K mean parameters

for the sake of brevity. The method is iterative. Its main steps are:

1. Initialization step: Start with an initial set of mean and constant hydraulic conductivity chosen randomly from a uniform distribution based on first estimated values, described in chapter 4, with a ± 1 $\log_{10}$ intervals.

2. Evaluation step: Evaluate the RMSE of the proposed parameter set. The current values of the parameters are used as input for the SGS simulations to generate the new hydraulic conductivity fields of the categorical facies and are assigned to the homogeneous layers. The steady-state model is then run and the RMSE score is computed to compare the model and the observations.

3. Acceptance step: Starting at the second iteration, decide whether to accept or reject the proposed parameter set. If the RMSE of the new parameter set is lower than the previous one, the new parameter set is kept and used for the updating step. If not, a new parameter set is generated (using the original distribution), and the current parameter set is then randomly selected between the old and the new, with the new having a fixed probability of selection of 0.9 and the old having a probability of selection of 0.1.

4. Updating step: Modify the selected parameter set by drawing random step values for each parameter in a normal distribution centered at 0 and with a standard deviation of 0.05 to avoid too large unrealistic changes in the K parameters. The random steps are added to the current parameter values. The algorithm then goes back to step 2 and repeats the same procedure during 50 iterations. This number of iterations was fixed after some testing, when we observed that the calibration of the model was not that sensitive to the number of iterations and reached acceptable scores. This maximal number of iteration was also fixed to ensure a reasonable computational time.

5. Post-processing step: Analyze the results to evaluate which parameter values are the most satisfying.

The same approach is used for the SIS and MPS parameter sets. This calibration process has only been performed for one MPS simulation and one SIS simulation. It does not cover the ensemble of simulations.

Scores and model comparison

This section presents the various scores used to compare models during the calibration steps. These scores are also used to compare the final un-calibrated model ensembles to the calibrated model ensembles.

There are several scores used to compare models, depending on the type of model and the objective of the analysis. In this work, we used the Root Mean Square Error (RMSE) to calibrate the mean hydraulic conductivity and the river hydraulic parameters. Once the models are calibrated, we calculate the Mean Absolute Error (MAE) to analyze more precisely the results, and compute the Constant Ranked Probability Score (CRPS) between the distribution of simulated values of the stochastic MPS and SIS sets and the true observation values. These different scores are used to evaluate the goodness of fit between the observed data and the model predictions.

The MAE measures the absolute difference between the predicted and observed values:

$$MAE = \frac{\sum_{i=1}^{N} |\tilde{y}_i - y_i|}{N} \tag{6.2}$$

with $\tilde{y}_i$ the i^{th} observation and y_i the corresponding i^{th} simulate value, and N the total number of observation. MAE is less sensitive to the outliers than RMSE. The MAE is used to compare a realization to a set of observations. For the ensembles' comparison, the MAE is calculated for each one of the realizations before comparing the mean MAE of the ensembles.

The last score calculated and used in this chapter is the CRPS score, which can be used to calculate the dissimilarity between two distributions [Gneiting et al., 2007]. The CRPS score can also be used to compare a simulated distribution with a single observation value by assimilating the single value to a step function. In this case, it is defined as the integral between the cumulative distribution function (CDF) of the predictions and the step-function CDF of the discrete observation:

$$CRPS(F, x) = \int_{-\infty}^{+\infty} \left(F(y) - \mathbb{1}(y - x)\right)^2 dy \tag{6.3}$$

where $\mathbb{1}$ is the Heaviside function, which is a step function equal to 1 when its argument is positive and 0 otherwise. F is the cumulative density function of the ensemble of predictions, and x is the observation. The minimum CRPS score is zero and is reached when the prediction is correct with no uncertainty. If the prediction has a small uncertainty and is not biased, the score will be

relatively small. Conversely, if the prediction is biased or the uncertainty is large, the CRPS increases. CRPS is sensitive to both bias and uncertainty. The CRPS score is used to compare the SIS and MPS simulation sets at the end of this initial calibration phase. The CRPS score is used to compare an ensemble value to an observation. For a realization, the mean CRPS score of the observations is calculated. We then compute the mean CRPS score of all realizations of a simulation ensemble to compare the different stochastic approaches.

6.3 Results

This section presents the results of the first calibration step of the Roussillon model, where the river hydraulic parameters, and the mean hydraulic conductivity of the sedimentary facies and the homogeneous conductivity of the buffer layers (the buffer layer on top of the model, the buffer layer between the Quaternary and the Continental Pliocene layer and the homogeneous bottom layer) were calibrated using a steady-state setup. In both calibration approaches, the performance of the models is evaluated by comparing the 123 head observations, which composed the steady-state data based, against the corresponding simulated head levels.

River parameters

As described in section 6.2, three calibrations of the river parameters were performed. The first one aimed to calibrate only the conductance of the river bed, the second one aimed to calibrate only the stage of the river, and the last one aimed to calibrate both sets of parameters simultaneously. The three calibration procedures were performed using the Nelder-Mead algorithm. All three approaches allowed reducing slightly the RMSE but failed to reach the convergence criterion (original one of the algorithm in SciPy), before reaching the maximum number of iterations, demonstrating the complexity of the problem. This also demonstrate that a good simulation fit is not often a one parameter calibration issue, but depends on many complex factors interacting together.

The final scores, RMSE and MAE of the un-calibrated base model and the three calibrated sets, are presented in table 6.1. The calibration approach that only modified the river bed conductance appears to be the best performing one. However, its performance is only slightly better than the other two approaches.

Figure 6.1 shows the calibrated river conductance fields. We can see that the upstream parts of the rivers are the main places where the values have undergone important changes. These zones correspond to complex zones of the system where either little observation is available or where many complex recharge processes and intakes take place. Calibration is therefore likely to be stronger in these zones, which are more sensitive to change.

Table 6.1: Scores of the river calibration approaches compared to the based original model. The scores are calculated using the simulated vs observed head in [m].

Optimization	RMSE $[m]$	MAE $[m]$
Base model	8.49	5.35
Conductance only	5.89	3.86
River stage only	6.17	3.93
River stage and conductance	6.18	4.31

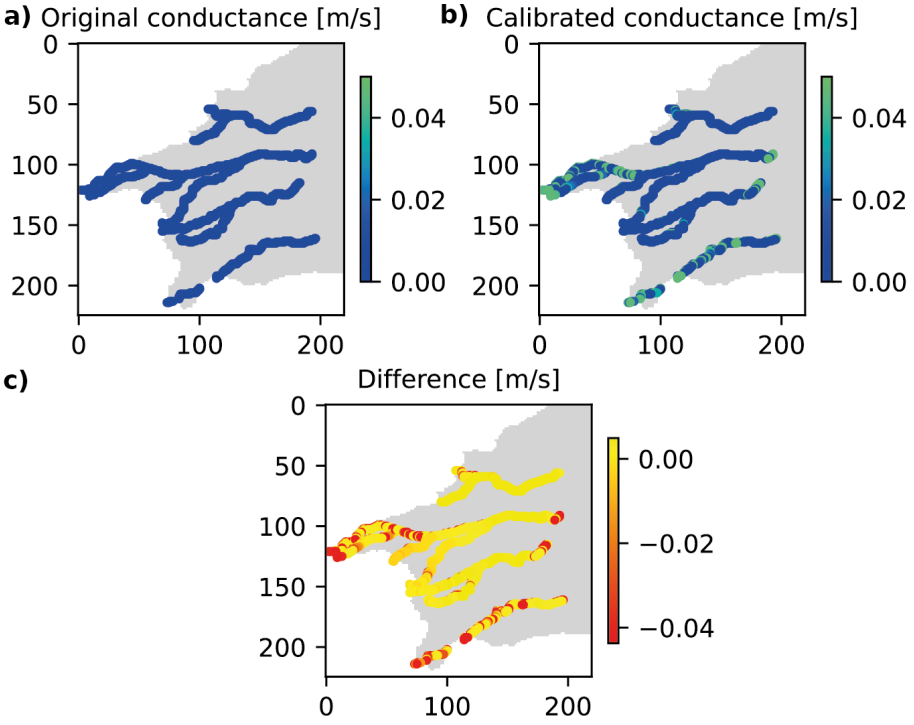

Figure 6.1: Original spatialized river conductance parameters versus calibrated parameters. The upper part of the rivers are the zones subject to the greatest changes.

All the calibrated approaches improved the initial base model using the initial constant parameters. We finally select the parameters obtained from the calibration approach that corrected only the river bed conductance for the remainder of the thesis. This approach gave the best results, and it seems more justifiable to calibrate the river bed conductance, which is a physical parameter that is difficult to measure in the field and is likely to vary rapidly within a river bed, rather than using a potentially unrealistic calibrated river stage

value.

Mean hydraulic conductivities

Sequential Indicator Simulation

Figures 6.2 to 6.4 present the results for the mean $\log_{10}(K)$ of the three simulated facies of the SIS simulations and the three homogeneous layers of the model.

These figures provide a synthetic view of the results of the Monte Carlo method. The figure is divided in sub-figures for each lithofacies. In each sub-figure, a circle or a cross in the graph represents one parameter set. All the parameter sets have been ranked from the best scores (lowest RMSE) to the poorest ones. The horizontal axis represents the rank of one parameter set, 0 being the best. For a given parameter set, and a given rank, a circle represents, along the right side of the vertical axis, the value of the RMSE calculated for this parameter set. For the same parameter set, the cross represents the $\log_{10}(K)$ for a certain facies in the corresponding sub-figure. Finally, the average $\log_{10}(K)$ of the 5 best parameter sets is calculated and displayed as a dashed line in the plot.

Figure 6.2 shows that many different combinations of the mean $\log_{10}(K)$ of the

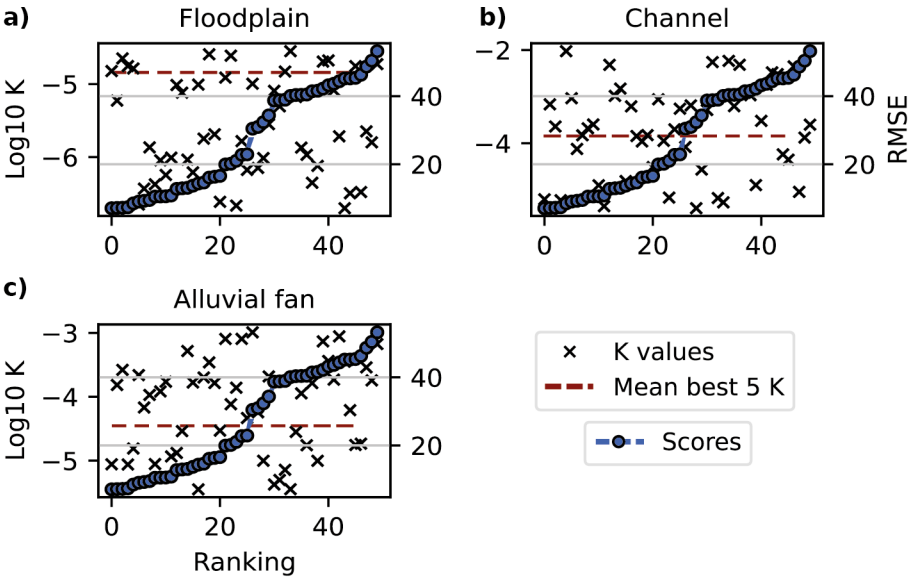

Figure 6.2: $\log_{10}(K)$ values of the Monte Carlo facies calibration approach of the SIS models set. The parameter sets are ranked based on the calculated RMSE between the observed and simulated head values. The red dashed line represents the mean $\log_{10}(K)$ values based on the top 5 parameter sets.

three simulated facies of the SIS simulations produce a score below 10. The best parameters values appear to be centered around the mean best values regarding the floodplain facies. This is not the case for the two other facies, where the best parameters are not centered around the mean best score, indicating that different parameter sets are likely to produce similar results. Looking at the scatter plot (Fig. 6.3) between the $\log_{10}(K)$ mean values and the RMSE, it appears that there is no clear correlation between the scores and the hydraulic conductivity values.

Figure 6.4 shows that similar observations can be made about the parameters of the homogeneous layers. Some parameter combinations are able to reduce significantly the RMSE, but the results are very noisy, and it is difficult to identify a clear combination of parameters that seems to return consistently the best results. Only the bottom layer seems to have preferred hydraulic conductivity values, with the best combination of parameters all being around 10^{-5} m/s.

This initial calibration demonstrates the sensitivity of the SIS model to its hydraulic parameters and the highly non-linear relationship that exists between the model parameters and the model performance. The calibration step can still be considered successful, as we could identify the initial parameters of the transient simulation for the next part of the study, taking the best parameters

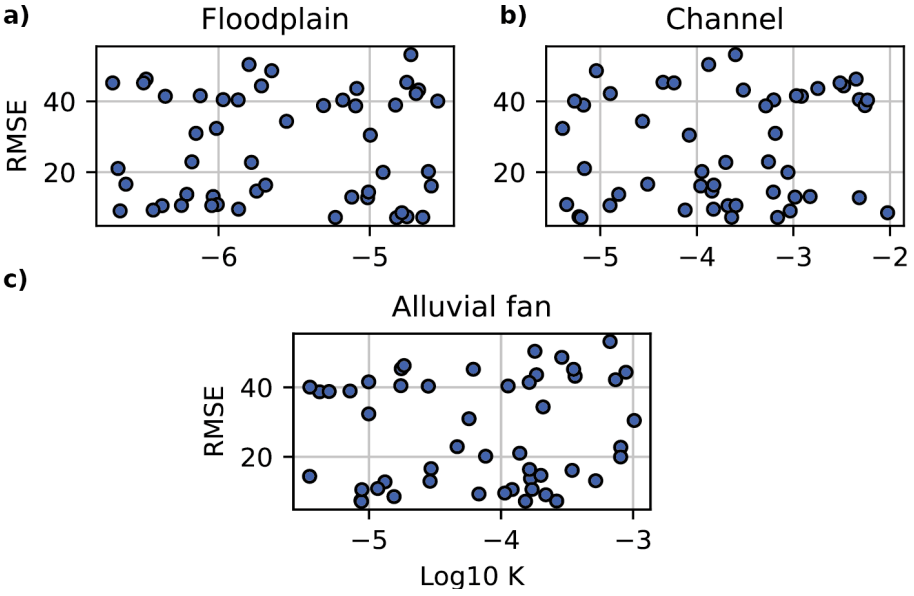

Figure 6.3: Scatter plot of the RMSE scores versus the hydraulic conductivity values of the calibrated SIS models. There is no observable correlation between the scores and the hydraulic conductivity parameters.

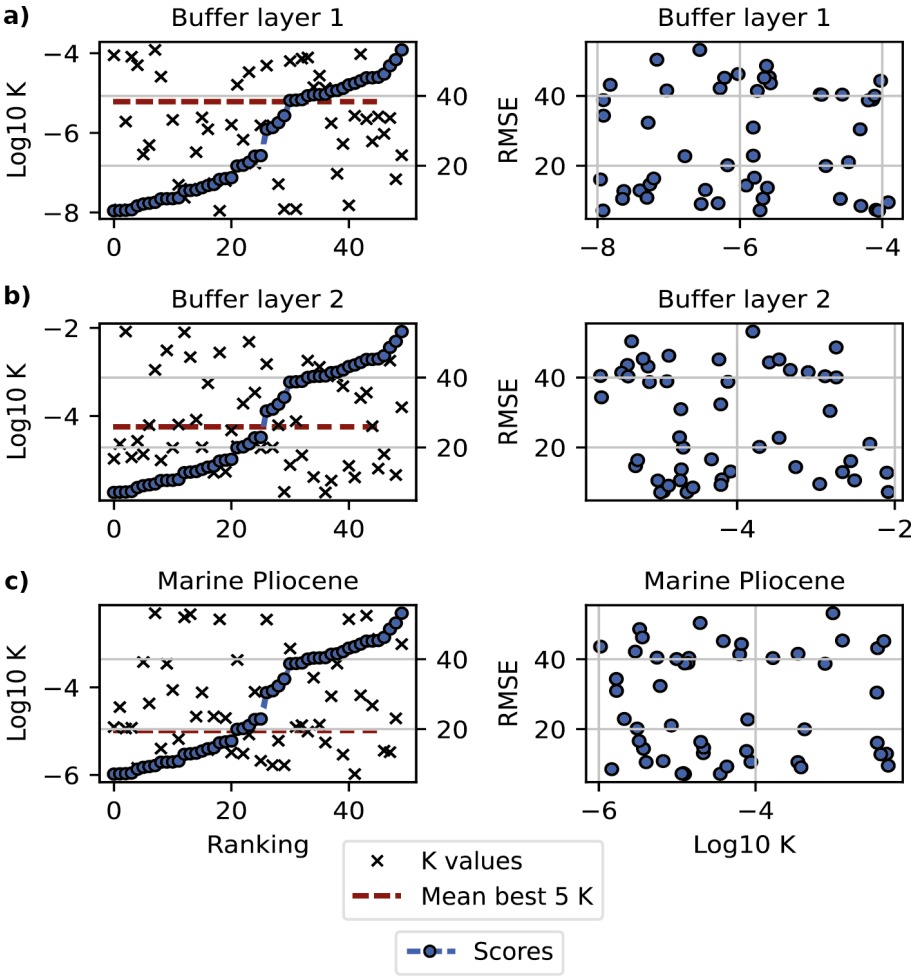

Figure 6.4: $\log_{10}(K)$ values of the Monte Carlo calibration approach of the homogeneous layers of the SIS model set. The parameter sets are ranked based on the calculated RMSE value between the observed and simulated head values. The red dotted line represents the mean $\log_{10}(K)$ values based on the top 5 parameter sets. Only the best $\log_{10}(K)$ values for the Marine Pliocene appear to be more concentrated across the simulations.

set, presented in the supplementary material (App. A.2. Tab. A.2).

Multiple-Point Statistics simulations

Similar to the SIS results, the MPS calibration also produces a wide range of parameter combinations with varying RMSE values (Figs. 6.5 to 6.7). Again, there are many combinations of hydraulic conductivity parameters producing reasonable fits to the data. Globally, the differences between the best and worst parameter sets are smaller as compared to the SIS simulations. Only the mean $\log_{10}(K)$ of the channel facies, and of the marshy deposits seem to be rather centered (Fig. 6.5). However, the corresponding scatter plot of these parameters does not show a linear relationship between the scores and the parameters (Fig. 6.6).

In comparison to the SIS homogeneous parameters, the MPS homogeneous layer hydraulic conductivity parameters of the best sets are slightly more centered around an optimal value (Fig. 6.7). This behavior informs us that the homogeneous layers are an important parameter in order for the model to perform correctly. These layers have more control on the model outputs simulation compared to the hydraulic conductivity parameters of the facies. This can be explained by the fact that the upscaling process mix the hydraulic parameters of the MPS simulations, which alleviate the importance of the hydraulic conductivity parameters of the facies on the control of the simulation outputs. Moreover, this can also inform us that the vertical fluxes, between the layers are an important process for the reproduction of piezometric level.

Overall, the MPS models seem to be less critically sensitive to the hydraulic parameters compared to the SIS simulation sets, with more combinations of parameters producing reasonable simulation results. This calibration step helped to better constrain the model for further work, but lacks information on the best parameter combination and therefore on the best conceptual hydrological model to describe the Roussillon system. The best parameter sets will be selected for the initial parameters of the transient simulation for the next part of the study, which are presented in the supplementary material (App. A.2. Tab. A.3).

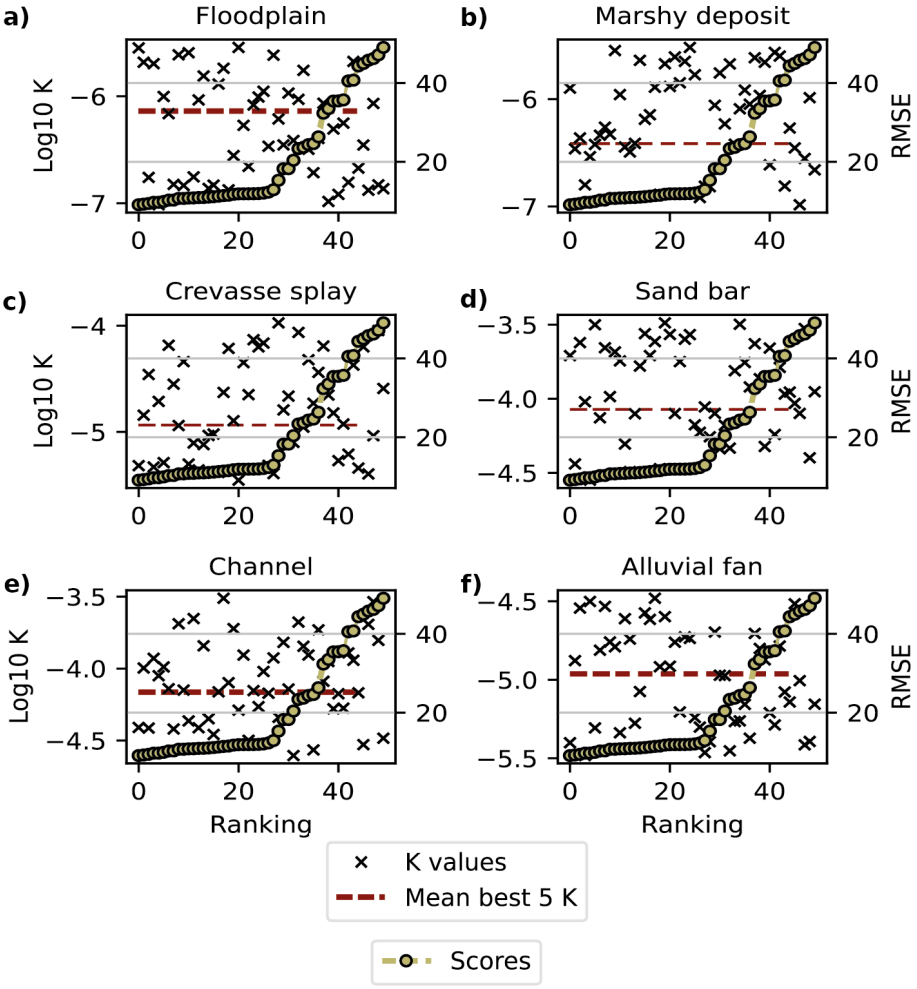

Figure 6.5: $\log_{10}(K)$ values of the Monte Carlo facies calibration approach of the MPS models set. The parameter sets are ranked based on the calculated RMSE between the observed and simulated head values. The red dotted line represents the mean $\log_{10}(K)$ values based on the top 5 parameter sets.

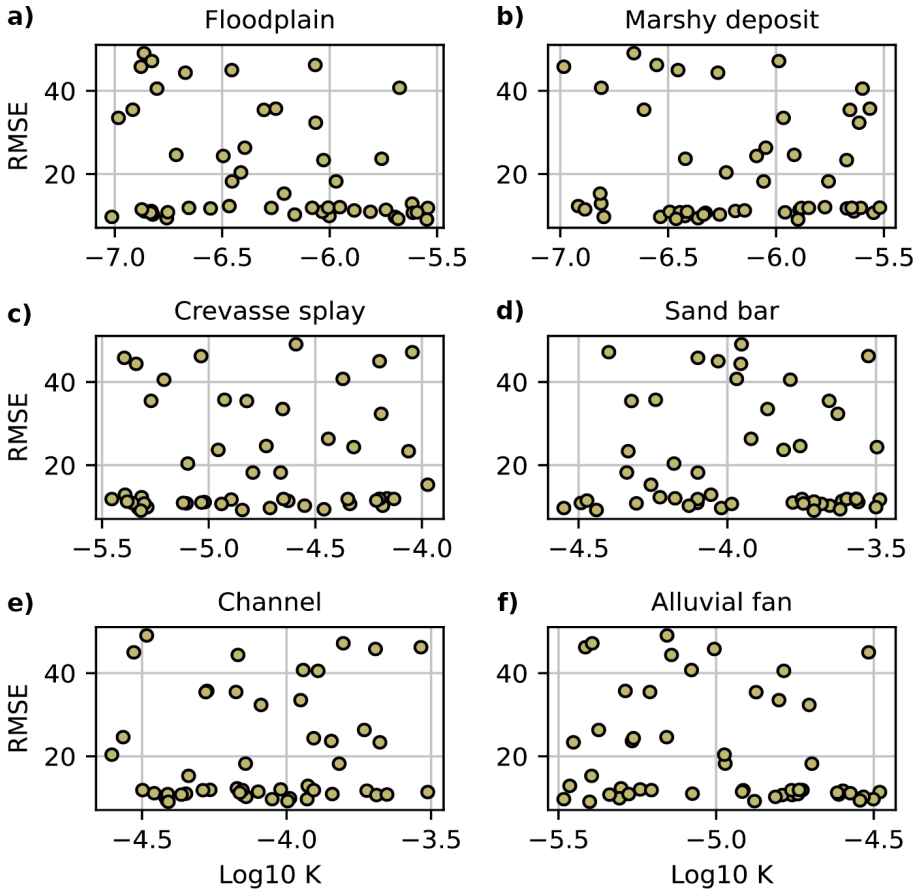

Figure 6.6: Scatter plot of RMSE scores versus hydraulic conductivity values of calibrated MPS models. There is no linear relationship between the scores and the hydraulic conductivity parameters.

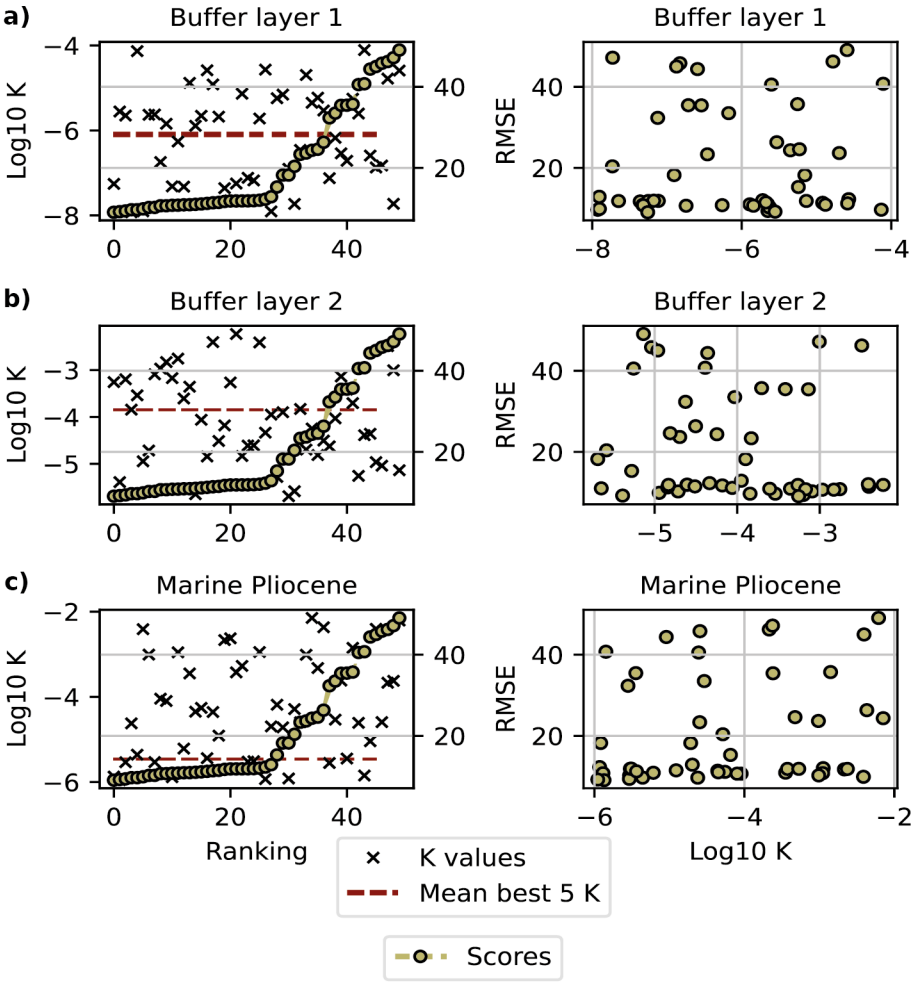

Figure 6.7: $\log_{10}(K)$ values of the Monte Carlo calibration approach of the homogeneous layers of the MPS model set. The parameter sets are ranked based on the calculated RMSE value between the observed and simulated head values. The red dotted line represents the mean $\log_{10}(K)$ values based on the top 5 parameter sets.

Models comparison

Finally, we compare the results obtained with the three conceptual approaches for the hydraulic conductivity fields (depth related model, SIS simulation and MPS simulation) with the available observations. Over the 50 simulations ensemble of the MPS and SIS sets, 43 MPS simulations succeed to converge, while the 50 SIS simulations reached convergence during simulation.

In addition to RMSE and MAE, we compute the CRPS. This allows comparing the statistical distribution of computed head values at a location with the actual measurement. These distributions were calculated using 50 simulations for the SIS and 43 simulations for the MPS approach. They represent the uncertainty of the head values resulting from the uncertainty of the spatial location of the sedimentary facies and uncertainty related to the simulated hydraulic conductivity values (SGS). The two stochastic sets of simulations represent different conceptual descriptions of the system, the MPS set being more complex and characterized by more realistic geological patterns and the SIS set being more blurred.

With RMSE and MAE scores of 5.38 and 3.75 (Tab. 6.2), the MPS model provides the best results of the three tested approaches. The depth-related model and the SIS model are not far behind, and both appear to perform correctly once calibrated.

Both stochastic sets show a low variability of their scores. This can be caused either by the ensemble of simulation having a too large similarity in their spatial patterns' distribution, or by the use of the upscaling step that tends to mix the sedimentological facies together, reducing the variability of the hydraulic conductivity ensemble. Finally, the CRPS scores of the MPS simulation set also indicate that the MPS model distributions are better at representing the observations, compared to the SIS simulation set.

Figure 6.8 shows the scatter plots of the three model sets, comparing the simulated head values to the observations. Looking at these plots, it appears that the three approaches are all performing globally correctly, with most of the

Table 6.2: Comparison of the three model sets using the calibrated hydraulic conductivity parameters and the calibrated stream parameters. The SIS and MPS scores present the mean scores of the sets. The results are calculated using the steady-state simulation setup and the observed head values. The best performing approach is the MPS sets.

Model set	RMSE $[m]$	Std	MAE $[m]$	Std	CRPS
Depth-related	6.03	-	3.91	-	-
MPS	5.38	0.03	3.75	0.02	3.68
SIS	6.09	0.13	4.29	0.04	4.21

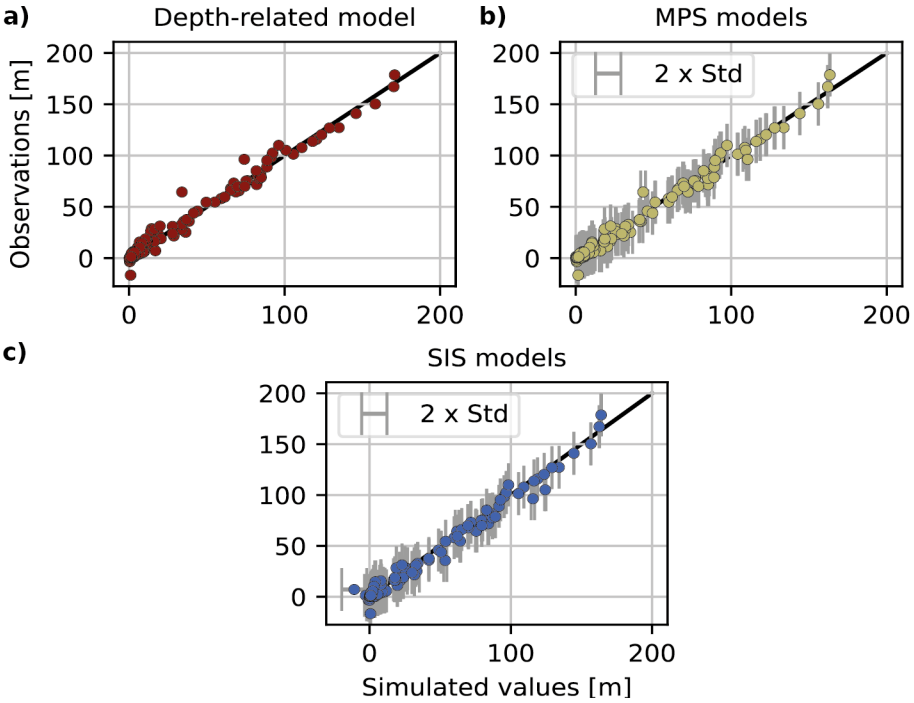

Figure 6.8: Scatter plots of simulated versus observed head values of the three approaches in the steady-state calibration setup. The three approaches correctly reproduce the observed head.

points centered around the diagonal, $x = y$, line. The three plots show the same "wavy" pattern around the values near 100 m, which tend to be too low in the simulations compared to the observations. The last observation concerns the outliers. The SIS and MPS sets seem to be less subject to outliers compared to the depth related model.

We also analyzed the spatial distribution of the differences between observed and simulated head values (Fig. 6.9). The depth-related model and the MPS model show a similar spatial distribution of their maximum error, with the larger errors located at the boundary of the domain. The SIS model shows a different behavior, having some central values that suffer from large errors. These maps also show, for the stochastic simulation, the standard deviation of their simulated head values. It seems that the main variation between simulations within the sets are located around the bad simulated head values. This may indicate that if the model is not performing well at these locations, it is not because it is incorrectly constrained by the simulations, but more likely because it is missing crucial information, or that the conceptual local hydraulic stresses within the hydrodynamical models are not set up correctly.

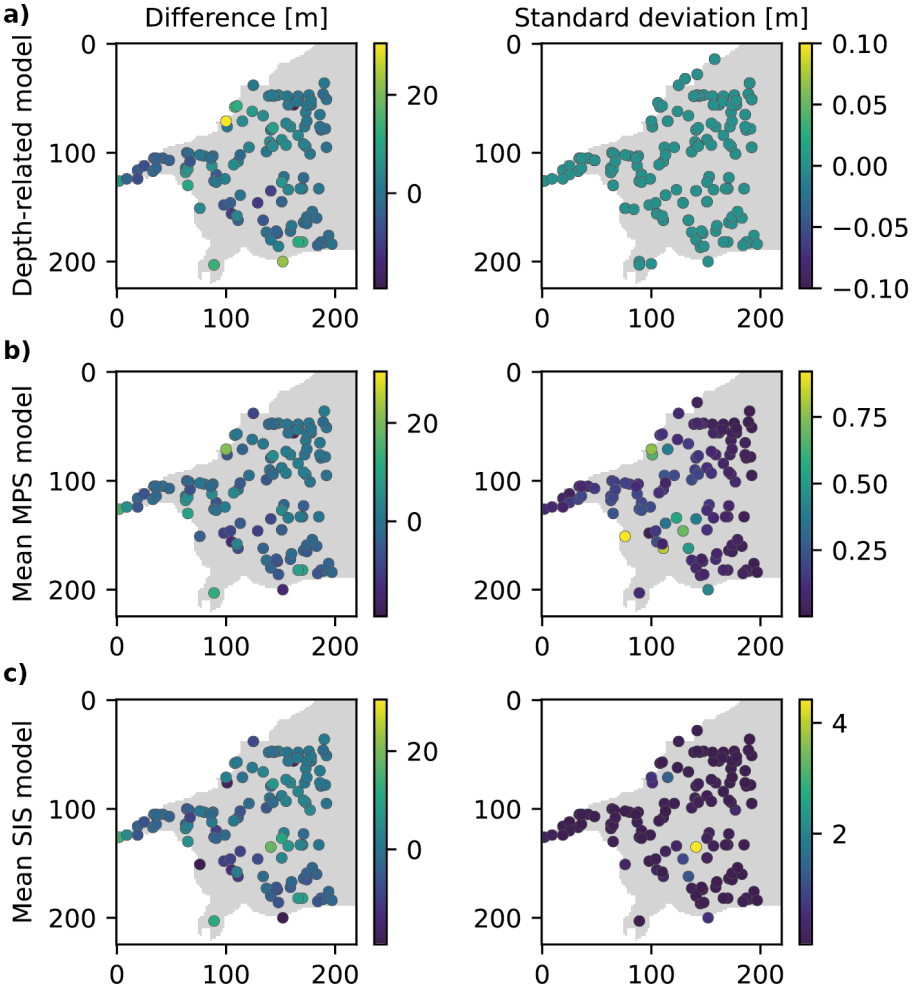

Figure 6.9: Map of the difference between the observed and simulated head values of the steady-state models.

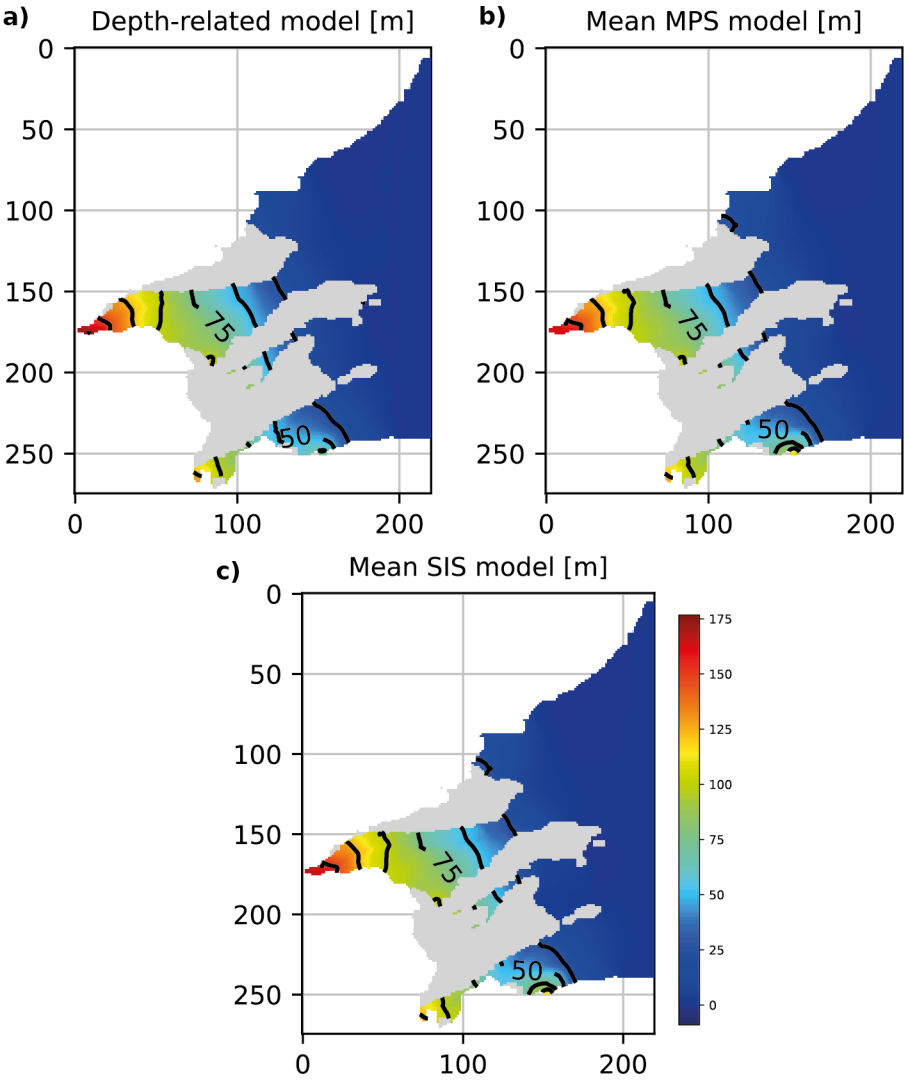

Figure 6.10: Piezometric map of the steady-state calibrated models of the Quaternary layer.

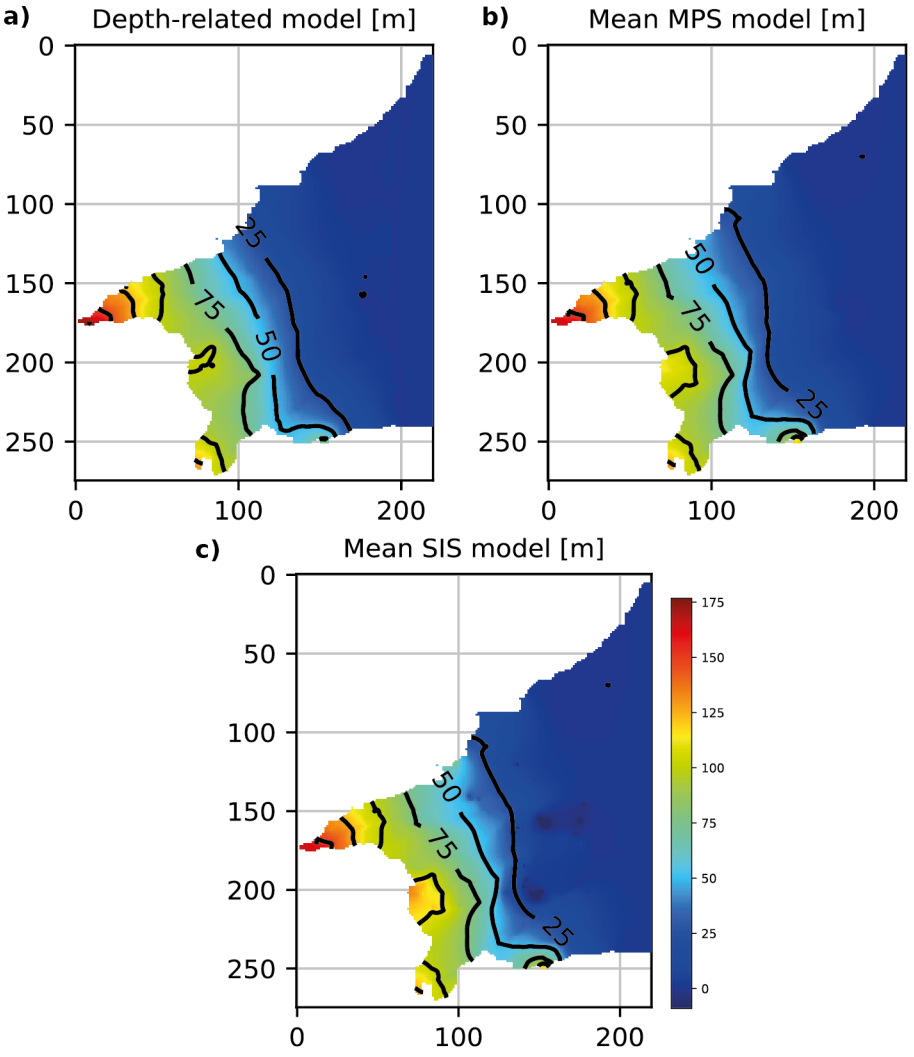

Figure 6.11: Piezometric map of the steady-state calibrated models of the Continental Pliocene layer.

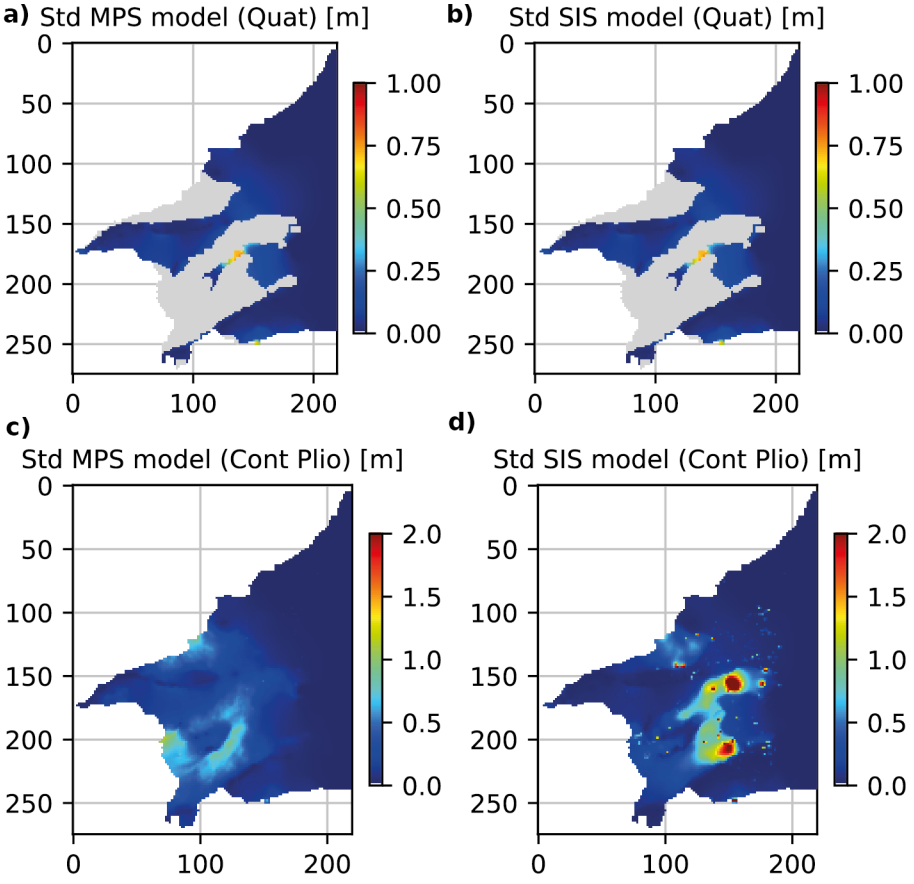

Figure 6.12: Standard deviation map of the MPS and SIS ensembles, for the Quaternary layer (a and b) and for the Continental Pliocene layer (c and d).

6.4 Discussion and Conclusion

This chapter presents the first calibration step conducted on the Roussillon hydrodynamical model. This initial calibration, performed using steady-state simulation, focused on parameters that are numerically demanding to simulate and calibrate, or that are constant over time and therefore can be represented as an averaged state of the system, which is suitable in a steady-state calibration framework.

The steady-state calibration of a hydrodynamic model is an important first step in the initial stages of a study. It requires the selection of an observation period with possibly the most informative system behavior, or at least the most data. A steady-state model is less computationally demanding than a transient model, making it an ideal choice for preliminary investigations. However, steady-state models have limitations in capturing the transient behavior of the system and may not provide a good representation of the system in regions where significant hydrodynamical differences occur between high and low water periods. Therefore, it is important to consider the potential limitations of such models.

In the case of the Roussillon model, the steady-state calibration approach was developed to accommodate the computational cost of the SGS hydraulic conductivity simulations and the upscaling process required to generate the hydraulic conductivity field of the MPS and SIS simulations. The calibration process of these parameters would have been difficult to calibrate in a transient setup due to the computational cost of the SGS simulations. In addition, this steady-state calibration approach demonstrates the good performance of the three tested approaches in reproducing hydraulic heads, in a specific steady-state setup, when compared to historical data.

The calibration of the river conductance parameter is satisfactory given the limited information available on the river systems. For this calibration, we made the assumption that the calibration process of the rivers is not sensitive to the chosen simulation approach (SIS simulation set, MPS simulation set or depth-related model). Since most of the rivers are located on the top layer of the grid, and for the majority of them are more influenced by the Quaternary layer than by the Continental Pliocene layer, which is deeper, we used the depth-related model, which is the simplest model, for the calibration of the river parameters.

The calibrated field has improved the simulations and provided realistic conductance values. The spatial distribution of these calibrated values, especially in the upstream part of the system, reflects the complexity of the river interaction system in this area, which is consistent with the known reality of the system. The fact that the calibrated values differ from the initial values in these zones suggests that they are complex and not well characterized in our

model description. Despite its success in improving the model fit, the calibration process was probably limited in its potential to improve the overall model performance. This limitation was due to the fact that only the river parameters were considered, and that other coupled interactions may have composed and controlled the model.

The Monte Carlo approach used to calibrate the hydraulic conductivity parameters provides a distribution of possible parameter values that reflects the uncertainty in the estimation. This approach has shown that there is no simple relationship between the performance of the models and the mean hydraulic conductivity of the simulated facies for both the MPS and SIS sets. The calibration shows the sensitivity of the models and the influence of the upscaling process, which tends to mix the facies, reducing the potential relationship that could exist between the geological and hydrodynamical models. The Monte Carlo approach informs us about the behavior of the models and provides conductivity values that, once implemented in the hydrodynamical models, work well to reproduce the observed head. However, we used only a maximum of 50 iterations, which is a very low number with respect to the dimension of the parameter space. Despite this, the method gave a reasonable result, and it was not possible to afford for more iterations within the time frame available.

Finally, the comparison of the different assumptions for the hydraulic conductivity fields demonstrates the advantages of using a stochastic approach in hydrodynamic modeling. Not only did the MPS and SIS sets outperform the classical depth-dependent model in the steady state, but they also provided valuable insights into how the models respond and how geological concepts influence the simulation results, and allow the simulation of confidence intervals regarding a specific variable of interest, such as the piezometric head. The MPS approach seems to perform slightly better than the other approaches, which is an encouraging result. By combining these different tools and approaches, an initial ensemble of models could be created and will be used as a starting point for the transient analysis presented in the following chapter.

Chapter 7

Transient-state and calibration

Abstract

This chapter presents the hydrodynamic transient simulations and the first calibration attempt of the Roussillon aquifer using an ensemble calibration approach.The transient models covered the period of 2000 to 2019. This ensemble is based on a depth-related model, and on the stochastic models simulated with MPS and SIS simulations. These models are first run using the pre-calibrated hydraulic conductivity fields (Chap. 6) and the specific storage fields derived from literature values and interpreted pumping test studies (Chap. 4). The simulations are compared with observed piezometric data, and zonal water budgets are calculated for each aquifer unit to evaluate the global state of the system.

Initial results show that the models generally failed to reproduce the amplitude of the seasonal signal, and that local adjustments of hydraulic conductivity and specific storage fields were required to better reproduce the observed signals. Therefore, we attempted to calibrate the models using the Ensemble Smoother Multiple Data Assimilation (ES-MDA) algorithm. The calibration approach, which calibrates pilot points used to interpolate correction coefficient factors, is applied to the hydraulic conductivity and specific storage fields. It results that the calibration approach did not succeed to correctly reproduce the transient water level observation series, and was limited in its applicability due to the sensitivity to convergence of the models. This final study highlights the importance of using transient simulations to understand and manage aquifer systems, but also underscores the need for continued research on calibration techniques for complex hydrodynamic models.

7.1 Introduction

While steady-state simulations represent either a snapshot of the state of a system or an averaged state, transient simulations are used to represent the temporal evolution, often characterized by non-linear time-dependent interactions between the components of the system. For example, precipitation is typically maximum during fall or winter, when crops are at rest and do not require water. During spring and summer, the groundwater is then heavily used and pumped out of the system for agricultural purposes. At the same time, drinking water supplies and industries have a constant need for water throughout the year and touristic activities provoke an intense seasonal increase of water demand. All of these stresses and recharges processes are interrelated and are likely to vary over the years, which makes supplying the evolving population, agricultural and industrial needs challenging. It is in these situations that transient simulations are required to properly describe and understand the aquifer system.

In the context of the Roussillon aquifer, the general trend of water demand is increasing, while precipitation and temperature have been highly variable over the years, with more recent dry and hot seasons observed (Chap. 5). As a result, the overall piezometric level of the aquifer has been decreasing globally in recent decades [Caballero et al., 2022b], and this trend is likely to continue as the population of the region is expected to continue increasing in the next decade. The use of a transient state model could help to understand the different zones at risk during the low water season, or the zones that are more "robust" in terms of their water potential extraction. The potential seawater intrusion is also an important risk for the region and the modeling of the interface zones, or the zero head potential, and the estimation of the global fluxes entering and leaving the system, and their evolution through the years are important asset for local and regional water management of the resource.

This chapter presents the final modeling steps and the transient models of the Roussillon aquifer. We used the pre-calibrated hydraulic conductivity fields presented in chapter 6 and the initial specific storage parameters presented in chapter 4 to construct a first ensemble of transient models covering the period from January 1, 2000 to December 31, 2019. The models are run with a daily time step. The three sets of models were simulated: the depth related, the SIS and the MPS set. These sets are compared to get a first understanding of the model responses in transient state simulations. Moreover, the transient state first simulations demonstrate the influence of the hydraulic conductivity fields, and the modeling approach on the piezometric level simulation in a context of a regional case study. This chapter also presents some preliminary attempts for the calibration of the transient models using the Ensemble Smoother Multiple Data Assimilation (ES-MDA) algorithm.

In this study, we test three conceptual approaches already presented in the previous chapters: the depth-related model, the MPS set, and the SIS set. For the MPS and SIS sets, the hydraulic conductivity fields of the continental Pliocene layers are simulated using stochastic approaches, where the simulated lithofacies have their hydraulic conductivity fields simulated using Sequential Gaussian Simulation (SGS). These fields are then upscaled to match the MODFLOW 6 simulation grid resolution. The specific storage fields of these simulations are created by directly upscaling the categorical litho-facies from the stochastic simulations to the MODFLOW 6 grid. These upscaled facies are then directly populated with homogeneous specific storage values. These upscaled fields exhibit spatial anisotropies, but are populated with global parameters.

The simulated transient piezometric data are compared with the 22 historical time-series available in the area, and presented in chapter 5. For the MPS and SIS simulation sets, the transient state is simulated for each one of the 50 geostatistical fields of the sets. To compare the influence of the hydrodynamical parameters distribution, this chapter also presents the yearly averaged zonal water budgets of the model sets. The zonal water budgets are calculated on defined hydraulic units in the simulation grid, and correspond to the main aquifers. For each hydraulic unit, the flux entering and leaving the unit are calculated at the simulation time step. These first results are important for the understanding of the behavior of the model and the influence of each conceptual hydraulic parameter simulation approach on the evaluation of the global state of the system.

These first simulations show that the reproduction of the piezometric signals is generally not satisfactory. On some observations, the piezometric signal is centered around the mean value and succeeds in reproducing the general yearly trend, but often it does not reproduce the amplitude of the seasonal signal. For some other observations, the seasonal fluctuations are well reproduced, but the mean value is biased. Globally, the three sets of models show similar trends in the simulated piezometric series. However, the zonal budgets of the three sets show different behaviors in their internal flux distributions, and demonstrate the large influence of the geological concept on the final hydrodynamical results. After some manual calibration tests, it appears that the behavior of the system requires local spatial adjustments of the hydraulic conductivity and specific storage fields to better reproduce the observed signals, and that the physical parameters associated with the categorical MPS and SIS simulations could not be calibrated globally.

Following these initial results, this chapter presents some preliminary work on the calibration approach that could be employed to improve the reproduction of the transient piezometric signals. In a first series of preliminary tests, not shown in the thesis, we attempted to calibrate the mean values of the specific storage of the different facies. But adjusting only these mean values did not allow reducing the misfit between the observations and the model. We therefore

decided to try to calibrate locally the hydraulic conductivity and the specific storage parameter fields of the models, while preserving the patterns of the spatial variability resulting from the geological modeling. How to solve this inverse problem with a large and complex model while trying to preserve the geological patterns is a challenge. Among the methods that have been published recently to solve this type of problems, the ensemble Kalman filters or smoother are promising [Xu and Gómez-Hernández, 2016; Bouzaglou et al., 2018; White, 2018; Lam et al., 2020; Todaro et al., 2021]. These methods have been applied, for example, on ensembles of models that were generated by combining MPS simulations to represent channelized structure and SGS simulations to represent the variability of the hydraulic conductivity within the channels [Xu and Gómez-Hernández, 2016]. They have also been shown to converge faster than other methods, even for complex 3D models [White, 2018].

Since the total number of parameters to be adjusted is very large, it is not feasible to correct hydraulic conductivity or specific storage in each cell of the 3D model independently using such ensemble methods. Therefore, we decided to reduce the number of parameters by applying a spatially correlated local correction based on the calibration of a limited number of pilot points. The idea is to estimate 2D maps of correction factors and apply them to the hydraulic conductivity and specific storage 3D parameter fields of the Continental Pliocene layer. The corrections are applied throughout the vertical depth of the layer. The values at the pilot points are adjusted using the Ensemble Smoother with Multiple Data Assimilation (ES-MDA) algorithm. We tested this approach for the calibration of the continental Pliocene layer and the homogeneous buffer layers (upper buffer layer covering the offshore part of the Quaternary layer, buffer zone between the Quaternary and Pliocene layers, and homogeneous bottom layer). Four different combinations of parameters to be calibrated were tested. These preliminary tests showed some improvement in the reproduction of the piezometric signals. However, a satisfactory calibration of all the observed time series could not be obtained. Nevertheless, the chapter presents these results and discusses what could be tried in the future to overcome these difficulties.

The chapter is organized as follows. It begins with the presentation of the transient model setup including the definition of the hydraulic units for the budget calculation. This section introduces the ES-MDA approach and the main steps and strategies of parameter combinations used for the calibration approach. The following section focuses on the presentation of the results of the initial pre-calibrated transient simulations using the depth-related model, SIS, and MPS model ensembles. This section presents the simulated piezometric time series of the approaches, where different metrics are used to rank the approaches, the zonal budget of the aquifer model, and some piezometric maps describing the general state of the system. The following section presents some initial calibration tests carried out following the ES-MDA approaches. The chapter ends with a discussion on the current state of the modeling of the

Roussillon aquifer and the proposed calibration approach.

7.2 Methods

Transient model setup

The transient MODFLOW 6 models are created using the grid and boundary conditions presented in chapter 5. The transient temporal discretization is composed of two simulation periods. The first simulation period is set up as a steady-state run. It is composed of one time step, and is used to initialize the model. The initial steady state period is set up using the average condition of January 2000.

The second period is set as transient. It is composed of 7'304 time steps, corresponding to the 20 years of the simulation, from January 1, 2000 to December 31, 2019. The duration of the time steps is fixed and is set to 86'400 seconds (one day). During this period, the pumping rates, the recharge by precipitation, or the anthropogenic recharge linked to the agriculture and the associated canals are varying daily as explained in detail in chapter 5.

The RMSE, MAE, and CRPS values are computed between the simulation results and the observations, and this for each time step, as presented in chapter 6.

Budget calculations

In addition to the calculated transient piezometric data, the simulations can be used to analyze the water budget between defined hydraulic units. This is an important tool to understand the global relationships between the water units and the main fluxes.

To calculate these fluxes, we used the ZONAL BUDGET software[10]. It computes subregional water budgets using the results from the MODFLOW 6 models and the definition of categorical cell-based hydraulic units corresponding to the MODFLOW 6 grid. A separate budget is computed for each unit by the algorithm. The final budget of a unit defines the inflow and outflow fluxes, summed for all cells in the unit, between the zone and its neighbors for all time steps. Finally, the ZONAL BUDGET also calculates, at each simulation time step, for the whole grid, the "storage in", corresponding to the volume of water stored in the porous media, and the "storage out", corresponding to the volume of water drained from the pores.

[10] https://www.usgs.gov/software/zonebudget-program-computing-subregional-water-budgets-modflow-groundwater-flow-models

For the Roussillon aquifer, nine hydraulic units are defined:

1. The first buffer layer, covering the top layer of the offshore domain.
2. The onshore Quaternary zone.
3. The offshore Quaternary zone.
4. The second onshore buffer layer zone, in between the Quaternary and Continental Pliocene layer, having the same extent of the Quaternary layer in the onshore domain.
5. The second offshore buffer layer zone, in between the Quaternary and Continental Pliocene layer, with the offshore extension.
6. The onshore Continental Pliocene zone.
7. The offshore Continental Pliocene zone.
8. The onshore Marine Pliocene zone.
9. The offshore Marine Pliocene zone.

We calculated the budget for one simulation of each of the three model sets. The use of more simulations could provide uncertainty estimates for the fluxes, but they are unlikely to show much variability in the global fluxes or budget calculations. Moreover, since these models are not calibrated, the budget calculation is used here only as a preliminary tool to compare the influence of the approaches, rather than as a predictive tool that could be used for water management.

The zonal budgets presented in the results correspond to the annual mean water budget calculated over the 20 years simulation period. The mean annual contribution of the different boundary conditions of the Roussillon hydrodynamical models is also calculated.

Ensemble Smoother with Multiple Data Assimilation

To fit the models based on all available piezometric time series, we implemented an approach based on the Ensemble Smoother with Multiple Data Assimilation (ES-MDA) algorithm introduced by Emerick and Reynolds [2013]. Only a brief introduction to ES-MDA is given in this section, more information on the method can be found directly in Emerick and Reynolds [2013].

ES-MDA is a variant of the Ensemble Smoother (ES) algorithm. This method estimates the relationships between state variables and parameters using an ensemble of models, and iteratively corrects a finite ensemble of N_m models using

a stochastic data assimilation approach. The data is then iteratively assimilated multiple times using a Monte Carlo approximation of the Kalman filters. At each iteration, the approach computes the Kalman gain matrix from the experimental covariance matrix between the data and the model parameters, and the data auto-covariance matrix. The Kalman gain is used to update the model parameters in each iteration of the ES-MDA algorithm. Previous studies have demonstrated the success of ES-MDA in various groundwater studies and complex nonlinear inverse problems. However, the method can still be computationally expensive due to the potentially large ensemble of models required to properly estimate the covariance matrices.

To perform the correction at each iteration k, the Kalman gain matrix K is computed from the experimental covariance matrix between the data and the model parameters C_{MD}^k, together with the data auto-covariance matrix C_{DD}^k and the expected uncertainty of the data C_{err}. The Kalman Gain formula is as follows:

$$K = C_{MD}^k \left(C_{DD}^k + \alpha_k C_{err} \right)^{-1}, \tag{7.1}$$

where the parameter α is the noise inflation ratio. To mitigate the problem of inbreeding often observed in ensemble smoother, the parameter α is proposed to be used by Emerick and Reynolds [2013]. The term inbreeding here refers to the underestimation of uncertainty that occurs when the same ensemble is used to compute the Kalman gain (K) and to estimate the error. Emerick and Reynolds [2013] observed that the inbreeding effect can be reduced by increasing the number of members of the ensemble and by using the inflation factor. Emerick [2016] show that α_k must follow this specific relationship:

$$\sum_{k=1}^{N_{iter}} \frac{1}{\alpha_k} = 1, \tag{7.2}$$

with N_{iter} being the number of iterations. It can be chosen constant $\alpha_k = \alpha$ through the iterations as long as the previous equation is satisfied.

The correction of the model parameters, at iteration k, is computed as follows:

$$m_i^{k+1} = m_i^k + K \cdot LM \cdot \left(\hat{d}_{obs,i}^k - g(m_i^k) \right), \tag{7.3}$$

$$\hat{d}_{obs,i}^k = d_{obs} + \sqrt{\alpha_{k+1}} C_{err}^{1/2} z_{d,i} \text{ with } z_{d,i} \sim N(0,1), \tag{7.4}$$

where $\hat{d}^k_{obs,i}$ represents the observed measurement augmented by the inflated noise, and $\hat{d}^k_{obs,i} - g(m^k_i)$ is the Euclidean distance between $\hat{d}^k_{obs,i}$ and the forward model prediction $g(m^k_i)$ of the ensemble member i at iteration k. The noise inflation is proportional to the expected standard deviation of the measurement error multiplied by a random factor following a normal distribution.

Finally, a localization matrix LM is added to reduce the risk of spurious correlations. Spurious correlations can be caused by the fact that ES-MDA approximates the covariance matrix using a finite number of members. This problem can be addressed either by increasing the number of members or by predefining the expected correlation for the algorithm using the localization matrix. In our case, the values of the localization matrix are set to be inversely proportional to the distance between parameters and observations with respect to the pilot point, and are set to 1 for the homogeneous hydraulic conductivity and specific storage values. This localization matrix is computed based on the correlation function introduced by Gaspari and Cohn [1999]. The Gaspari correlation function is defined as follows:

$$R_{GC}(r) = \begin{cases} 1 - \frac{5}{3}\left(\frac{r}{r_c}\right)^2 + \frac{5}{8}\left(\frac{r}{r_c}\right)^3 + \frac{1}{2}\left(\frac{r}{r_c}\right)^4 - \frac{1}{4}\left(\frac{r}{r_c}\right)^5 & 0 \leq \frac{r}{r_c} < 1 \\ 4 - \frac{2}{3}\left(\frac{r}{r_c}\right)^{-1} - 5\left(\frac{r}{r_c}\right) - \frac{5}{3}\left(\frac{r}{r_c}\right)^2 + \frac{5}{8}\left(\frac{r}{r_c}\right)^3 + \frac{1}{2}\left(\frac{r}{r_c}\right)^4 + \frac{1}{12}\left(\frac{r}{r_c}\right)^5 & 1 \leq \frac{r}{r_c} < 2 \\ 0 & \frac{r}{r_c} \geq 2 \end{cases} \tag{7.5}$$

This correlation function uses the Euclidean distance, r, between the parameters (in our case the pilot point locations) and the observations, and a user-defined critical distance parameter r_c, which represents the maximum distance from which a parameter is influenced by an observation. In the case of Roussillon, we set the critical distance to a fixed value of 1km. The localization matrix has the same size as the Kalman gain matrix K.

Proposed calibration approach

The size of the Kalman gain matrix, defined in equation (7.1), is equal to the number of parameters times the number of observations. When the number of model parameters or observations are very large, doing direct computations with such a matrix poses some implementation problems. Therefore, it was decided to reduce the number of parameters by defining a new parametrization of the problem.

The first set of parameters corresponds of the pilot points sets, used to create two bi-dimensional coefficient maps $c(x, y)$: one for the correction of hydraulic conductivity parameters, one for the correction of specific storage parameters. These maps are obtained by simple kriging of the values defined at 45 pilot points. The pilot points are manually placed between the available observation

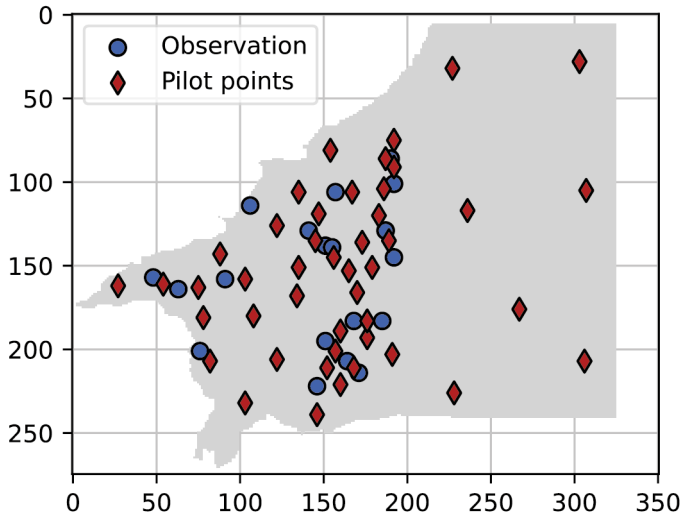

Figure 7.1: Location of the pilot points used to estimate the correction coefficient maps. The pilot points are manually positioned between observation points to correctly impact the observations after the calibration phase.

locations (Fig. 7.1). The location of these pilot points allows for the correction of intermediate zones that are influenced by multiple observations.

The initial value of the pilot points are simulated using a sequential Gaussian simulation method. The mean of the correction coefficient is fixed at 0 with a standard deviation of 0.5. The x and y ranges used for the kriging estimation are set to 4 km in both x and y direction, corresponding to 20 cells in the MODFLOW 6 grid resolution.

Using this approach, the model parameters m_k of the ES-MDA algorithm at iteration k are the vectors of the values of the correction factors at the pilot points. From this small number of parameters, we obtain the 2D maps of correction factors $c_k(x, y)$ at iteration k by kriging the pilot points values using the same variogram model used to simulate the original pilot points values. These maps are then used to correct the 3D physical parameter field $p_0(x, y, z)$ obtained from MPS or SIS approaches and SGS as described in chapter 4. The correction coefficient map is applied to the parameter field as follows:

$$p_k(x, y, z) = p_0(x, y, z) \times 10^{c_k(x,y)} \tag{7.6}$$

Note that the same correction is applied along the z axis at each x and y location.

The second set of parameters used in the calibration process corresponds to the homogeneous hydraulic conductivity and specific storage values of the buffer layers of the models and of the Marine Pliocene layer (three parameters for the hydraulic conductivity and three parameters for the specific storage). The initial parameter sets for these values are selected based on the pre-calibration tests presented in chapter 6. The initial values of the constant parameters are drawn from these mean values, following a Gaussian distribution of standard deviation values 0.25 with respect to the unit of the hydraulic conductivity and specific storage parameters.

Once the new parametrization is defined, we apply the ES-MDA algorithm in a standard manner. At each iteration, the main steps are the following:

1. Based on the pilot point and constant parameter values, computes the 2D coefficient maps and the hydrogeological parameter fields in 3D for all the members of the ensemble.

2. Run all the forward transient flow models. When the forward model converges, save the results. If not, flag the simulation.

3. The simulations that failed to converge are re-simulated using a parameter set randomly sampled from successful simulations. The selected correction parameter is slightly modified using a random value draw from a Gaussian distribution (mean=0, standard deviation=0.05).

4. All the results are analyzed to update the covariances, compute the Kalman gain and update the model parameters (pilot point and constant parameter values).

Finally, we tested this calibration approach on four different parameter sets. The first one considered only the specific storage field of the Continental Pliocene layer and is composed of 45 parameters. The second one considered both the specific storage and hydraulic conductivity fields, it included two 2D correction maps, and is therefore composed of 90 parameters. The third one considered both sets of pilot points and the homogeneous storage values; it is composed of 93 parameters. The last one considered the hydraulic conductivity and specific storage fields of the Continental Pliocene layer, as well as the homogeneous buffer parameters (hydraulic conductivity and specific storage). This set consists of 96 parameters.

The calibration of these four parameter sets has been performed for the three model sets: the depth-related model, the MPS model, and the SIS model (using one MPS model and one SIS model). The calibration process was performed using only a 1-year MODFLOW 6 transient simulation for the forward run. The observation set consists of 5'186 observations. The number of members is

fixed to 60 and the number of iterations is fixed to five, including the initial run.

7.3 Initial transient models results

This section presents the results of the pre-calibrated, 20-years models belonging to the depth-related, MPS and SIS sets (pre-calibrated from the steady-state calibration approach presented in chapter 6). The MPS and SIS sets are initially composed of 50 members derived from the initial stochastic litho-facies simulation presented in chapter 4. These fields used the hydraulic conductivity values calibrated in steady-state and specific storage values extracted from the literature (Chap. 6). All 50 SIS members successfully converged, while only 38 of the 50 MPS members converged. This chapter aims to present the main differences between the three conceptual approaches results.

Global model scores

To get a first idea of the global performance of the models, we calculated the RMSE, MAE, and CRPS values of the three methods based on the reproduction of the piezometric observation time series.

Table 7.1 shows the calculated scores of the three approaches (the SIS and MPS scores are calculated as the mean of their ensemble of simulations). It appears that the depth-related model and the MPS sets perform best and are close to each other, with the depth-related RMSE scores being smaller than the mean of the MPS ensemble, but with the MAE of the MPS sets being smaller. The SIS sets appear to be less reliable based on these results. Between the two stochastic methods, the MPS performed the best, as indicated by its lowest CRPS scores. These scores are global and do not provide detailed information about the local performance of the models. It is even more difficult to interpret these global scores, since the simulated head varies from 1 m close to the coast to more than 150 m up in the Têt valley.

Table 7.1: RMSE, MAE and CRPS values of the three simulation approaches, calculated for 20 years of transient simulations.

Model set	RMSE [m]	Std RMSE	MAE [m]	Std MAE	CRPS
Depth-related	6,10	-	3,63	-	-
MPS	6,24	0,33	3,56	0,13	3,42
SIS	7,34	0,19	4,93	0,06	4,80

Piezometric time-series

After calculating the global scores for the three approaches, we are now interested in comparing the influence of these approaches on the local piezometric time series reproduction.

Eight selected observation time series are shown in figure 7.2, together with the depth-related simulated piezometric time series and the mean MPS and SIS time series. The complete set of observations and simulations are presented in the supplementary material (App. A.3, Figs. A.1, A.2, A.3, A.4, A.5, A.6, A.7, A.8, and A.9).

Different observations can be made from figure 7.2:

- The simulated piezometric time-series show similar types of responses such as seasonal variations, trends, or reactions to high recharge events for the three approaches (blue, purple and red curves). However, these approaches also show clearly different behaviors, with different mean values or different amplitudes of the variations (see for example obs. 0 or 32). The three types of models react consistently to the boundary conditions but produced different piezometric signals.
- Since no calibration was done, it is not surprising that none of the approaches reproduce accurately all the observed data (in orange for the quaternary aquifer or in green for the Continental Pliocene aquifer). However, for some locations the simulated heads are close to the observed data (see for example the results of the depth related model in obs. 29).
- The simulated piezometric levels are sometimes globally shifted from the observed data. For example, in observation 28, the three approaches overestimate the mean water level by around 5m. This shift can be positive (obs. 28) or negative (obs. 1).
- In some locations, the simulated levels reproduce well the amplitude of the signal and its seasonal variability, even if the mean value is shifted (e.g. observations 1 or 6).
- In some other locations, the simulated signals show trends that are completely different from the observations. For example, in obs. 1, the measurements show that the piezometric level is rather stable over the 20 years of observations, while all the models show a systematic rising trend. This type of error is probably caused due to a problem with the initialization period of the transient state that is not representative of the averaged state of the model on these locations.

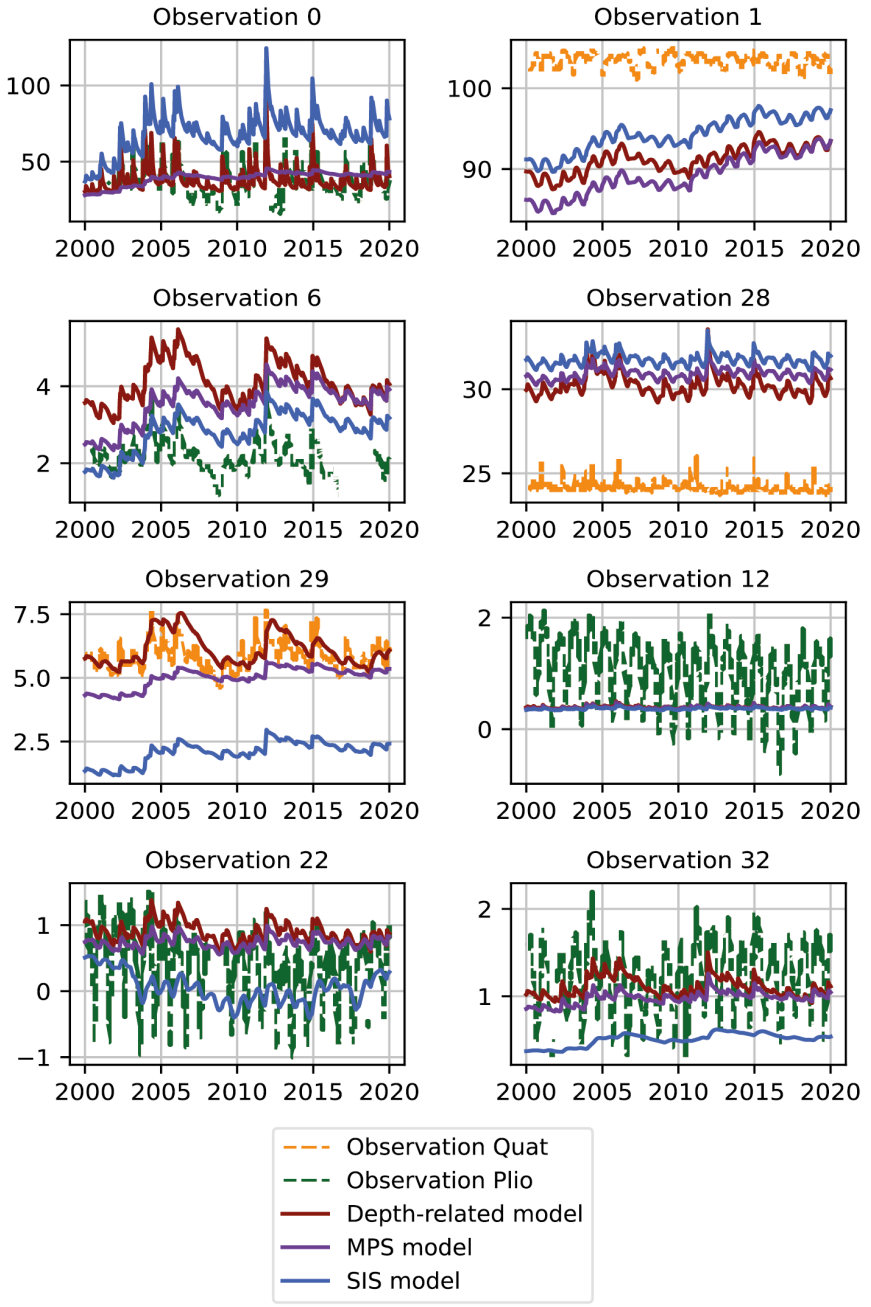

Figure 7.2: Piezometric transient data series of selected observations and the corresponding simulations of the three model sets. The MPS and SIS simulated series correspond to the mean simulated values of the ensemble of each method.

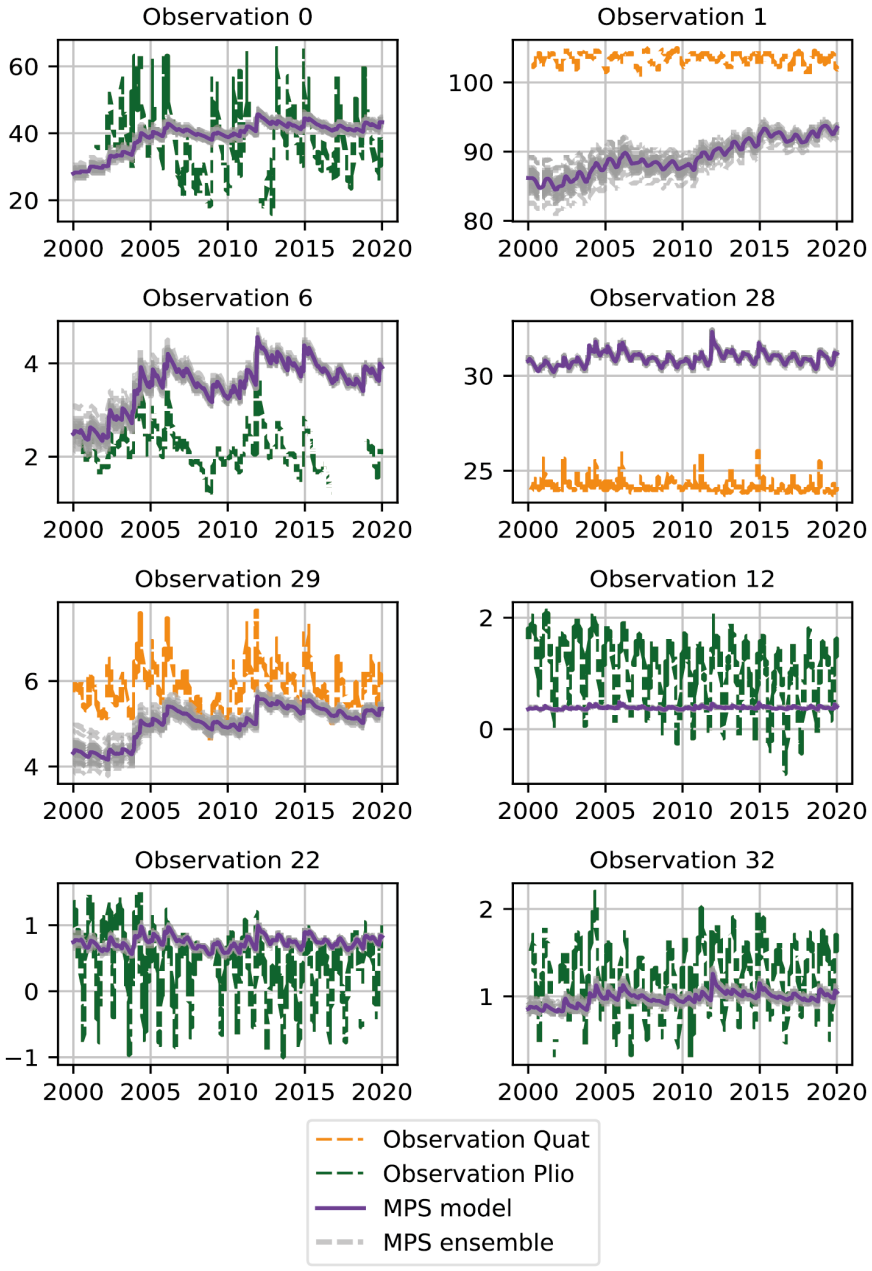

Figure 7.3: Piezometric transient data series of selected observation points for the MPS ensemble models. The models are derived from the ensemble of categorical MPS litho-facies simulations (Chap. 3).

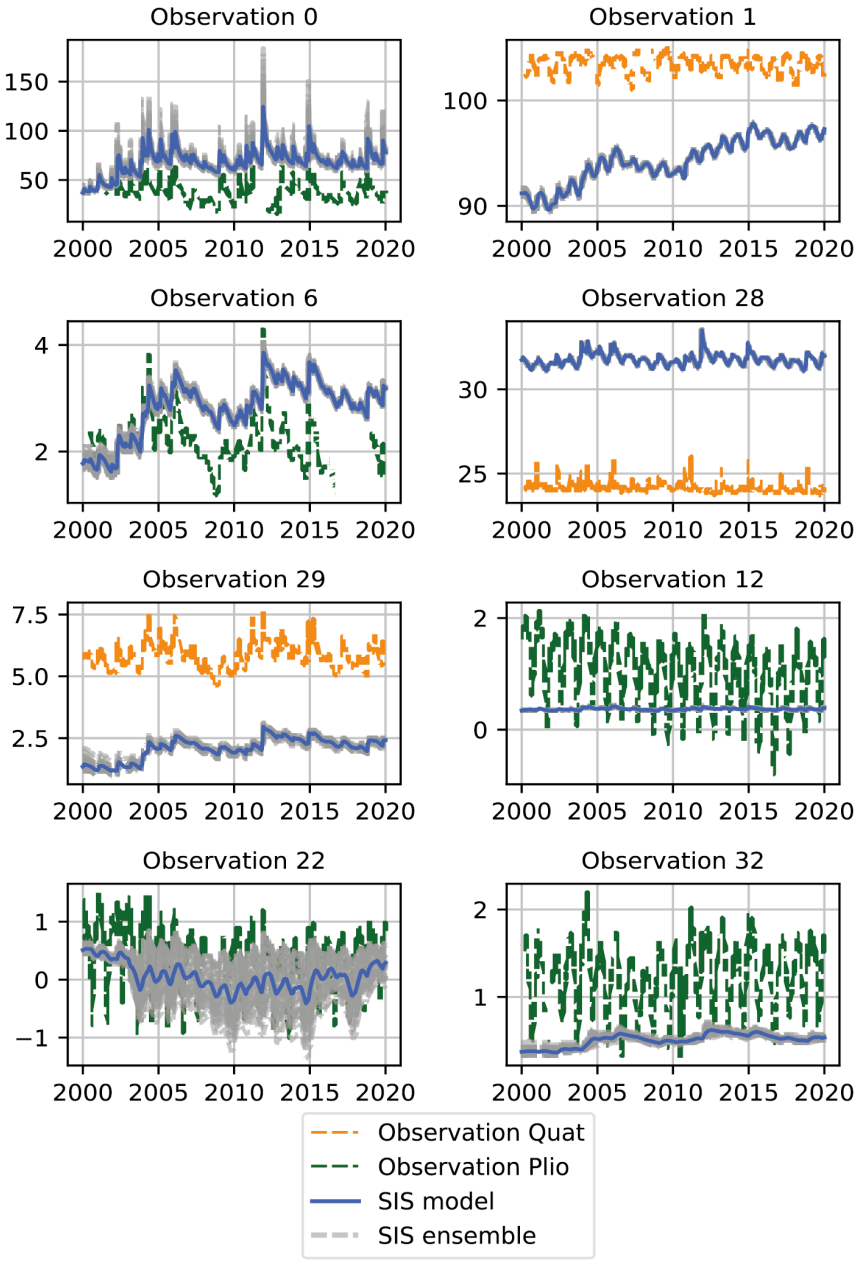

Figure 7.4: Piezometric transient data series of selected observation points for the SIS ensemble models. The models are derived from the ensemble of categorical SIS litho-facies simulations (Chap. 4).

In summary, these results show that the initial transient models do not seem to suffer from a simple and systematic type of error that would be visible on all the piezometers. The global dynamic of the aquifer seems to be at least partly captured by the model. But locally, the models are not accurately reproduced. Based on these observations, it seems that the model mainly needs to be adjusted at a local level.

If we look at the variability of the responses computed with the MPS and SIS ensembles of simulations, created from the ensemble of litho-facies simulations, respectively presented in figure 7.3 and figure 7.4, we see that these ensembles do not cover a wide range of piezometric levels. Furthermore, the observed data often do not fall within the range of simulated values. The SIS ensemble tends to be characterized by a larger variance between its members compared to the MPS ensemble on most observations. This lack of variability within the ensemble my lead to difficulties later in the ES-MDA calibration.

Zonal budgets

We now present the water budget distributions for the three approaches. We used the ZONAL BUDGET software to calculate the global volumetric fluxes in and out of the hydraulic units of interest.

Figure 7.5 shows the mean annual volumetric fluxes for the three tested approaches. Note that we used only one MPS and one SIS simulation for this zonal budget analysis. First, we observe large differences in the internal flux distribution between the three model sets. While the piezometric transient analysis shows rather similar behaviors for the three approaches, the zonal budget analysis shows that the internal fluxes of the depth-related approach are almost two times larger than the internal fluxes distribution of the SIS model. The total volumetric flux exchange of the MPS model are intermediate. The three approaches show a similar relative distribution of fluxes between the different hydraulic units, and it is mainly the total amount of fluxes going in or out of each units that seems to scale between the three approaches. This difference of internal fluxes is not related to the prescribed boundary conditions of the system, or to an anomalous behavior of a prescribed fixed head condition, as shown in figure 7.6, which compares the mean annual input and output fluxes for each boundary condition and for the three approaches. All three mean annual budgets are similar and are not characterized by extreme behavior of a specific fixed hydrodynamical component.

The differences in the distribution of the internal fluxes between the three approaches can therefore be explained by their different hydraulic conductivity and specific storage parameters, within the Continental Pliocene. It is interesting to note that two approaches such as the MPS and the depth-related approach, which produce reasonably similar piezometric results, have such an important difference in their internal flux distribution. This result is impor-

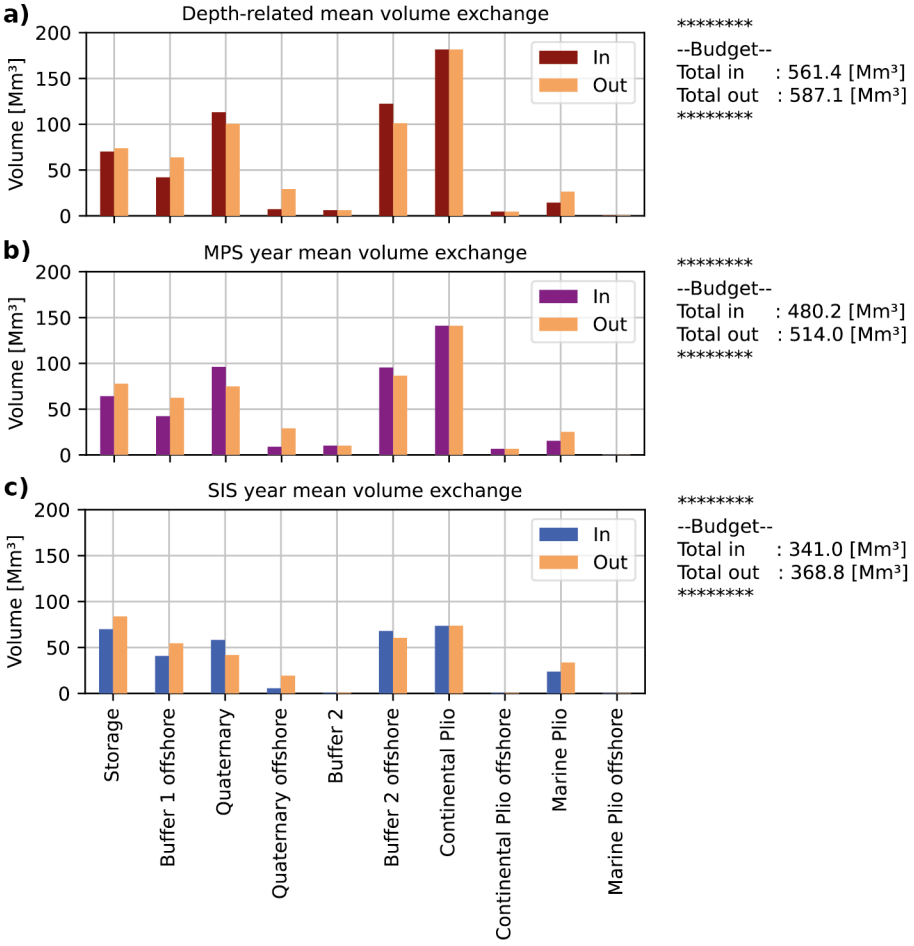

Figure 7.5: Mean annual zonal volumetric exchanges, going in/out of the main hydraulic units.

tant because the internal fluxes between the aquifer hydraulic units can affect possible seawater intrusion in the context of coastal aquifers.

These initial results demonstrate the sensitivity of the global flux estimation on the initial geological concept and hydraulic parameters simulation approaches.

Piezometric maps evolution

Finally, even if the piezometric data have not been calibrated and therefore suffer from some bias on different locations, it is interesting to analyze the behavior of the regional model. We first present with figure 7.7, and 7.8 the simulated piezometric map of the Quaternary and Continental Pliocene lay-

ers, for April 2019 (corresponding to the high water level period). The same piezometric water level maps, for August 2019, corresponding to the lower water period of the model, can be found in the Appendix section A.3 in figure A.10, and A.11. We can see from these maps, that while the quaternary piezometric level appears to have a similar piezometric level, this is not the case for the Continental Pliocene layer of the three approaches. Influenced by the litho-facies simulations, the MPS and SIS models present more important piezometric water level than the depth-related model. This is particularly visible in the upper-river part of the model, and in the west part of the model. These differences of the piezometric level are probably due to the difference of the hydraulic conductivity and specific storage fields, that are directly linked to the facies simulations.

We are also interested in the long term evolution of the system. To quantify

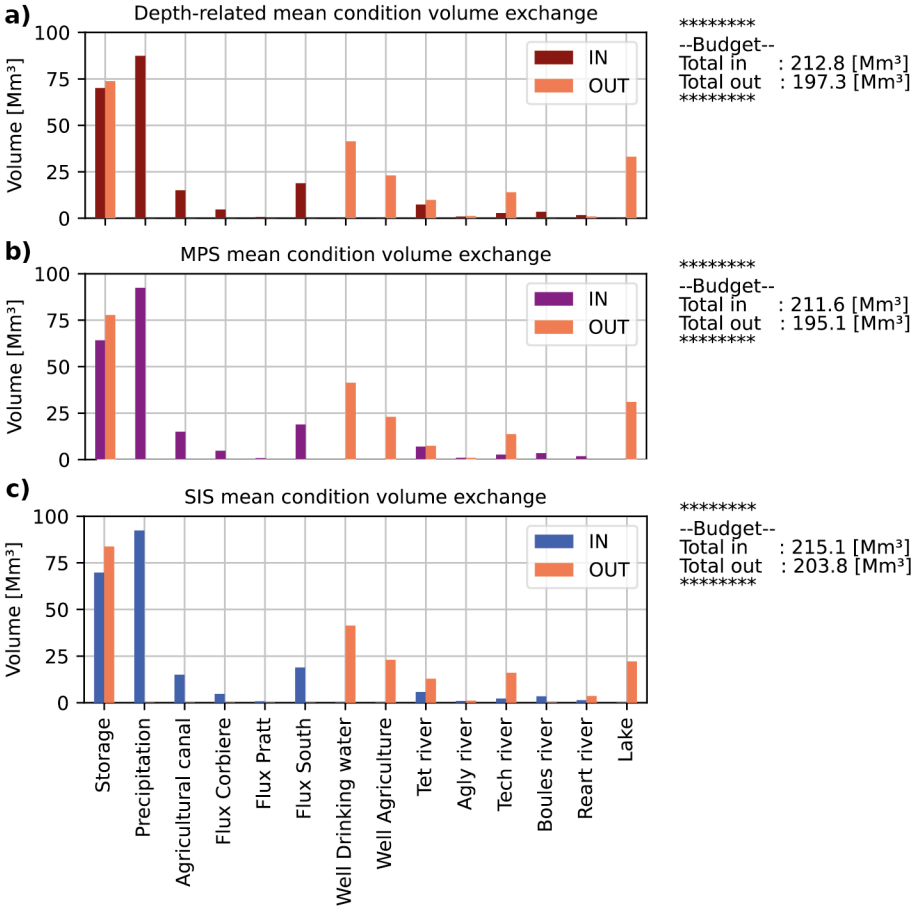

Figure 7.6: Mean annual boundary condition exchanges.

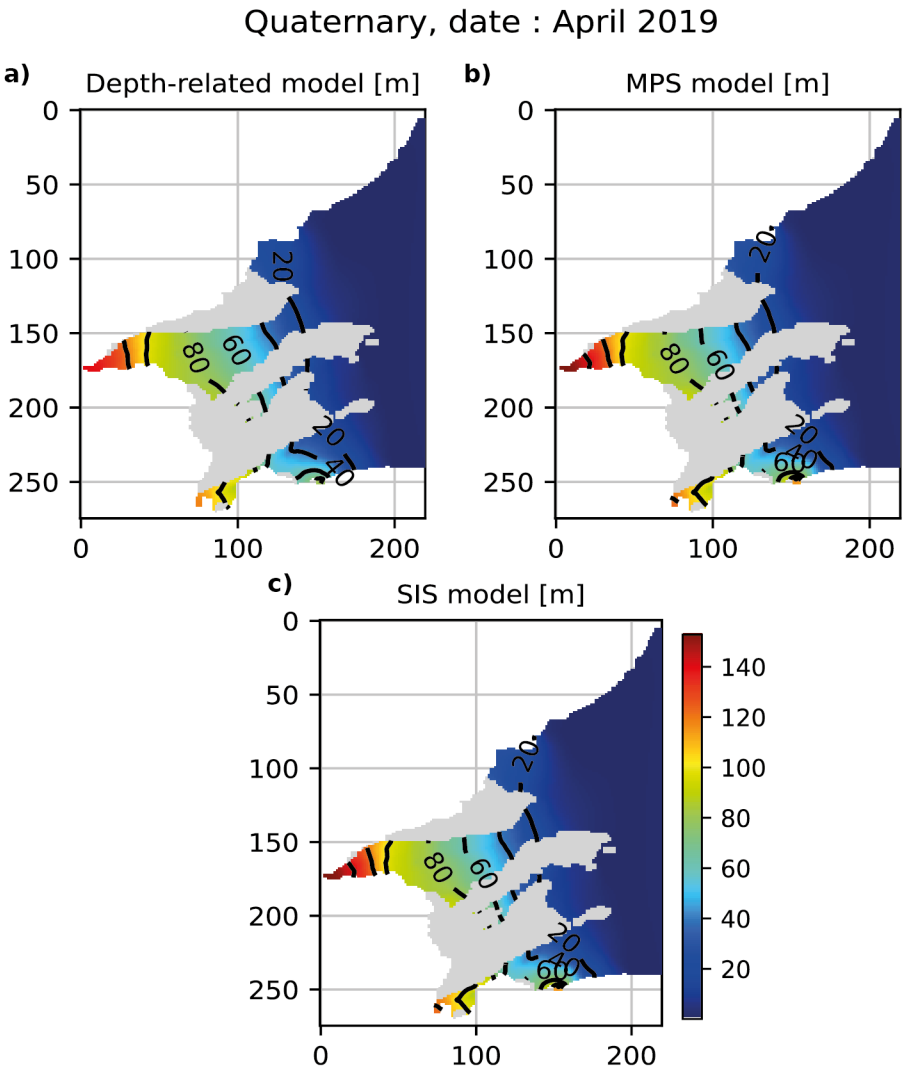

Figure 7.7: Piezometric water level map of the Quaternary layer for April 2019.

this, we simply computed the total difference between the beginning and the end of the simulation period (2000 to 2019). We calculated the difference of the piezometric map for the Quaternary and Continental Pliocene layers, for two months of the year, April and August, corresponding (from the observation) to the highest and lowest piezometric level periods.

The Quaternary piezometric difference maps (Fig. 7.9), show an increase in piezometric level of about 0.8m. There is not much difference between the high (Fig. 7.9) and low water maps (A.12, in Appendix A.3). The main increase in

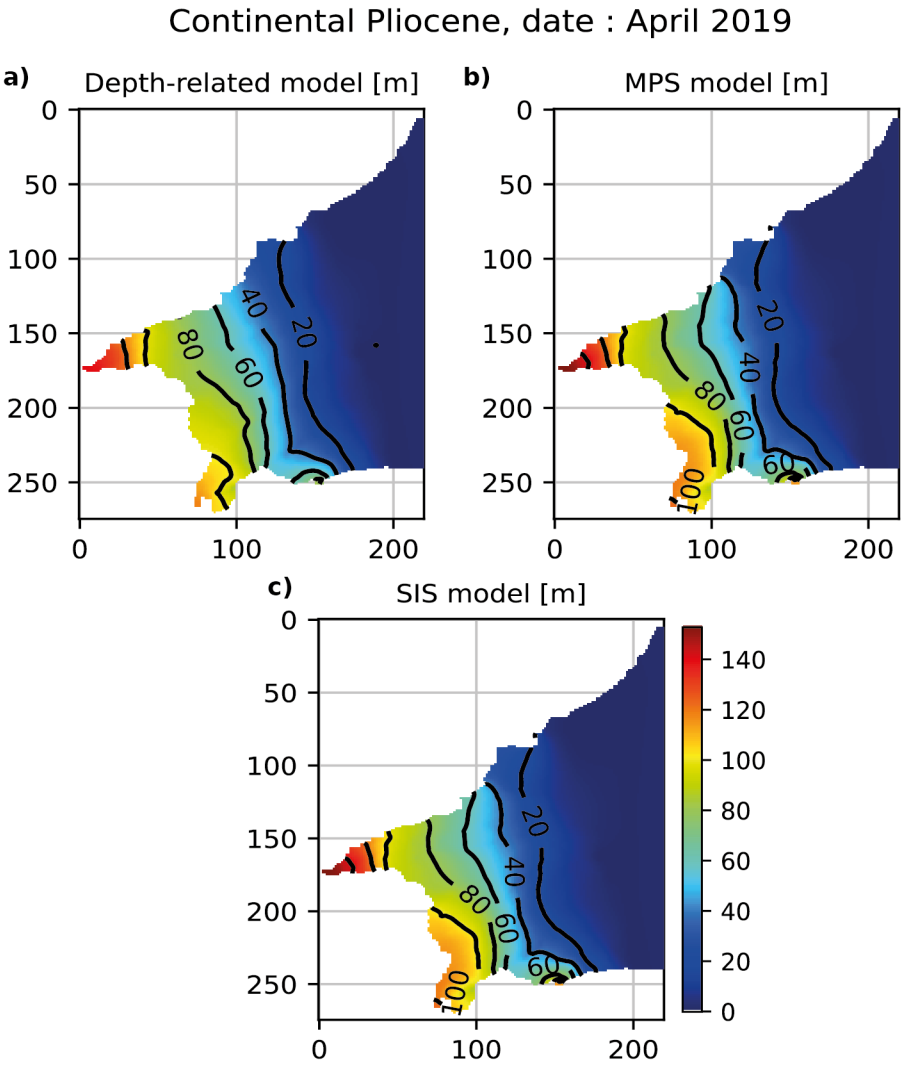

Figure 7.8: Piezometric water level map of the Continental Pliocene layer for April 2019.

water level in both cases seems to be located in the upper part of the plain, along the Tet River valley. The MPS and SIS simulations show a more significant increase in local water levels compared to the depth-related approach.

Regarding the evolution of the piezometric level in the Continental Pliocene layer, we observe (Fig. 7.10) a greater difference between the depth-related model and the MPS and SIS models. All three models show an increase of the global water level in both high (Fig. 7.10) and low water periods (A.13,

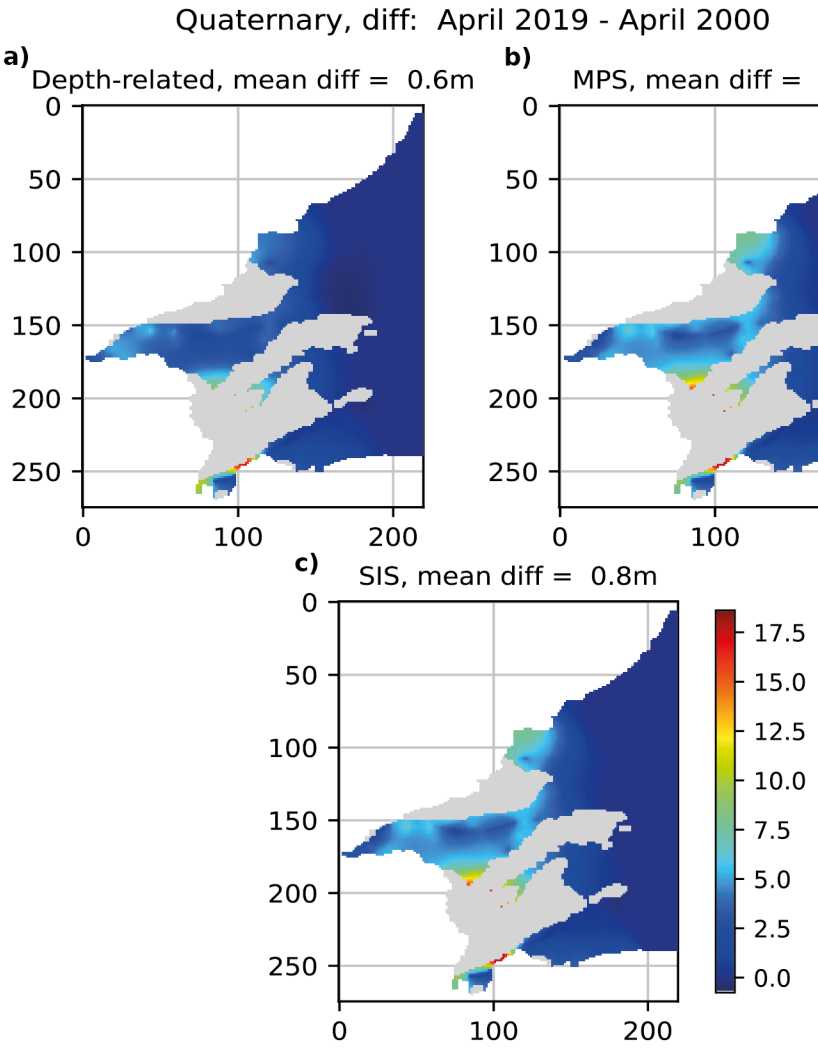

Figure 7.9: Evolution of the piezometric water level of the Quaternary layer, between the simulated piezometric water level of April 2000 and the simulated piezometric water level of April 2019.

presented in Appendix A.3).

The piezometric level of the Continental Pliocene aquifer level has increased by 1 m in average for the depth-related model and by 2 m for the MPS and SIS models (Fig. 7.10). Furthermore, two zones appear to be characterized by unexpected and much larger increases, one in the northern part of the model and one in the south-western part of the models. These two zones are present in all three models, but are more visible in the SIS and MPS models.

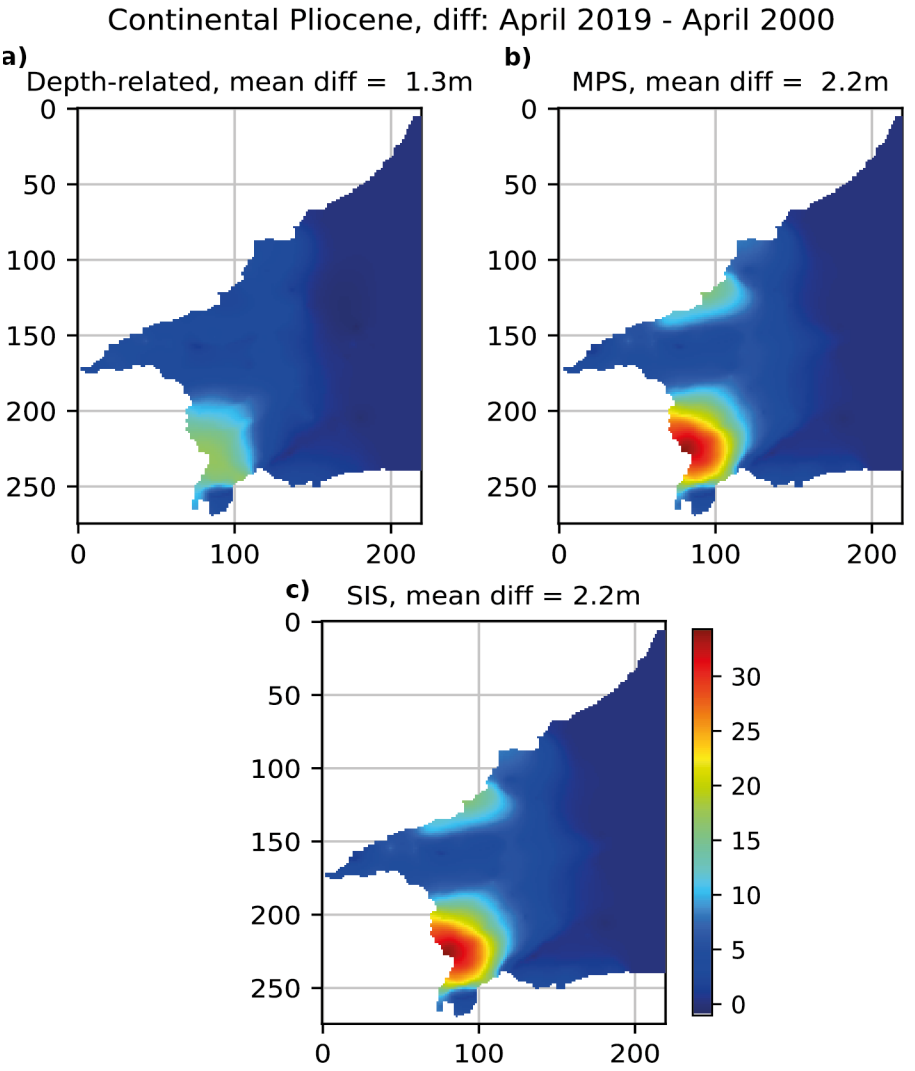

Figure 7.10: Evolution of the piezometric water level of the Continental Pliocene first layer, between the simulated piezometric water level of April 2000 and the simulated piezometric water level of April 2019.

This specific water level increased, calculated between two snapshots of the simulation model, could be simply explained by the recharge from precipitation that was at a higher level in 2018 and 2019, compare to the year 2000, or by a decreased of the volume of drinking water pumped out in this zone.

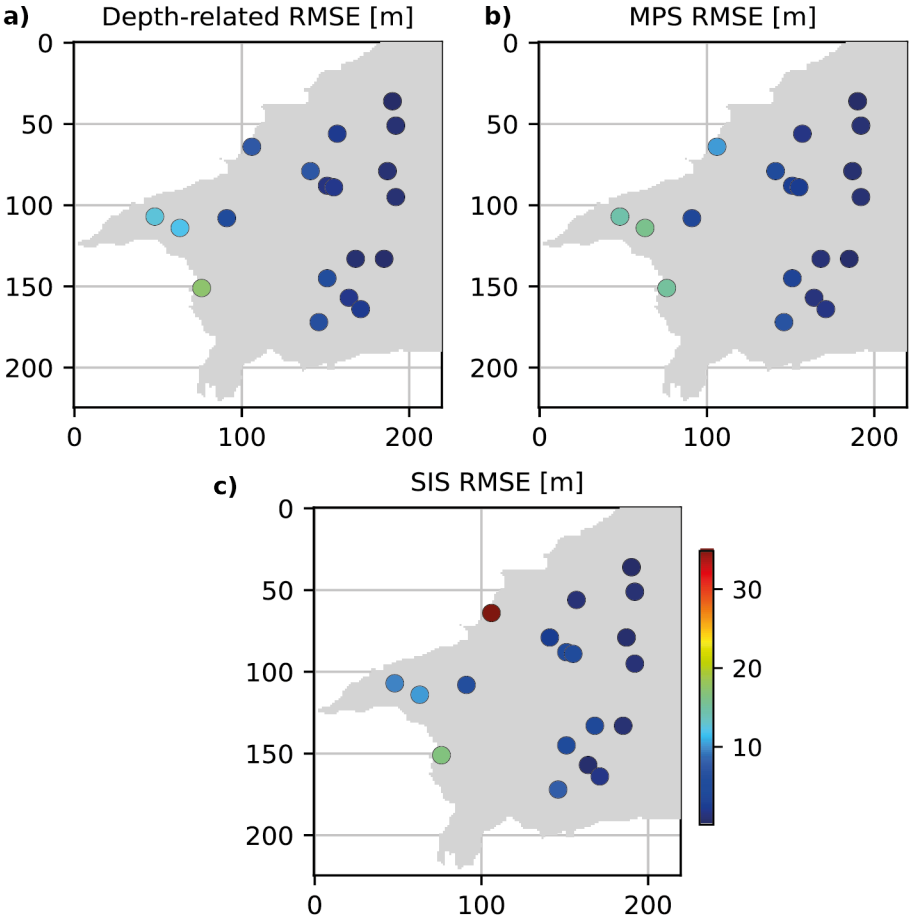

Figure 7.11: Root Mean Square Error (RMSE) calculated for each method (before the calibration).

These maps confirm the trends that were visible in the simulated time series at several locations, as shown for example in Fig. 7.2. Globally, the modeled piezometric levels have a tendency to rise while the observed piezometric levels do not show this trend and on the opposite are slightly decreasing. This issue is discussed more in detail in the discussion section of this chapter.

Finally, the largest abnormal rise of the piezometric level in the south western area is located in a place where the model is very poorly constrained. It is a zone that is not well described in the conceptual model of the Roussillon aquifer, having only one observation point located nearby this area (Fig. 7.11). Moreover, this zone is not constrained by boundary conditions such as pumping wells and therefore its characterization is highly uncertainty. Finally, this zone is characterized by the presence of alluvial fan facies in the stochastic

simulations, which, if incorrectly simulated, could have a large impact on the simulated water level.

7.4 Es-MDA calibration tests

This final section presents the results of the first attempts to calibrate the Roussillon models. Based on the initial transient simulations presented in the previous sections, we designed an approach to adjust locally the fields of hydraulic conductivity and specific storage parameters to better reproduce the piezometric transient data series. This approach was implemented for the four parameters sets, and for each conceptual approach.

Calibration global results

Figure 7.12 shows globally the results of the calibration approaches. It shows the evolution of the mean RMSE scores during the iterations of the ES-MDA algorithm. The general impression is that the behavior of the algorithm is unstable and does not always improve the initial pre-calibrated results. It is important to note that many simulations suffer from convergence issues during calibration. Our approaches flag and re-simulate the inconclusive simulations using the converging ones, which tends to reduce the ensemble diversity and thus the benefit of the Kalman gain calculation. In the most extreme case, as for all the SIS calibration sets, only one or two simulations were converging after the first iteration, rendering the calibration approach inconclusive.

In figure 7.12, the depth related models are the ones that show the most reasonable or expected behavior, with three of the four calibration approaches displaying a significant improvement of the global scores during the first iterations, while the following iterations did not improve much the calibration of the model parameters. The first two simplest calibration approaches (pilot points only for S_s or pilot points for both S_s and K), show little to no improvements through the iterations. The two more complex calibration approaches succeed in reducing initially the general misfits, but the misfit increases during the fourth iteration. Only the second calibration approach reaches the pre-calibrated RMSE score of the depth-related model (Tab. 7.1), and this during its fourth iteration.

Regarding the calibration of the MPS simulations, we see a consistent but small improvement between the first and second iterations, while the next iterations are more messy in their behavior. The more complex approach, calibrating the larger number of parameters, produced the best final score, but it is not converging steadily to this solution.

The calibration of the SIS simulations were not successful at all compared to the other two types of models. The strange behavior of the calibration curves is due to the fact that only two models successfully converged in the first

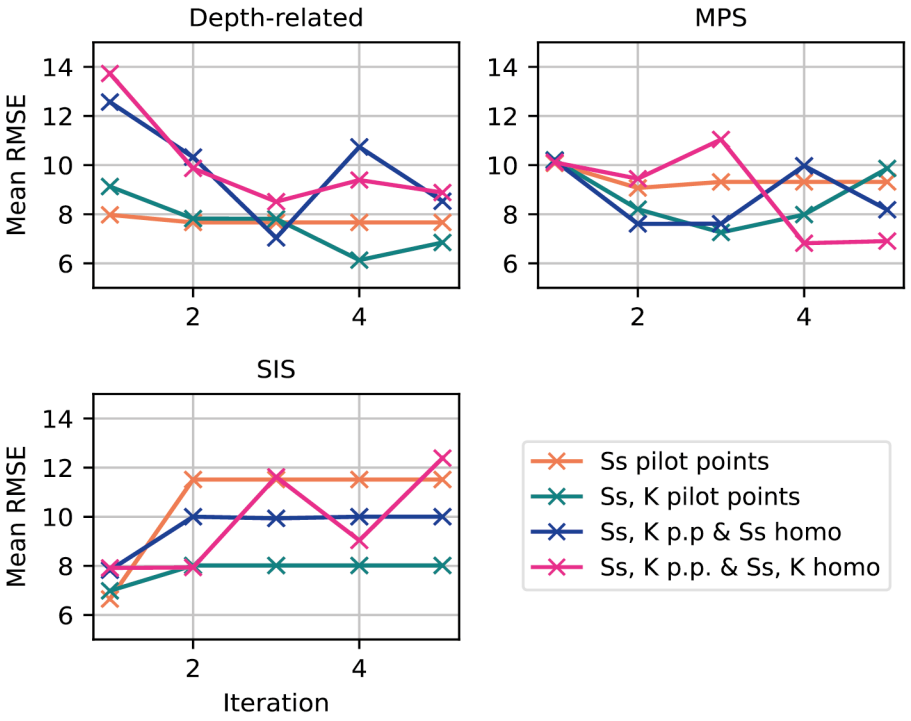

Figure 7.12: Evolution of the mean scores of the calibration approaches at each iteration. While depth-related, and MPS calibration sets produce reasonable calibration convergence patterns, the SIS calibration approach completely failed to calibrate the parameter sets, with almost all of its models failing to converge.

iteration, leading to a degeneration of the ensemble. These results illustrate one limitation of the ensemble approach when applied to sensitive models that are highly susceptible to failure when slightly perturbed.

Overall, we observe that ES-MDA is capable of slightly reducing the misfit, but none of the proposed calibration approaches performed systematically better than the others. The mean ensemble scores are not significantly improved as compared to the original pre-calibrated model ensembles. We also cannot identify a specific relationship between the calibrated parameters and the improvement of the ensemble score.

Results for the MPS models

Transient series

We now show the effect of the calibration on the reproduction of the piezometric data for the best set of MPS simulations corresponding to the fourth calibration approach. It corresponds to the more complex approach, where two pilot point sets and six homogeneous parameters are calibrated. The calibration is applied during a 1 year simulation period.

Figure 7.13 presents the evolution of the piezometric heads over the iterations during the ES-MDA process. We can see that the parameters adjustment allows, in general, a better fit between the simulated piezometric levels and the observations. Globally, the simulated heads tend to better represent the central values of the observations. However, the amplitude of the piezometric variations are often reduced, and the simulated heads do not represent correctly the variability of the actual measurements. Furthermore, the variability between the members of the final ensemble of simulations (represented in gray in the figure) is not always covering the actual data (for example Obs. 12).

To illustrate the effect of the calibrated parameters on the model outputs, we extracted from the ensemble the best parameter sets and run one 20 years transient model. Since the calibration results are only preliminary ones, and are not satisfactory in terms of signal reproduction, we only run a single MPS model. This transient model provides only a first visual representation of the effect of the calibration on the complete time-series, and represents the best calibration model of the ensemble, but it does not show the complete range of model predictions.

Figure 7.14 presents the calibrated model, and the original MPS ensemble. While the mean values of the simulated series are closer to the mean value of the observations, the calibrated model shows almost no seasonal nor annual variation. The global score of the calibrated model is improved, with a mean RMSE value of, 5.88m compared to the mean RMSE values of the original MPS set of 6.24m. However, it is difficult to argue that the simulated series are a better or a more realistic representation than the un-calibrated model, which succeeded in reproducing the seasonal behavior of some observations even if it was biased in some locations.

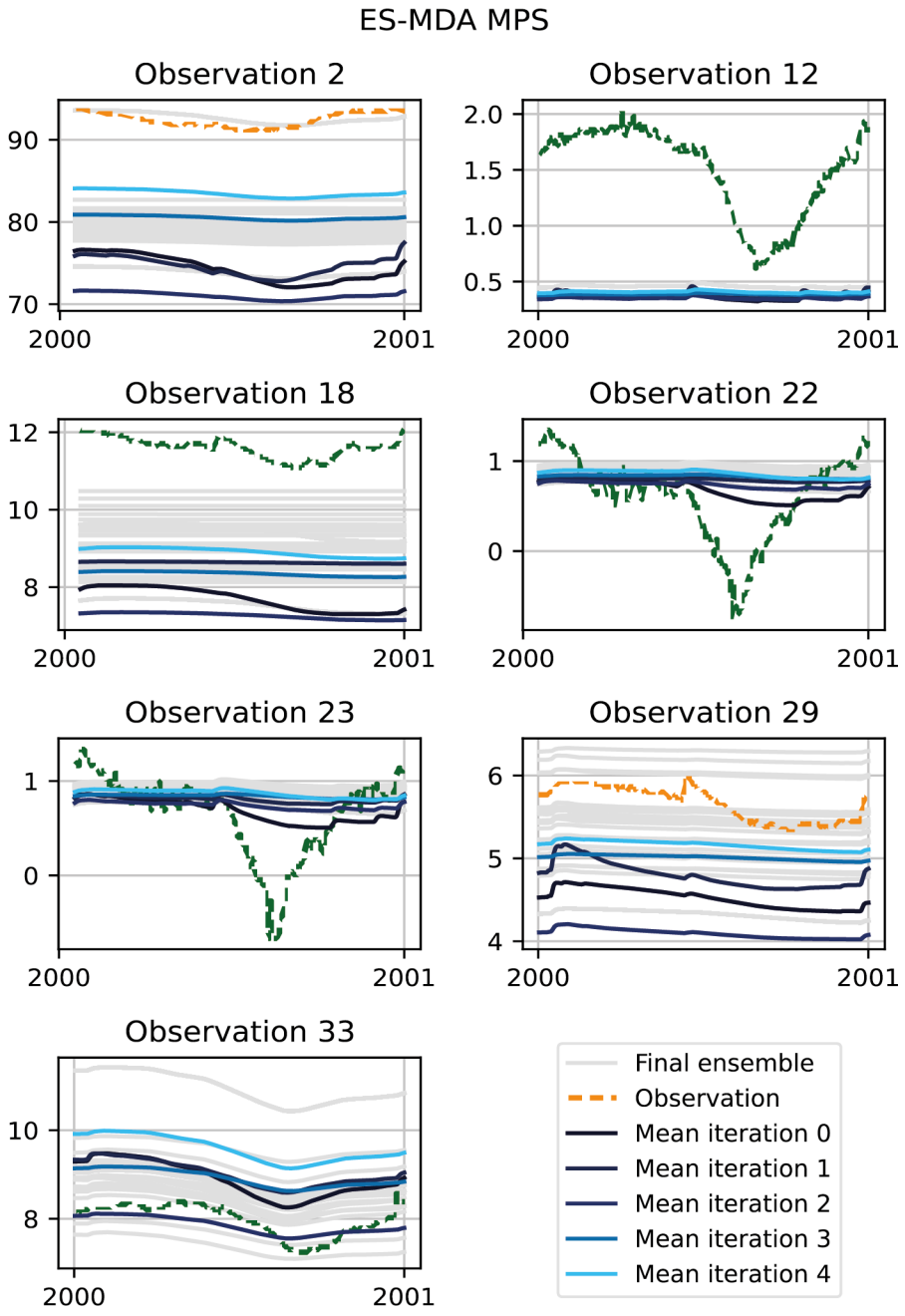

Figure 7.13: Evolution of the mean piezometric signal through the five ES-MDA iterations for the MPS simulations and the most complex calibration approach (two sets of pilot points and six homogeneous values).

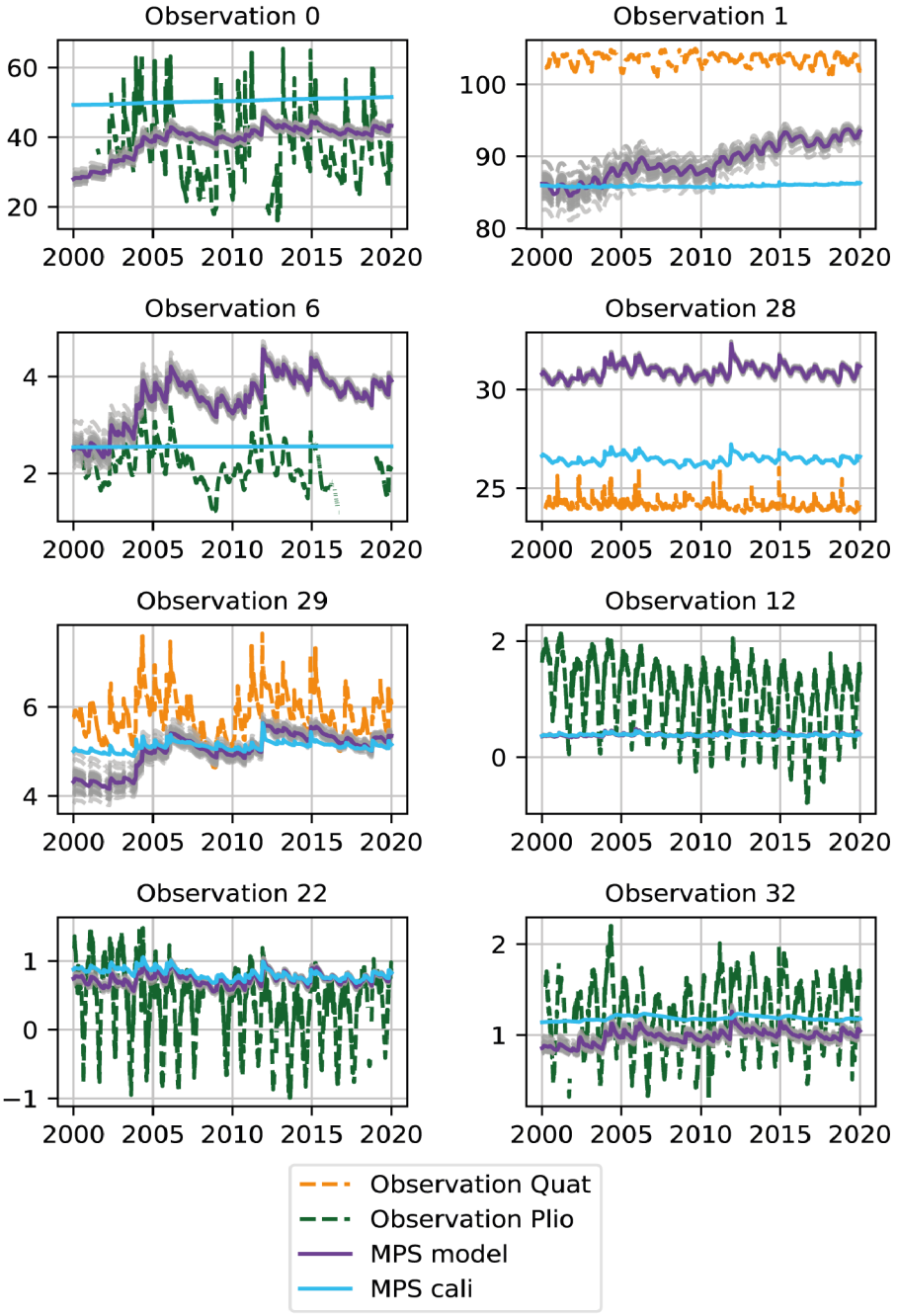

Figure 7.14: Piezometric transient data series of selected observation points for the MPS ensemble calibration simulations.

Calibrated parameters

If we look at the calibrated homogeneous parameters, presented in table 7.2, we can see that the calibrated specific storage values have undergone extreme modification between their initial values and their final calibrated values. These parameters were not pre-calibrated as it was the case for the homogeneous hydraulic conductivity parameters, which after calibration are closer to their initial values. The buffer layer 1, presents extremely modify values, with the specific storage being set extremely low (10^{-10} 1/m) and the hydraulic conductivity relatively high ($10^{-1.9}$ m/s). Even if these values are extreme, they correspond to the conceptual definition of this layer that only transport water between the sea and the Quaternary aquifer. The buffer layer 2 calibrated parameters are also in accordance with the layer original conceptual definition, and are calibrated to a low specific storage parameter ($10^{-8.9}$ 1/m), and a medium hydraulic conductivity parameters ($10^{4.75}$ m/s), acting as a semi-permeable unit that conducts the water between the Quaternary and Continental Pliocene layer. Finally, the Marine Pliocene layer, is associated with an extremely high specific storage ($10^{-1.6}$ 1/m), acting as a preferential storage unit of the system. The realism of these calibrated values are questionable, but their conceptual implications are in accordance with the initial conceptual description of these layers.

Table 7.2: Evolution of the homogeneous hydraulic conductivity and specific storage coefficients, before and after calibration, for the best MPS calibrated set.

	Buffer layer 1	Buffer layer 2	Marine Pliocene
Ss initial [1/m] ($\log_{10}$)	-5.22	-4.64	-4.99
Ss cali [1/m] ($\log_{10}$)	-10.15	-8.93	-1.60
K ini [m/s] ($\log_{10}$)	-3.77	-3.38	-4.68
K cali [m/s] ($\log_{10}$)	-1.88	-4.75	-5.42

Finally, when looking at the interpolated correction maps (Fig. 7.15), and the initial and calibrated fields associated (Fig. 7.16), of the best member of the ES-MDA calibration, it is interesting to see that two zones are clearly affected by the main corrections. The first one (zone 1), is the zone showing the main correction of the specific storage coefficient, with an extreme pilot point value influencing the surrounding area. This zone is located near a constant flux boundary condition, corresponding to the karstic recharge of the Corbière massif. The second one (zone 2), is the zone affected by the largest change in hydraulic conductivity. These two zones corresponds to locations where the Continental Pliocene layer of the MPS (and SIS) piezometric maps difference were displaying large and unexpected changes in their piezometric levels' evolution (Fig. 7.10). The fact that the calibration process imposed important changes in these zones is important information regarding both the possible miss-conceptualization of the sedimentological models or the importance of

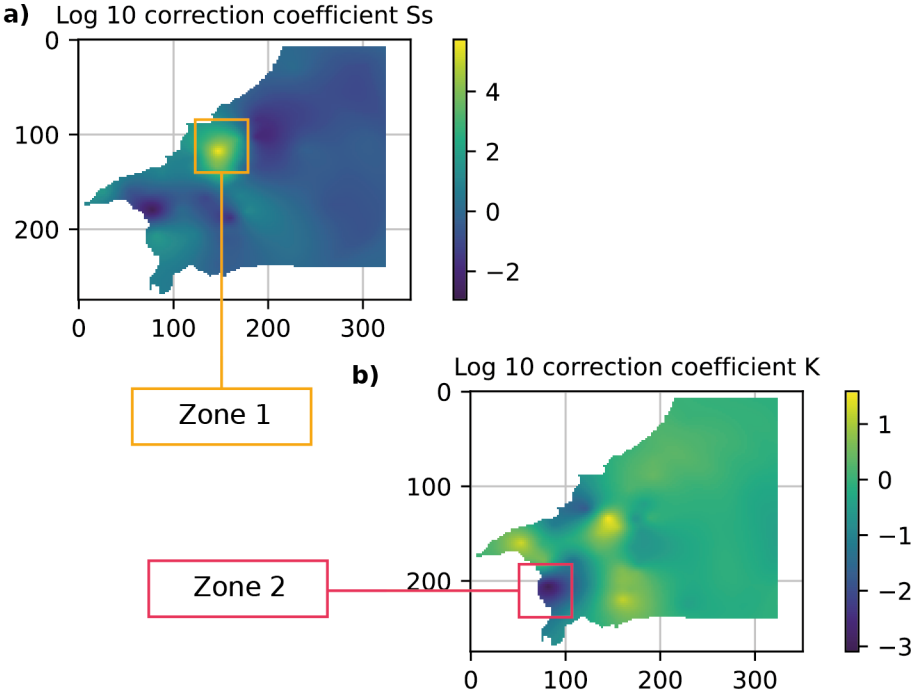

Figure 7.15: Maps of the correction coefficients obtained for the best MPS simulation after application of the proposed ES-MDA algorithm.

these two poorly characterized zones on the global model outputs.

Figure 7.16 shows that the application of the correction coefficient maps, to the initial parameters fields, succeed to preserve the original simulated MPS channels, and modify locally the parameters fields. This method of correction allows preserving the simulated litho-facies patterns, which are important to save through the calibration process, since they can create internal preferential flow paths.

Furthermore, these maps show that the specific storage has been globally increased in most regions. This explains why the seasonal piezometric variations have been damped almost everywhere, as we observed in figure 7.14. This result may be due to a compensation effect if the ES-MDA corrected the bias in the mean piezometric values by adjusting preferentially the specific storage values because there were no other way in the model setup to adjust any parameter that would correct properly the simulated heads without modifying the seasonal variations. Figure 7.15 also shows that the hydraulic conductivities have in general increased, except in zone 2 where it has been drastically reduced. Increasing the permeability allowed to let the water circulate faster from the

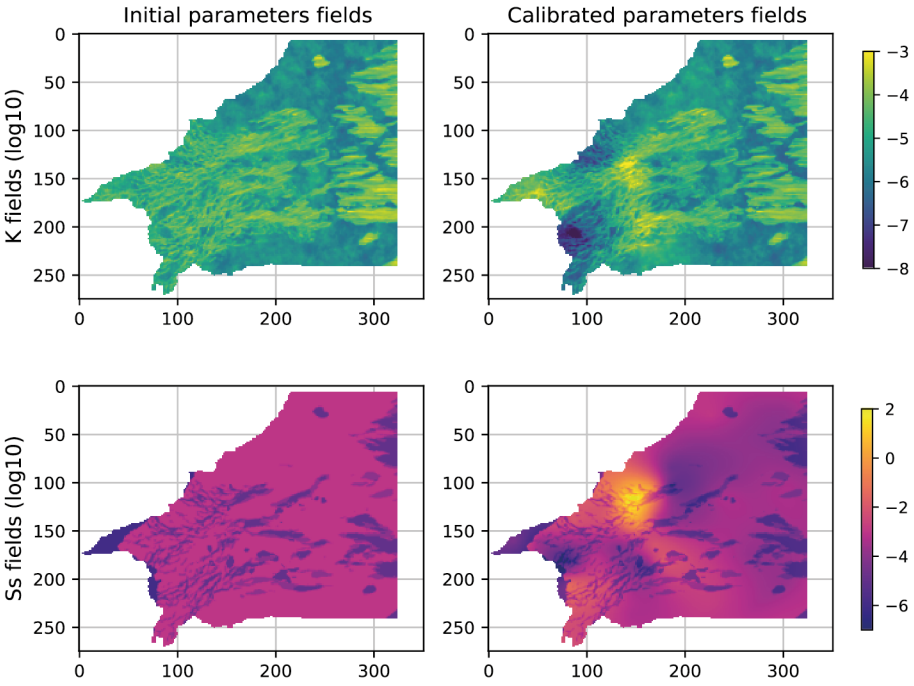

Figure 7.16: Initial and calibrated ($\log_{10}$) hydraulic conductivity and specific storage fields of the Continental Pliocene layer, using the correction coefficient maps presented in figure 7.15.

recharge to the outlet, and it reduced very significantly the rising trend that was observed on the simulations before the calibration. The recharge could flow to the sea faster and would not accumulate in the aquifer. This result of the calibration tends to show that the initial values for the hydraulic conductivities could be underestimated.

7.5 Discussion and conclusion

This chapter presented the transient models of the Roussillon aquifer for the three tested conceptual approaches, the depth-related model, the MPS models ensemble, and the SIS models ensemble. Due to the complexity of the models, and their sensibility to their hydrodynamical parameters, we started by running ensembles of transient simulations using the parameters calibrated in steady-state from chapter 6. These first runs showed that the three models fail to correctly reproduce the observed piezometric time series. In some locations, the time series are simply globally shifted, but still succeed in reproducing the observed seasonal variability. In some other locations, the signal is completely wrongly simulated.

An important conclusion of this work is that it was not possible to identify clear benefits of using complex physical parameters fields, generated from MPS and SIS, to reproduce the piezometric signal of the Roussillon aquifer. The MPS and SIS approaches still present some advantages, since they allow incorporating geological conceptual knowledge in the hydrodynamical simulations and generating multiple realizations from which we can derive predictive uncertainty. Moreover, the MPS simulations, where the underground is described with more realistic connection between the water components, could produce more realistic results if used for transport simulations.

While some observations display a roughly constant piezometric level over the 20 years of observations, the global observed trend corresponds to a decrease of the piezometric levels. The main issue with the transient models before calibration is that the simulated water level tend to increase during the simulation period. This general trend reproduction problem is common to the three types of models, but is accentuated on two locations for the MPS and SIS models. This main issue could be explained by different hypothesis:

- The initial steady-state water level could be underestimated. On some observations, the initial time series are too low compared to the initial piezometric levels of the system. This issue could lead the model to re-equilibrate itself during the first few years of the simulation, until it reaches its true equilibrium state after a few years of simulation. This phenomenon could continue for several years due to the inertia of the system. However, since the initial state was obtained from a previously calibrated steady state computation, it is surprising that the computed heads in transient regime are so far from the mean measured piezometric level.

- Another possibility is that we miscalculated or missed some important boundary conditions. We have already seen that the agricultural intake dataset was not trustworthy prior to 2018, where many agricultural wells were not reported. This could be a much larger problem, and the accuracy of the drinking water and industrial data base could also be questioned. The fluxes that recharge the aquifer due to the use of agricultural canals also contain a large uncertainty. These fluxes are generalized over large uniform zones with constant annual fluctuations. These approximations could lead to an overestimation of the recharge. What we did not consider in the transient model was the possibility of calibrating some of the boundary conditions within ranges of plausible values. This is something that could be explored in the future.

- The river systems are approximated with simple constant head conditions and the simulated fluxes are controlled by an exchange coefficient. It is clear that the river systems would benefit from a better definition of their flows along the plain, which could potentially correct some of

the water level reproduction problems. In addition, the historical river base flow, if available, could also be used to validate and calibrate the models. However, this first simplified approach does not seem to produce unrealistic fluxes when we check the global water balance, and they do not excessively influence the piezometric level near the imposed river conditions. The only phenomenon that could lead to an overestimation of the inflow in the model could be when the piezometric level disconnects from the river or when the river becomes dry and the influx to the aquifer stops in reality. These situations cannot be modeled properly with the current implementation of the river systems in the model that uses only a lower limit for the inflow. This mechanism may be insufficient.

- The hydraulic conductivity and specific storage values are also likely to play an important role in the issue related to the global piezometric trend reproduction. The initial specific storage values, derived from the literature and from the interpretation of hydraulic pumping test on the plain, are inevitably an approximation of the real values of these parameters. Regarding the stochastic simulations, the geological conceptual description can carry some generalization of a sedimentary concept, and may not be representative on some location. We have seen that the two zones, corresponding to the main unusual water level, correspond to zones where alluvial fan are simulated. These facies could be wrongly spatially located, which could decrease the piezometric signal reproduction of the zone.

All these hypotheses should be further tested by running the transient models with different parameter values and configurations. However, this is computationally demanding since a model run to simulate the 20 years of simulations requires around 4 hours on a high performance Linux cluster, and many simulations were simply not converging properly. Many tests have been conducted in this spirit, but the time available has not been sufficient to identify the proper parameter set.

An important problem is that the issue of global trend reproduction and biased piezometric level in some regions were not clearly visible during the steady-state modeling phase. This hindered the identification of the conceptual issue regarding the model description. Therefore, in addition to tests and calibration, an essential point would also be to have more piezometric time series available, especially in the zones where the simulated water levels are well above the assumed level.

We tried to improve the models and identify the parameters by implementing a novel ES-MDA approach, using maps of correction coefficients applied to the hydraulic conductivity and specific storage fields. By calibrating these maps at pilot point locations, we wanted to locally modify the hydrodynamics conditions of the system in the hope to correct the local difference between the simulated

time series and the observations. We decided to limit the number of pilot points used as parameters for the estimation of the 2D correction maps, in order to apply similar correction coefficients to large areas of the parameter fields. By applying a similar coefficient to a large zone, we wanted to preserve the sedimentological realism of the simulations and the original simulated patterns on a local scale. The results of the calibration were not as successful as hoped. The calibration approaches did not succeed to significantly reduce the misfit between the un-calibrated and calibrated models. When tested, it appears that the best parameter sets for the MPS simulations resulted in a flatten piezometric signal, which is better at reproducing the mean observed values but miss to reproduce the seasonal signal fluctuations.

Since the ES-MDA method has been producing good results in previous studies [Lam et al., 2020; Juda et al., 2023], it is likely that the problem lies either in a conceptual issue with the boundary conditions as discussed above or in the manner that it was parametrized. Therefore, the method could benefit from a larger number of pilot points. More pilot points could be located on different layers along the z axis and could be used to calibrated intermediate layers independently. A denser set of pilot points could also been tested. It could lead to more local changes in the parameter fields, which could potentially improve the local piezometric reproduction, but would degrade the simulated geological patterns which could lead to the disconnection of water component and impact the simulated fluxes.

Globally, one of the main issue that made all this work difficult is the large computing time required for the transient flow simulation at each iteration of the ES-MDA algorithm. This leads us to fix the number of members to 60. This number can be considered as pretty low. It should be increased to obtain better estimates of the covariances that are used in the calculation of the Kalman gain. It is possible that the method did not work because the covariances were poorly estimated and the ES-MDA method could not estimate properly the link between the data misfit and the parameters.

Finally, in order to get a complete calibration of all the stochastic models, this approach, if successful, should be applied to each MPS and SIS simulations, multiplying drastically the total number of flow simulations required to calibrate the initial ensemble (number of initial MPS/SIS simulations $\times$ number members $\times$ number of iterations).

Overall, this chapter shows the difficulty to calibrate a complex transient regional model, and demonstrates the limitations encountered in practice to calibrate an ensemble of stochastic simulations. Even if we did not succeed in properly simulating the transient state of the Roussillon aquifer, we hope that this work contributes to a better understanding of the problem at hand.

Chapter 8

General conclusions

Abstract

The main objective of the thesis was to improve the geological knowledge of the Roussillon aquifer and build a hydrodynamic model to better understand the system, as well as establish a suitable ground to study the potential impacts of climate change on this regional resource.

This final chapter summarizes the main ideas and contributions developed in the different chapters of this thesis. It also summarizes the main limitations of our results and proposes some perspectives for future research and possible improvements.

8.1 The structural geological model and concept

The first phase of the project involved defining the main sedimentary envelopes and compiling a geological database using onshore and offshore data sets. The data sets, together with general geological knowledge from previous studies, were used to develop a conceptual understanding of the main structures composing the Roussillon aquifer. The resulting geological model of the Roussillon aquifer is composed of three main geological units: the Marine Pliocene unit, the Continental Pliocene unit, and the Quaternary unit at the top of the formation. Four new sub-intervals were defined for the Continental Pliocene layer. These new sub-intervals are divided by three newly defined surfaces that represent major changes in the state of deposition of the sediments, mimicking the main eustatic level variations of the period. Using geophysical logs and offshore seismic data, the elevation map of these three surfaces dividing was mapped and interpolated. The final hydrogeological model of the Roussillon aquifer used for this study covers about 800 km^2 onshore and extends 30 km offshore.

The onshore and offshore geological data set, served as conditioning data for the geostatistical simulation of the Continental Pliocene layer. The conditioning data play an important role in geostatistical simulations, since they control the proportion and spatial distribution of facies during simulations. Although the data set is well distributed onshore, the number of interpreted wells is small compared to the actual size of the domain, and the model could benefit from an additional geological data set. Moreover, the Roussillon geological data set suffers from heterogeneity in its resolution between onshore and offshore regions. The offshore seismic data set is much denser than the onshore one but at a lower resolution. Seismic data in the onshore domain would be useful to better constrain the 2D intermediate surfaces, and to better constrain the size and shape of the river deposit facies in the proximal part of the alluvial plain. For better geostatistical modeling, enlarging the offshore data set by interpreting the entire set of seismic lines could be a potential improvement. A complementary geophysical data set, acquired at low resolution on large areas of the plain, could also be used as auxiliary variables during geostatistical simulations to improve the accuracy of the model. Overall, this chapter introduced the necessary steps and data required to create the structural model and the intermediate sub-layers. It also introduced the litho-facies conditioning data set available for the Roussillon and used during the MPS and SIS litho-facies simulation.

8.2 MPS simulations

In chapter three, we presented the simulation of the litho-facies composing the Continental Pliocene layer using the direct sampling (DeeSse) multiple-point simulation approach. In particular, we introduce a new workflow for simulating complex heterogeneous aquifers, which relies on conceptual knowledge and auxiliary information. The proposed approach is simpler than traditional 3D methods, as it relies on the use of stacked 2D simulations. This approach offers more flexibility during the model development, since 2D training data sets (TDS) are easier to create and test as compared to 3D TDS. This method was used to model independently the four sub-intervals of the Continental Pliocene layer, where each one of the sub-intervals were assigned its own TDS set.

The results show satisfactory structures reproduction that succeed to account for the important sedimentary concepts of the TDS and reproduce rather correctly the facies proportion. However, the simulations can suffer from the lack of hard data, which can wrongly influence some of the global facies proportion reproduction. Furthermore, the simulation of the 3D structures by stacking 2D simulations is not completely satisfying. While this process helps to increase the vertical connectivity of the simulated channels along the z axis, the 3D tortuosity and complete shape of the channel bed are not directly controlled during the simulation

As a perspective, the confidence in the model could be increased by acquiring additional borehole data and more onshore geophysical data. These data could provide additional information on the geometry of the sedimentological objects and could be used to perform a meaningful 3D cross-validation exercise.

Generally, the proposed workflow has proved its potential to simulate complex internal aquifer heterogeneity on a regional scale, has demonstrated the applicability and flexibility of the DeeSse MPS algorithm to work on complex realistic study case, and has succeeds in simulating the most important sedimentological features of the sub-intervals, composed of complex realistic sedimentary patterns.

8.3 SIS simulations and hydrodynamical fields properties

In the chapter four, we presented two other approaches to generate hydrophysical property fields for the Roussillon aquifer. The first approach is a deterministic one, that we called depth-related approach. This approach is based on the interpretation of hydraulic pumping tests results, that are used to assigned hydraulic conductivity values to cells of the grid, based on their location and depth. The second approach is the Sequential Indicator Simulation (SIS), which is a two-point variogram based algorithm. It incorporates some descriptive information of the system, through the use of rotation and probability maps. This approach is simple to set up, but is not able to simulate complex shapes and patterns. It was used to create simple litho-facies simulations, composed of three facies, alluvial fan deposits, sand deposits, and clay deposits. The two approaches, together with the MPS one, are used to create hydraulic conductivity and specific storage fields sets, used during the hydrodynamic MODFLOW simulations.

One of the limitations of this aspect of the work is the difference in resolution between the stochastic facies simulation grid and the flow simulation grid, which requires the use of an upscaling approach to transfer the physical parameters to the flow simulation grid. This upscaling step tends to aggregate the properties of the fields and can be an important source of inaccuracy in the modeling approach. This is visible in the upscaled MPS fields, where the alluvial channels appear to be mixed together after upscaling.

This chapter also summarizes the initial hydraulic conductivity and specific storage parameters used to populate the various modeling approaches. The correct estimation of the initial parameters is subject to large uncertainties. Values from the literature are often not clear regarding the values to be assigned to different types of sediments or litho-facies. This work would have benefited from in-situ measurements of the permeability of the sediments (which are not completely representative), or from local low scale parameter calibration on a

small study site for the estimation of the simulated litho-facies parameters.

These three approaches allow describing the geological uncertainty derived from the conceptual geological model of the Roussillon aquifer. These fields are then used for both steady and transient state flow simulations.

8.4 Hydrodynamic conceptual description

Chapter five presented the different features of the hydrodynamic model of the Roussillon aquifer. The main aquifer components, hydraulic boundaries and modeling assumptions and parameterization are presented along with the description of the numerical model setup and the available piezometric observations.

In this study, we use the hydrodynamic data set of the Roussillon covering the period from January 1, 2000 to December 31, 2019. The mean recharge from precipitation is estimated to be around 120 mm/an, while the mean annual agriculture water withdraw fluctuated around 20 Mm^3, and the drinking water and industrial uses correspond to about 40 Mm^3 per year.

One of the main limitations of the model is the simplified representation of the river flow dynamics. In the MODFLOW 6 RIV package, rivers are described only by their cell-based conductivity and river stage. These two parameters are assumed to be constant over time for the majority of river systems. Additional work could be done to calibrate the river stage values by river section instead of using a constant fixed value. The river system flows could also be directly simulated in the model using a more advanced MODFLOW package. This approach would require transient river flow information to be set up correctly, which would have required large additional complex work in order to correctly interpolate the transient flux series of the different river systems, and their complex interaction with the irrigation channels of the plain.

Another limitation is the lack of observations data. Observations are essential in the calibration process of numerical hydrogeological models. The transient observation data set for Roussillon is sparse compared to the size of the study area, and the observation points are not homogeneously distributed over the plain.

Some uncertainties regarding the hydraulic boundary conditions are also important to be noted. The total amount of wells and volumes of water withdraw from the agriculture is not known with certainty. In addition, effective infiltration from precipitation was calculated using classical soil water balance techniques coupled with a transfer function to represent the transfer of water through the unsaturated zone, but little data were available to calibrate the parameters of the transfer function. Remote sensing analysis or in situ experiments or models could help calibrate the parameters of the transfer function.

Alternative recharge calculation methods and models could also be considered to better constrain the recharge time series.

Designing a correct and rigorous model, in a detailed manner, for hydrodynamical numerical modeling in hydrogeology is critical for accurately simulating groundwater flow, which can be a complicated task depending on the system at hand and the data available. We are confident that the conceptual model integrates most of the important elements of the Roussillon aquifer, but some components are more reliable than others, both in their conceptual description and in their assignment to transient series, which are often estimated or generalized for several boundary conditions.

8.5 Steady-state calibration

In chapter six, we proposed a first calibration method for the river and the main hydraulic conductivity parameters of the MPS and SIS simulations of the Roussillon model, using a steady-state simulation framework. The use of steady-state models allowed providing rapid preliminary results due to their lower computational requirements. The steady-state calibration approach was developed to address the computational cost of hydraulic conductivity simulations and the upscaling process required for the MPS and SIS simulations. In general, calibration approaches either calibrate the categorical simulation process or modify directly the entire hydraulic conductivity field. The objective of this chapter was to calibrate the mean hydraulic conductivity of the simulated facies in order to preserve the simulated patterns of the SIS and MPS simulations while respecting the piezometric observations.

The calibration of the river parameters helped to improve the three model sets and is judged satisfactory in terms of the available information and the simulation assumption associated with the definition of the river streams in the MODFLOW RIV package. The Monte Carlo approach used for hydraulic conductivity calibration captured the parameter uncertainty, but was limited by the maximal number of iterations. The calibrated hydraulic conductivity parameter sets presented many different working configurations of parameter values, highlighting the sensitivity of the model to its parameters and complicating the task of identifying the best parameters set. Despite these limitations, the work provided a robust basis for understanding the behavior of the model and exploring the benefits of stochastic approaches in hydrodynamic modeling.

Future calibration process could include other boundary conditions or coupled interactions that may affect the performance of the model. This would help to capture the full system complexity and improve the overall representation of the hydrodynamic processes. Finally, the calibration of such complex MPS and regional model, is not well documented in the literature, and it appeared complicated to find approaches that ensure the reproduction of the target observation while preserving the simulated litho-facies pattern and working with

ensembles of stochastic simulations.

8.6 Transient regime and data assimilation

In chapter seven, we presented the transient models of the Roussillon aquifer using three different conceptual approaches: the depth-related model, the MPS models ensemble, and the SIS models ensemble. Initial ensembles of transient simulations were run to understand the models' responses and behavior. However, all three models failed to accurately reproduce most of the observed piezometric time series. While some series exhibited a shift from the mean value of the observations but still captured seasonal variability, others were completely wrongly simulated. Moreover, the global water level trend in the observations indicated a general decrease, while the simulated models tended to show an increasing trend over time.

This trend reproduction issue was common to all three models, but was more pronounced in certain locations for the MPS and SIS models. Several hypotheses were considered to explain this problem, including inaccurate initialization of water levels, missing boundary conditions, simplified river systems, and uncertainties in hydraulic conductivity and specific storage fields. However, further tests and calibration were limited by time constraints. Insufficient data series, especially in areas with high simulated water levels, also posed a significant challenge. These issues were not visible during the steady-state modeling phase, complicating the identification of a potential problem in the system's conceptual description or stresses definition.

Attempts were made to address the local trend reproduction through an ES-MDA approach, but the calibration results were not as successful as anticipated. The method faced limitations due to the sensibility to converge of the models. More parameters could have been set up in order to correct more locally the hydraulic conductivity and specific storage parameters, but this would have required increasing the number of parameters and the computational cost of the test. Overall, this chapter highlights the difficulty of calibrating complex transient regional models, demonstrates the influence of sedimentological models on hydrodynamic models outputs, and provides insights into the major sources of uncertainty in the Roussillon aquifer model.

To address the challenges encountered during the calibrating of the Roussillon aquifer model and improving its performance in future work, one important step would be to obtain more reliable observations' data series, particularly in areas where simulated water levels significantly deviate from assumed levels. This will facilitate a better understanding of the system's behavior, additionally to also benefit to the calibration process. This would allow for more localized modifications of the hydrodynamic conditions.

Despite the challenges and limitations faced, this work contributes to a better understanding of the transient state of the Roussillon aquifer, highlights the importance of sedimentological models in hydrodynamic studies, and identifies major sources of uncertainty. These findings serve as essential steps towards a complete description of the region water resources of the Roussillon aquifer.

8.7 Perspectives

Looking back at the whole project and the main simulation steps, we would like to point out some recommendations and general conclusions that can be drawn from this regional study of the Roussillon aquifer.

While the geostatistical application of the MPS approach to such a complex 3D regional model is novel and successful in producing realistic sedimentological patterns, the resolution of the MPS simulations appears to be too fine for the final use of the litho-facies models. By directly simulating the MPS at the final MODFLOW grid resolution, the calibration chain process, from the modification of the conceptual description of the system to the transient state simulation, could have been more direct and easier to implement. This would have facilitated the sensitivity analysis between the sedimentological model and the hydrodynamic simulations, and would have allowed the implementation of a possibly different calibration process that would directly influence the categorical facies simulations. The current MPS concepts could be reused in this perspective by slightly adjusting and upscaling the TDS to the MODFLOW grid resolution.

Another point is that it would be beneficial to first create a simple transient model of the Roussillon. Using a really coarse resolution, it could be possible to adjust first the boundary conditions to reproduce the general trends of the observations. Since the amount of observations available in the plain is scarce, the use of a low resolution model, focusing on the reproduction of the general trend, could have allowed us to get more insights on the interactions between the different hydrodynamic components.

Using such a coarser model, we could also have calibrated low resolution hydraulic conductivity and specific storage values or zones, which could have been used to better understand the behavior of the Roussillon aquifer and later constrain the finer MPS models. The hydraulic conductivity and specific storage of the MPS patterns could have been simulated and calibrated by zones to reproduce the coarser statistics, while at the same time simulating realistic sedimentological patterns continuous on the plain.

Finally, an important perspective for future research is to continue the effort of transient model calibration, if possible in a stochastic framework, in order to have a suitable basis to ultimately assess how climate change may affect the groundwater resources of the region.

Appendix A

Supplementary material

A.1 Observation data

Table A.1: Correspondence between BSS name and observation point number of the transient observation data.

Name	BSS	X Coord	Y Coord	Point
10904X0104/PIEZO	10904X0104	685787.2810	6185065.6593	0
10906X0039/C2-1	10906X0039	674183.3208	6176282.1990	1
10907X0129/CONTE	10907X0129	677133.6580	6174956.5825	2
10908X0394/RIBERA	10908X0394	682779.1103	6176217.7614	4
10911X0219/HIPPO2	10911X0219	696084.4124	6186625.8488	6
10912X0024/F	10912X0024	702558.2156	6190642.7783	7
10912X0111/BAR4	10912X0111	703110.6986	6187643.3530	12
10912X0112/BAR3	10912X0112	703106.8871	6187667.4076	13
10912X0134/BARQUA	10912X0134	702578.8732	6190597.5673	15
10915X0255/F2N3	10915X0255	694894.5359	6180102.7029	18
10915X0316/F3	10915X0316	692878.0746	6182040.0293	19
10915X0395/PZ	10915X0395	695657.2546	6179987.6787	20
10916X0061/F1N4	10916X0061	702057.1739	6181981.0030	22
10916X0062/F1N3	10916X0062	702060.1848	6181981.9804	23
10916X0090/PHARE	10916X0090	703111.9131	6178695.0768	24
10963X0059/MEDALU	10963X0059	679737.0012	6167674.1982	25
10971X0155/PD5	10971X0155	694818.7584	6168745.9238	27
10971X0198/LAFAR	10971X0198	693828.0242	6163347.7509	28
10972X0003/ALENYA	10972X0003	698160.1627	6171184.7097	29
10972X0094/111111	10972X0094	697407.3562	6166348.3254	31
10972X0098/FE1	10972X0098	701572.4657	6171248.3377	32
10972X0137/PONT	10972X0137	698805.5162	6164927.4371	33

A.2 Steady-state calibration

Table A.2: Best parameters set of the SIS calibrated model.

Facies	$\log_{10}(K)$
Floodplain	-4.82
Channel	-5.20
Alluvial fan	-5.06
Layer	**$\log_{10}(K)$**
Buffer layer 1	-4.05
Buffer layer 2	-4.97
Marine Pliocene	-4.91

Table A.3: Best parameters set of the MPS calibrated model.

Facies	$\log_{10}(K)$
Floodplain	-5.55
Marshy deposit	-5.90
Crevasse splay	-5.32
Sand bar	-3.71
Channel	-4.41
Alluvial fan	-5.40
Layer	**$\log_{10}(K)$**
Buffer layer 1	-7.26
Buffer layer 2	-3.26
Marine Pliocene	-5.87

A.3 Pre-calibrated transient simulations

Piezometric simulated time series

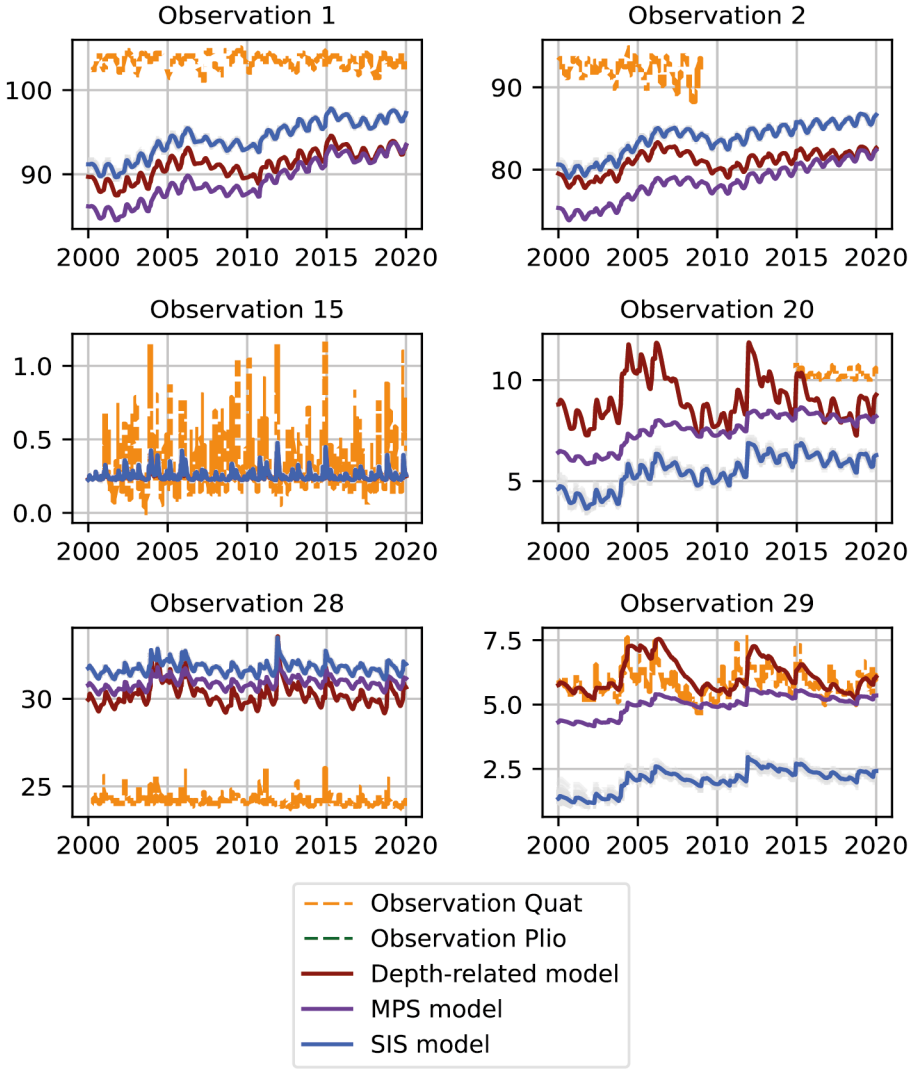

Figure A.1: Piezometric series of the three simulated approaches (not calibrated), compared to the available observations located in the Quaternary layer.

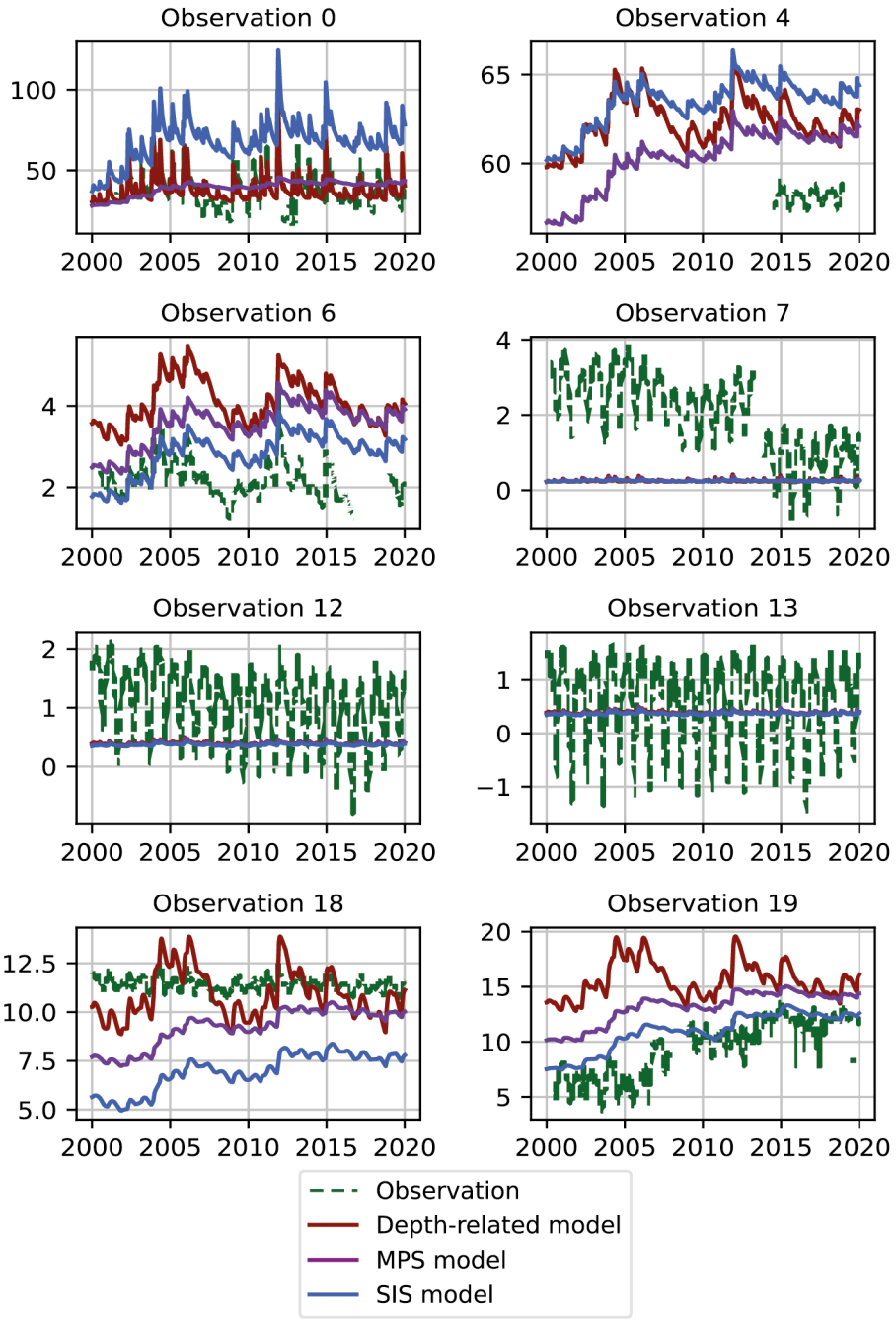

Figure A.2: Piezometric series of the three simulated approaches (not calibrated), compared to the available observations located in the Continental Pliocene layer.

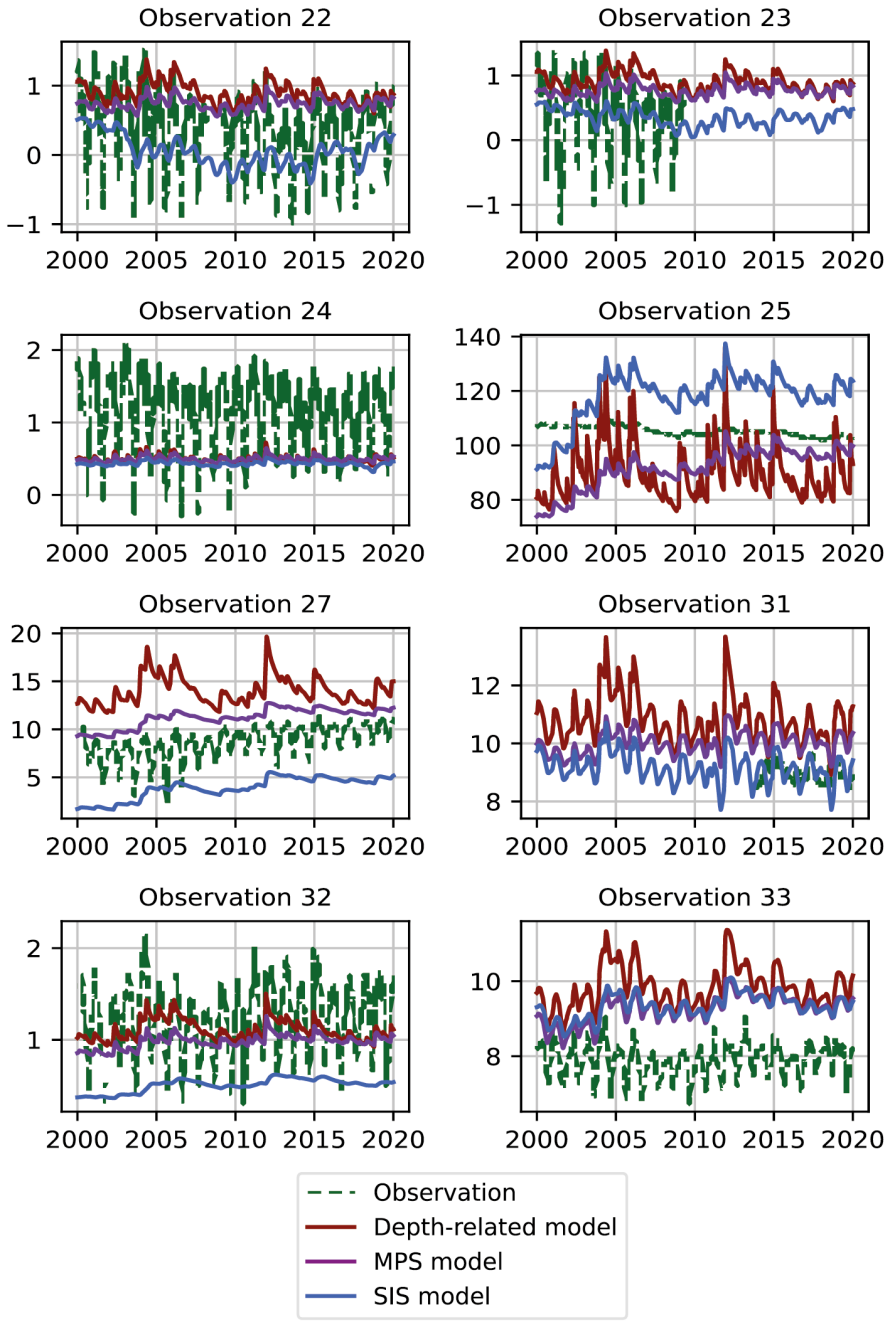

Figure A.3: Piezometric series of the three simulated approaches (not calibrated), compared to the available observations located in the Continental Pliocene layer.

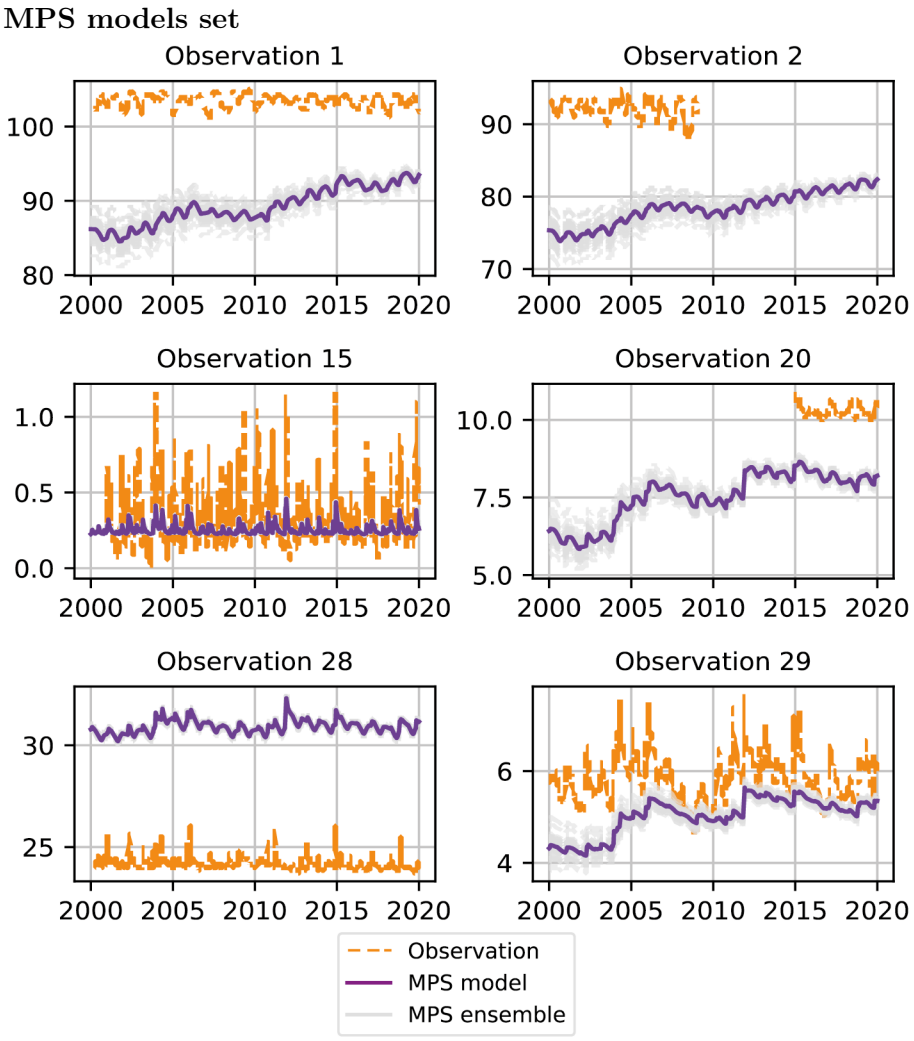

Figure A.4: Piezometric series of the MPS ensemble set (not calibrated), located in the Quaternary layer.

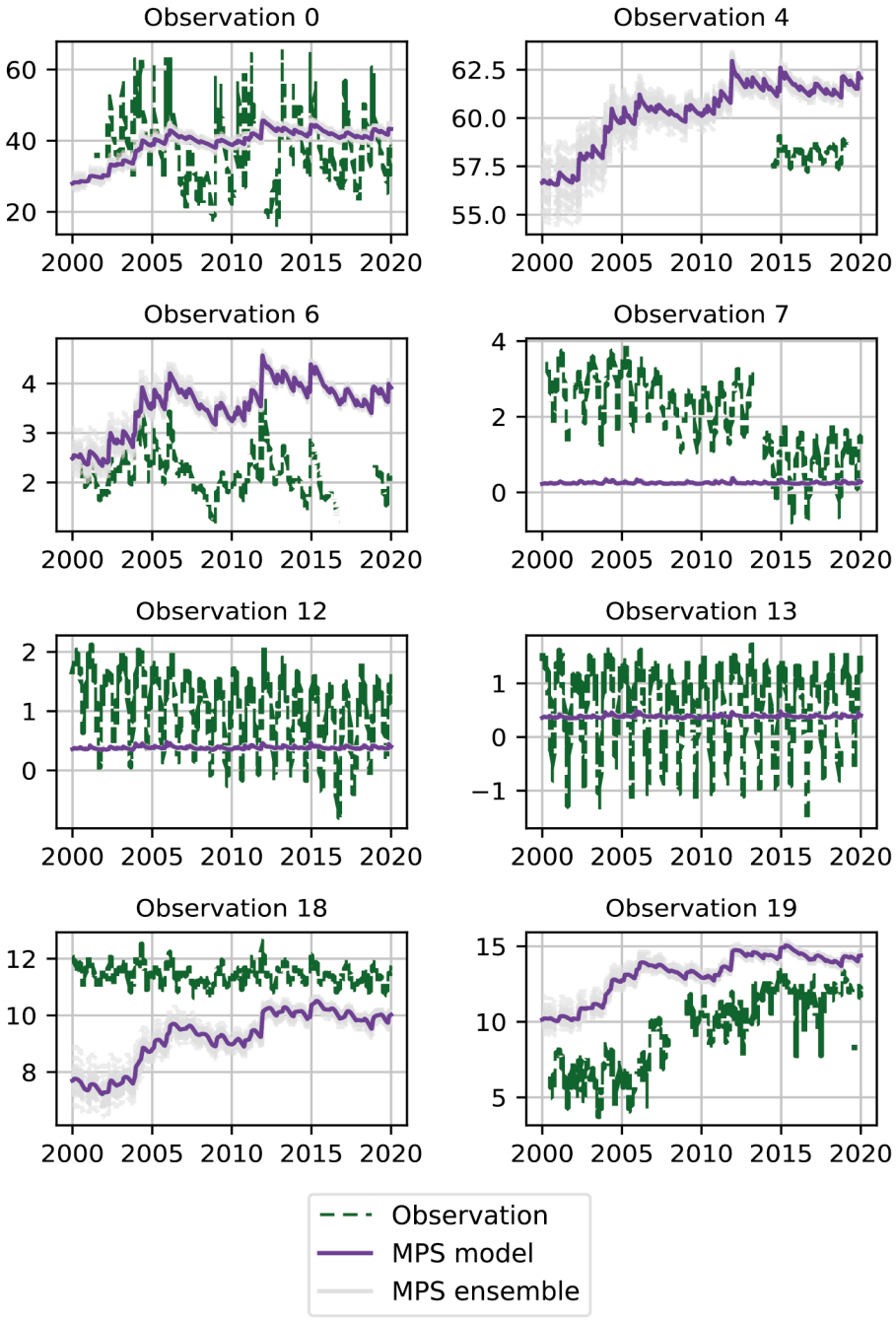

Figure A.5: Piezometric series of the MPS ensemble set (not calibrated), located in the Continental Pliocene layer.

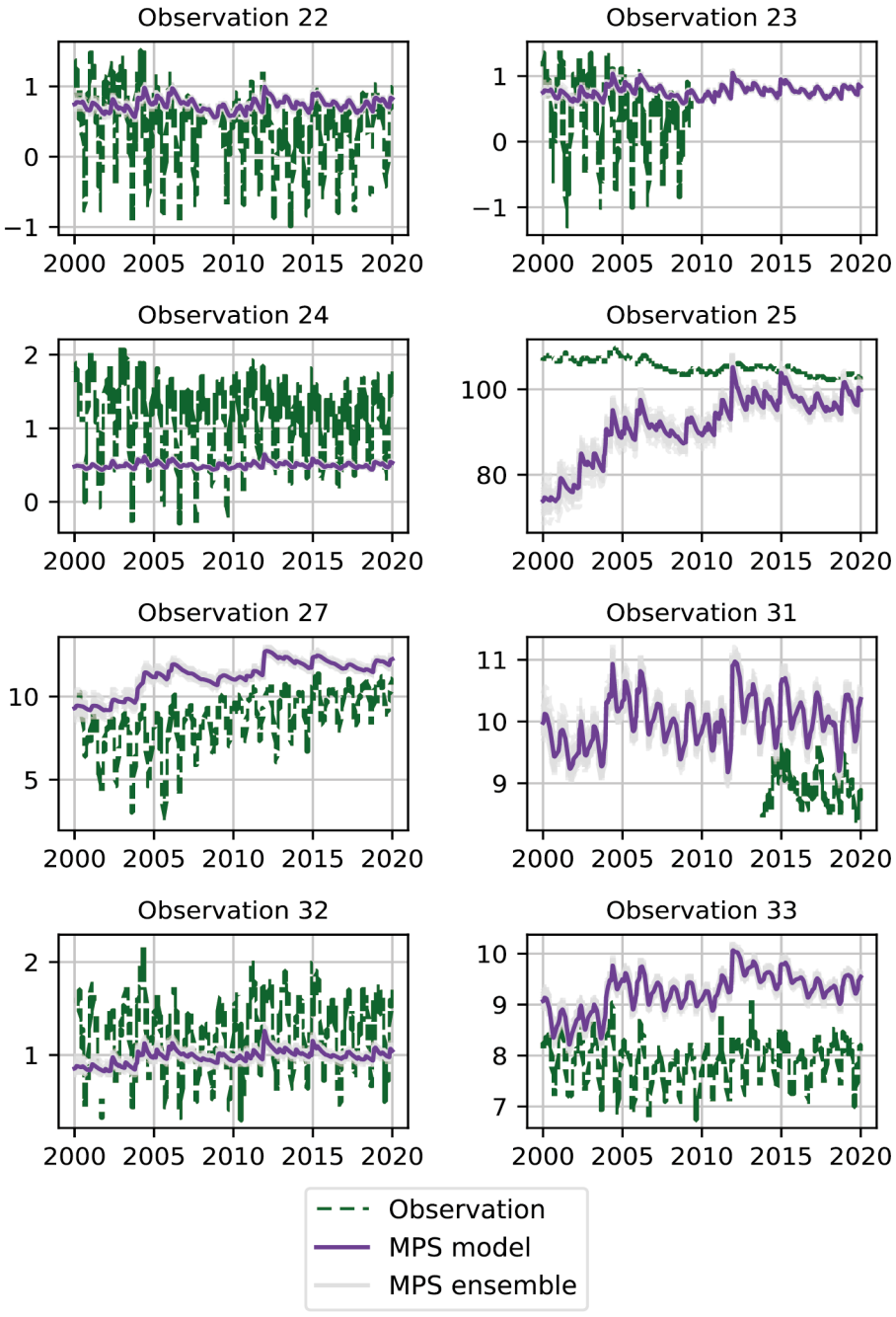

Figure A.6: Piezometric series of the MPS ensemble set (not calibrated), located in the Continental Pliocene layer.

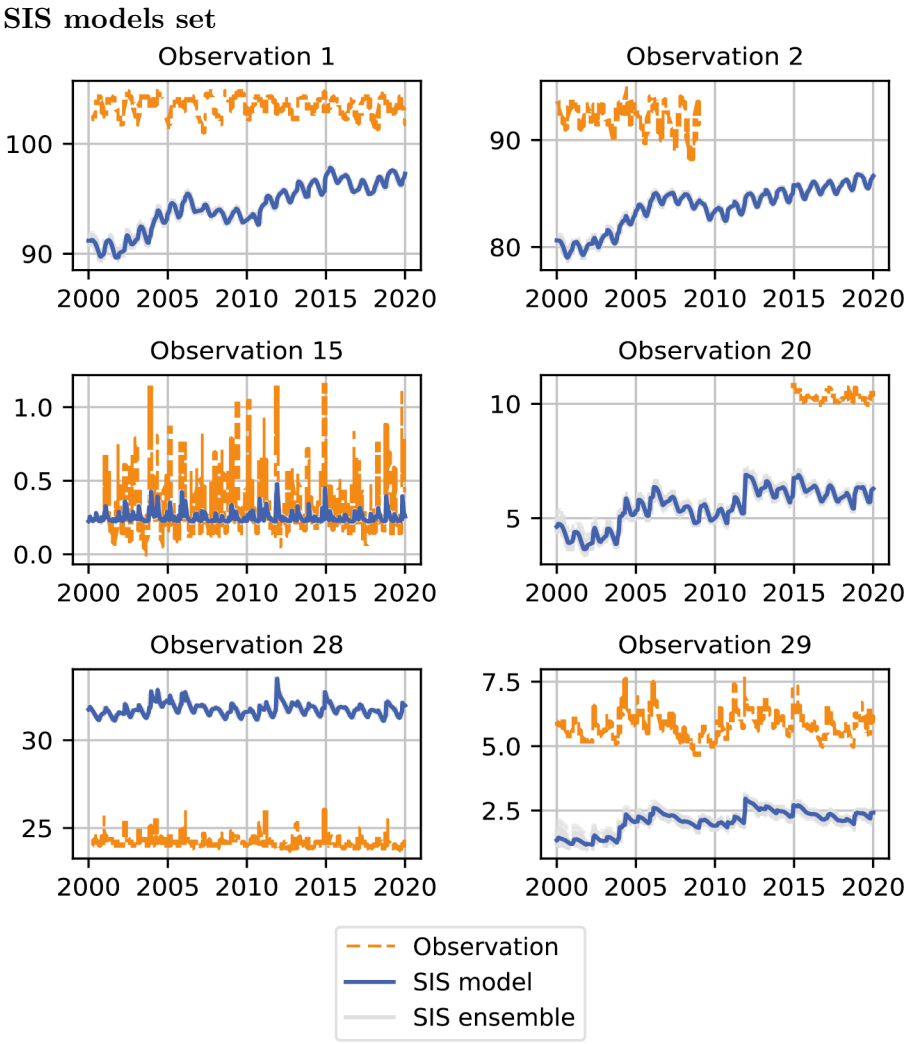

Figure A.7: Piezometric series of the SIS ensemble set (not calibrated), located in the Quaternary layer.

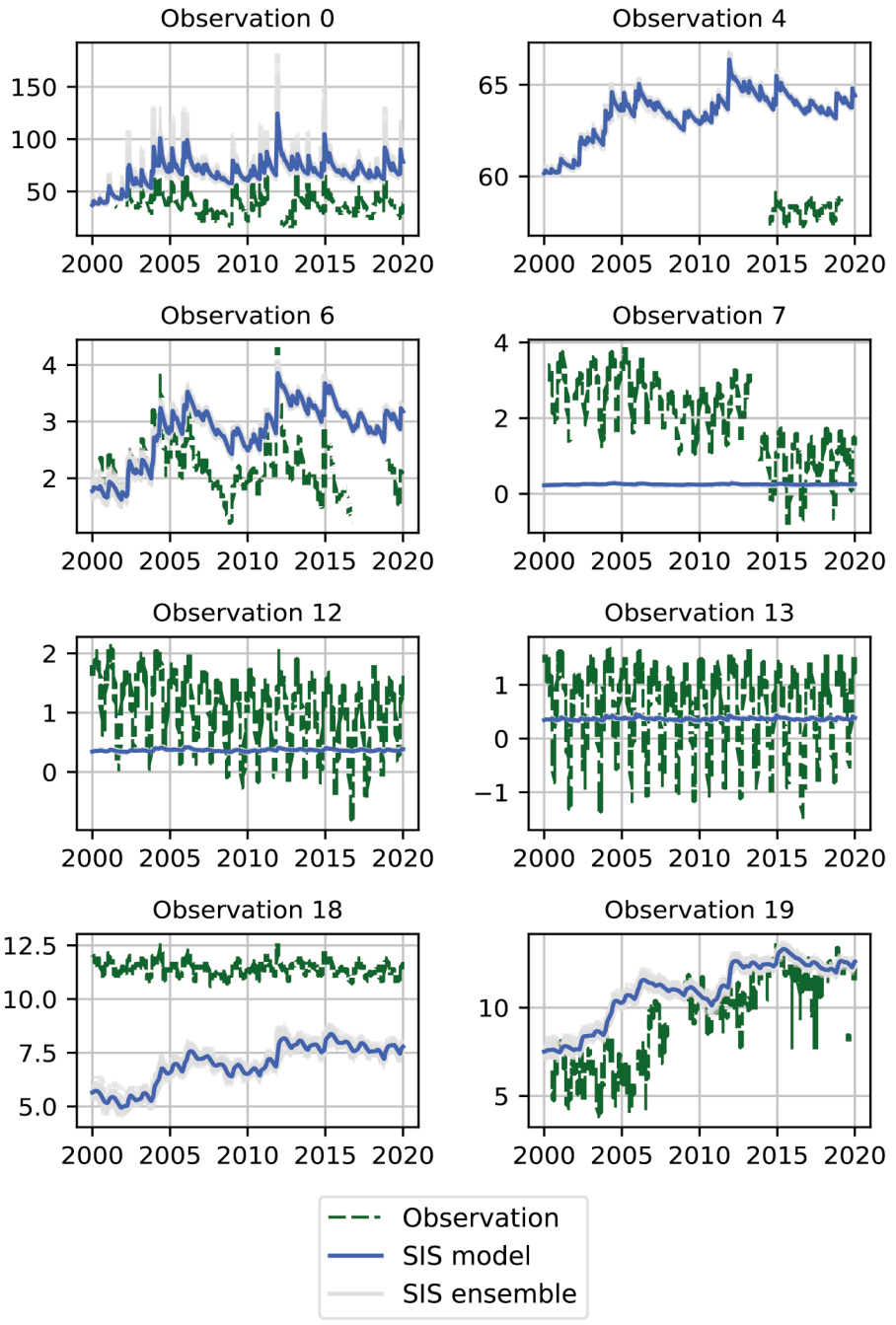

Figure A.8: Piezometric series of the SIS ensemble set (not calibrated), located in the Continental Pliocene layer.

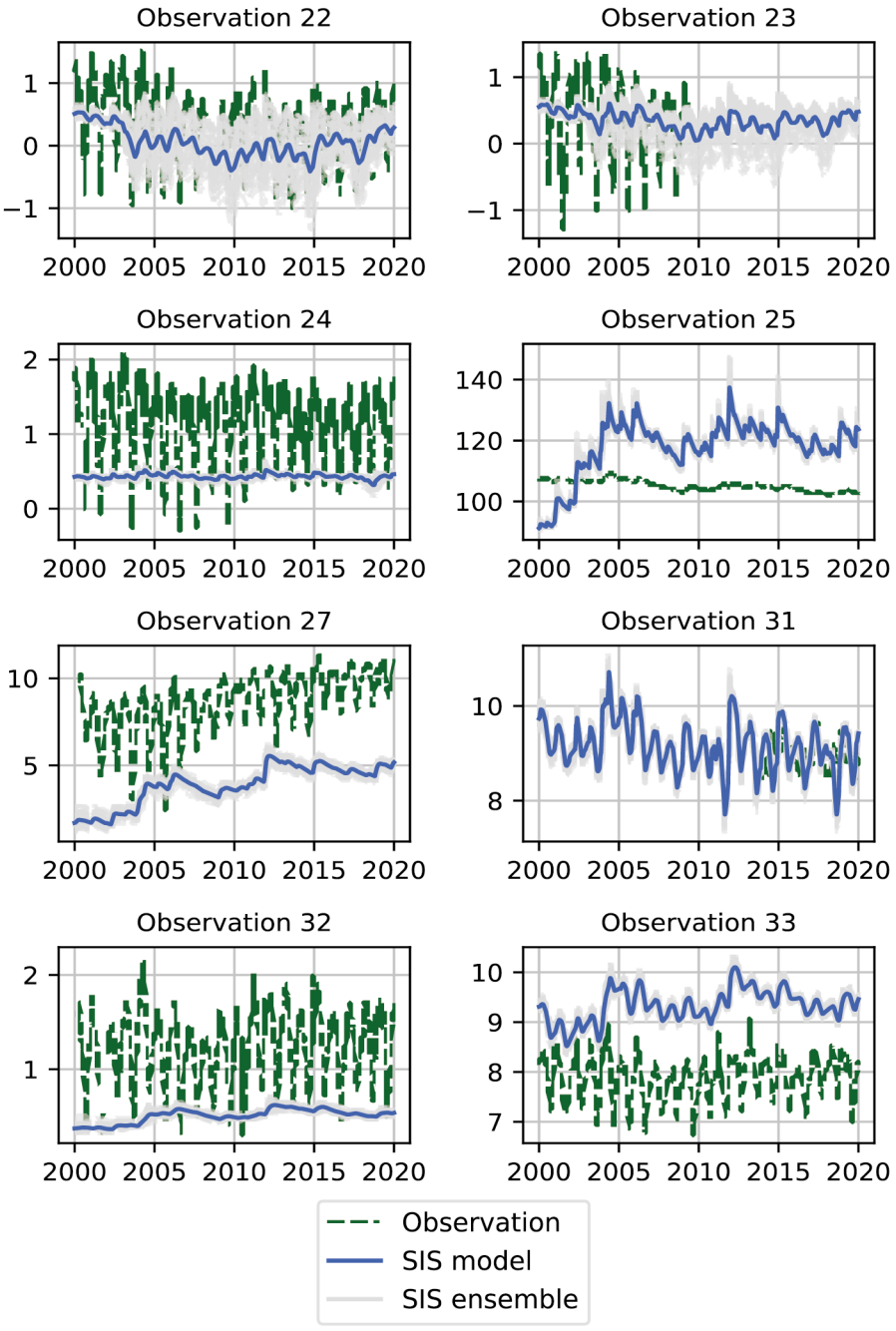

Figure A.9: Piezometric series of the MPS ensemble set (not calibrated), located in the Continental Pliocene layer.

Piezometric maps

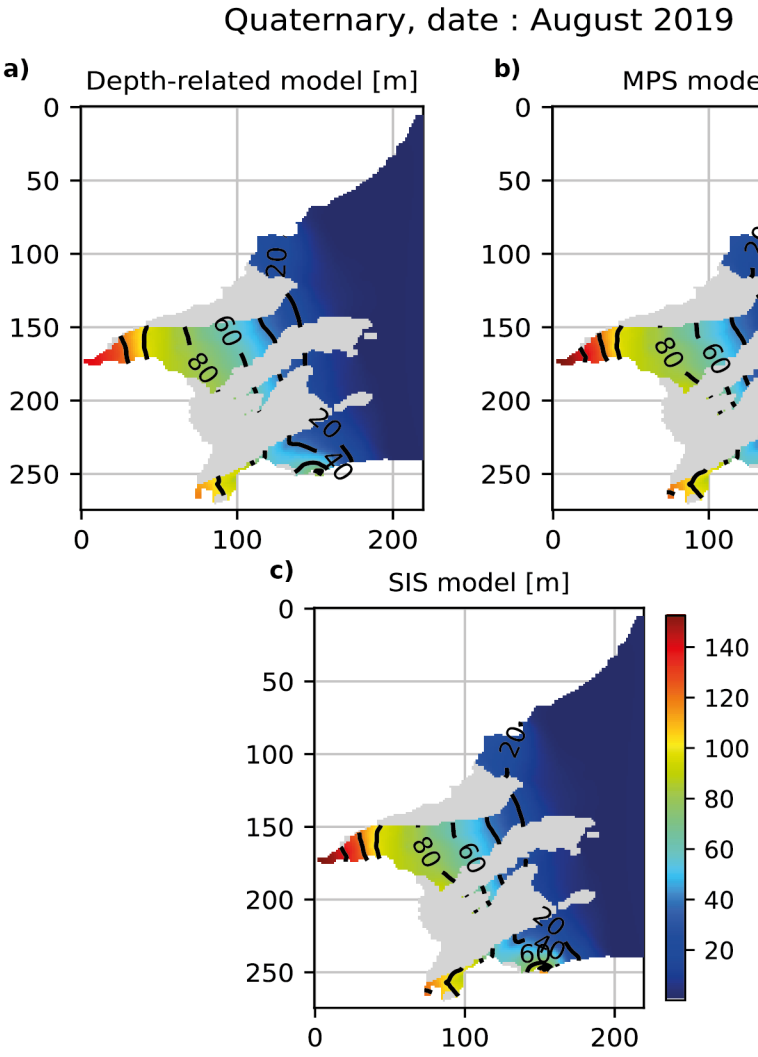

Figure A.10: Piezometric water level map of the Continental Pliocene layer for August 2019.

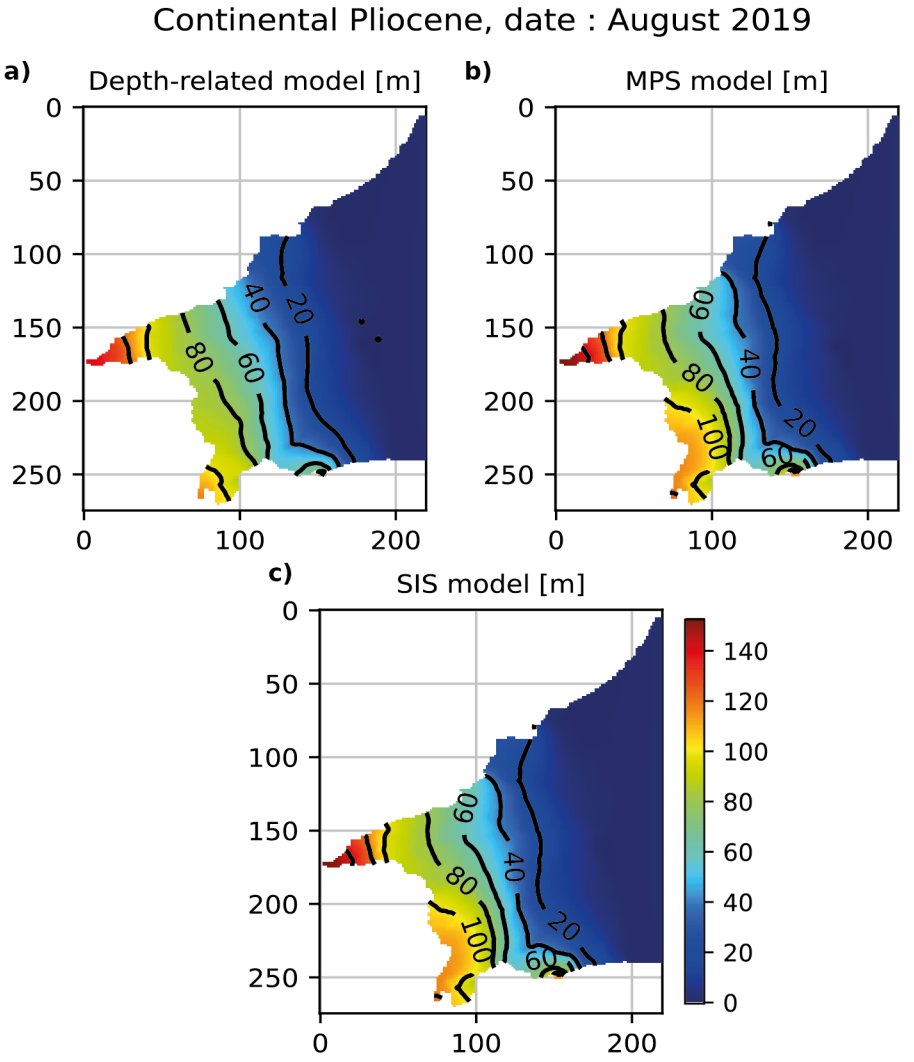

Figure A.11: Piezometric water level map of the Continental Pliocene layer for August 2019.

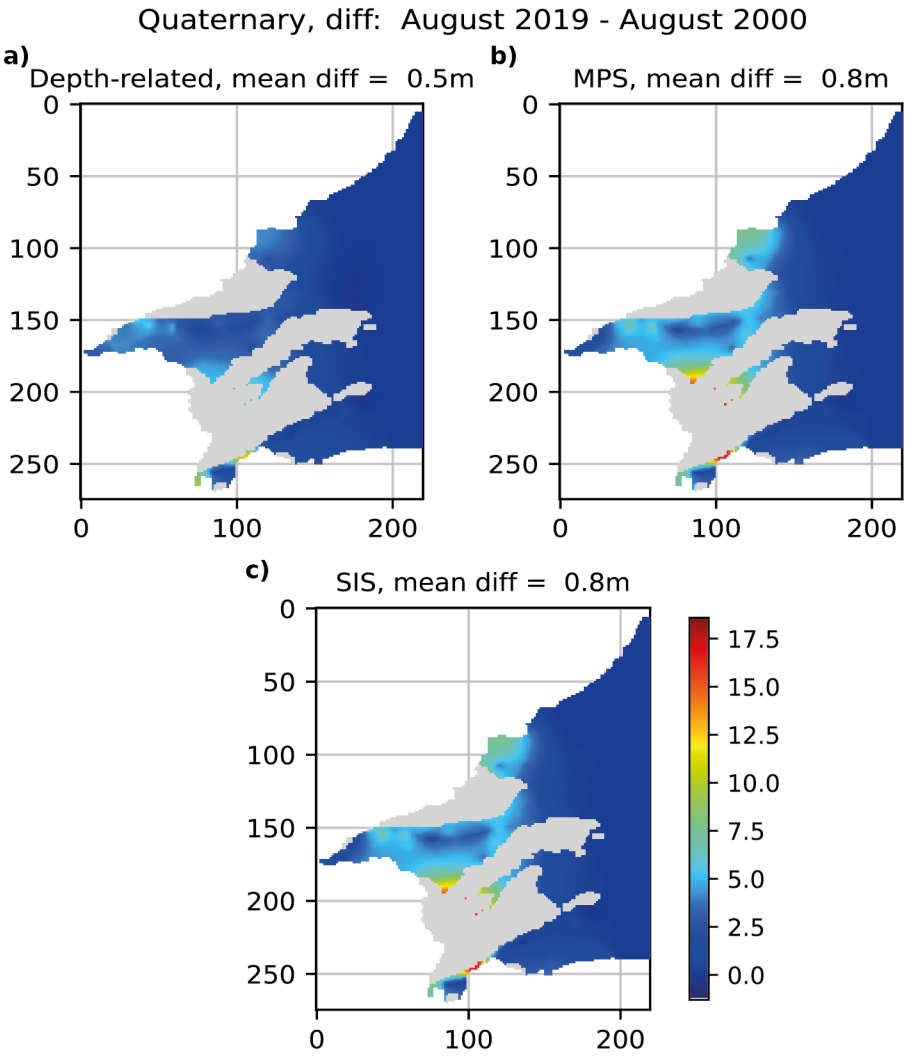

Figure A.12: Evolution of the piezometric water level of the Quaternary layer, between the simulated piezometric water level of August 2000 and the simulated piezometric water level of August 2019.

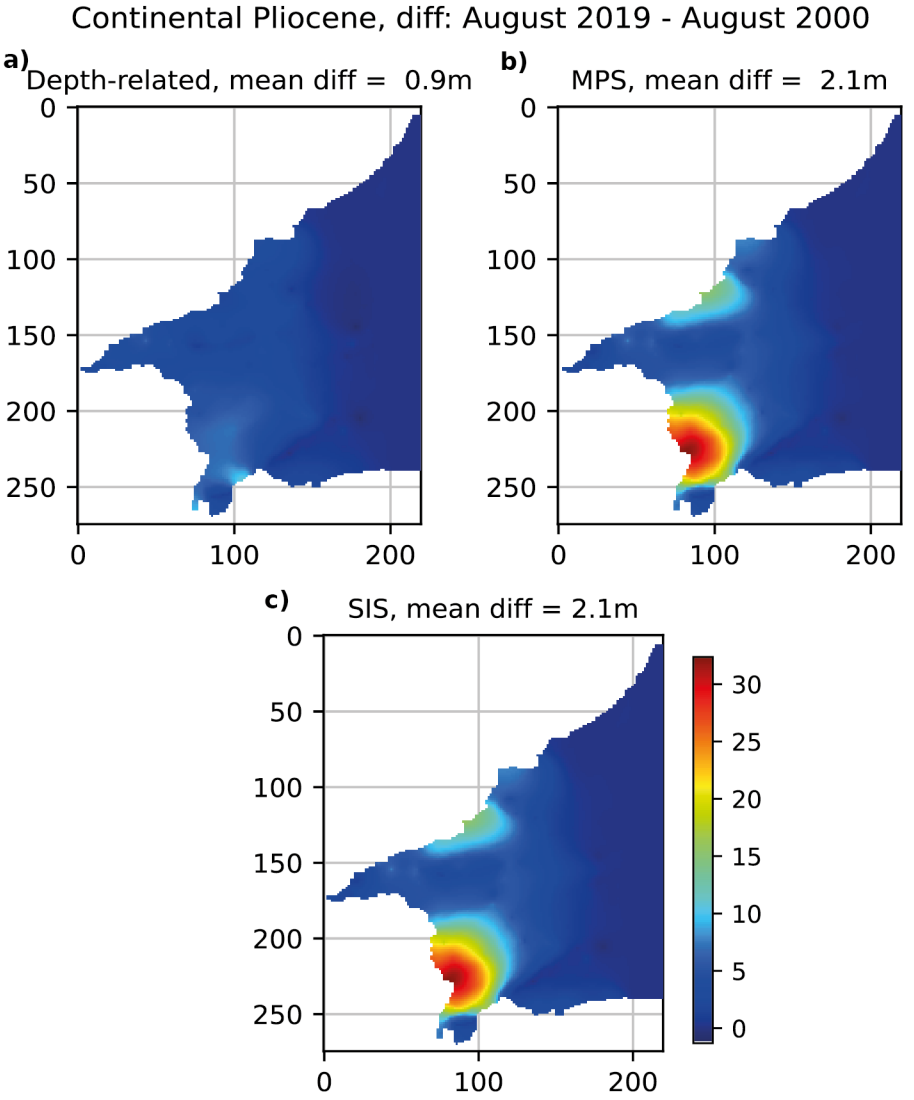

Figure A.13: Evolution of the piezometric water level of the Continental Pliocene first layer, between the simulated piezometric water level of August 2000 and the simulated piezometric water level of August 2019.

Bibliography

B. Aunay. *Apport de la stratigraphie séquentielle à la gestion et à la modélisation des ressources en eau des aquifères côtiers.* Theses, Université Montpellier II - Sciences et Techniques du Languedoc, 2007.

B. Aunay, C. Duvail, P. Le Strat, N. Dörfliger, P. Lachassagne, and S. Pistre. Importance of a high resolution lithological and geometrical knowledge for mediterranean coastal sedimentary aquifers management. application to the roussillon basin, south of france. In *Groundwater and Saline Intrusion, 18th Salt Water Intrusion Meeting–IAH, IHPUNESCO, IGME, Cartagena, Spain*, volume 15, pages 259–271, 2004.

B. Aunay, C. Duvail, G. Giordana, N. Doerfliger, P. Le Strat, M. Montginoul, and S. Pistre. A pluridisciplinary methodology for integrated management of a coastal aquifer: Geological, hydrogeological and economic studies of the Roussillon aquifer (Pyrénées-Orientales, France). *Vie et Milieu*, 56, 2006.

M. Bakker, V. Post, C. D. Langevin, J. D. Hughes, J. T. White, J. J. Starn, and M. N. Fienen. Scripting MODFLOW model development using python and FloPy. *Groundwater*, 54(5):733–739, Mar. 2016. doi: 10.1111/gwat.12413.

A. A. Barfod, I. Møller, A. V. Christiansen, A. S. Hoyer, J. Hoffimann, J. Straubhaar, and J. Caers. Hydrostratigraphic modeling using multiple-point statistics and airborne transient electromagnetic methods. *Hydrology and Earth System Sciences*, 22(6):3351–3373, 2018. ISSN 16077938. doi: 10.5194/hess-22-3351-2018.

Y. Barthélemy and J. Seguin. Modélisation maillée des écoulements souterrains – principes, démarche et recommandations. Technical report, BRGM, 2016.

M. Besbes and G. de Marsily. From infiltration to recharge: use of a parametric transfer function. *Journal of Hydrology*, 74(3-4):271–293, 1984.

M. Blouin, R. Martel, and E. Gloaguen. Accounting for aquifer heterogeneity from geological data to management tools. *Ground Water*, pages no–no, Aug. 2012. doi: 10.1111/j.1745-6584.2012.00982.x.

J. B. Boisvert, M. J. Pyrcz, and C. V. Deutsch. Multiple-point statistics for training image selection. *Natural Resources Research*, 16(4):313–321, 2007.

V. Bouzaglou, E. Crestani, P. Salandin, E. Gloaguen, and M. Camporese. Ensemble kalman filter assimilation of ert data for numerical modeling of seawater intrusion in a laboratory experiment. *Water*, 10(4):397, 2018.

BRLI. L11. Rapport de campagne de mesure sur la Têt et conclusion sur les flux de surfaces et souterrains. Technical Report 11, Brli ingénieurs, Nov. 2018a.

BRLI. L9. Rapport sur l'analyse détaillée de l'usage irrigation. Technical Report L9, Brl ingénieurs, Sept. 2018b.

P. Brunner and C. T. Simmons. Hydrogeosphere: a fully integrated, physically based hydrological model. *Ground water*, 50(2):170–176, 2012.

Y. Caballero and B. Ladouche. Impact of climate change on groundwater in a confined Mediterranean aquifer. *Hydrology and Earth System Sciences Discussions*, 12(10):10109–10156, 2015.

Y. Caballero, S. Lanini, J. Lechevalier, and J.-C. Maréchal. Caractérisation de la recharge des aquifères et évolution future en contexte de changement climatique- application au bassin rhône- méditerranée-corse. Technical report, BRGM, 2021.

Y. Caballero, Y. Balouin, L. Baudouy, S. Berne, F. Bouchette, B. Bourgine, F. Bourrin, L. Brun, C. Champollion, C. Duvail, V. Dall'Alba, B. Dewandel, A. Fioravanti, P. Garin, G. Henry, B. Issautier, T. Jacob, B. Ladouche, S. Lanini, E. Lasseur, J. Loffi, C. Loiselet, M.-A. Mauffrey, F. Meslard, M. Montginoul, N. N, P. Pezard, J.-B. Raynaud, P. Renard, J.-D. Rinaudo, L. Schorpp, L. Seguin, and A. Soulignac. Caractérisation transdisciplinaire d'un aquifère côtier complexe, pour une exploitation maitrisée et durable de sa ressource en eau en contexte méditerranéen : Le projet dem'eaux roussillon. rapport final. Technical report, BRGM, 2022a.

Y. Caballero, B. Ladouche, and B. Dewandel. Modèle conceptuel du comportement des eaux souterraines de l'aquifère plio-quaternaire de la plaine du roussillon, de 1960 à nos jours. Technical report, BRGM, 2022b.

M. L. Calvache and A. Pulido-Bosch. Effects of geology and human activity on the dynamics of salt-water intrusion in three coastal aquifers in southern spain. *Environmental Geology*, 30(3-4):215–223, Apr. 1997. doi: 10.1007/s002540050149.

P. C. Carman. Fluid flow through a granular bed. *Trans. Inst. Chem. Eng. London*, 15:150–156, 1937.

M. Chabart. *La recharge de l'aquifère multicouche du Roussillon et les conséquences d'un éventuel changement climatique sur la gestion de la recharge*. Éd. BRGM, Orléans, Jan. 1996. ISBN 978-2-7159-0839-0.

M. Chauveau, S. Chazot, C. Perrin, P.-Y. Bourgin, E. Sauquet, J.-P. Vidal, N. Rouchy, E. Martin, J. David, T. Norotte, P. Maugis, and X. De Lacaze. Quels impacts des changements climatiques sur les eaux de surface en France à l'horizon 2070 ? *La Houille Blanche*, (4):5–15, 2013. doi: 10.1051/lhb/2013027.

T. Chugunova and L. Hu. Multiple-point simulations constrained by continuous auxiliary data. *Mathematical Geosciences*, 40(2):133–146, 2008. doi: 10.1007/s11004-007-9142-4.

G. Clauzon, P. L. Strat, C. Duvail, D. D. Couto, J.-P. Suc, S. Molliex, F. Bache, D. Besson, E. H. Lindsay, N. D. Opdyke, J.-L. Rubino, S.-M. Popescu, B. U. Haq, and C. Gorini. The roussillon basin (s. france): A case-study to distinguish local and regional events between 6 and 3 ma. *Marine and Petroleum Geology*, 66:18–40, Sept. 2015. doi: 10.1016/j.marpetgeo.2015.03.012.

L. Colombera, F. Felletti, N. P. Mountney, and W. D. McCaffrey. A database approach for constraining stochastic simulations of the sedimentary heterogeneity of fluvial reservoirs. *AAPG bulletin*, 96(11):2143–2166, 2012.

A. Comunian, P. Renard, and J. Straubhaar. 3d multiple-point statistics simulation using 2D training images. *Computers & Geosciences*, 40:49–65, 2012.

K. S. Cordua, T. M. Hansen, M. L. Gulbrandsen, C. Barnes, and K. Mosegaard. Mixed-point geostatistical simulation: A combination of two-and multiple-point geostatistics. *Geophysical Research Letters*, 43(17):9030–9037, 2016.

V. Dall'Alba, P. Renard, J. Straubhaar, B. Issautier, C. Duvail, and Y. Caballero. 3d multiple-point statistics simulations of the roussillon continental pliocene aquifer using DeeSse. *Hess*, 2020. doi: 10.5194/hess-2020-96.

P. R. M. de Carvalho, J. F. C. L. da Costa, L. G. Rasera, and L. E. S. Varella. Geostatistical facies simulation with geometric patterns of a petroleum reservoir. *Stochastic Environmental Research and Risk Assessment*, 31(7):1805–1822, 2017. doi: 10.1007/s00477-016-1243-5.

G. de Marsily. *Cours d'hydrogéologie*. 2004.

G. de Marsily, F. Delay, J. Gonçalvès, P. Renard, V. Teles, and S. Violette. Dealing with spatial heterogeneity. *Hydrogeology Journal*, 13(1):161–183, 2005.

C. Deutsch and A. Journel. *GSLIB: Geostatistical Software Library and User's Guide, 2nd ed.* Oxford Univ. Press, Oxford, New York, 1998.

B. Dewandel, B. Ladouche, and Y. Caballero. Synthèse et valorisation des données d'essai par pompage réalisés sur les sites Dem'Mer et Dem'Ter dans le cadre du projet Dem'Eaux Roussillon. Technical report, BRGM, 2022.

H.-J. G. Diersch. Fundamental concepts of finite element method (FEM). In *FEFLOW*, pages 239–404. Springer Berlin Heidelberg, Aug. 2013. doi: 10.1007/978-3-642-38739-5_8.

J. Doherty. *Calibration and uncertainty analysis for complex environmental models*. Watermark Numerical Computing Brisbane, Australia, 2015.

J. Donea and A. Huerta. *Finite element methods for flow problems*. John Wiley & Sons, 2003.

C. Duvail. Expression des facteurs régionaux et locaux dans l'enregistrement sédimentaire d'une marge passive. Exemple de la marge du Golfe du Lion, étudiée selon un continuum terre-mer. *Université de Montpellier 2*, 2008. doi: tel-00438146.

C. Duvail. Caractérisation de la géométrie et de l ' architecture des formations du Pliocène de la plaine du Roussillon pour la modélisation hydrodynamique. Technical report, BRGM, Geoter, 2012.

C. Duvail, P. L. Strat, and B. Bourgine. Atlas géologique des formations plio-quaternaires de la plaine du roussillon (pyrénées-orientales). Technical report, BRGM, 2001.

C. Duvail, L. Baudouy, and A. Fioravanti. Synthèse géologique des forages Dem ' Mer et Dem ' Ter. Technical report, BRGM, 2021.

C. Duvail, S. Berné, C. Champollion, S. Delahaie, B. Issautier, T. Jacob, S. Laouenan, E. Lasseur, and M.-A. Mauffrey. Corrélation géologique terre-mer des formations du Plio-Quaternaire du Roussillon. Technical report, BRGM, 2022.

C. Edijatno & Michel. Un modèle pluie-débit à trois paramètres (a three-parameter daily rainfall-runoff model, in french). *La Houille Blanche*, pages 2–113, 1989.

A. A. Emerick. Analysis of the performance of ensemble-based assimilation of production and seismic data. *Journal of Petroleum Science and Engineering*, 139:219–239, Mar. 2016. doi: 10.1016/j.petrol.2016.01.029.

A. A. Emerick and A. C. Reynolds. Ensemble smoother with multiple data assimilation. *Computers & Geosciences*, 55:3–15, June 2013. doi: 10.1016/j.cageo.2012.03.011.

J. S. Famiglietti. The global groundwater crisis. *Nature Climate Change*, 4 (11):945–948, Oct. 2014. doi: 10.1038/nclimate2425.

A. Fioravanti, B. Bourgine, C. Loiselet, and Y. Caballero. Modélisation géologique 3D des formations quaternaires et pliocènes de la plaine du Roussillon et de leur continuum terre-mer Modélisation géologique 3D des formations quaternaires et pliocènes de la plaine du Roussillon et de leur continuum terre-mer. Technical report, BRGM, 2022.

R. A. Freeze, J. Massmann, L. Smith, T. Sperling, and B. James. Hydrogeological decision analysis: 1. a framework. *Ground Water*, 28(5):738–766, Sept. 1990. doi: 10.1111/j.1745-6584.1990.tb01989.x.

G. Galassi and G. Spada. Sea-level rise in the mediterranean sea by 2050: Roles of terrestrial ice melt, steric effects and glacial isostatic adjustment. *Global and Planetary Change*, 123:55–66, Dec. 2014. doi: 10.1016/j.gloplacha.2014.10.007.

G. Gaspari and S. E. Cohn. Construction of correlation functions in two and three dimensions. *Quarterly Journal of the Royal Meteorological Society*, 125 (554):723–757, Jan. 1999. doi: 10.1002/qj.49712555417.

A. Genna. Carte géologique harmonisée du département des pyrénées-orientales. notice technique. rapport final. rp-57032fr. Technical report, BRGM, 2009.

T. Gneiting, F. Balabdaoui, and A. E. Raftery. Probabilistic forecasts, calibration and sharpness. *Journal of the Royal Statistical Society: Series B (Statistical Methodology)*, 69(2):243–268, 2007.

J. J. Gómez-Hernández and R. M. Srivastava. Isim3d: An ansi-c three-dimensional multiple indicator conditional simulation program. *Computers & Geosciences*, 16(4):395–440, 1990.

H. Guo and J. J. Jiao. Impact of coastal land reclamation on ground water level and the sea water interface. *Ground Water*, 45(3):362–367, may 2007. doi: 10.1111/j.1745-6584.2006.00290.x.

J. Hoffimann, C. Scheidt, A. Barfod, and J. Caers. Stochastic simulation by image quilting of process-based geological models. *Computers & Geosciences*, 106:18–32, Sept. 2017. doi: 10.1016/j.cageo.2017.05.012.

A. S. Høyer, G. Vignoli, T. M. Hansen, L. T. Vu, D. A. Keefer, and F. Jørgensen. Multiple-point statistical simulation for hydrogeological models: 3-D training image development and conditioning strategies. *Hydrology and Earth System Sciences*, 21(12):6069–6089, 2017. ISSN 16077938. doi: 10.5194/hess-21-6069-2017.

L. Y. Hu and T. Chugunova. Multiple-point geostatistics for modeling subsurface heterogeneity: A comprehensive review. *Water Resources Research*, 44 (11):1–14, 2008. doi: 10.1029/2008WR006993.

M. Huysmans and A. Dassargues. Application of multiple-point geostatistics on modelling groundwater flow and transport in a cross-bedded aquifer (belgium). *Hydrogeology Journal*, 17(8):1901–1911, Aug. 2009. doi: 10.1007/s10040-009-0495-2.

IPCC. *Climate Change 2022: Impacts, Adaptation and Vulnerability*. Summary for Policymakers. Cambridge University Press, Cambridge, UK and New York, USA, 2022. ISBN 9781009325844.

B. Issautier, C. Duvail, J. Briais, and E. Lasseur. Caractérisation géologique du Pliocène de la Plaine du Roussillon : synthèse de la tâche « Terrain ». Technical report, BRGM, 2021.

C. Jäggli, J. Straubhaar, and P. Renard. Posterior population expansion for solving inverse problems. *Water Resources Research*, 53(4):2902–2916, Apr. 2017. doi: 10.1002/2016wr019550.

A. Journel and F. Alabert. Focusing on spatial connectivity of extreme-valued attributes: Stochastic indicator models of reservoir heterogeneities. *AAPG Bull.;(United States)*, 73(CONF-890404-), 1989.

A. G. Journel. Nonparametric estimation of spatial distributions. *Journal of the International Association for Mathematical Geology*, 15:445–468, 1983.

P. Juda, P. Renard, and J. Straubhaar. A framework for the cross-validation of categorical geostatistical simulations. *Earth and Space Science*, 2020. doi: 10.1029/2020ea001152.

P. Juda, J. Straubhaar, and P. Renard. Comparison of three recent discrete stochastic inversion methods and influence of the prior choice. *Comptes Rendus. Géoscience*, 355(S1):1–26, Oct. 2022. doi: 10.5802/crgeos.160.

P. Juda, J. Straubhaar, and P. Renard. Comparison of three recent discrete stochastic inversion methods and influence of the prior choice. *Comptes Rendus. Géoscience*, 355(S1):1–26, 2023.

C. E. Koltermann and S. M. Gorelick. Heterogeneity in sedimentary deposits: A review of structure-imitating, process-imitating, and descriptive approaches. *Water Resources Research*, 32(9):2617–2658, 1996.

R. Kruel Romeu. *Fluid flow in heterogenous media-Evaluation of permeability in steady state and transient case*. PhD thesis, IFP, Rueil-Malmaison, France, 1994.

X. Kuang, J. J. Jiao, C. Zheng, J. A. Cherry, and H. Li. A review of specific storage in aquifers. *Journal of Hydrology*, 581:124383, Feb. 2020. doi: 10.1016/j.jhydrol.2019.124383.

B. Ladouche and N. Dörflinger. Évaluation des ressources en eau des Corbières. Phase I - Synthèse de la caractérisation des systèmes karstiques des Corbières orientales. Rapport final. Volume 2 - Caractérisation géologique et hydrogéologique du système karstique du synclinal du Bas-Agly. Technical report, BRGM, 2016.

D.-T. Lam, P. Renard, J. Straubhaar, and J. Kerrou. Multiresolution approach to condition categorical multiple-point realizations to dynamic data with iterative ensemble smoothing. *Water Resources Research*, 56(2): e2019WR025875, 2020.

C. D. Langevin, J. D. Hughes, E. Banta, A. Provost, R. Niswonger, and S. Panday. *MODFLOW 6, the U.S. Geological Survey Modular Hydrologic Model*. U.S. Geological Survey, 2017. doi: 10.5066/F76Q1VQV.

S. Lanini, L. Schorpp, and V. Dall'Alba. Modélisation des écoulements souterrains dans la plaine du Roussillon : modèle MartROUSS. Technical report, BRGM, 2022.

A. T. Leaf, M. N. Fienen, and H. W. Reeves. Sfrmaker and linesink-maker: Rapid construction of streamflow routing networks from hydrography data. *Groundwater*, 59(5):761–771, Apr. 2021. doi: 10.1111/gwat.13095.

N. Linde, P. Renard, T. Mukerji, and J. Caers. Geological realism in hydrogeological and geophysical inverse modeling: A review. *Advances in Water Resources*, 86:86–101, Dec. 2015. doi: 10.1016/j.advwatres.2015.09.019.

J. Lofi, C. Gorini, S. Berné, G. Clauzon, A. T. D. Reis, W. B. Ryan, and M. S. Steckler. Erosional processes and paleo-environmental changes in the western gulf of lions (SW france) during the messinian salinity crisis. *Marine Geology*, 217(1-2):1–30, May 2005. doi: 10.1016/j.margeo.2005.02.014.

J. L. Mallet. GOCAD: A computer aided design program for geological applications. In *Three-Dimensional Modeling with Geoscientific Information Systems*, pages 123–141. Springer Netherlands, 1992. doi: 10.1007/978-94-011-2556-7_11.

J. C. Manning. *Applied principles of hydrology*. Waveland Press, 2016.

G. Mariethoz and J. Caers. *Multiple-Point Geostatistics: stochastic modeling with training images*. Wiley-Blackwell. A John wiley and Sons, LTD, Publication, 2014.

G. Mariethoz, P. Renard, and J. Straubhaar. The direct sampling method to perform multiple-point geostatistical simulations. *Water Resources Research*, 46(11):1–14, 2010. doi: 10.1029/2008WR007621.

M. Martínez, A. Intralawan, G. Vázquez, O. Pérez-Maqueo, P. Sutton, and R. Landgrave. The coasts of our world: Ecological, economic and social importance. *Ecological Economics*, 63(2-3):254–272, Aug. 2007. doi: 10.1016/j.ecolecon.2006.10.022.

G. Martinsen, H. Bessiere, Y. Caballero, J. Koch, A. J. Collados-Lara, M. Mansour, O. Sallasmaa, D. Pulido-Velazquez, N. H. Williams, W. J. Zaadnoordijk, and S. Stisen. Developing a pan-european high-resolution groundwater recharge map – combining satellite data and national survey data using machine learning. *Science of The Total Environment*, 822:153464, May 2022. doi: 10.1016/j.scitotenv.2022.153464.

J. P. Masterson and S. P. Garabedian. Effects of sea-level rise on ground water flow in a coastal aquifer system. *Ground Water*, 45(2):209–217, Mar. 2007. doi: 10.1111/j.1745-6584.2006.00279.x.

G. Matheron. Principles of geostatistics. *Economic Geology*, 58(8):1246–1266, 1963. doi: 10.2113/gsecongeo.58.8.1246.

G. Matheron, H. Beucher, C. De Fouquet, A. Galli, D. Guerillot, C. Ravenne, et al. Conditional simulation of the geometry of fluvio-deltaic reservoirs. *Society of Petroleum Engineers*, 1987.

G. McGranahan, D. Balk, and B. Anderson. The rising tide: assessing the risks of climate change and human settlements in low elevation coastal zones. *Environment and Urbanization*, 19(1):17–37, Apr. 2007. doi: 10.1177/0956247807076960.

H. K. McMillan, I. K. Westerberg, and T. Krueger. Hydrological data uncertainty and its implications. *WIREs Water*, 5(6), Sept. 2018. doi: 10.1002/wat2.1319.

E. Meerschman, G. Pirot, G. Mariethoz, J. Straubhaar, M. Van Meirvenne, and P. Renard. A practical guide to performing multiple-point statistical simulations with the Direct Sampling algorithm. *Computers and Geosciences*, 52: 307–324, 2013. doi: 10.1016/j.cageo.2012.09.019.

N. Metropolis and S. Ulam. The monte carlo method. *Journal of the American Statistical Association*, 44(247):335–341, Sept. 1949. doi: 10.1080/01621459.1949.10483310.

R. Meyer, P. Engesgaard, A.-S. Høyer, F. Jørgensen, G. Vignoli, and T. O. Sonnenborg. Regional flow in a complex coastal aquifer system: Combining voxel geological modelling with regularized calibration. *Journal of Hydrology*, 562:544–563, July 2018. doi: 10.1016/j.jhydrol.2018.05.020.

A. Micallef, M. Person, A. Haroon, B. A. Weymer, M. Jegen, K. Schwalenberg, Z. Faghih, S. Duan, D. Cohen, J. J. Mountjoy, S. Woelz, C. W. Gable, T. Averes, and A. K. Tiwari. 3d characterisation and quantification of an offshore freshened groundwater system in the canterbury bight. *Nature Communications*, 11(1), Mar. 2020. doi: 10.1038/s41467-020-14770-7.

A. M. Mood. The distribution theory of runs. *The Annals of Mathematical Statistics*, 11(4):367–392, 1940.

P. Mourlanette, P. Biver, P. Renard, B. Nœtinger, G. Caumon, and Y. A. Perrier. Direct simulation of non-additive properties on unstructured grids. *Advances in Water Resources*, 143:103665, 2020.

N. Naranjo-Fernández, C. Guardiola-Albert, and E. Montero-González. Applying 3D geostatistical simulation to improve the groundwater management modelling of sedimentary aquifers: The case of Doñana (Southwest Spain). *Water (Switzerland)*, 11(1), 2018. doi: 10.3390/w11010039.

A. Neven, V. Dall'Alba, P. Juda, J. Straubhaar, and P. Renard. Ice volume and basal topography estimation using geostatistical methods and ground-penetrating radar measurements: application to the tsanfleuron and scex rouge glaciers, swiss alps. *The Cryosphere*, 15(11):5169–5186, Nov. 2021. doi: 10.5194/tc-15-5169-2021.

A. Neven, A. V. Christiansen, and P. Renard. Automatic stochastic 3D clay fraction model from tTEM survey and borehole data. *Scientific Reports*, 12 (1), Oct. 2022a. doi: 10.1038/s41598-022-21555-z.

A. Neven, L. Schorpp, and P. Renard. Stochastic multi-fidelity joint hydro-geophysical inversion of consistent geological models. *Frontiers in Water*, 4, Oct. 2022b. doi: 10.3389/frwa.2022.989440.

N. Neverre and A. Mathey. Modèle d'optimisation de l'approvisionnement en eau potable de la plaine du roussillon par rapport aux ressources disponibles. Technical report, BRGM, 2022.

G. J. Nichols and J. A. Fisher. Processes, facies and architecture of fluvial distributary system deposits. *Sedimentary Geology*, 195(1-2):75–90, 2007. doi: 10.1016/j.sedgeo.2006.07.004.

V. E. Post, J. Groen, H. Kooi, M. Person, S. Ge, and W. M. Edmunds. Offshore fresh groundwater reserves as a global phenomenon. *Nature*, 504(7478):71–78, Dec. 2013. doi: 10.1038/nature12858.

P. Renard and R. Ababou. Equivalent permeability tensor of heterogeneous media: Upscaling methods and criteria (review and analyses). *Geosciences*, 12(7):269, July 2022. doi: 10.3390/geosciences12070269.

P. Renard and G. de Marsily. Calculating equivalent permeability: a review. *Advances in Water Resources*, 20(5-6):253–278, Oct. 1997. doi: 10.1016/s0309-1708(96)00050-4.

P. Renard, G. L. Loc'h, E. Ledoux, G. de Marsily, and R. Mackay. A fast algorithm for the estimation of the equivalent hydraulic conductivity of heterogeneous media. *Water Resources Research*, 36(12):3567–3580, Dec. 2000. doi: 10.1029/2000wr900203.

P. Renard, A. Alcolea, and D. Ginsbourger. Stochastic versus deterministic approaches. In *Environmental Modelling*, pages 133–149. John Wiley & Sons, Ltd, Jan. 2013. doi: 10.1002/9781118351475.ch8.

L. Schorpp, J. Straubhaar, and P. Renard. Automated hierarchical 3d modeling of quaternary aquifers: The ArchPy approach. *Frontiers in Earth Science*, 10, May 2022. doi: 10.3389/feart.2022.884075.

L. Schorpp, V. Dall'Alba, P. Renard, S. Lanini, and Y. Caballero. Hydrogeological modeling of the roussillon coastal aquifer (france): stochastic inversion and analysis of future stresses. *Environmental Earth Sciences*, 82(9), Apr. 2023. doi: 10.1007/s12665-023-10877-4.

S. L. Serra O. et al. *Sedimentological analysis of shale-sand series from well logs*. Society of Petrophysicists and Well-Log Analysts, 1975.

C. E. Shannon. A Mathematical Theory of Communication. *Bell System Technical Journal*, 5(3), 1948. doi: 10.1002/j.1538-7305.1948.tb01338.x.

L. Shi and J. J. Jiao. Seawater intrusion and coastal aquifer management in china: a review. *Environmental Earth Sciences*, 72(8):2811–2819, Mar. 2014. doi: 10.1007/s12665-014-3186-9.

J. Straubhaar. DeeSse user's guide. Technical report, The Centre for Hydrogeology and Geothermics (CHYN), University of Neuchâtel: Neuchâtel, Switzerland, 2019.

J. Straubhaar and P. Renard. Conditioning multiple-point statistics simulation to inequality data. *Earth and Space Science*, 8(5), May 2021. doi: 10.1029/2020ea001515.

J. Straubhaar, P. Renard, G. Mariethoz, R. Froidevaux, and O. Besson. An improved parallel multiple-point algorithm using a list approach. *Mathematical Geosciences*, 43(3):305–328, 2011. doi: 10.1007/s11004-011-9328-7.

J. Straubhaar, A. Walgenwitz, and P. Renard. Parallel multiple-point statistics algorithm based on list and tree structures. *Mathematical Geosciences*, 45 (2):131–147, 2013. doi: 10.1007/s11004-012-9437-y.

J. Straubhaar, P. Renard, and G. Mariethoz. Conditioning multiple-point statistics simulations to block data. *Spatial Statistics*, 16:53–71, 2016.

J. Straubhaar, P. Renard, and T. Chugunova. Multiple-point statistics using multi-resolution images. *Stochastic Environmental Research and Risk Assessment*, 34(2):251–273, Feb. 2020a. doi: 10.1007/s00477-020-01770-8.

J. Straubhaar, P. Renard, and T. Chugunova. Multiple-point statistics using multi-resolution images. *Stochastic Environmental Research and Risk Assessment*, 34(2):251–273, Feb. 2020b. doi: 10.1007/s00477-020-01770-8.

S. Strebelle, K. Payrazyan, and J. Caers. Modeling of a Deepwater Turbidite Reservoir Conditional to Seismic Data Using Multiple-Point Geostatistics. *SPE Annual Technical Conference and Exhibition*, 2002. doi: 10.2118/77425-MS.

P. Tahmasebi, A. Hezarkhani, and M. Sahimi. Multiple-point geostatistical modeling based on the cross-correlation functions. *Computational Geosciences*, 16(3):779–797, 2012. doi: 10.1007/s10596-012-9287-1.

A. Tarantola. *Inverse Problem Theory and Methods for Model Parameter Estimation*. Society for Industrial and Applied Mathematics, Jan. 2005. doi: 10.1137/1.9780898717921.

V. Todaro, M. D'Oria, M. G. Tanda, and J. J. Gómez-Hernández. Ensemble smoother with multiple data assimilation to simultaneously estimate the source location and the release history of a contaminant spill in an aquifer. *Journal of Hydrology*, 598:126215, 2021.

J.-P. Vidal, E. Martin, L. Franchistéguy, M. Baillon, and J.-M. Soubeyroux. A 50-year high-resolution atmospheric reanalysis over france with the safran system. *International Journal of Climatology*, 30(11):1627–1644, Sept. 2009. doi: 10.1002/joc.2003.

J. F. Wellmann and K. Regenauer-lieb. Uncertainties have a meaning : Information entropy as a quality measure for 3-D geological models. *Tectonophysics*, 526-529:207–216, 2012. doi: 10.1016/j.tecto.2011.05.001.

X.-H. Wen and J. J. Gómez-Hernández. Upscaling hydraulic conductivities in heterogeneous media: An overview. *Journal of Hydrology*, 183(1-2):ix–xxxii, 1996.

A. D. Werner and C. T. Simmons. Impact of sea-level rise on sea water intrusion in coastal aquifers. *Ground Water*, 47(2):197–204, Mar. 2009. doi: 10.1111/j.1745-6584.2008.00535.x.

J. T. White. A model-independent iterative ensemble smoother for efficient history-matching and uncertainty quantification in very high dimensions. *Environmental Modelling & Software*, 109:191–201, 2018.

T. Xu and J. J. Gómez-Hernández. Characterization of non-gaussian conductivities and porosities with hydraulic heads, solute concentrations, and water temperatures. *Water Resources Research*, 52(8):6111–6136, 2016.

T. Zhang, P. Switzer, and A. Journel. Filter-based classification of training image patterns for spatial simulation. *Mathematical Geology*, 38(1):63–80, 2006. doi: 10.1007/s11004-005-9004-x.